Filipe Luís Alves Ribeiro

Mestre em Engenharia Civil

Robustness Analysis of Structures in Post-Earthquake Scenarios Considering Multiple Hazards

Dissertação para obtenção do Grau de Doutor em Engenharia Civil

Orientador:	Prof. Doutor Luís Armando Canhoto Neves Professor Auxiliar, Faculdade de Ciências e Tecnologia, Universidade Nova de Lisboa, Portugal
Co-orientador:	Prof. Doutor André Ramos Barbosa Professor Auxiliar, School of Civil and Construction Engineering, Oregon State University, E.U.A.

Júri:

Presidente:	Prof. Doutor Fernando Manuel Anjos Henriques
Arguentes:	Prof. Doutora Rita Nogueira Leite Pereira Bento Prof. Doutor Eduardo Soares Ribeiro Gomes Cavaco
Vogais:	Prof. Doutor Luís Manuel Soares dos Santos Castro Prof. Doutor José Miguel de Freitas Castro Prof. Doutor Filipe Pimentel Amarante dos Santos

FACULDADE DE CIÊNCIAS E TECNOLOGIA
UNIVERSIDADE NOVA DE LISBOA

Janeiro 2017

Dissertação apresentada para cumprimento dos requisitos necessários à obtenção do grau de Doutor em Engenharia Civil, realizada sob a orientação científica do Doutor Luís A.C. Neves e do Doutor André R. Barbosa.

Trabalho financiado pela Fundação para a Ciência e a Tecnologia através dos fundos nacionais do Ministério da Ciência, Tecnologia e Ensino Superior ao abrigo da bolsa individual de Doutoramento com referência SFRH/BD/77722/2011.

Robustness Analysis of Structures in Post-Earthquake Scenarios Considering Multiple Hazards

To my family

Acknowledgements

This work is the result of a four-year research that could not have been possible without the support of several people to whom I would like to dedicate some words.

First of all, I would like to thank my advisor, Professor Luís Canhoto Neves, his patience, incentive, joy in developing research, and friendship. The advice he gave me, both technical and personal, as well as his experience, were fundamental and helped me discovering and exploring this new world of research. I am also thankful for the opportunity of studying at the University of Nottingham. The period I spent there was a catalyst of new projects and ideas. I do not forget the opportunity Professor Luís Neves created for me to continue developing my work there. This time at Nottingham was particularly pleasant due to his support and friendship, as well as his family.

I am also very thankful to my co-advisor, Professor André Ramos Barbosa, who is a reference that I have always tried to follow. His participation in this work was absolutely fundamental. In spite of the distance that separated us during most of the time period of this research, Professor André Barbosa have always been available and actively participating in the development of numeral analysis. His knowledge and experience in this field were the light that guided me throughout this time. The time I spent at the Oregon State University (OSU) was a very important first step in the development of this work. The opportunity to study of the OSU was unique, both in the professional and personal point of view. I have to thank him for this and so many other opportunities that him and his proactivity, excellence, and tenacity, helped me figuring out. I have to mention and truly thank the long hours we spent skyping at early or late hours in the US. I also thank his active and key participation in the workshop OpenSees Days Portugal 2014, and in my Research Plan defense.

I cannot forget the support of Professor Rita Bento and Professor José Miguel Castro. Their help and availability during the course of this work were great, as well as their support and valuable input in the evaluation moments, such as the defense of the research plan. I thank Professor Rita Bento for welcoming me in *Instituto Superior Técnico* and giving me the chance to attend some lectures there. I also thank Professor José Miguel Castro for the mentoring, active participation and support in the OpenSees Days Portugal 2014. Without his and Professor Xavier Romão help it could not have been possible to organize the workshop and bring to Portugal dozens of researchers.

I would like to thank to other Professor and researchers who helped me at various stages of this research. I thank Professor Michael H. Scott, Professor Eduardo Cavaco, Professor Filipe Santos, Professor Corneliu Cismasiu, Professora Ildi Cismasiu, Professor João Rocha de Almeida, Professor António Pinho Ramos, and Professor Válter Lúcio.

I also thank my fellow Ph.D. student Nuno S. Pereira, with whom I kept long and inspiring conversation and with whom I have had the pleasure of organizing the mentioned OpenSees Days Portugal 2014 workshop. I do not know a Ph.D. student with such deeper knowledge of this field of study than Nuno and truly hope that the future brings him chal-

lenges that meet his excellence.

I am also very pleased to have had the opportunity of sharing so many working hours with mu colleague Rúben Rosário. I started to collaborate with him in 2013 during his master thesis and since then his help has been really important to this work, namely in what concerns structural fire analysis. I also thank Sérgio Domingues, with whom I collaborated in his master thesis. I thank them for their patience and friendship and for not giving up towards the adversities that came into our way.

I thank to my colleagues at the universities I have been during this period. The share of ideas, motivation, mutual help, and fun are some of the most important memories that will remain in my memory. I thank Hugo Fernandes, Renato Pereira, Leonardo Rodrigues, Cláudia Ferreira, Nuno Deusdado, André Oliveira, Fernando Jorne, Nuno Mamede, André Rodrigues, Micael Inácio, Mariana Barros, Hugo Silva, Pedro Saldanha Santos, André Belejo, Therese Pflaum, Mohsen, Ravi Challa, Simon Stubbs, and many others that have seen our paths crossed.

The support of *Faculdade de Ciências e Tecnologia* of NOVA Lisbon University is greatly acknowledged. I have spent the last nine years as a student at NOVA University. I am proud to say that I take with me amazing memories and experiences. In spite of all contingencies NOVA University is the best. I also thank the support of the Oregon State University and the University of Nottingham during the time I spent at each of them. The support of Engineering Faculty of Porto University in the organization of the OpenSees Days Portugal 2014 is also greatly acknowledged.

The support of the Portuguese Science and Technology Foundation, from the Ministry of Science, Technology, and Higher Education, which financed this work through an individual doctoral grant is also acknowledged. My choice to stay in Portugal was hard but I conscientiously think that I am able and I want to support the development of my beloved country and return the investment that was made in my own development.

A sincere acknowledgment has to be made to *Profico - Projetos, Fiscalização e Consultoria, Lda.*, in particular to Eng. Jorge Meneses and to Eng. Carlos Lopes, who gave me the opportunity to continue my learning process after the Ph.D., as a Structural Engineer. I truly hope that my time at Profico will be full of success for many and good years.

I want to thank my friends, for the moments of fun, joy, and emotion that inspired me and gave me energy to complete this work. A special work for Filipe Pereira, for his friendship and incentive at all times.

Finally, but not less important, I want to thank the infinite love, support, incentive and comfort of my family, in particular to my parents, sister, and grandmother. They are a central key in my whole life and, of course, in the course of this work. The example and the advice they give me are essential to me, and without them I would not have followed this path.

At last, the biggest of all acknowledgments is due to my precious and beloved wife, Rosa, whose generosity, altruism, love, and infinite patience and support, I am not able to describe by words. She has been always by my side and I hope she will always be. No words exist to describe my gratitude and love.

In addition to the people mentioned in here, I have had the privilege to meet many others during the course of this work. They inspired me, encouraged me, helped me, criticized me, and will remain in my memory. As it is not possible to individually mention all, here is my sincere acknowledgment to all of them.

Abstract

Recent earthquakes have highlighted that the consideration of isolated seismic events, although necessary, may not be sufficient to prevent building collapse. In fact, the occurrence of a large number of aftershocks with significant intensity, as well as the occurrence of tsunamis, fires, and explosions, poses a safety threat that has not been addressed properly in the design and assessment of building structures over the last decade. Although research has been developed in order to evaluate the impact of multiple and/or cascading hazards in structural safety and economical losses, there is no established framework to perform such analysis. In addition, the available numerical tools lack a unified implementation in a widely used software in order to allow for the development of large numerical simulations involving these hazard events.

This work proposes a probabilistic framework for quantifying the robustness of structures considering the occurrence of a major earthquake (mainshock) and the subsequent cascading hazard events, namely fire and aftershocks. These events can significantly increase the probability of collapse of buildings, especially for structures that are damaged during the mainshock. In order to assess the structural performance under post-earthquake hazards, it is of paramount importance to accurately simulate the damage attained during the earthquake, which is strongly correlated to the residual structural capacity to withstand cascading events. In this context, the influence of ground motion characteristics, namely ground motion duration, has been identified as one of the parameters that may induce significant bias on damage patterns associated with the mainshock. Thus, ground motion duration influence on structural damage is analyzed in this work.

Steel moment resisting frame buildings designed according to pre-Northridge codes are analyzed using the proposed framework. These buildings are representative of the design practice in the US and Europe for decades, and the conclusions of this work can be significant in the assessment/retrofit of thousands of buildings. Fragility curves and reliability-based robustness measures are obtained using the proposed framework. The fragility curve parameters obtained herein can be used in the development of future probabilistic-based studies considering post-earthquake hazards. The results highlight the importance of the post-earthquake hazard events in the structural safety assessment. Further work is needed in order to better characterize these hazards as to include them in the code-based design and assessment methodologies.

Keywords:

Aftershocks, Fire, Non-linear Dynamic Analysis, Reliability, Robustness, Seismic Analysis.

Resumo

Título em Português: Análise da Robustez de Estruturas em Cenários Pós-Sismo Considerando Exposições Múltiplas

Nas últimas décadas a ocorrência de eventos sísmicos de elevada intensidade tem exposto a necessidade de considerar os eventos secundários que normalmente se seguem ao sismo principal, i.e. ao sismo de maior intensidade. Estes eventos secundários, como réplicas do sismo principal, incêndios, tsunamis e explosões, colocam em risco os edifícios que, resistindo ao sismo principal, se encontrem danificados e, consequentemente, com a sua capacidade resistente diminuída face ao considerado em projeto. Embora tenham sido desenvolvidos recentemente esforços no sentido de desenvolver métodos de análise e dimensionamento que consideram eventos múltiplos e/ou sequenciais, não se encontra estabelecida nenhuma ferramenta de análise para avaliar a segurança estrutural em cenários pós-sismo. Além disso, para executar tal avaliação é necessário dispor de modelos numéricos cuja implementação em ferramentas de simulação estrutural permitam a realização de análises neste tipo de cenários.

Neste trabalho é desenvolvida uma nova metodologia probabilística de análise da robustez de estruturas considerando a ocorrência de um evento sísmico (sismo principal) e de eventos secundários, nomeadamente réplicas e fogo. De modo a avaliar a resposta estrutural em cenários pós-sismo é fundamental que o dano induzido pelo sismo principal seja simulado de forma fidedigna. A capacidade resistente residual pós-sismo encontra-se correlacionada com o dano estrutural devido ao sismo. Assim, as características do sismo principal, em particular a sua duração, e a sua influência no dano estrutural é estudada neste trabalho.

A metodologia proposta é aplicada ao estudo de edifícios metálicos porticados dimensionados de acordo com regulamentos pré-Northridge. Este tipo de edifícios é representativo de uma elevada percentagem dos edifícios de estrutura metálica existentes nos E.U.A. e na Europa. Desta forma, as conclusões deste trabalho poderão ser úteis para a avaliação futura da segurança e/ou reforço desses edifícios. Usando a metodologia proposta são obtidas curvas de fragilidade e indicadores de robustez baseados em conceitos de fiabilidade. Os resultados obtidos indicam que os eventos pós-sismo poderão ter uma influência significativa na segurança e, como tal, será importante a sua consideração em futuros estudos de risco pós-sismo. No entanto, investigação futura é necessária de forma a melhor caracterizar estes riscos no sentido de os incluir nos regulamentos de análise e dimensionamento.

Palavras chave:

Análise Dinâmica Não-Linear, Análise Sísmica, Fiabilidade, Réplicas, Robustez, Fogo.

Contents

List of Figures

List of Tables

List of Symbols and Abbreviations

Symbols - Latin Alphabet

Symbol	**Description**	**Units**
A	Cross-section area	[m^2]
A_{pinch}	Reloading factor: ratio of the reloading force to the target force	$[-]$
A_f	Room plan area	[m^2]
b	Thermal inertia	[J m^{-2} K^{-1} s$^{-1/2}$]
$b(x)$	Interpolation function matrix	$[-]$
C_i	Structural capacity	[F]
CAV	Cumulative absolute velocity	[m/s]
D	Demand	[N]
d^{member}	Deformation of the member committed in the previous converged step	[mm]
D_{5-75}	Significant duration	[s]
d_{i-1}^{max}	Maximum deformation observed up to the $i-1$ excursion	[mm]
d_{pc}	Post-capping deformation capacity	[m or rad]
d_i	Target deformation of the member	[mm]
d_m	Maximum deformation	[m or rad]
d_p	Plastic deformation capacity	[m or rad]
d_u	Ultimate deformation	[m or rad]
d_y	Yield deformation	[m or rad]
DI_{PA}	Park and Ang damage index	[-]
$DI_{PA}^{max-member}$	Park and Ang maximum recorded damage index	[-]
$DI_{PA}^{structural}$	Park and Ang structural damage index	[-]
DI_{RV}	Reinhorn and Valles damage index	[-]
$DI_{RV}^{max-member}$	Reinhorn and Valles maximum recorded damage index	$[-]$
$DI_{RV}^{structural}$	Reinhorn and Valles structural damage index	$[-]$
DS^f	Damage state after fire/blast	$[-]$
DS^m	Damage state after mainshock	$[-]$
dU_f	Increment of the displacement of the control DOF	[m]
E	Elastic modulus	[GPa]
$e(x)$	Vector of section deformations	$[-]$
E_t	Hysteretic energy dissipation capacity	[kNm.m]
E_0	Modulus of elasticity at ambiente temperature	[GPa]
E_f	Efficiency	$[\%]$
E_i	Hysteretic energy dissipated in excursion i	[kNm.m]
EI	Cross-section flexural stiffness	[kNm.m]
EI_{mod}	Modified elastic stiffness of the element interior	[kNm.m]
f	Fire or blast scenario following mainshock	[-]
$F(d^{member})$	Force associated with the displacement d^{member}	[kNm or kN]
$f_{I/J}$	Flexibility of the I/J end spring	[m/kN]
f_{int}	Flexibility of the element interior	[m/kN]

$F_{r,p/n}$	Reloading factor: ratio of the reloading deformation to the target deformation	[-]
$F_{y,0.2\%}$	Reference steel yield strength with strain offset of 0.2% (at ambiente temperature)	[MPa]
$F_{y,2\%}$	Effective steel yield strength with strain offset of 2% (at ambiente temperature)	[MPa]
F_c	Capping strength	[kN or kNm]
F_P	Proportional limit strength	[MPa]
F_r	Residual strength	[kN or kNm]
f_S	Section flexibility	[-]
F_y	Yield strength	[kN or kNm]
i_{max}	Maximum number of iterations	$[-]$
I_{rob}	Robustness index	$[-]$
IA	Arias intensity	[m/s]
$im^{a,c}$	Minimum aftershock ground motion intensity leading to collapse	[g]
IM^a	Aftershock intensity measure	[g]
IM^m	Mainshock intensity measure	[g]
IM_F	Fire intensity measure	$[^\circ C]$
IPs	Integration points	$[-]$
$K_{E,\theta}$	Modulus of elasticity reduction coefficient	$[-]$
$K_{P,\theta}$	Proportional limit strength reduction coefficient	$[-]$
$K_{y,\theta}$	Effective yield strength reduction coefficient	$[-]$
K_{int}	Stiffness of the element interior	[kN/m]
K_{mem}	Stiffness of the member	[kN/m]
$K_{T,m}$	Tangent stiffness	[kN/m]
$K_{u,n}^{spring}$	Updated unloading stiffness of the zero-length spring (load step n)	[kN/m]
K_0	Initial stiffness/Undamaged structure stiffness	[kN/m]
K_e	Effective stiffness	[kN/m]
K_j	Stiffness matrix of the structure after removal of the j^{th} element or connection	[kN/m]
k_m	Linear elastic stiffness	[kN/m]
K_S	Secant Stiffness	[kN/m]
k_S	Section stiffness	[kN/m]
$\hat{k_{y,\theta}^*}$	Normalized effective yield strength based on EC3	$[-]$
L	Element length	[m]
L_{int}	Length of the element interior (between plastic hinges)	[m]
L_p	Plastic hinge length	[m]
LL	Live load	[kN/m]
M_c	Capping moment	[kNm]
m_e	Effective mass	[ton]
M_r	Residual moment	[kNm]
M_W	Moment magnitude	$[-]$
M_y	Yielding moment	[kNm]
N_p	Number of integration points	$[-]$

O	Compartment opening factor	$m^{1/2}$
$P_{f(dmg)}$	Probability of failure of the damaged structure	$[-]$
$P_{f(int)}$	Probability of failure of the intact structure	$[-]$
P_{ref}	Load pattern	[kN]
P_h	Section perimeter exposed to fire	[m]
P_y	Yield axial load	[kN]
q	Vector of basic forces	[kN and kNm]
$Q(t)$	Functionality function	$[\%]$
q_{fd}	Fire load density	[MJ/m^2]
R	Earthquake source-to-site distance	[km]
$R^{X,10\%}$	Structural response recorded when random variable X is equal to its 10% percentile	$[\%]$
$R^{X,90\%}$	Structural response recorded when random variable X is equal to its 90% percentile	$[\%]$
$R^{X,median}$	Structural response recorded when random variable X is equal to its median	$[\%]$
R^2	Determination coefficient	$[-]$
R_{dir}	Direct risk	$[e]$
R_{ij}	Robustness against events i and j	$[-]$
R_{ind}	Indirect risk	$[e]$
r_0	Resistance of the undamaged system	$[kN]$
r_d	Resistance of the damaged system	$[kN]$
R_L	Resilience loss	$[\%]$
R_S	Robustness measure	$[-]$
RF	Robustness factor	$[-]$
$s(x)$	Internal section forces	$[-]$
$S_a(T_1)$	Spectral acceleration at the fundamental period of vibration	[g]
S^{GM}	Original ground motion spectral acceleration	[g]
S^a	Ground motion spectral accelerations associated with the aftershock at the fundamental period of the intact structure	[g]
S^m	Ground motion spectral accelerations associated with the mainshock at the fundamental period of the intact structure	[g]
S_{mf}	Section massivity factor	[1/m]
$s_0(x)$	Internal section forces particular solution associated with element loads	[kN and kNm]
SF	Crustal ground motions scale factor	$[-]$
t	Time	[s]
T_e	Effective period	[s]
U_f	Displacement of the control DOF	[m]
V	Vulnerability	$[-]$
v	Vector of element deformations	[m and rad]
$v(F)$	Probability of ignition	$[-]$
V_B	Design base shear	[kN]
W	Structure weight	[kN]

Symbols - Greek Alphabet

Symbol	Description	Units
α'	Ratio of post-yield to elastic stiffness of the spring	$[-]$
β	Standard deviation of ln(IM) (dispersion of IM)	[g]
$\beta_{1/2/3}$	Section flexural stiffness modification parameters	$[-]$
β_{conn}	Dispersion due to fragile connection variability	$[\%]$
$\beta_{damaged}$	Reliability index of the damaged structure	$[-]$
β_{intact}	Reliability index of the intact structure	$[-]$
β_{RTR}	Dispersion due to record-to-record variability	$[\%]$
β_i	Cyclic deterioration parameter in excursion i	$[-]$
β_R	Redundancy index	$[-]$
β_s	Empirical non-negative strength deteriorating R constant	$[-]$
$\hat{\beta}$	Estimated standard deviation of ln(IM) (dispersion of IM)	[g]
Δ_t	Time period	[months/days]
$\int E_h$	Hysteretic energy dissipated	[kNm]
$\varepsilon(E)$	Variable with standard normal distribution (used for uncertainty of E)	$[-]$
$\varepsilon(F_y)$	Variable with standard normal distribution (used for uncertainty of F_y)	$[-]$
$\varepsilon(q_{fd})$	Variable with standard normal distribution (used for uncertainty of q_{fd})	$[-]$
$\varepsilon(Th)$	Variable with standard normal distribution (used for uncertainty of thermal elongation)	$[-]$
γ_k	Cumulative deterioration of the unloading stiffness	$[-]$
κ	Residual moment ratio	$[-]$
λ	Pseudo-time	$[-]$
Λ	Ratio between the total hysteretic energy dissipation capacity and the yielding moment	$[-]$
$\lambda_{element,i}$	Ratio of the energy dissipated by element i to total element energy dissipated by all elements	$[-]$
μ	Mean	
Φ	Standard normal cumulative distribution function	$[-]$
ϕ	Standard normal probability distribution function	$[-]$
σ	Standard deviation	
θ	Median of the fragility function (IM with 50% of collapse)	[g]
θ_f	Fracture rotation	[rad]
θ_p	Plastic rotation capacity	[rad]
θ_{pc}	Post-capping rotation capacity	[rad]
θ_u	Ultimate rotation	[rad]
θ_y	Yielding rotation	[rad]
$\hat{\theta}$	Estimated median of the fragility function (IM with 50% of collapse)	[g]
ξ_i	Integration point location	[-]
w_i	Integration point weight	$[-]$

Abbreviations and Acronyms

Abbreviations	**Description**
AFE	Annual frequency of exceedance
AIDA	Aftershock incremental dynamic analysis
ASCE	American Society of Civil Engineers
ATC	Applied Technology Council
BSSC	Building Seismic Safety Council
CDF	Cumulative distribution function
Comp	Earthquake ground motion component
CPH	Concentrated plastic hinge
DBE	Design Base Earthquake
DDBD	Direct Displacement-Based Design Method
DI	Damage index
DM	(Structural) Damage measure
DS	Damage state
DV	Decision variable
EC1	Eurocode 1
EC2	Eurocode 2
EC3	Eurocode 3
EC8	Eurocode 8
EDP	(Structural) Engineering demand parameter
FEMA	Federal Emergency Management Agency
FLPH	Finite-length plastic hinge
FLPH M	Finite-length plastic hinge using the proposed calibration procedure
FLPH S	Finite-lenth plastic hinge using directly scaled moment-rotation laws without calibration
FMRB	Force-based Column and Finite-length Modified Gauss-Radau with Bilin Beam Model
FMRH	Force-based Column and Finite-length Modified Gauss-Radau with Hardening Beam Model
FZLB	Force-based Column and Zero-length Modified Gauss-Radau with Bilin Beam Model
FZLH	Force-based Column and Zero-length Modified Gauss-Radau with Hardening Beam Model
FO	Flashover
ID	Dispersion index
IDA	I ncremental dynamic analysis
IDR	Interstory Drift Ratio
IFA	Incremental fire analysis
IL	Intensity level
IM	Intensity measure
LA20	20-Story SAC Project building designed to Los Angeles
LA3	3-Story SAC Project building designed to Los Angeles
LA9	9-Story SAC Project building designed to Los Angeles
LS	Limit state
MAF	Mean annual frequency

Mag	Earthquake magnitude
MAR	Mean annual rate
MCE	Maximum Considered Earthquake
MDOF	Multi-degree-of-freedom
ModIMK	Modified Ibarra-Medina-Krawinkler models
MSA	Multiple stripe analysis
NCREE	National Center for Research on Earthquake Engineering
NEHRP	National Earthquake Hazards Reduction Program
OpenSees	Open System for Earthquake Engineering Simulation framework
OSU	Oregon State University
P/P_y	Axial load ratio
PBEE	Performance-Based Earthquake Engineering
PBFE	Performance-based fire engineering
PBSE	Performance-based structural engineering
PC	Partial collapse
PDF	Probability distribution function
PEER	Pacific Earthquake Engineering Research center
PFC	Percentage of fractured connections
PGA	Peak Ground Acceleration
PGC	Progressive collapse
PGV	Peak Ground Velocity
P-M	Axial force - bending moment interaction
PMC	Probabilistic Model Code
POE	Probability of exceedance
PSHA	Probabilistic seismic hazard analysis
RC	Reinforced concrete
RCR	Repair cost ratio
RDR	Roof drift ratio
RIDR	Residual interstory drift ratio
RMSE	Root mean square error
RPE	Return period of exceedance
RTR	Record-to-record
SAC Project	Project leaded by three Joint Venture partners: the Structural Engineers Association of California (SEAOC), the Applied Technology Council (ATC), and Consortium of Universities for Research in Earthquake Engineering (CUREE)
SDOF	Single-degree-of-freedom
SEA20	20-Story SAC Project building designed to Seattle
SEA3	3-Story SAC Project building designed to Seattle
SEA9	9-Story SAC Project building designed to Seattle
SEAOC	Structural Engineers Association of California
SMRF	Steel Moment Resisting Frame
TAFE	Total annual frequency of exceedance

TDA	Tornado Diagram Analysis
UNL	Universidade Nova de Lisboa
USGS	United States Geological Survey
WFBW	Welded-flange-bolted-web connection

Chapter 1

Introduction

1.1 Background and Motivation

The study of the behavior of earthquake damaged structures still poses several challenges to the scientific community. This is, in part, due to the complexity of modeling the accumulated deterioration attained during the earthquake and taking it into account on the simulation of post-earthquake behavior. Additionally, the occurrence of an earthquake is hardly ever an isolated event. In fact, an earthquake is usually preceded by foreshocks (or premonitory earthquakes) and followed by aftershocks of the main earthquake, designated as mainshock. Moreover, other secondary events, such as fires, blasts, and tsunamis, are often recorded following a major earthquake.

Recent earthquakes have highlighted the potential risk arising from earthquake aftershocks [1]. According to data provided by the United States Geological Survey (USGS), the 2010 M8.8 Chile earthquake on February 27 triggered approximately 90 aftershocks with magnitudes of at least 5.0 in the next 24 hours. After the 2011, Great Tohoku earthquake in Japan, about 588 aftershocks with moment magnitudes of 5.0 or greater were recorded. The M8.6 Indonesia earthquake on April 11, 2012, was followed by several aftershocks with the largest measured at M8.2 just over two hours after the mainshock. In addition, a large number of aftershocks were recorded after the M7.9 earthquake in Nepal on 25 April 2015. As of 7 June 2015, over 304 aftershocks have occurred, the largest one having a magnitude of M7.3. Otherwise, in what concerns fire following earthquake, in the 1971 M6.6 San Fernando earthquake, 109 post-earthquake fires were recorded. After the 1989 M7.2 Loma Prieta earthquake, 67 fires were recorded, in the M6.7 1994 Northridge event, 97 fires broke out after the earthquake, while in 1995, 285 fires followed the M6.9 Kobe seismic event. Finally, the fire at a nuclear plant after the M9.0 2011 Tohoku earthquake induced great social, economic, and environmental losses [2]. Also tsunamis, have devastated entire regions after major earthquakes. After the M9.1 Sumatra earthquake in 2004 and the 2011 Tohoku earthquake there was, apart from the social and economic losses, a great number of human losses. As a consequence, the evaluation of the structural safety in post-earthquake scenarios should account for these multiple hazards that may affect the mainshock-damaged structures.

Although research has been developed in order to evaluate the impact of cascading hazards in structural safety and economical losses, there is no established framework to perform such analysis. In addition, the available numerical tools lack a unified implementation in a widely used software in order to allow for the development of large numerical simulations

Figure 1.1: A three-story RC building collapsed during an aftershock (M5.7) of the 2010 M6.2 Taiwan earthquake (left; source: NCREE) and a fire at an oil refinery after the 2011 Tohoku earthquake (right; source: The Times)

involving these hazards. In this thesis, the assessment of structural behavior under post-earthquake hazards is carried out. In particular, two secondary events are studied, earthquake aftershocks and fire following earthquake. Methodologies are developed in order to study the influence of these hazard events on structural safety. As extremely rare events are being studied, the most effective way to assess the influence of these events on structural safety is to compute robustness metrics associated with the mainshock-damaged structure and the intact structure, considering the secondary multiple hazard events. Reliability-based measures that allow for estimation of the structural capacity to face these extreme events are used.

This work focuses on Steel Moment Resisting Frame (SMRF) structures designed according to pre-Northridge codes. Although these have long been identified as source of major uncertainties and possible problems, SMRF's still persist as a large percentage of the existing steel buildings in the US and Europe. During the last decade, the seismic performance of SMRF buildings has raised many concerns regarding the occurrence of unexpected collapse mechanisms. Even in cases in which collapse is not reached, the behavior of steel buildings can change significantly during an earthquake, mainly due to deterioration of strength and stiffness of the structure, which results in the reduction of the capacity and, ultimately, leads to the failure of the structural system [3]. To quantify the structural susceptibility to sequences of events, reliable analytical tools that capture component deterioration need to be considered [4].

In order to accurately simulate structural response under sequences of events triggered by an initial earthquake, structural models should be developed so that: (i) the main phenomena influencing structural behavior of SMRF's are taken into account; (ii) accumulated damage is simulated accurately on the different structural components (on SMRF's the most relevant are: beams, columns, and beam-to-column connections); (iii) different hazard events can be sequentially simulated, in a flexible way; (iv) large number of simulations require a rational amount of time, namely by allowing parallel processing using computer networks. The first part of this thesis is devoted to the development of numerical models that comply with these requirements. The Open System for Earthquake Engineering Simulation (OpenSees) framework, which is an open-source framework, is used mainly due to its versatility and flexibility in simulating combined hazard events and accumulated damage. The fact that the OpenSees is a open-source framework was a major point of this work.

Changes to the OpenSees source code were made as a result of the developed work, making these new contributions available to other users and to the public. The new implementations solved incongruences in previous models and made them usable in different finite element formulations. In addition, a new finite element formulation was proposed and implemented.

The application of the proposed methodologies to assess the structural capacity to resist post-earthquake hazard events is exemplified by assessing the response of the 3-, 9-, and 20-story buildings designed as part of the SAC Steel Project [5] using pre-Northridge codes. Different designs were carried out in this project for Los Angeles, Seattle, and Boston. Due to this, different seismic hazard scenarios must be considered when analyzing these buildings. The various seismic hazard sources must be considered when defining the seismic scenarios. In this context, ground motion duration has been referred as an important variable to be considered in structural performance assessment, namely due to the potential to trigger additional structural damage. In spite of this, no consensus exists on the influence of ground motion duration on structural ductility and damage. Thus, a study of the influence of ground motion duration on structural damage is carried out in this work. The conclusions of this study are important to identify deformation and energy dissipation patterns that produce increases in accumulated damage and significantly affect their post-earthquake structural damage. The study of the 3-, 9-, and 20-story Seattle SAC Steel Project buildings is presented as a representative case study.

In what concerns the aftershock hazard, the application of the proposed methodology is exemplified through the study of 3-, 9-, and 20-story Los Angeles SAC Steel Project buildings. Otherwise, the application of the proposed methodology for post-earthquake fire assessment was hindered by the validation and verification of the OpenSees models used to simulate structural response under fire. Moreover, the probabilistic structural response assessment under fire is still an open topic, in which several variables are involved. Due to this, it was decided that, prior to the application of the methodology to study post-earthquake fire, a sensitivity analysis should be carried out in order to identify the most important parameters influencing the structural response under fire. Due to this extra work that was required to develop, the application of the methodology is still on going and is not presented in this thesis and should be part of future works.

The following section summarizes the main objectives and tasks of this work.

1.2 Objectives and Tasks

The main goal of this work is to contribute to the performance assessment of building structures under cascading events occurring after an earthquake. In this work reliability-based metrics are used to assess the structural robustness under the considered cascading hazards. Structural robustness is a key measure to ensure an adequate resilience [6]. In fact, the physical resilience dimension strongly depends on the robustness of the infrastructures. Thus, the study of structural robustness is seen as the first step towards the quantification of the community resilience to cascading hazard events triggered by an earthquake. However, the accurate assessment of the other resilience dimensions (economical, social, and organizational) is fundamental in order to develop strategies to increase community preparedness to these events. In spite of this, the study of these other dimensions falls outside the scope of this work.

In this work, a review of the state of the art, namely in what concerns performance-

based engineering methods, structural performance under seismic events, post-earthquake risk scenarios, and structural performance under cascading hazards is first carried out. Then, the work is divided into three main parts, described next and summarized in Figures 1.2 (general outline), 1.3 (part I), 1.4 (part II), and 1.5 (part III). A brief description is provided next:

Part I - Development of enhanced finite element formulations and models for seismic analysis

A new plastic hinge calibration procedure for force-based finite-length plastic hinge (FLPH) beam-column elements is developed, so that empirical moment-rotation relationships may be used in defining flexural behavior of these elements (*Task I.1.1*). The use of empirical relationships proved to be fundamental, as the reproduction of observed experimental behavior at element level is the most efficient yet credible way to simulate structural response. A unified implementation of a widely used empirical model is made in the OpenSees (*Task I.1.2*). This implementation allows for the use of this model in both concentrated plasticity models, which is the reference approach for simulating structural response under earthquake action, and finite-length plastic hinge (FLPH) models, making use of the proposed calibration procedure. A model extension is proposed for considering connection fracture. This extension uses FLPH elements to simulate member behavior, including nonlinear behavior, and zero-length fracture springs at both ends of the member to simulate connections (*Task I.2*). After validating the model, a probabilistic study is carried out to assess the influence of fractured connections on the structural performance and fragility assessment.

Part II - Assessment of the influence of ground motion duration on structural damage.

A methodology for studying the influence of ground motion duration on structural damage is developed. A large database of earthquake records from different sources, namely from short-duration, shallow crustal, and long-duration, subduction zone, ground motions, is created. The combined influence of spectral acceleration and significant duration on structural performance is evaluated in this part. Next, pairs of spectrally equivalent short and long duration ground motions are created and the isolated influence of duration is assessed. The relationship between structural deformations and damage is assessed for the different ground motion types, allowing for establishing comparison between damage pattern for short and long duration ground motions and between the three buildings analyzed.

Part III - Development of a framework for the robustness assessment of structures subjected to post-earthquake cascading hazards.

The last part of the research program is devoted to the development of a framework methodology, based on reliability metrics, that allows for the robustness assessment of structures subjected to post-earthquake cascading hazards. An application is presented to study mainshock-aftershock sequences (*Task III.1*). An application of the proposed framework is made by studying the 3-, 9-, and 20-story Los Angeles SAC buildings under artificial mainshock-aftershock sequences. In the case of fire following earthquake, an extension of the PEER PBEE formulation is presented (*Task III.2.1*). A sensitivity analysis is carried out to study the most important parameters that influence steel structural response under fire (*Task III.2.2*). Then, an incremental

fire analysis is performed to assess the structural response under fires with different intensities (*Task III.2.3*). These studies are necessary before proceeding to the implementation the proposed framework for fire following earthquake, which is envisioned for a near future.

The dissemination of the developed research is done mainly through the publication of technical papers in international scientific journals. Accordingly, the following papers, which are detailed at the end of the corresponding chapter, are written as a results of the work developed during the time of this research project:

- 4 Papers published in international scientific journals.
- 2 Papers being prepared to be submitted to international scientific journals.
- 3 Papers in national conferences.
- 3 Papers in international conferences.
- 2 Papers in international workshops.

1.3 Thesis Organization

The present chapter is devoted to the introductory review of the research topic in which this work is integrated. The main objectives of the work are summarized and the associated tasks are described. In addition, a concise review of the main concepts involved in this work is presented next, including the concepts of structural resilience and robustness, as well as the formulation and the main steps of the Performance-Based Earthquake Engineering (PBEE).

In the following, the thesis is divided into chapters that follow the tasks described in the previous section. Thus, the thesis is divided in three main parts. The first part presents the development of numerical tools. The second, the analysis of the influence of ground motion duration on structural damage. Finally, the third part presents the developed methodologies to assess the post-earthquake structural safety considering fire and/or aftershocks.

The development of numerical tools that are able to simulate the behavior of SMRF's under multiple cascading hazard events is divided into three chapters, which correspond to the three tasks identified in the previous section. Chapter 2 presents the new formulation and implementation of a finite-length plastic hinge integration scheme that allows for the use of empirically calibrated moment-rotation laws to define hinge section behavior in force-based finite element integration. Chapter 3 builds on the formulation proposed and performs a calibration, as well as a new implementation, of recently developed empirical models (Modified Ibarra-Medina-Krawinkler models, ModIMK in short) [4] in order to be used in both finite-length plastic hinge elements and in the traditional concentrated plastic hinge approach. Chapter 4 is the last one associated with the first part of the work. This chapter presents the proposed modeling approach to add fracture elements that simulate fragile connections in SMRF's. A case study of 3- and 9-story buildings is presented to illustrate the assessment of the influence of fragile connections on the fragility curves computation and in the estimated repair cost.

After the development of the numerical tools used in this work, a comprehensive study on the influence of earthquake ground motion duration on structural damage is performed

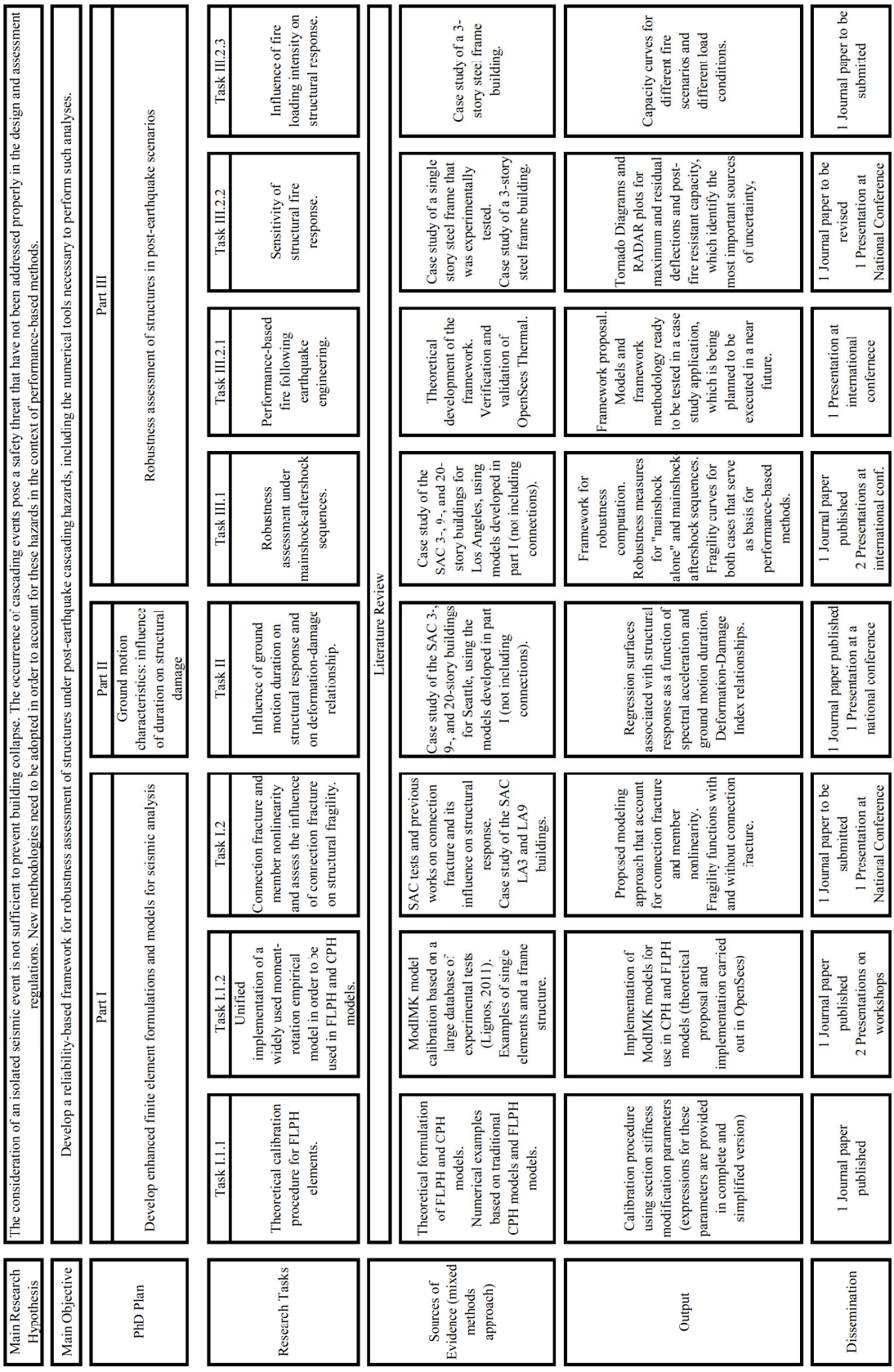

Figure 1.2: PhD research program - general outline

Robustness Analysis of Steel Structures in Post-Earthquake Scenarios Considering Cascading Hazards

PhD Plan	Part I Develop enhanced finite element formulations and models for seismic analysis		
General Objective	Develop numerical tools that allow for simulation of structural response under seismic cascading hazards.Test and validate the developed model through numerical examples.		
Subpart	Subpart I.1 Using empirical laws in FLPH elements		Subpart I.2 Accounting for Connection Fracture
Research Hypotheses	The reproduction of observed experimental behavior is fundamental in simulating structural seismic response. In addition FLPH offer significant advantages over CPH models.		Connection failure can be modeled in conjunction with FLPH elements.
Objectives	Develop a new plastic hinge calibration procedure for force-based finite-length plastic hinge (FLPH) elements, so that empirical moment-rotation relationships may be used in defining flexural behavior of these elements.		Develop a model extension for considering connection fracture and assess the influence of connection fracture on structural fragility.
Research Tasks	Task I.1.1 Theoretical calibration procedure for FLPH elements.	Task I.1.2 Unified implementation of recently proposed empirically calibrated moment-rotation model in order to be used in FLPH and CPH models.	Task I.2 Connection fracture and member nonlinearity and assess the influence of connection fracture on structural fragility.
Analysis	Theoretical deduction of section stiffness modification parameters for the calibration procedure. Validation through numerical examples using nonlinear static cyclic pushover analyses.	Theoretical implementation of ModIMK, focusing on accurate update of model parameters due to the various modes of deterioration for both CPH and FLPH models. Validation through numerical examples using nonlinear static cyclic pushover analyses.	Model development in OpenSees. Validation of the proposed modeling approach through comparison with experimental results from SAC tests. Define a probabilistic distribution for connection fracture rotation based on SAC tests. Perform a probabilistic analysis considering ground motion and fracture rotation uncertainty and using Latin Hypercube Sampling.
Output	Calibration procedure using section stiffness modification parameters (expressions for these parameters are provided in complete and simplified version)	Implementation of ModIMK models for use in CPH and FLPH models (theoretical proposal and implementation carried out in OpenSees)	Proposed modeling approach that account for connection fracture and member nonlinearity. Fragility functions for 3- and 9-story buildings with and without connection fracture
Dissemination	1 Paper published in the Jorunal of Structural Engineering	1 Paper published in the Journal of Earthquake Engineering 2 Presentations on the OpenSees Days Workshops in Portugal and Italy (2014 and 2015)	1 Paper to be submitted to the Journal of Performance of Constructed Facilities 1 Presentation at National Conference (Sísmica 2016)

Figure 1.3: PhD research program - part I outline

Robustness Analysis of Steel Structures in Post-Earthquake Scenarios Considering Cascading Hazards

PhD Plan	Part II Ground motion characteristics: influence of duration on structural damage
General Objective	Evaluate the influence of ground motion duration on structural damage and residual resistant capacity.
Research Hypotheses	Long duration ground motions significantly increase structural damage and lead to collapse prior to short duration motions. Relationship between deformation and damage is dependent on ground motion duration.
Objectives	Develop a methodology to study the combined influence of spectral acceleration and duration on structural response. Study the isolated influence of duration on structural damage and on the deformation-damage relationship.
Analysis	Generate a database of short and long duration earthquake records from crustal and subduction earthquakes, respectively. Perform a series of numerical analysis with the unscaled records and then with spectrally equivalent ground motion pairs. Use damage indices that account for ductility and energy dissipation demands. Perform incremental dynamic analysis using parallel processing computation.
Output	3-D Multi-linear regression surfaces associated with structural response (deformation and damage indices) as a function of spectral acceleration and ground motion duration. Deformation-Damage Index relationships (including uncertainty) for short duration and long duration ground motions.
Dissemination	1 Paper published in the Earthquake Engineering & Structural Dynamics Journal (March 2016) 1 Presentation at the U.S. National Conference on Earthquake Engineering and Seismology (2014)

Figure 1.4: PhD research program - part II outline

Robustness Analysis of Steel Structures in Post-Earthquake Scenarios Considering Cascading Hazards

PhD Plan	Part III Robustness assessment of structures in post-earthquake scenarios			
General Objective	Develop a framework methodology, based on reliability metrics, that allows for robustness assessment of structures subjected to post-earthquake cascading hazards, namely aftershock sequences and fire following earthquake. Exemplify the applicability of these framework through analysis of case studies.			
Subpart	Subpart III.1 Mainshock-Aftershock Sequences	Subpart III.2 Fire Following Earthquake		
Research Hypotheses	Aftershocks pose a significant threat to buildings damage during the mainshock, thus increasing collapse probability in post-earthquake scenarios	Fire loading affects structural properties and lead to large deformation, as well as lower loading bearing capacities, thus inducing severe consequences. These consequences increase in the case of earthquake-damaged structures, thus increasing collapse probabilities in post-earthquake scenarios.		
Objectives	Develop a specific framework for robustness assessment of structures considering mainshock-aftershock sequences. Exemplify the applicability of this framework.	Develop a specific framework for including fire following earthquake in performance-based methods. Exemplify the applicability of this framework.	Develop a sensitivity analysis to identify the most important parameters that influence steel structural response under fire.	Develop an incremental fire analysis to identify patterns in the structural fire response under fires with different intensities.
Research Tasks	Task III.1 Robustness assessment under mainshock-aftershock sequences.	Task III.2.1 Performance-based fire following earthquake engineering.	Task III.2.2 Sensitivity of structural fire response.	Task III.2.3 Influence of fire loading intensity on structural response.
Analysis	Application of the proposed framework by dividing the sample space associated with the mainshock spectral acceleration in a finite number of intervals (stratified sampling) and performing aftershock incremental dynamic analysis. Compute robustness measures.	Theoretical development of an extension to the performance-based earthquake engineering framework in order to include fire following earthquake. Verification and validation of OpenSees Thermal.	Sensitivity analysis using OpenSees Thermal modeling capabilities, which have been tested by us. Tornado Diagram Analysis and RADAR plots (spider diagrams) are used to evaluate the most relevant variables. Post-fire pushover and pushdown analysis are carried out to assess post-fire structural capacity.	Incremental fire analysis considering 10 different fire scenarios and pushover and pushdown analyses. Pushdown is carried out during fire and after fire. Pushover is carried out only after fire.
Output	Framework for robustness computation under mainshock-aftershock sequences. Robustness measures that allow for comparison between a "mainshock alone" and mainshock-aftershock sequences. Fragility curves for both cases that serve as basis for performance-based methods.	Framework proposal. Models and framework methodology ready to be tested in a case study application, which is being planned to be executed in a near future.	Tornado Diagrams and RADAR plots for maximum and residual deflections and post-fire resistant capacity, which identify the most important sources of uncertainty.	Capacity curves for different fire scenarios and different load conditions.
Dissemination	1 Paper published in the Journal of Structural Engineering 1 Poster presentation at the World Conference of Earthquake Engineering (2012) 1 Presentation at the ICOSSAR 2013	1 Presentation at the PLSE 2012	1 Paper to be revised 1 Presentation at National Conference (Sísmica 2016)	1 Paper to be submitted to the Journal of Structural Fire Engineering

Figure 1.5: PhD research program - part III outline

and presented in Chapter 5. A case study of the 3-, 9-, and 20-story Seattle SAC Steel Project buildings is presented.

Finally, Chapters 6 and 7 present the proposed methodologies to assess the robustness of structures under post-earthquake multiple hazards, namely aftershocks and fire, respectively. The conclusions of the developed research, as well as the envisioned future developments, are presented in 8.

Each Chapter follow a sequential organization composed by: (i) scope; (ii) introduction; (iii) literature review; (iv) framework description/analysis methodology; (v) case study; and (vi) conclusion.

1.4 Resilience to Catastrophic Events

1.4.1 Concept of Resilience

Resilience is usually seen as a measure of strength and flexibility. Ecologists were the first to introduce the notion of resilience. Holling [7] defined resilience as a measure of the systems persistence and their ability to absorb change and disturbance and still keep the same relationships between populations and state variables. In certain disciplines, such as sociology and psychology, resilience can be defined as the ability to recover quickly from illness, change, or misfortune. The dictionary also provides us an alternative vision by defining resilience as a property of a material that enables it to assume its original shape or position after being bent, stretched, or compressed (New International Webster's Dictionary, 1996). Wildavsky [8] defines resilience as the capacity to cope with unanticipated dangers after they have become manifest, and learning to bounce back. Home and Orr [9], in turn, define resilience as the ability of a system to withstand stresses of environmental loading. Extensive discussions on the concept of resilience and community resilience were presented by Ainuddin and Routray [10] and Longstaff et al. [11]. Bruneau et al. [6] made the first approach into bringing resilience to the earthquake engineering field. This will be discussed on Section 1.4.4.

Resilience is thus seen as an intrinsic characteristic of systems or communities. Resilient communities and systems are generally associated with high capacity to either prevent hazard-related damage and losses through execution of pre-event measures and cope with and minimize disaster impacts by following post-event strategies.

The development of disaster-resilient communities are one of the topics that have gathered more attention of agencies and groups engaged in disaster mitigation. The main goals of enhancing community resilience are to minimize losses, in terms of lifes, injuries, and economic losses. Improvement of seismic resilience, for example, can be achieved by improving the performance of the community's infrastructure during and after an earthquake, as well as through post-disaster response that efficiently cope with and minimize losses and recovery strategies that allow communities to bounce back to the pre-disaster functioning as quickly as possible.

In spite of the work that has been done in the last decades, no general strategies and methods have been proposed to improve awareness and preparedness of communities to catastrophic events, such as earthquakes, floods, and others. This is also due to the fact that cultural, economical, and organizational characteristics that differentiate communities inhibit the proposal of a unified approach. Due to this lack of strategies, community's response to these events remains largely unknown. To overcome these issues, new projects

have been launched. Among others of interest, the TACTIC project (2014-2016), a 1.3M€ European Union funded project, aims at increasing preparedness to large-scale and cross-border disasters among communities and societies in Europe. This project focuses on identifying and categorizing good practices of communication and education practices for preparedness. Four types of disasters are considered, namely terrorism, floods, epidemics, and earthquakes. The European Union Framework Programme for Research and Innovation (2014-2020) has also funds available for studying resilience, for example through the "DRS-14-2015: Critical Infrastructure Protection topic 3" which aims at developing a critical infrastructure resilience indicator, as well as perform analysis and develop methods for assessing resilience.

One of the main challenges in achieving high community resilience is that it involves a continued work, thus not being possible to set a final deadline or an expected end for the project. For example in the United States, the Disaster Mitigation Act of 2000 requires communities to engage in mitigation and preparedness planning and offers incentives for disaster mitigation, thus bringing community into the center of the action. The community enrollment is fundamental for enhancing high resilience to catastrophic events.

1.4.2 Resilience Quantification

According to Bruneau et al. [6] resilience is strongly correlated to complementary measures such as failure probabilities, consequences from failures, and time to recovery. High resilience usually leads to low values of these measures.

Resilience loss can be assessed through a functionality measure that takes into account the consequences of a disaster and the time to re-establish the normal performance. This functionality function, Q(t), vary in time and range from 0% to 100%, where 100% means perfect condition in service and 0% means total disruption. An example of the variation of this function throughout the life time of an infrastructure system is presented in Figure 1.6. In this Figure it is possible to see that a disaster (e.g., an earthquake), occurred at time t_0, causing a significant damage and thus reducing infrastructure functionality to 70%. Service is then reestablished over a time period Δ_t, until 100% functionality being achieved again at time t_1.

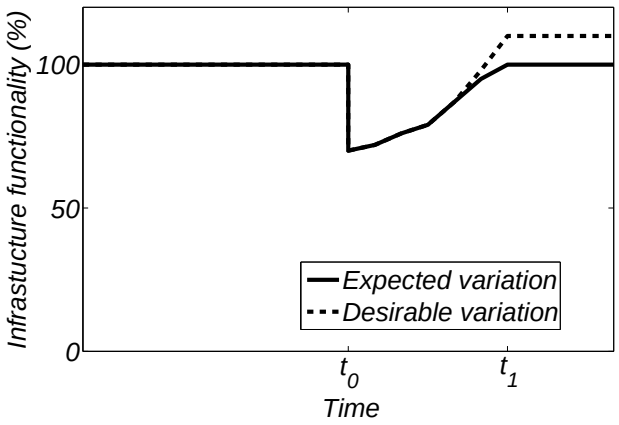

Figure 1.6: Representation of the functionality function (adapted from Bruneau *et al.* [6])

According to this definition, resilience loss R_L induced by the event can be computed

by the integral of functionality loss between t_0 and t_1:

$$R = \int_{t_0}^{t_1} [100 - Q(t)]dt \tag{1.1}$$

where $[100 - Q(t)]$ represents the decrease in the infrastructure functionality over time until complete recovery. This is the base of the MCEER triangle [12].

It is worth noting that, in many cases returning to the pre-event state of the infrastructure is not enough, especially in communities with low disaster-resilience. In these cases efforts must be made to ensure that rehabilitation or reconstruction includes measures to improve seismic resistance as represented by the dashed line in Figure 1.6. Consideration of several disasters and the associated probabilities over the life-cycle of the infrastructure, as well as a meaninguful definition of $Q(t)$ is fundamental to accurately access resilience.

A similar proposal for resilience quantification was made by Franchin and Cavalieri [13] that stated, through a comprehensive probabilistic study, that resilience is well predicted based on the normalized efficiency drop $[E_{f,0} - E_f(0)]/E_{f,0}$, where $E_{f,0}$ is the initial efficiency and $E_f(0)$ is the efficiency immediately after the disaster event, i.e. at time t_0. The authors stated that the normalized efficiency drop relation, presented by the following equation, presents a very low dispersion around a clear, geometrically explainable linear trend:

$$R = 1 - 0.5 \times \frac{\Delta E_f(0)}{E_{f,0}} \tag{1.2}$$

1.4.3 Resilience Dimensions

Resilience can be analyzed through the study of quantitative measures, namely robustness, rapidity, resourcefulness, and redundancy [6,14]. Robustness is defined as the ability of a system to sustain an initial damage without suffering disproportionate loss of functionality [15]. Resourcefulness is provided by the capacity of the system to respond after functionality has been affected due to some event. This implies the capacity to identify problems, to establish priorities and, finally, to mobilize resources (human, monetary, physical, technological, and informational).

Rapidity is associated with the capacity to meet priorities and achieve goals in a time interval that minimize losses and avoid future functionality disruption. Finally, redundancy is related to the existence of multiple paths within the system to respond to the demand.

The framework proposed by Bruneau et al. [6] integrates these measures into the four dimensions of community resilience. These are the technical, organizational, social, and economical dimensions. All of these dimensions can draw performance targets that allow to evaluate resilience of communities and system with different organizational and physical complexities. Examples of performance targets are presented by Bruneau et al. [6]. It is worth noting that different performance targets are required for different systems. An example of system and community seismic resilience performance targets associated with a university campus are presented in Figure 1.7.

In structural engineering redundancy is provided by the capacity of redistributing load between structural members in case of failure of any of them without global loss of functionality. For buildings, the existence of alternative load paths are the primary mechanisms providing robustness, thus highlighting the correlation between redundancy and robustness.

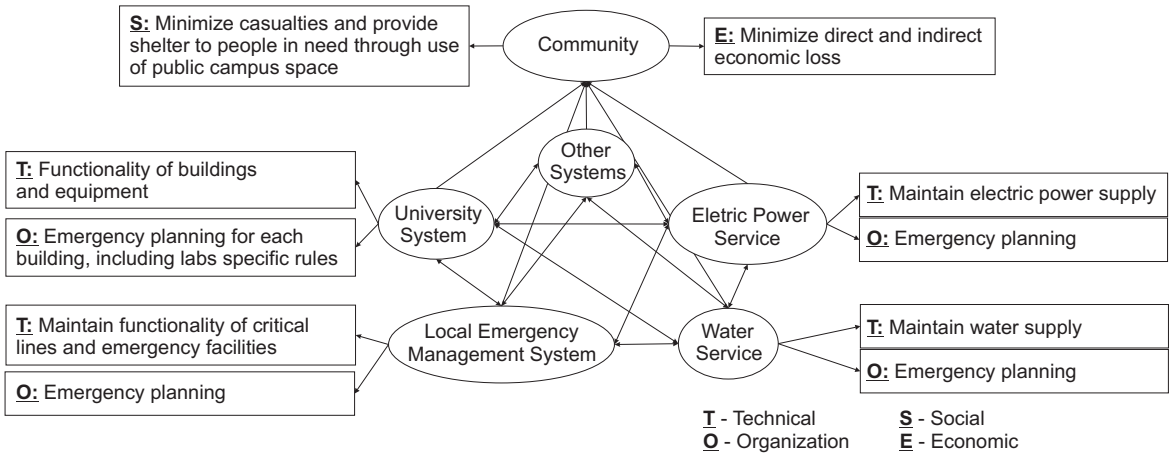

Figure 1.7: Example of performance targets associated with a university campus

1.4.4 Seismic Resilience

The potential of earthquakes to produce high losses and extensive community disruption has given earthquakes high priority in efforts to enhance community disaster-resilience. Although the consequences of an earthquake are usually seen as unavoidable, efficient mitigation strategies can increase seismic resilience and minimize vulnerability and expected losses due to earthquakes. This can only be achieved with the support of governmental institutions that have the capability to implement mandatory policies aimed at reducing the consequences of an earthquake. Communities should also be encouraged to engage in training and preparedness actions to optimize their capacity to respond after a seismic event. The first framework to define and quantify seismic resilience was proposed by Bruneau *et al.* [6]. This defines community seismic resilience as the ability of social units (e.g., organizations, communities) to contain the effects of earthquakes when they occur by dealing with the abrupt reduction of functionality, and carry out recovery activities in ways that minimize social disruption and mitigate the effects of future earthquakes. Figure 1.8 shows the seismic resilience diagram. The area on which the present work is focused is highlight with dashed line.

This methodology assumes that resilience dimensions can be assessed by means of the measures mentioned above, i.e. robustness, rapidity, resourcefulness, and redundancy. For a building structure subjected to earthquakes, technical and organizational resilience dimensions can be quantified by assessing the robustness and rapidity of the system and community performance. Robustness and rapidity assessment corresponds to the analysis of the structural behavior under seismic events, the associated losses and the time needed to restore pre-event functionality. This analysis renders a probability indicating the global resilience reliability of the structural system. If the obtained value is below the target value, mitigation procedures can be implemented, namely improving preparedness and recovery response (resources) and modifying the system to enhance its resilience. The social and economic resilience dimensions can be evaluated in a similar manner, i.e. by computing the expected economic losses and the associated probabilities. The evaluation of the obtained probabilities for the considered scenarios provides a good indication of system and community resilience.

Besides the definition of an appropriate resilience metric, another key element of resilience evaluation is modeling the recovery process. Modern databases and modeling tech-

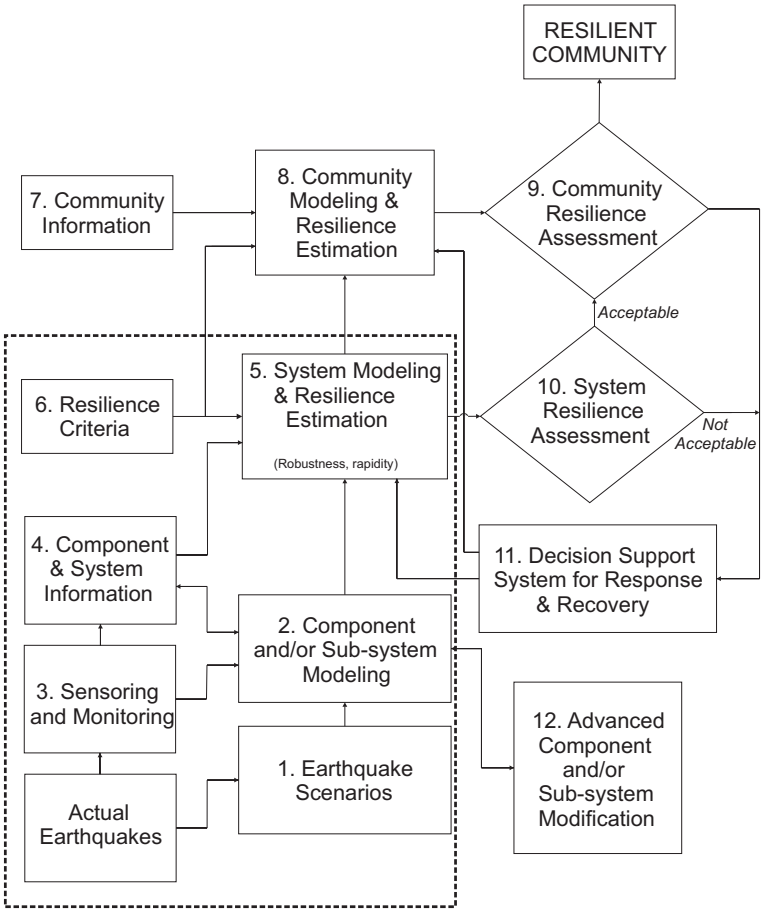

Figure 1.8: Resilience diagram [6]

niques, such as the framework developed by Silva *et al.* [16], provide assessment of building damage and casualties within a few minutes after an earthquake event, thus improving the reduction of losses, accelerating the recovery process and increasing the community resilience.

1.4.5 Increasing Resilience

New frameworks have been proposed to assist building owners and decision makers in developing mitigation strategies that respond to the specific needs of each community and embrace their own characteristics and particularities. One of them was proposed by Zobel [17], based on the resilience framework proposed by Bruneau *et al.* [6] and consists in a methodology for adjusting the resilience prediction given some preferences and priorities for a given decision maker. In addition, Alesch et al. [18] developed a platform combining a probabilistic model of ground shaking, engineering fragility curves, statistical estimates of potential damage costs, and a financial model of the costs and benefits of rehabilitation. These frameworks support seismic rehabilitation decisions.

1.4.6 Contribution to Resilience Quantification

This work is focused on quantifying structural capacity to sustain damage introduced by earthquakes, including different seismic sources, and secondary events such as aftershocks and fires. To this end, the work builds on a set of finite element models that are able to capture degradation introduced by the earthquakes and secondary events, as well as an analysis methodology that allows for quantification of the influence of these events on structural safety. The main outcomes of this work are intended to help identifying structural weaknesses that may increase vulnerability and improve design and assessment regulations by studying these secondary events that are not addressed by codes. In the near future, these shall be integrated in broader frameworks to evaluate global system resilience.

1.5 Structural Robustness

1.5.1 Concept of Robustness

Robustness is related to system's capacity to limit consequences of a damaging action, thus avoiding disproportionate consequences [15]. Minimizing direct and indirect losses and maintaining functionality are also desirable results of an adequate robustness [19]. Another definition of robustness is proposed by Starossek [20], who states that robustness can be seen as insensitivity to local failure, where insensitivity and local failure are to be quantified by the design objectives. The robustness of a system is a consequence of choices made during design, construction, and service phases. Improving system's robustness requires physical interventions. For example, structural robustness to fire loading may be improved by adding sprinklers. For an electrical system, modifying system's architecture is the main way of improving robustness. A good robustness allows the system to minimize damage through its automate performance.

As stated in the previous section, robustness is fundamental for guaranteeing an adequate system resilience. In fact, the extent of consequences that a community faces after a disaster event is strongly correlated to the robustness of their infrastructures.

Research has turned attention into robustness due to the fact that society is highly dependent on several complex systems. The failure of one of these systems leads to devastating social, economic, health and political consequences. As a result, the importance of minimizing the risk of failure of these system's infrastructures demanded research to be developed. Moreover, robustness has also been studied due to economical reasons [21]. In case retrofitting actions are to be planned, prioritizing strategies must be employed in order to defined the structures in need of more urgent and/or deeper intervention.

The case of structural collapse after a localized damage/failure, designated as progressive collapse, has been addressed during the last decades and has become a main concern of the structural engineering research community. Well-known failures, such as the partial collapses of the Ronan Point Building (1968) and the Charles de Gaulle Airport Terminal (2004), shown in Figure 1.9, remind us of the importance of robustness in structural design. However, a deeper research on structural robustness started after the collapse of the WTC in 2001. In addition, the acknowledgment that the possible losses associated with global structural collapse are much greater than the ones associated with the initial damage is one of the main boosters of robustness interest. Robustness concepts have been applied to study progressive collapse resulting from errors, explosions, deterioration or harmful human actions (e.g., [22,23], among others). However, robustness can also be useful in the analysis of structures subjected to multiple cascading hazards, namely those associated with multiple severe events such as post-earthquake cascading hazards.

Figure 1.9: Partial collapses of the Ronan Point Building (left) and the Charles de Gaulle Airport Terminal (right)

1.5.2 Quantifying Robustness

Among the different methodologies that have been presented to evaluate structural robustness, two groups can be identified [24,25]. The first group integrates methodologies that consider robustness as a property of each structure. The second group of methodologies includes the ones that define robustness in terms of the structure and the surrounding environment, including activities/actions that may cause damage and the associated losses. According to Neves and Cruz [25] the assessment of structural robustness can be executed by comparing indicators of structural performance associated with the intact structure and the damaged structure. These comparison can be made through the load bearing capacity, the reliability index, the probability of failure, among others.

Robustness can be quantified using deterministic, reliability or risk-based indicators. Deterministic indicators are based on the comparison of structural response parameters (e.g.,

displacements, stiffness, or dissipated energy) between the damaged and undamaged structure [24,26]. Starossek and Haberland [26] proposed the robustness measure R_S as:

$$R_s = min\frac{det(\boldsymbol{K}_j)}{\boldsymbol{K}_0} \tag{1.3}$$

where $\boldsymbol{K}_0$ is the stiffness matrix of the undamaged structure and $\boldsymbol{K}_j$ the stiffness matrix of the structure after removal of the jth element or connection. Although simple and adequate for implementation in engineering practice, these response parameters cannot be considered as indicators of the ability of different structures to sustain damage. In fact, these response parameters are not real indicators of structural safety and no correlation between their values and structural safety or resilience can be found across different structural designs.

Risk-based indicators involve the most accurate methods for quantification of robustness, as both probability of failure and the consequences of failure are explicitly addressed and computed. Baker et al. [15] proposed a robustness index defined in terms of direct and indirect risk, which is given by:

$$I_{rob} = \frac{R_{dir}}{R_{dir} + R_{ind}} \tag{1.4}$$

where R_{dir} is the risk associated with the initial event only and $R_{dir} + R_{ind}$ is the sum of direct and indirect risk, also labeled as the total risk. Although not developed for seismic risk analysis, this measure could be used in the present problem. However, the definition and quantification of consequences in seismic risk analysis is extremely complex, requiring not only the analysis of the structure, but also of its surrounding environment.

Reliability or probabilistic-based measures of robustness, which compare safety indices of the damaged and undamaged structure and explicitly accounting for uncertainties, have been proposed among others by Frangopol and Curley [27] and Lind [28]. It should be noted that these measures are not direct indicators of robustness, as the consequences of partial or global failures are not explicitly considered, but are, in fact, structural redundancy indicators. To clarify how redundancy can be linked to robustness, Starossek [29] described that there are two main alternatives to improve robustness: (i) increased redundancy, and (ii) increased compartmentalization. The first is associated with the existence of alternative load paths, achieved through improvements in ductility and/or resistance of structural components and their connections. The second alternative is associated with the compartmentalization of the structure, which reduces the consequences of failure by limiting damage to a restricted part of the structure. However, for multi-story buildings, compartmentalization is rarely an alternative, and robustness can only be achieved through the existence of alternate load paths. As a consequence, for buildings, reliability-based measures are an acceptable, albeit indirect, indicator of robustness.

The redundancy indicator proposed by Frangopol and Curley [27], which is considered to be a proxy of robustness, is given by:

$$\beta_R = \frac{\beta_{intact}}{\beta_{intact} - \beta_{damaged}} \tag{1.5}$$

where β_{intact} and $\beta_{damaged}$ are the reliability index considering the intact and damaged structure, respectively. The index varies between 0, corresponding to a structure without ability to sustain damage, and ∞, corresponding to a structure that suffers no reduction in safety due to the initial damage - indicating that in fact no damage was sustained.

Lind [28] proposed a generic measure of system damage tolerance, based on the increase in failure probability resulting from the occurrence of damage. The vulnerability (V) of a system is defined as:

$$V = \frac{P(r_d, S)}{P(r_0, S)} \tag{1.6}$$

where r_d is the resistance of the damaged system, r_0 is the resistance of the undamaged system, S is the applied loading, and $P(.)$ is the probability of failure of the system. The index varies between 1, corresponding to the ideal system where damage does not increase the probability of failure, to ∞ when the probability of failure of the damage system is several orders of magnitude above that of the intact system.

In the context of robustness assessment, structural damage is usually induced by direct removal of a principal structural member [30]. In fact, this approach has been proposed in some codes as a reference method for assessing robustness (e.g., [31]). If structural collapse is avoided for a period of time that is long enough to allow for rehabilitation and restoration of the structural state, a positive response is recorded. This procedure was applied to several structures by Starossek and Wolff [29]. In this work, which focuses on the post-earthquake structural performance, damage is directly introduced by seismic loading. This is accomplished by performing nonlinear dynamic time-history response analysis that allow for simulating the post-earthquake structural damage state.

A key aspect for adequately evaluating the safety of structures when computing a robustness measure is the ability to develop computational models capable of capturing component and system structural collapse mechanisms. Thus, these models must combine computational efficiency of numerical methods and algorithms with ability to accurately model damage to collapse.

1.5.3 Robustness in the Design and Assessment of Structures

Structural engineering design has been based mostly on individual member safety verifications. Each member has been designed to resist the calculated loads based on design actions. Although this approach is present is almost all current codes, consensus has been reached among the scientific community in respect to its unsuitability in guaranteeing an adequate system robustness. According to Faber [19], it is fundamental that the current codes and design methodologies, exclusively based on individual verifications, can integrate a global assessment of structural robustness, independently of the design of structural members. The inefficiency of the current codes in guaranteeing structural robustness to accidental events has been highlighted by Starossek [20]. In this context, the Capacity Design Method that analyzes the structures as a whole by defining the sets of members that may experience nonlinear deformations and the ones that should remain elastic, presents a great achievement in structural design practice. This method, albeit indirectly, is a first step into a global analysis of the structural system, thus guaranteeing an adequate structural robustness.

As referred above, robustness is usually seen as being dependent on structural redundancy, i.e. the existence of alternative load paths, energy absorption capacity, as well as member and material ductility [25]. However, generalization on the positive effect of these characteristics in avoiding progressive collapse is not possible [30]. Depending on the system, these characteristics may have a positive or negative influence on structural robustness, as the examples studied by Izzuddin et al. [30] show.

1.5.4 Structural Robustness Under Seismic Events

Structures that have been designed considering seismic action usually have an adequate robustness [32]. However, strategies to improve structural robustness may in some cases be prejudicial to seismic performance [33]. In addition to withstand seismic events, structures must be designed taking into account possible cascading events, i.e. events that usually follow a major earthquake, designated as mainshock. Examples of cascading events are aftershocks, fires, blasts, and tsunamis. Safety assessment of structures in post-earthquake scenarios can only be accurately performed when these events are taken into account. Robustness is important to ensure that, after an earthquake, structures remain safe, and preferably functional. This infers that structures have the capacity to not only resist the main seismic event, but also the post-earthquakes hazards.

Current codes do not consider cascading events or combined hazard in the design and assessment of structures. Research focusing on cascading events and multi-hazard safety assessments has shown current design can be unconservative. As a consequence, strategies to include multi-event/multi-hazard risk scenarios in current regulations have been developed [34–36]. However, an efficient formulation for structural robustness assessment in post-earthquake scenarios considering cascading hazard events is lacking in the literature.

1.5.5 Robustness Assessment Considering Multiple Hazard Events

A methodology for computing robustness measures under multiple hazards, namely post-earthquake cascading hazard events, is developed in this work. This methodology has been used by Belejo and Barbosa [37], who studied mainshock-aftershock seismic sequences for a 3D plan-asymmetric structure, and has recently been adapted for simultaneous actions (for any type of hazard but under a deterministic approach) by Asprone et al. [21]. Although the proposed formulation for post-earthquake hazards will be described later on in this work, the approach presented by Asprone et al. is summarized next.

This methodology considers a set of n different hazardous events that may trigger damage in a structure. Each event is characterized by an intensity measure IM, and an intensity demand value D, which depends on IM and is imposed by design codes to ensure the required safety level. For each event i, an appropriate model is developed in order to compute, as a function of IM, the corresponding structural capacity C_i. The developed model should account for all possible resisting mechanisms, and should neglect all safety factors that are considered in design. Accurate simulation of structural performance at damage states close to collapse is fundamental as the aim of this methodology is to define the maximum structural capacity to withstand the considered hazards. Moreover, the model should also be able to simulate any possible combination of events $i - j$, which requires an extremely versatile software to be used. In this case of event combination, structural capacity to face event j assuming that an event i with intensity d_i is applied on the structure is $C_j(d_i)$.

Once the structural capacities for all events and all combination of events have been defined, structural capacity over demand ratios (C/D) are calculated. These can be represented in a C_i/D_i-C_j/D_j plot, as illustrated in Figure 1.10. This plot represents an interaction diagram between each two events. The area inside the solid lines corresponds to the capacity domain but the structure is safe only in the grey area.

Based on these measures robustness can be quantified. Following a deterministic approach, robustness against single events corresponds to the intersection of the capacity do-

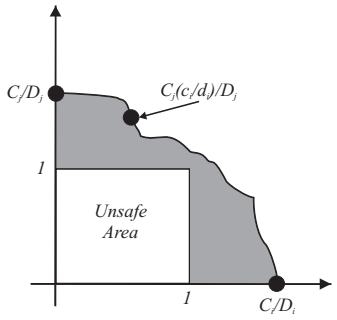

Figure 1.10: Interaction Diagram - Graphical representation of the capacity over demand ratio to simultaneous hazard events (adapted from [21])

main with the axes, i.e. $R_i = C_i/D_i$. This represents the capability of the structure to face event i, overcoming the reference demand D_i. On the other hand, robustness against events i and j, $R_{i,j}$, is given by the grey area, i.e. the area within the capacity domain and outside the unsafe area. This value corresponds to an integral measure of the capability of the structure to withstand simultaneous events, overcoming the reference intensity used by structural codes. Although it is desirable that the shape of the unsafe area represent exactly the demand actions, so that the shaded area can be accurately computed, this is not necessary and the assumption of a square area in Figure 1.10 is enough to compute robustness measures.

Assuming that the events i and j are simultaneous $R_{i,j} = R_{j,i}$, robustness measures $R_{i,j}$ can be aggregated in a symmetric matrix named robustness matrix $\boldsymbol{R}$, of dimension n. In case $i = j$, matrix element represent the robustness R_i against a single event i, whereas if $i \neq j$ matrix element $R(i, j)$ represents the robustness against simultaneous events i and j.

1.6 Performance-Based Earthquake Engineering

1.6.1 Overview

Traditional earthquake design is based on a three-level philosophy: (i) prevent damage in low-intensity earthquakes; (ii) limit damage to repairable levels in medium-intensity earthquakes; and (iii) prevent collapse in high-intensity earthquakes. Historical earthquakes have shown evidences that his philosophy is necessary but not sufficient. For example, during the 1994 Northridge and 1995 Kobe earthquakes, an unacceptable amount of damage, economic loss due to downtime, and repair cost of structures was recorded. Moreover, the 2009 L'Aquila and the 2010 Chile earthquakes also exposed problems in what concerns functionality of vital buildings. A traditionally designed hospital building was evacuated immediately after L'Aquila earthquake, at the same time that ambulances were arriving with injured people. After the Chile earthquake some hospitals were evacuated due to non-structural damage and damage to infill walls. In addition, some people refused to return to their homes despite satisfactory performance according to the available codes.

In the last decades the concept of Performance Objectives has been introduced as a way to achieve a desired system performance at a given seismic hazard. Several projects contributed to the development of Performance-Based procedures, namely the Vision 2000 project [38], a project of the Structural Engineers Association of California (SEAOC), as well as the Guidelines and Commentary for Seismic Rehabilitation of Buildings [39], a

Federal Emergency Management Agency (FEMA) project being jointly executed by the Applied Technology Council (ATC), the Building Seismic Safety Council (BSSC) and the American Society of Civil Engineers (ASCE). In Figure 1.11 the performance objectives matrix is shown, which is the basis of the PBEE. The upright positions correspond to an unacceptable performance, while the bottom left positions are associated with different levels of earthquake resistance and different performance targets. This approach allows for a differentiation to be considered in the structural performance for the same hazard level.

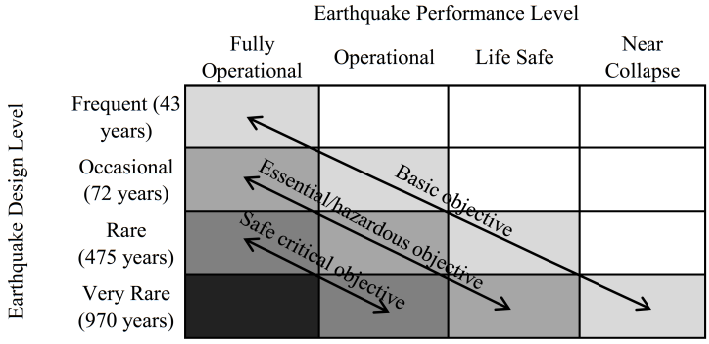

Figure 1.11: Performance Objectives in a performance-based approach (adapted from [40])

The first generation of PBEE methods developed following this approach presented several shortcoming, namely due to fact that the performance assessment was purely deterministic, thus ignoring any source of uncertainty. Moreover, the evaluation at the element level was not consistently tied to a global system performance. As a consequence, it results in a reduced contribution to stakeholders in the decision process [40].

To estimate the displacement limits when a performance-based design is followed, a probabilistic assessment, which takes into account the variability of seismic input, material and geometrical properties, level of gravity loads and financial consequences associated with damage, collapse or disruption time, has to be performed.

The Pacific Earthquake Engineering Research (PEER) center developed a PBEE framework in the past decades (Moehle and Deierlein 2004, Porter 2003). Figure 1.12 presents an overview of the PEER's PBEE framework that includes four main analytical steps (white boxes): (i) probabilistic seismic hazard analysis, (ii) probabilistic seismic demand analysis, (iii) probabilistic seismic damage analysis, and (iv) loss analysis. For each of the analytical steps, the outcomes are organized into four generalized variables, which are respectively: (i) ground-motion intensity measure (IM), (ii) structural engineering demand parameter (EDP), (iii) structural damage measures (DM), and (iv) decision variables (DV). The final decision making is based on variables of interest, such as downtime or cost to repair. The outcome of each analytical step corresponds to a probability or a mean annual rate (MAR) of exceedance of the generalized random variable. The total probability theorem allows for the consideration of the propagation of the uncertainty observed in each analytical step, and the MAR of the loss exceeding a given value $\nu(DV)$ is given by PEER PBEE's general framework equation:

$$\nu DV = \int\int\int P(DV|DM)dP(DM|EDP)dP(EDP|IM)d\nu(IM) \qquad (1.7)$$

where $\nu(IM)$ corresponds to the seismic hazard curve, which corresponds to the MAR of exceeding a specified IM, and $d\nu(IM)$ is its derivative; $dP(EDP|IM)$ is the probability of EDP conditional on IM, $dP(DM|EDP)$ is the probability of DM conditional on EDP, and $dP(DV|DM)$ represents the probability of DV conditional on DM.

Equation 1.7 involves pair-wise sequences of the four random variables IM-EDP-DM-DV. It assumes a one-step memory in the individual components and presumes that the last component is sufficient to describe the current step [41]. For example, in the seismic damage analysis step, EDP is said to be sufficient to characterize the DM and thus the IM does not need to be considered, which, in mathematical terms, corresponds to $P(DM|EDP, IM) = P(DM|EDP)$ and DM is thus a function of EDP only.

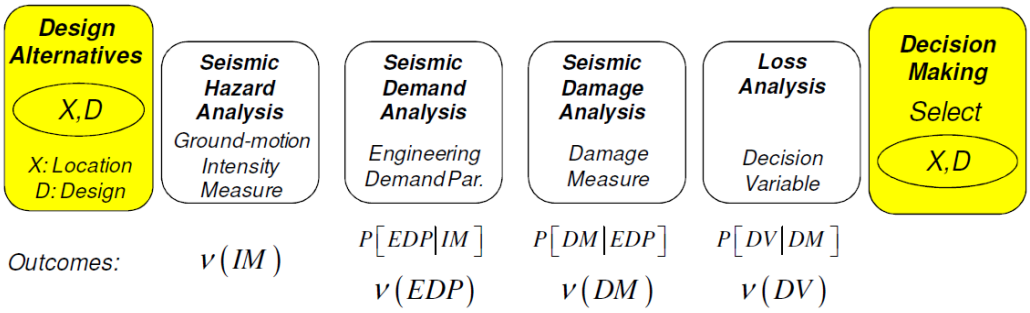

Figure 1.12: Framework for performance-based assessment of structural (adapted from [42])

The PEER PBEE presented several improvements to the original PBEE methods, namely by assessing performance in a rigorous probabilistic manner, i.e. considering uncertainty, and by defining performance decision variables which reflect the global system performance. So far, several researchers have concluded that among all uncertainties, the ground motion input has the highest influence on structural reliability, especially in the case of performance levels associated with severe structural and non-structural damage [43,44]. In order to extend this framework to include other seismic-related hazards, such as fire, the corresponding influence on structural response uncertainty need to be estimated.

In addition, the framework linearity and flexibility allow for potential applications to other types of extreme loading. Although the framework is still not particularly popular among practicing engineers, Performance-Based Engineering Design (PBED) methods, which are based on the same approach as the PEER PBEE framework, are being increasingly used for standard design codes [40].

The codes that have been used in the last decades (e.g., [45]) are based on limit states design approach. Nevertheless, an approximation to performance-based design has been made over the last decades. The main methods present in the codes aiming at filling the gap between force-based design and performance-based design are the Capacity Spectrum approach [46] and the N2 Method [47]. Other methods, such as the Direct Displacement-Based Design (DDBD) Method [48] are becoming increasingly used and are making their way into current practice.

Finally, reference should also be made to the Capacity Design approach, which consists in a performance-based design methodology that allows for explicit consideration of structural performance at the initial stage of the design process. When applied to an individual structural element, the Capacity Design approach explicitly considers the problem of determining member's failure mechanism. The basic idea is to force the member to fail

in a ductile manner by making the capacity of the member in other possible failure modes greater. It involves the simple application of plastic analysis on an element-wise basis as shown below. Otherwise, when applied to the global structural system, the Capacity Design approach defines which members will be permitted to yield (ductile components) and which ones will remain elastic (brittle components). Once ductile and brittle systems are defined, design process should provide ductile components deformation capacity so that they may satisfy adequate displacement-based demand-capacity levels, and brittle components sufficient strength levels so that they may satisfy strength-based demand-capacity levels. In order for Capacity Design to work, it is vital that reasonable, accurate capacities for each structural member be determined.

As a conclusion, one should note that performance-based design is expected to indirectly contribute to a better structural capacity to face extreme loading conditions and, as a consequence, to resist multiple hazard events that induce accumulated damage, in particular seismic-triggered sequences of events.

1.6.2 Hazard Analysis and Ground Motion Selection

The first step in the PEER PBEE lies in the computation of the seismic hazard. The output of this step is a single or vector-valued intensity measure [41]. The calculation of the intensity measure follows broadly the methodology employed in probabilistic seismic hazard analysis (PSHA). Although PSHA usually calculates a rate or a probability of exceeding an intensity measure, the calculation required for the PEER framework results in a mean annual probability of exceedance. In this step, uncertainty is considered, for example, in fault locations, magnitude, recurrence rates, and level of attenuation.

The PSHA is usually divided in three main steps: (i) determine the potential fault locations; (ii) determine the magnitude-recurrence relationships for the faults, i.e. rate of each possible magnitude; and (iii) for all the potential earthquake scenarios defined by [Magnitude, Rate, Location]:

1. Using ground motion prediction models, calculate the mean and standard deviation (μ, σ) of intensity measure, IM, as a function of Magnitude and Distance.

2. Determine the probability distribution function (PDF) and probability of exceedance (POE), of IM using μ and σ.

3. Multiply POE and Rate to compute the annual frequency of exceedance (AFE) of IM:

4. Sum AFE for all possible scenarios to obtain the total annual frequency of exceedance (TAFE) of IM (Figure 1.13(a)). Alternatively, a simpler way of representation of TAFE is the return period of exceedance RPE, given by RPE=1/TAFE.

5. From Poisson's model, calculate the POE of IM in T years from TAFE (Figure 1.13(b)):

$$P(IM) = 1 - e^{-\lambda(IM)T} \tag{1.8}$$

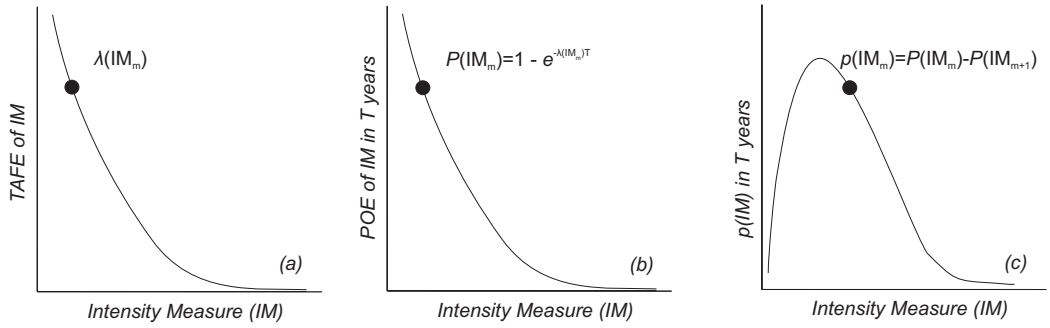

Figure 1.13: Characterization of intensity measure (IM) as: (a) total annual frequency of exceedance; (b) probability of exceedance in T years; and (c) probability of occurrence in T years (adapted from [40])

6. Calculate the probability of IM in T years from POE (Figure 1.13(c)):

$$\begin{aligned} for \quad & m = 1 : n^{IM} \\ & if \quad m = n^{IM} \\ & \qquad p(IM_m) = P(IM_m) \\ & else \\ & \qquad p(IM_m) = P(IM_m) - P(IM_{m+1}) \end{aligned} \tag{1.9}$$

where n^{IM} is the number of IM data points.

The most commonly used IMs are the Peak Ground Acceleration (PGA), the Peak Ground Velocity (PGV), and the Spectral Acceleration at the fundamental period of vibration ($S_a(T_1)$). For these measures, a large amount of ground motion prediction equations are available. Alternative IMs have been proposed, among many others, by Tothong and Cornell [49], who proposed the Inelastic Spectral Displacement as an efficient intensity measure.

$S_a(T_1)$ has been found to be an effective IM [50], but among records with the same value of $S_a(T_1)$, there is still a large variability in the response of multi-degree-of-freedom (MDOF) structural models. If some of this remaining record-to-record variability could be accounted for by an improved intensity measure, then the accuracy and efficient of structured response assessments could be improved. In this context, Baker and Cornell [41] proposed a vector-valued intensity measure consisting in a two-parameter definition of the intensity of a ground motion. The first parameter is the spectral acceleration, similarly to what is usually done, while the second one is the *epsilon* parameter, which is defined as a measure of the difference between the spectral acceleration of a record and the mean of a ground motion prediction equation at the given period. This parameter is in fact an indicator of the spectral shape and predicts with significant accuracy the structural response.

After choosing the most adequate IM, the selection of ground motion time histories to perform nonlinear dynamic time-history response analyses is a fundamental step. The selected ground motions must be compatible with the hazard curve for each intensity level, i.e. each IM value, and with the seismic hazard sources at the local. An adequate number of ground motions should be selected in order to provide meaningful statistical data in the structural analysis phase. In addition, the use of unscaled ground motions is preferable whenever possible. However, the need for performing a large number of numerical simu-

lations usually leads to the use of scaled ground motions. Due to this, record selection and scaling is of major importance in the PBEE application process [51].

1.6.3 Structural Modeling and Performance Assessment

The structural analysis is based on the simulation of the structural response through the development of nonlinear models. Although complex methodologies have been proposed for performing nonlinear static analysis, it is recognized that nonlinear dynamic time-history analysis provides the most insightful results and information about structural behavior [52]. However, the complexity and computational costs associated with this type of analysis have hindered its use in practical applications. The development of large sets of numerical tools and earthquake databases that became available to the general public in the last decades has allowed the development of analysis that are expected to make their way into the design practice in a near future.

The output of the structural analysis is a response measure of the structure which will be related to the damage analysis which follows in subsequent stages of the framework. A typical example of engineering demand parameter is the inter-story drift.

The structural analysis should reflect the response of the structure across the whole vector of the Intensity Measure. In this step, uncertainty is considered, for example, in ground motion type, material properties, damping, and modeling considerations.

The structural analysis often relies on a catalogue of earthquake records to determine the likely response given a peak ground acceleration (or other intensity measure). However the calculation of the structural response is based on the contents of entire records of earthquakes and not just the variable which is chosen to reflect the intensity measure [53]. The following dynamic structural analysis procedures are often used to assess the structural response to the selected earthquake ground motions:

- Incremental Dynamic Analysis (IDA) [54] - a suite of ground motions is repeatedly scaled in order to find the IM level at which each ground motion leading to violation of the limit state function.

- Truncated IDA [55] - perform IDA only up to some level, IM_{max}, above which no further analyses are performed. If n ground motions are used in this analysis, there will be m ground motions that caused collapse at IM levels lower than IM_{max}, and $n - m$ ground motions that did not cause collapse prior to the analyses being stopped.

- Multiple Stripe Analysis (MSA) [56] - analysis is performed at a specific set of IM levels, each of which has a unique ground motion set. It is commonly used with Conditional Spectrum or other approaches to select ground motions representative of a specific site and IM level (because the target properties of the ground motions change at each IM level and thus so do the representative ground motions) [57–59].

The influence of ground motion records on structural performance assessment has been investigated in the past [60–62]. These studies concluded that a significant variability arises from the different type of ground motion (real or artificial) and the scaling process [51]. To avoid such variability, current codes usually define a minimum number of ground motions to be used in performance-based assessments. The influence of the code-based record selection and scaling methods proposed by different codes on median seismic demands was analyzed

by Araujo et al. [63], who concluded that American regulation (ASCE 41-13) [64] leads to more conservative estimations than the Eurocode 8 [45] and the New Zealand codes (NZS 1170.5:2004) [65].

1.6.4 Damage Assessment and Loss Analysis

Following the structural analysis, a damage analysis should be carried out in terms of the direct interest of not only engineers, but also various stakeholders. This is achieved by defining a Damage Measure (DM) at the component or system levels as a function of structural response.

In the damage analysis, fragility functions are used to represent the POE of a DM for different values of EDP. In Figure 1.14 a graphical representation of a fragility function is shown. In this figure four Damage States (DS) are represented. These damage states correspond to predefined levels of the chosen DM, and are usually associated with physical thresholds (e.g., loss of functionality, non-reparable structural damage, collapse of the building). In the damage and loss analysis, uncertainty is considered, for example, in damage type and distribution capacity, damage levels, and corresponding direct and indirect consequences.

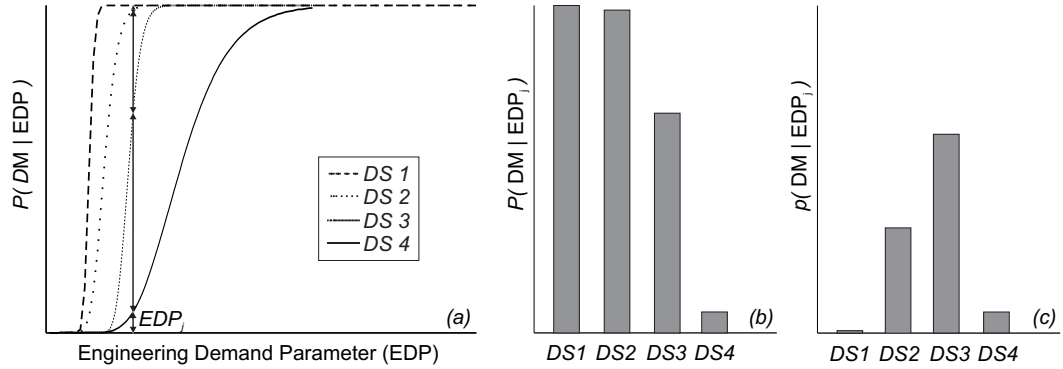

Figure 1.14: Representation of damage measures (DM) as: (a) fragility curves (POE of DM|EDP); (b) probability of exceedance of DM (P(DM|EDP)); and (c) probability of DM (P(DM|EDP))

Damage sustained by a structure during an earthquake is a result of several phenomena, typically described as a function of deformation, ductility, energy dissipated, stiffness degradation, strength degradation, among others. To account for the complex combination of these parameters, different damage measures have been proposed in the literature. These damage measures, also designated damage indices (DI), provide an indication of the accumulated damage sustained by the components of the structure or by the entire structure. Usual DIs are directly correlated to damage levels corresponding to repair measures needed to restore components of a facility to the original conditions [40]. DI's are often calibrated based on experimental data for each loading condition and for a set of failure modes. The indices associated with the entire structure are usually based on a weighted average of the damage indices for components.

Damage Indices

The main damage indices used for seismic damage assessment can be divided into three main groups: (i) indices based on peak drift-based response measures; (ii) indices based on measures related to the inelastic cyclic response; and (iii) indices that combine peak drift-based response measures and inelastic cyclic response measures. For example, in the first group, Veletsos and Newmark [66] proposed a damage index, which is based on the peak inelastic deformation. Lybas and Sozen [67] incorporated the concepts of cyclic deterioration and proposed a damage index that consists in the ratio of the initial stiffness to the secant stiffness corresponding to maximum deformation. Roufaiel and Meyer [68] defined a local index for components, based on the ratio between the minimum secant stiffness recorded and the secant stiffness at onset of failure, but also for global measures, based on peak roof displacement and roof displacement at failure. In the second group, some damage indices consider, explicitly, the energy dissipated as the measure of the severity of inelastic response [69,70], while some others consider the number and amplitude [71,72], or even the history of the inelastic cyclic response [73]. These indices, which focus on the effects of cumulative loading, combine inelastic measures of the response to account for fatigue, namely low-cycle fatigue [74]. In the third, and last group, the response parameters considered individually in each of the former groups are merged into single indices. For example, Park and Ang [75] defined a damage index, which is a linear combination of the ratio of the peak observed to ultimate deformation and hysteretic energy dissipated. Reinhorn and Valles [76] developed an index, entitled Fatigue Based Damage Model, that relates to low plastic cycles fatigue. The index, which was calibrated with experimental data, is based on an initial development by Park and Ang [75].

The damage index proposed by Park and Ang [75] is based on the linear combination of the ratio of the maximum to ultimate deformations and the ratio of the maximum hysteretic energy dissipated to the maximum monotonic energy as:

$$DI_{PA} = \frac{d_m}{d_u} + \beta_s \frac{\int E_h}{d_u \times F_y} \tag{1.10}$$

where d_m is the maximum attained deformation, d_u is the ultimate deformation under monotonic loading, β_s is the empirical non-negative strength deteriorating constant, and $\int E_h$ denotes the hysteretic energy dissipated during the cyclic loading, and F_y is the yield strength. According to FEMA355 [77] the ultimate deformation, d_u, for steel structures can be assumed as $11 \times d_y$, where d_y is the yield deformation. β_s depends on the value of shear and axial forces in the section and, for RC components, on the total amount of longitudinal and confining reinforcement. Available test data for 402 RC components of rectangular cross-sections and 132 steel specimens of H-shaped sections tested in the US and Japan, were used to estimate β_s, resulting in a value of $\beta_s = 0.05$ for concrete structures and $\beta_s = 0.025$ for steel structures

The index proposed by Reinhorn and Valles [76] is based on the product of the ratio of the maximum to ultimate deformations and a low inelastic cyclic fatigue rule calibrated by the authors using experimental data. This index is given by:

$$DI_{RV} = \begin{cases} 0, & (d_m - d_y) \leq 0 \\ \frac{d_m - d_y}{d_u - d_y} \times \frac{1}{1 - \frac{\int E_h}{4 \times (d_u - d_y) \times F_y}}, & (d_m - d_y) > 0 \quad \& \quad \int E_h < 4 \times (d_u - d_y) \times F_y \\ 1, & \int E_h \geq 4 \times (d_u - d_y) \times F_y \end{cases} \tag{1.11}$$

where $4 \times (d_u - d_y) \times F_y$ represents the reference hysteretic energy dissipation capacity associated with the low inelastic cyclic fatigue.

While the Park and Ang, DI_{PA}, and the Reinhorn and Valles, DI_{RV}, indices have been extensively used, for example by Loh et al. [78] and Kunnath et al. [79,80], the main disadvantage of these indices is that it is not possible to take into account the history of the inelastic cyclic response, but to consider only the global amount of dissipated energy. Observed structural damage of nine reinforced concrete buildings and calibration of damage indices performed by Park et al. [81] are presented in Table 1.1, as well as the degree of observed damage in the structures.

Table 1.1: Physical Interpretation of the Damage Indices [81]

Degree of Damage	Damage Index, DI	State
Collapse	> 1.0	Loss of building
Severe	0.4 - 1.0	Beyond repair
Moderate	< 0.4	Repairable
Minor/Slight	< 0.2	

Analytical fragility function computation based on structural analysis

Collapse fragility functions are increasingly popular in structural assessment procedures [82,83]. Analytical fragility curves can be computed based on results obtained through numerical simulation. In this context, fragility function computation is basically the process of fitting a function to the data produced in the structural analysis. One of the main challenges in this procedure is to perform structural analysis, which are often computational expensive, in a way that fragility functions computation can be optimized while the number of required structural analysis is minimized. As a consequence, a methodology, such as the one proposed by Baker [55], to evaluate the efficiency of different analysis strategies is fundamental. Nonlinear dynamic analysis has been, in the last decade, greatly used in the fragility function computation procedure, mainly due to the amount of information that can be gathered in this type of analysis. However, it is not required that structural analysis output is generated through nonlinear dynamic analysis. Figure 1.15 presents a conceptual framework of the tasks involved in the fragility function computation.

A lognormal cumulative distribution function is often used to define a fragility function:

$$P(C|IM = x) = \Phi\left(\frac{ln(x/\theta)}{\beta}\right) \tag{1.12}$$

where $P(C|IM = x)$ is the probability that a ground motion with $IM = x$ will cause the structure to collapse, $\Phi()$ is the standard normal cumulative distribution function (CDF),

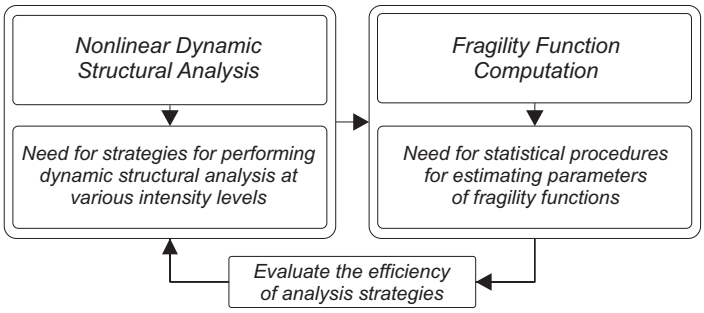

Figure 1.15: Assessment of the efficiency of dynamic structural analysis for computing fragility curves

θ is the median of the fragility function (IM with 50% probability of collapse), and β is the standard deviation of $ln(IM)$ (sometimes referred to as dispersion of IM). The assumption that IM values are lognormally distributed has been confirmed by several authors (e.g., [84–86], among others). Fragility function computation consists in the estimation of the parameters θ and β that best fit the analysis results obtained for a specific structure. These parameters do have unavoidable uncertainty due to record-to-record variability, which causes ground motions with the same IM level to produce different demands.

An estimated fragility function can also be combined with a ground motion hazard curve to compute the mean annual rate of structural collapse [84,87–89].

Estimating fragility function parameters

There are two commonly used statistical approaches for estimating parameters from data: (i) method of moments [85]; and (ii) maximum likelihood method [55]. The first method finds parameters such that the resulting distribution has the same moments (e.g., mean and standard deviation) as the sample moments of the observed data. The second method finds parameters such that, given a candidate function, the resulting distribution has the highest likelihood of having produced the observed data.

The most appropriate method vary according to the analysis strategy. When IDA is performed, the method of moments provides good estimates of the fragility function parameters. However, when truncated IDA is performed, the obtained data can only be used to estimate fragility functions with the maximum likelihood method. Finally, if MSA is performed the maximum likelihood method should be used, although with some modifications.

IDA produces a set of IM values associated with the onset of collapse for each ground motion. The probability of collapse can be estimated as the fraction of records for which collapse occurs at a level lower than x. Fragility function parameters are then estimated from this data as the mean and standard deviation of the logarithms of the IM's associated with collapse of each ground motion:

$$ln(\hat{\theta}) = \frac{1}{n}\sum_{i=1}^{n} ln(IM_i) \tag{1.13}$$

$$\hat{\beta} = \sqrt{\frac{1}{n-1}\sum_{i=1}^{n}(ln(IM_i/\hat{\theta}))^2} \tag{1.14}$$

where $\hat{\theta}$ and $\hat{\beta}$ are the estimated θ and β, n is the number of ground motions considered, and IM_i is the IM value associated with onset of collapse for the i^{th} ground motion. Alternatively, fractiles of the IM_i values can be used, rather than their moments, to estimate θ and β [90].

When truncated IDA is performed, for the m ground motions that recorded collapse, their IM values at collapse (IM_i) are known. The likelihood that an arbitrary ground motion causes collapse at IM_i, given a fragility function, is:

$$Likelihood = \phi\left(\frac{ln(IM_i/\theta)}{\beta}\right) \tag{1.15}$$

where $\phi()$ is the standard normal distribution probability density function (PDF). The $n-m$ ground motions that did not cause collapse at IM_{max} (recall that in truncated IDA, IDA is only performed up to IM_{max} level, above which no further analyses are performed) are called censored data, as we only know that IM_i is greater than IM_{max}.

The likelihood that a given ground motion can be scaled to IM_{max} without causing collapse is the probability that IM_i is greater than IM_{max}:

$$Likelihood = 1 - \Phi\left(\frac{ln(IM_{max}/\theta)}{\beta}\right) \tag{1.16}$$

Making the reasonable assumption that the IM_i value associated with each ground motion is independent, the likelihood of the entire data set being observed is the product of the individual likelihoods:

$$Likelihood = \left(\prod_{i=1}^{m} \phi\left(\frac{ln(IM_i/\theta)}{\beta}\right)\right)\left(1 - \Phi\left(\frac{ln(IM_{max}/\theta)}{\beta}\right)\right)^{n-m} \tag{1.17}$$

Using this equation, the fragility function parameters are then obtained by varying the parameters until the likelihood function is maximized. It is mathematically equivalent and numerically easier to maximize the logarithm of the likelihood function:

$$\{\hat{\theta};\hat{\beta}\} = argmax_{(\theta,\beta)}\left[\sum_{j=1}^{m}\left(ln\left(\phi\left(\frac{ln(IM_i/\theta)}{\beta}\right)\right)\right) + (n-m) \times ln\left(1 - \Phi\left(\frac{ln(IM_{max}\theta)}{\beta}\right)\right)\right] \tag{1.18}$$

In the particular case where all the n ground motions cause collapse at IM values lower than IM_{max}, this equation has an analytical solution for the values $\hat{\theta}$ and $\hat{\beta}$ that maximixe the equation, and the solution is equivalent to that of Equations 1.13 and 1.14, except that the "$n-1$" in equation 1.14 is an "n" in this equation. It is worth noting that the normal distribution PDF and CDF in Equation 1.18 can be replaced by other distribution, in order to fit the fragility function to any other distribution.

In case the MSA strategy is followed, the approach presented above cannot be used because the IM_i values associated with the onset of collapse of a given ground motion is not available. Instead, the structural analysis results provide the fraction of ground motion at each IM level that cause collapse. The appropriate fitting technique for this type of data is to use the method of maximum likelihood [55], as noted by several authors [91–93].

At each $IM = x_j$, the probability of observing z_j collapses out of n_j ground motions is:

$$p(z_j \text{ collapses out of } n_j \text{ GM's}) = \binom{n_j}{z_j} p_j^{z_j}(1-p_j)^{n_j - z_j} \tag{1.19}$$

where p_j is the probability that a ground motion with $IM = x_j$ will cause collapse of the structure. The objective of the method is to identify the fragility function that will predict p_j.

When analysis is performed at multiple IM levels, the product of the binomial probabilities at each IM level is taken to get the likelihood of the entire set:

$$Likelihood = \prod_{j=1}^{m} \binom{n_j}{z_j} p_j^{z_j} (1 - p_j)^{n_j - z_j} \tag{1.20}$$

where m is the number of IM levels. Substituting p_j by Equation 1.12, the fragility function parameters are explicited:

$$Likelihood = \prod_{j=1}^{m} \binom{n_j}{z_j} \Phi\left(\frac{ln(x_j/\theta)}{\beta}\right)^{z_j} \left(1 - \Phi\left(\frac{ln(x_j/\theta)}{\beta}\right)\right)^{n_j - z_j} \tag{1.21}$$

Estimates of the fragility function parameters are obtained by maximizing this likelihood function. As referred above, it is equivalent and numerically easier to maximize the logarithm of the likelihood function:

$$\{\hat{\theta}; \hat{\beta}\} = argmax_{(\theta,\beta)} \left[\sum_{j=1}^{m} \left(ln\binom{n_j}{z_j} + z_j \times ln\left(\Phi\left(\frac{ln(x_j/\theta)}{\beta}\right)\right) + (n_j - z_j) \times ln\left(1 - \Phi\left(\frac{ln(x_j\theta)}{\beta}\right)\right)\right)\right] \tag{1.22}$$

It is worth noting that this formulation is valid in the particular case of singular observations at each IM level, i.e. when $n_i = 1$. This is useful, for example, when fitting a fragility function using unscaled ground motions, each having unique IM amplitudes. Furthermore, this formulation assumes independence of observations, so that the overall likelihood is the product of the likelihoods at each IM level. This independence may not be strictly true if the same ground motion is used for structural analysis at more than one x_i level, although quantifying this dependence may be somewhat challenging and anecdotal evidence suggests that relaxing this assumption typically makes no significant in the estimated parameters [55]. In fact, Baker [55] example analyses appear to indicate that the approach produces effective fragility estimates even with IDA data, where identical ground motions are used at all IM levels. Straub and Kiureghian [93] discuss a generalization of the maximum likelihood method that allows for consideration of dependent samples, though the formulation is more complex to implement than the one described above.

As a conclusion, it appears that an effective strategy for fragility fitting is to focus on structural analyses at a limited number of IM levels using MSA, rather than doing IDA [55]. This observation is consistent with the recommendations of Eads *et al.* [86]. That strategy also has the benefit of allowing the analyst to use different ground motions at each IM level, which allows for more accurate representation of ground motion characteristics [41]. Results suggest that choosing IM levels near the lower tail of the fragility function and up to IM levels slightly above the median would be a generally effective strategy [55].

Loss Estimation

Loss analysis is the last step of the PEER PBEE framework and is based on the considered damage measure. In fact, it consists in converting damage information obtained from damage analysis in final decision variables DVs. Commonly used DVs are fatalities, economic losses, repair cost or duration, and injuries.

The loss analysis therefore relies on the results of the damage analysis to derive consequence curves based on whether or not a damage state exists given the EDP hazard curve. In PBEE consequence curves are used to provide an estimate of the annual impact of an earthquake for, e.g. budgetary reasons in order to allow developers to better assess the impact of performance based structural engineering decisions on their own project. The outcome of the loss analysis is a loss function, which provides a POE of a DV for different damageable groups and DMs.

A specific value of DM corresponds to various DVs with different probabilities, thus accounting for uncertainty in loss analysis. The lack of information about structural and nonstructural components, their monetary values, can be considered as sources of uncertainty in loss analysis. In addition, uncertainty arising from the economical values, such as fluctuation in the market prices, can also be account for.

One convenient way to represent the expected losses is to compute average repair cost ratios (RCR) of the damaged buildings. Each DM is associated with an expected RCR, which can be given for example by statistical treatment of past damage on similar building types. The average RCR of a building at a given intensity level IM is given by Basoz and Mander [94]:

$$\mu_{RCR} = \sum_{i=1}^{n_{DM}} RCR_i \times P(DM = dm_i|IM) \tag{1.23}$$

1.6.5 PBEE in the Design and Assessment of Structures

Important solutions have mostly been achieved for the assessment problem, which are influencing the new generation of seismic codes dealing with the assessment of existing structures, such as Eurocode 8 [45] and ASCE/SEI 41-06 [95], and the establishment of design parameters for seismic force-resisting systems, e.g. FEMA P-695 [83] and FEMA P-795 [96]. In particular, PEER PBEE finds excellent uses but it is presently limited to assessment, i.e. forward derivation of a given structural performance [97]. A proper performance-based design would mean at least inverting such equation to allow deriving the desired properties of the structure that would satisfy a given value of DV. In order to accomplish such a goal, Vamvatsikos *et al.* [97] suggest that, from an engineer point of view, it would be more productive to consider DV and DM as simple indicator variables that become 1 when a given limit state (LS) is exceed, and thus transform Equation 1.7 to estimate λ_{LS}, the Mean Annual Frequency (MAF) of exceeding LS, as:

$$\lambda_{LS} = \int G(EDP|IM)|d\lambda(IM)| \tag{1.24}$$

Then, closed-form approximation of the integral can provide significant help in doing so. Cornell *et al.* [98], Vamvatsikos [99], and Lazar and Dolsek [100] proposed expressions for that.

Chapter 2

Development of Enhanced Finite Element Models for Seismic Analysis. Part I: Formulation

2.1 Scope

PBEE methodologies rely on accurate nonlinear finite element models that can capture the full range of structural response associated with various performance targets. This Chapter is focused on the never ending problem of finite element simulation of member response. The main challenge in this area is the simulation of deterioration phenomena that affects member capacity. In this Chapter, a plastic-hinge calibration approach is presented. This calibration procedure allows for member modeling through finite-length plastic-hinge elements that use the *modified* Gauss-Radau integration scheme and make use of recent multilinear moment-rotation constitutive laws that have been derived from experimental results. This calibration procedure can be used as an alternative to the traditional concentrated plastic hinge approach. It can be implemented in a finite element framework, decreasing the user's modeling effort, while providing accurate and reliable results.

The proposed calibration procedure includes the definition of section flexural stiffness modification parameters at the beginning of the nonlinear structural analysis. These modification parameters are computed as a function of the plastic hinge to span length ratio by comparison of the element flexibility and the target flexibility. The calibration procedure is validated using a set of simply supported beams and a steel frame.

2.2 Introduction

In the development of realistic finite element models, two main aspects need to be taken into consideration. First, modes of strength and stiffness deterioration due to damage accumulation that could lead to local or global collapse need to be identified. Second, the models for structural components need to be reliable, robust, and computationally efficient for the entire range of the analysis.

The use of empirically calibrated moment-rotation models that account for strength and stiffness deterioration of steel frame members is paramount in evaluating the performance of steel structures prone to collapse under seismic loading. These deterioration

models are typically used as zero-length springs in a concentrated plasticity formulation; however, a calibration procedure is required when they are used to represent the moment-curvature $(M-\chi)$ behavior in distributed plasticity formulations because the resulting moment-rotation $(M-\theta)$ response depends on the element integration method. A plastic hinge integration method for using deterioration models in force-based elements is developed and validated using flexural stiffness modifications parameters to recover the exact solution for linear problems while ensuring objective softening response. To guarantee accurate results in both the linear and nonlinear range of response, the flexural stiffness modification parameters are computed at the beginning of the analysis as a function of the user-specified plastic hinge length. With this approach, moment-rotation models that account for strength and stiffness deterioration can be applied in conjunction with force-based plastic hinge beam-column elements to support collapse prediction without increased modeling complexity.

The proposed calibration methodology improves the quality and reliability of the results obtained without a notable increase either in computation cost or in the complexity of structural model. Nonetheless, it is worth noting that the influence of other effects that are typically considered in 2-D frame modeling of built infrastructure still need to be taken into account. Examples of relevant effects are slab stiffness and strength deterioration on cyclic performance of beams, diaphragm action, load distribution, and mathematical representation of damping, among others [101]. The validation of the calibration approach is performed for nonlinear static (pushover) analyses. However, for full implementation in finite element software, nonlinear cyclic static and dynamic analyses including strength and stiffness deterioration are needed in the future, as these cases fall outside the scope of this work. In addition, the proposed calibration scheme was only developed for the *modified* Gauss-Radau scheme, as it is found to be advantageous over other methods, namely by avoiding localization issues, in the analysis of structures to seismic loading and is implemented in a finite-length plastic hinge (FLPH) element [102]. The application of the calibration approach to other integration methods falls outside the scope of this thesis.

2.3 Literature Review

Idealized beam and column models for nonlinear structural analysis vary greatly in terms of complexity and computational efficiency, from phenomenological models, such as concentrated plasticity models and distributed plasticity beam-column elements, to complex continuum models based on plane-stress or solid finite-elements.

Concentrated plasticity models (CPH) [103], consist of two parallel elements, one with elastic-perfectly plastic behavior to represent yielding and the other with elastic response to represent post-yield hardening. Following the formal proposal by Giberson [104], where nonlinear zero-length moment rotation springs are located at both ends of a linear-elastic beam-column element, this type of approach became the reference model in the development of the CPH models. Many hysteretic laws have been proposed in the last decades accounting for the most relevant phenomena influencing member response up to collapse: cyclic deterioration in stiffness [105] and strength [106,107], pinching under load reversal [68], among many others have developed different phenomenological models that define the behavior of the concentrated plastic hinges. Even though these models were developed several years ago, they have been recently proposed as the main method for estimating seismic

demands of frame structures [84,88,108] and have been presented as the preferred modeling approach in the ATC-72 guidelines [109]. These models allow for reliable estimation of the seismic demands in structures up to the onset of collapse with limited computational cost.

On the opposite end of the spectrum to *CPH* models, continuum models are generally accepted as the most reliable approach for estimating the seismic demands of structures to localized and global collapse. However, these models are typically complex and require very time-consuming computations. Distributed plasticity finite elements offer a compromise between CPH models and continuum finite element models.

Three formulations for distributed plasticity elements have been proposed in the literature: force-based beam-column elements [110,111], displacement based beam-column elements [112,113], and the mixed formulation based beam-column elements [114]. Mixed formulations typically yield the best results in nonlinear structural analysis, but they have not been widely adopted in the finite element software typically employed in PBEE analyses.

Force-based beam-column elements have been shown to be advantageous over displacement-based elements for material nonlinear frame analysis [111,114,115] by avoiding the discretization of structural members into numerous finite elements, thereby reducing the number of model degrees of freedom. In these formulations, the behavior of a section is described by a fiber model or a stress resultant plasticity model [116].

Despite these advantages, localization issues related to non-objective strain-softening response [117] led to the development of FLPH elements by Scott and Fenves [102] and Addessi and Ciampi [118]. Conceptually, these elements are composed of two discrete plastic hinges and a linear elastic region, all of which are incorporated in the element integration method. Through the selection of experimentally calibrated plastic hinge lengths and appropriate definition of the integration scheme, localization can be avoided.

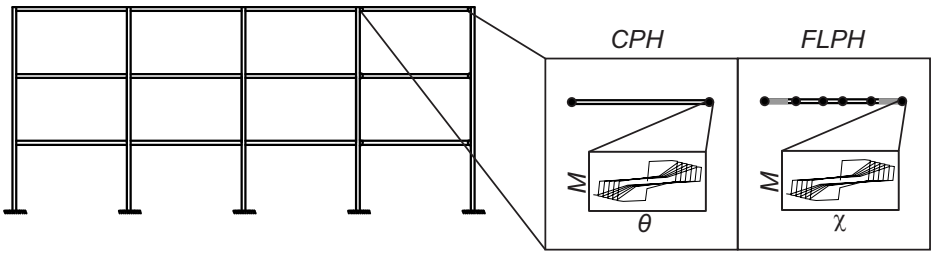

Figure 2.1: Representation of member simulation approaches used in this work

The main advantages of the *FLPH* elements are: (i) the explicit definition of the plastic hinge length, which allows for the recovery of meaningful local cross-section results (e.g. curvatures and bending moments), (ii) a clear distinction between beam-column inelasticity from the nonlinear behavior of connections, and (iii) a reduced number of nodes, elements and degrees of freedom. These advantages motivate the search for alternate calibration approaches as presented in this chapter. Although these elements have been used successfully in simulating the seismic response of structures [119], they require the definition of a moment-curvature relationship and plastic hinge length to represent a desired moment-rotation behavior.

2.3.1 Review on Concentrated Plasticity Hinge (CPH) Models

The empirical models described above can be used directly in the zero-length moment-rotation springs of *CPH* elements. In the case of double curvature or anti-symmetric bend-

ing, which is the reference case for the empirical moment-rotation models used by Ibarra and Krawinkler [84] as well as by Lignos and Krawinkler [4], the global element initial flexural stiffness of the one component *CPH* becomes $6EI/L$, where EI is the cross-section flexural stiffness and L is the element length. The flexibilities of the zero-length moment-rotation springs and the element interior are additive, giving the total element flexibility:

$$\mathbf{f} = \mathbf{f}_I + \mathbf{f}_{int} + \mathbf{f}_J \tag{2.1}$$

where $\mathbf{f}_{int}$ is the flexibility of the linear-elastic element interior and $\mathbf{f}_I$ and $\mathbf{f}_J$ are the flexibilities of the springs at ends I and J, respectively.

The correct linear-elastic solution for the entire element is only obtained if the end rotational springs are approximated as rigid-plastic. Thus, linear elastic cross-section stiffness of the springs at both ends are affected by a constant n_{Factor} (typically greater than 10) such that the initial stiffness of the springs is large, but not so large as to pose numerical instability. Since the elastic stiffness of the member is related to the elastic stiffness of the rotational springs and the beam-column element, which are connected in series, the stiffness of the element interior is also affected by n_{Factor}, and is expressed as:

$$EI_{mod} = EI\frac{n_{Factor}+1}{n_{Factor}} \tag{2.2}$$

which translates to spring initial stiffness given by:

$$k_m = n_{Factor}\frac{6EI_{mod}}{L}, \qquad m = I, J \tag{2.3}$$

Following the methodology by Ibarra and Krawinkler [84], the ratio of post-yield to elastic stiffness of the spring, α' (ratio of the tangent stiffness, k_{Tm}, to the linear elastic stiffness, k_m) is given by:

$$\alpha' = \frac{k_{Tm}}{k_m} = \frac{\alpha}{1 + n_{Factor} \times (1-\alpha)} \tag{2.4}$$

where α is the nominal post-yielding to elastic stiffness ratio and α' is assigned to the end springs in the *CPH* model to reproduce the correct moment-rotation behavior of the member. The ratio α' is thus defined such that the correct nonlinear moment-rotation stiffness of the member, defined as $\alpha \times 6EI/L$, is recovered.

Error in the model elastic stiffness associated with the CPH springs elastic stiffness amplification factor

In CPH models, the n_{Factor} should be chosen carefully as an excessively large value would pose numerical problems, while a value that is not sufficiently large will lead to erroneous results in the elastic range.

Considering that each member can be represented by two end rotational springs and an elastic frame element in series, the flexibilities of the springs and the frame element in a CPH element are additive. Using the tangent stiffnesses, k_{TI} and k_{TJ}, of each rotational spring, the member flexibility is:

$$f_b = \begin{bmatrix} 1/k_{TI} & 0 \\ 0 & 0 \end{bmatrix} + \frac{L}{6EI_{mod}} \times \begin{bmatrix} 2 & -1 \\ -1 & 2 \end{bmatrix} + \begin{bmatrix} 0 & 0 \\ 0 & 1/k_{TJ} \end{bmatrix} \tag{2.5}$$

To recover the correct linear-elastic solution for the entire CPH model, the end rotational springs need to be approximated as rigid-plastic with an initial stiffness that is large, but not so large to pose numerical instability. This is akin to the selection of large penalty values when enforcing multi-point constraints in a structural model [120]. The ratio of flexibility coefficient $f_b(1,1)$ to the exact linear-elastic solution $L/(3EI)$ is plotted in Figure 2.2 versus the elastic stiffness amplification factor, which scales the characteristic element stiffness $6EI/L$ ($k_I = n_{Factor} \times 6EI_{mod}/L$).

As shown in Figure 2.2, the ratio between the elastic stiffness recovered using different n_{Factor} values for the CPH model and the target elastic stiffness ($L/3EI$) varies from 0.9545 (4.55% error) for $n_{Factor} = 10$ to 0.9995 (0.05% error) for $n_{Factor} = 1000$. Thus, to recover the elastic solution with negligible errors, it is suggested that a value of $n_{Factor} = 1000$ be used.

Although the suggested value of $n_{Factor} \geq 1000$ allows for recovery of the elastic stiffness, several authors have highlighted that there is an increased likelihood of non-convergence of nonlinear time-history response analyses if such a large value of n_{Factor} is used. For this reason, Zareian and Medina [121] have suggested the use of $n_{Factor} = 10$. However, the use of such a low value of n_{Factor} can lead to underestimating the elastic flexibility of the elements up to 4.55%.

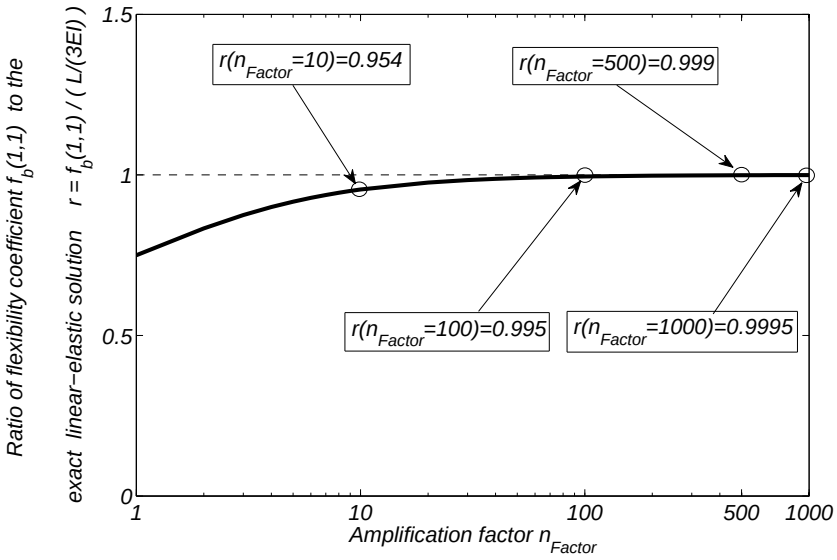

Figure 2.2: Computed elastic flexibility coefficient of concentrated plasticity model versus rigid-plastic approximation of end springs

2.3.2 Review on Finite Length Plastic Hinge (FLPH) Models

The *FLPH* element developed by Scott and Fenves [102] is based on the force-based beam-column finite element formulation by Spacone et al. [122] and uses alternative numerical integration schemes to account for user-defined plastic hinge lengths. The force-based beam-column finite element is formulated assuming small displacements in a simply-supported basic system free of rigid-body displacements. Figure 2.3 illustrates the basic system in which the vector of element-end forces, $\mathbf{q}$, the vector of element deformations, $\mathbf{v}$, the internal section forces, $\mathbf{s}(x)$, and section deformations, $\mathbf{e}(x)$, are shown for a two-dimensional

element. Section forces correspond to the axial force and bending moments, while the section deformations correspond to axial strain and curvature.

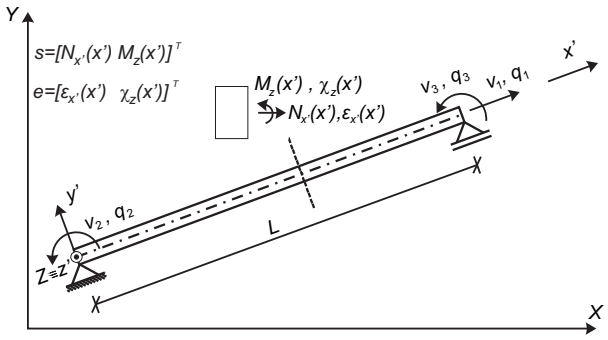

Figure 2.3: Basic system for two-dimensional frame elements

Equilibrium between the section forces $\mathbf{s}(x)$ at a location x, and basic element forces $\mathbf{q}$ is given by:

$$\mathbf{s}(x) = \mathbf{b}(x)\mathbf{q} + \mathbf{s_0}(x) \tag{2.6}$$

where $\mathbf{b}(x)$ is the interpolation function matrix, and $\mathbf{s_0}(x)$ corresponds to a particular solution associated with element loads. Equation 2.6 can be expanded into different forms depending on the number of dimensions of the problem and the beam theory selected. For the two-dimensional Euler−Bernoulli beam-column element, the basic forces are $\mathbf{q} = \{q_1, q_2, q_3\}^T$ and the section forces are $\mathbf{s}(x) = \{N(x), M(x)\}^T$, all of which are shown in Figure 2.3. Compatibility between element deformations $\mathbf{v}$ and section deformations $\mathbf{e}$ is expressed as:

$$\mathbf{v} = \int_0^L \mathbf{b}(x)^T \mathbf{e}(x)\ dx \tag{2.7}$$

The element flexibility matrix is obtained through linearization of the element deformations $\mathbf{v}$ with respect to basic forces $\mathbf{q}$ and is given by:

$$\mathbf{f} = \frac{\partial \mathbf{v}}{\partial \mathbf{q}} = \int_0^L \mathbf{b}(x)^T \mathbf{f}_S(x) \mathbf{b}(x)\ dx \tag{2.8}$$

where $\mathbf{f}_S$ is the section flexibility, equal to the inverse of the section stiffness $\mathbf{f}_S = \mathbf{k}_S^{-1}$. The section stiffness is obtained from linearization of the constitutive relationship between section forces and section deformations, $\mathbf{k}_S = \partial \mathbf{s}/\partial \mathbf{e}$, at the current element state. The implementation details of the force-based element formulation into a displacement-based software were presented by Neuenhofer and Filippou [111] and are not reproduced here for brevity.

Numerical evaluation of Equation 2.7 is given by:

$$\mathbf{v} = \sum_{i=1}^{N_P} \left(\mathbf{b}^T \mathbf{e}|_{x=\xi_i}\right) w_i \tag{2.9}$$

where N_P is the number of integration points over the element length, and ξ_i and w_i are the associated locations and weights. The element flexibility is therefore given by:

$$\mathbf{f} = \sum_{i=1}^{N_P} (\mathbf{b}^T \mathbf{f}_S \mathbf{b}|_{x=\xi_i}) w_i \tag{2.10}$$

The main issue related to use of this formulation is the localization of strain and displacement responses that can be obtained in the case of strain-softening response of force-based distributed plasticity elements [117]. Scott and Fenves [102] and Addessi and Ciampi [118] proposed methods for force-based finite length plastic hinge (*FLPH*) integration, where the element is divided in three segments, two corresponding to the plastic hinges at both ends, with length L_{pI} and L_{pJ}, and a linear segment connecting both hinges (see Figure 2.4). Thus, Equation 2.7 simplifies to:

$$\mathbf{v} = \int_0^{L_{pI}} \mathbf{b}(x)^T \mathbf{e}(x) dx + \int_{L_{pI}}^{L-L_{pJ}} \mathbf{b}(x)^T \mathbf{e}(x) dx + \int_{L-L_{pJ}}^{L} \mathbf{b}(x)^T \mathbf{e}(x) dx \tag{2.11}$$

Various approaches were proposed to evaluate this integral numerically; however, the focus herein is the *Modified* Gauss-Radau integration scheme which retains the correct linear elastic solution while using the specified plastic hinge lengths as the integration weights at the element ends.

In this method both end sections are assigned a nonlinear behavior, whereas the element interior is typically assumed to have an elastic behavior, although this assumption is not necessary. The flexibility of the *FLPH* element can be computed as:

$$\mathbf{f} = \int_{L_{pI}} \mathbf{b}(x)^T \mathbf{f}_S(x) \mathbf{b}(x) dx + \int_{L_{int}} \mathbf{b}(x)^T \mathbf{f}_S(x) \mathbf{b}(x) dx + \int_{L_{pJ}} \mathbf{b}(x)^T \mathbf{f}_S(x) \mathbf{b}(x) dx \tag{2.12}$$

where L_{int} is the length of the element interior (although not necessary, usually assumed as linear-elastic).

Using the *modified* Gauss-Radau integration scheme for the plastic hinge regions, Equation 2.12 can be rewritten as:

$$\mathbf{f} = \sum_{i=1}^{N_{pI}} (\mathbf{b}^T \mathbf{f}_s \mathbf{b}|_{x=\xi_i}) w_i + \int_{L_{int}} \mathbf{b}(x)^T \mathbf{f}_S(x) \mathbf{b}(x) dx + \sum_{i=N_{pI}+1}^{N_{pI}+N_{pJ}} (\mathbf{b}^T \mathbf{f}_s \mathbf{b}|_{x=\xi_i}) w_i \tag{2.13}$$

where N_{pI} and N_{pJ} are the number of integration points associated with the plastic hinges at the element ends. For the *modified* Gauss-Radau integration $N_{pI} = N_{pJ} = 2$. The element interior term can be computed exactly when the element interior is elastic and there are no member loads. Nonetheless, the element interior can also be analyzed numerically. In this case, the Gauss-Legendre integration scheme is appropriate to integrate the element interior. If two integration points are placed in this region, a total of six integration points are defined along the element length. The location ξ_i of the integration points associated with the *modified* Gauss-Radau plastic hinge integration, represented in Figure 2.4, are given by:

$$\xi = \{\xi_{\mathbf{I}}, \xi_{\mathbf{int}}, \xi_{\mathbf{J}}\} \tag{2.14}$$

where:

$$\begin{gathered} \xi_{\mathbf{I}} = \left\{0; \tfrac{8L_{pI}}{3}\right\} \\ \xi_{\mathbf{int}} = \left\{4L_p + \tfrac{L_{int}}{2} \times \left(1 - \tfrac{1}{\sqrt{3}}\right); 4L_p + \tfrac{L_{int}}{2} \times \left(1 + \tfrac{1}{\sqrt{3}}\right)\right\} \\ \xi_{\mathbf{J}} = \left\{L - \tfrac{8L_{pJ}}{3}; L\right\} \end{gathered} \tag{2.15}$$

The corresponding weights w_i are given by:

$$\mathbf{w} = \{\mathbf{w_I}, \mathbf{w_{int}}, \mathbf{w_J}\} \tag{2.16}$$

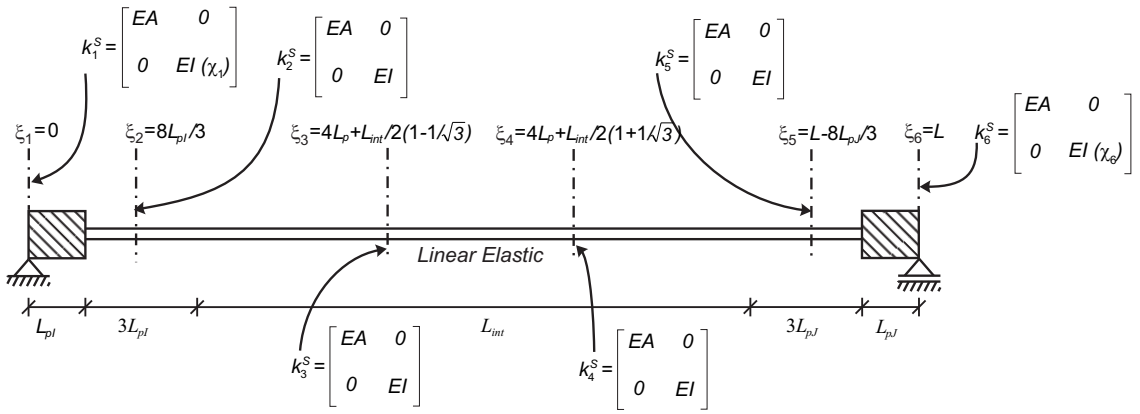

Figure 2.4: Modified Gauss-Radau integration scheme

where:

$$\begin{aligned} \mathbf{w_I} &= \{L_{pI}; 3L_{pI}\} \\ \mathbf{w_{int}} &= \left\{\tfrac{L_{int}}{2}; \tfrac{L_{int}}{2}\right\} \\ \mathbf{w_J} &= \{3L_{pJ}; L_{pJ}\} \end{aligned} \tag{2.17}$$

In this case, the element flexibility is then given by:

$$\mathbf{f} = \sum_{i=1}^{6} (\mathbf{b}^T \mathbf{f}_s \mathbf{b}|_{x=\xi_i}) w_i \tag{2.18}$$

where this equation is consistent with points and weights shown in Figure 2.4.

2.4 Calibration of Force-Based Finite-Length Plastic Hinge Elements

The *FLPH* formulation requires the definition of moment-curvature relationships in the plastic hinge region, and subsequent procedures to relate these relationships to the moment-rotation response of the element. In this section, a novel method for calibration of the moment-rotation behavior of finite-length plastic hinge force-based frame elements is proposed for arbitrary plastic hinge lengths. With this approach, moment-rotation models that account for strength and stiffness deterioration can be applied in conjunction with *FLPH* models to support collapse prediction of frame structures. The approach includes an automatic calibration procedure embedded in the numerical integration of the element, freeing the analyst of this task. The calibration procedure is formulated for the *modified* Gauss-Radau integration scheme. However, it can be applied to other plastic hinge methods proposed by Scott and Fenves [102] and Addessi and Ciampi [118], function of the weight and location of the integration points used in the calibration.

2.4.1 Calibration Procedure

The main goals of this procedure are to:

1. Use empirical moment-rotation relationships that account for strength and stiffness deterioration to model the flexural behavior of the plastic hinge region;

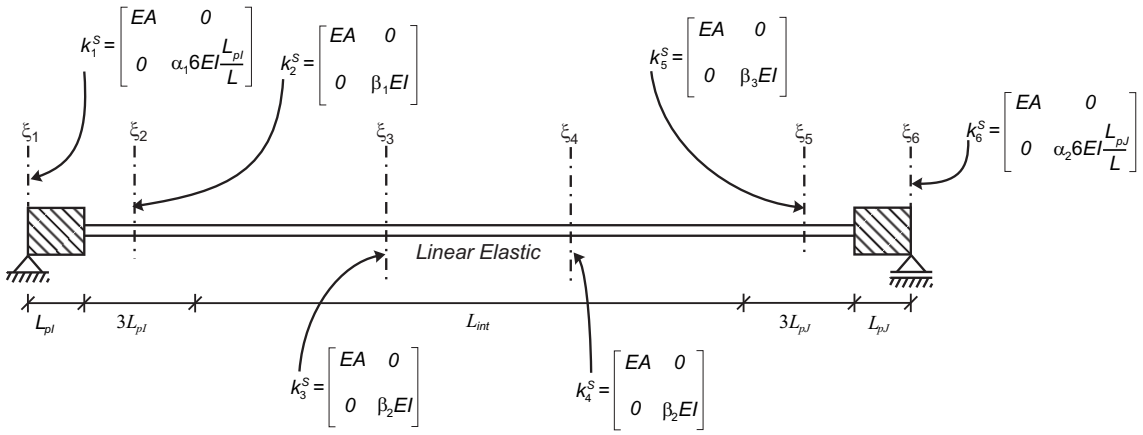

Figure 2.5: Modified Gauss-Radau integration scheme with section flexural stiffness modification parameters

2. Guarantee that the flexural stiffness is recovered for the nominal prismatic element during the entire analysis; and

3. Allow the definition of arbitrary plastic hinge lengths by the analyst.

The presented calibration procedure is performed at the element level through the introduction of section flexural stiffness modification parameters at internal sections of the beam-column element making it possible to scale a moment-rotation relation in order to obtain moment-curvature relations for the plastic hinge regions. Defining the moment-rotation stiffness of the plastic hinge regions as:

$$k_{M-\theta} = \frac{\alpha 6EI}{L} \tag{2.19}$$

and making use of a user-defined plastic hinge length at either end of the element (L_{pI} and L_{pJ} for ends I and J, respectively), the moment-curvature relations can be defined as:

$$k_{M-\chi} = \frac{\alpha 6EI}{L} \times L_{P\{I,J\}} \tag{2.20}$$

As highlighted by Scott and Ryan [123], the moment-rotation and moment-curvature relations are identical for $L_{P\{I,J\}}/L = 1/6$. However, for any other plastic hinge length, the definition of the moment-curvature via direct scaling of the moment-rotation given by Equation 2.20 yields incorrect section stiffness, which in turn lead to incorrect member stiffness. The calibration procedure presented herein compensates for the incorrect stiffness of the plastic hinge moment-curvature relationship by modifying the flexural stiffness of each of the four internal sections (integration points ξ_2, ξ_3, ξ_4 and ξ_5 in Figure 2.4), assumed to remain linear elastic throughout the analysis, using one of three different parameters, β_1, β_2, and β_3, shown in Figure 2.5.

The β modification parameters are quantified such that the element flexibility matrix is: (i) within the elastic region, equal to the analytical solution for an elastic prismatic element; (ii) after yielding, identical to the target flexibility, i.e. is similar to the user-defined $M - \theta$ behavior. The target flexibility matrix in the elastic and nonlinear regions can be provided by the *CPH* model using Equations 2.1 to 2.4. Then, the modification

parameters are defined based on the equivalence of the flexibility matrices associated with the *CPH* and *FLPH* models. The target flexibility can be computed using different models and herein the models defined by Lignos and Krawinkler [4] are used in the derivations. In the calibration procedure, double curvature or anti-symmetric bending is assumed to obtain the elastic stiffness of the structural element. This is a common result of the lateral loading and boundary conditions considered in seismic analysis of frame structures. In this case, the elastic element $M-\theta$ stiffness is $6EI/L$. However, the calibration procedure shown herein is valid for any element moment-rotation stiffness and moment gradient.

2.4.2 Derivation of Modification Parameters

For the 2D beam-column element, a system of three integral equations corresponding to each of the unique flexural coefficients of the element flexibility matrix is constructed. The flexibility matrix coefficients obtained from Equation 2.18, corresponding to the *FLPH*, are equated to the flexibility matrix coefficients obtained from Equation 2.1, associated with a *CPH* model and the empirical model. From this system of equations, the three elastic stiffness modification parameters, β_1, β_2, and β_3, can be computed as a function of L_{pI}, L_{pJ}, L and n_{Factor}, which is the elastic stiffness modification parameter of the *CPH* model. The code for solving the system of equations, which is implemented in the *wxMaxima* software [124] and is presented in the Appendix A. When n_{Factor} tends to infinity, β_1, β_2 and β_3 are given by:

$$\begin{aligned}
\beta_1 &= -\frac{54L_{pI}L^3 - 6L_{pI}(60L_{pI}+60L_{pJ})L^2 + 6L_{pI}(96L_{pI}^2+288L_{pI}L_{pJ}+96L_{pJ}^2)L - 6L_{pI}(256L_{pI}^2L_{pJ}+256L_{pI}L_{pJ}^2)}{L(3L-16L_{pJ})(L^2-20LL_{pI}+4L_{pJ}L+64L_{pI}^2)} \\
\beta_2 &= -\frac{3(4L_{pI}-L+4L_{pJ})(3L^2-12LL_{pI}-12LL_{pJ}+32L_{pI}L_{pJ})}{L(3L-16L_{pI})(3L-16L_{pJ})} \\
\beta_3 &= -\frac{54L_{pJ}L^3 - 6L_{pJ}(60L_{pI}+60L_{pJ})L^2 + 6L_{pJ}(96L_{pI}^2+288L_{pI}L_{pJ}+96L_{pJ}^2)L - 6L_{pJ}(256L_{pI}^2L_{pJ}+256L_{pI}L_{pJ}^2)}{L(3L-16L_{pI})(L^2-20LL_{pJ}+4L_{pI}L+64L_{pJ}^2)}
\end{aligned} \tag{2.21}$$

If both plastic hinges have the same length, i.e. $L_p = L_{pI} = L_{pJ}$, Equation 2.21 simplifies significantly to:

$$\begin{aligned}
\beta_1 &= \beta_3 = -\frac{6\left(3\,L^2\,L_p - 24\,L\,L_p^2 + 32\,L_p^3\right)}{L(L-8\,L_p)^2} \\
\beta_2 &= \frac{3\left(3\,L^3 - 48\,L^2\,L_p + 224\,L\,L_p^2 - 256\,L_p^3\right)}{L(3L-16\,L_p)^2}
\end{aligned} \tag{2.22}$$

It is worth noting that in Equation 2.22 there are singularities in β_1 and β_3 for $L_p/L = 1/8$ and in β_2 for $L_p/L = 3/16$, which correspond to cases in which: (i) the length of the elastic element interior, L_{int}, is equal to zero and (ii) the two internal integration points ξ_2 and ξ_5 shown in Figure 2.5 are co-located.

In Figure 2.6 the flexural stiffness modification parameters of Equation 2.22 are represented as a function of the plastic hinge length to span ratio L_p/L. Both parameters β_1 and β_3 are equal for all L_p/L ratios, as both plastic hinges have the same flexural stiffness $\alpha_1 6EIL_p/L = \alpha_2 6EIL_p/L$. Note that the calibration procedure is valid when $L_{int} < 0$, i.e. $L_p/L > 1/8$.

The proposed calibration procedure is illustrated in Figure 2.7 for the specific case of a nonlinear static (pushover) analysis. The pushover analysis is conducted by controlling

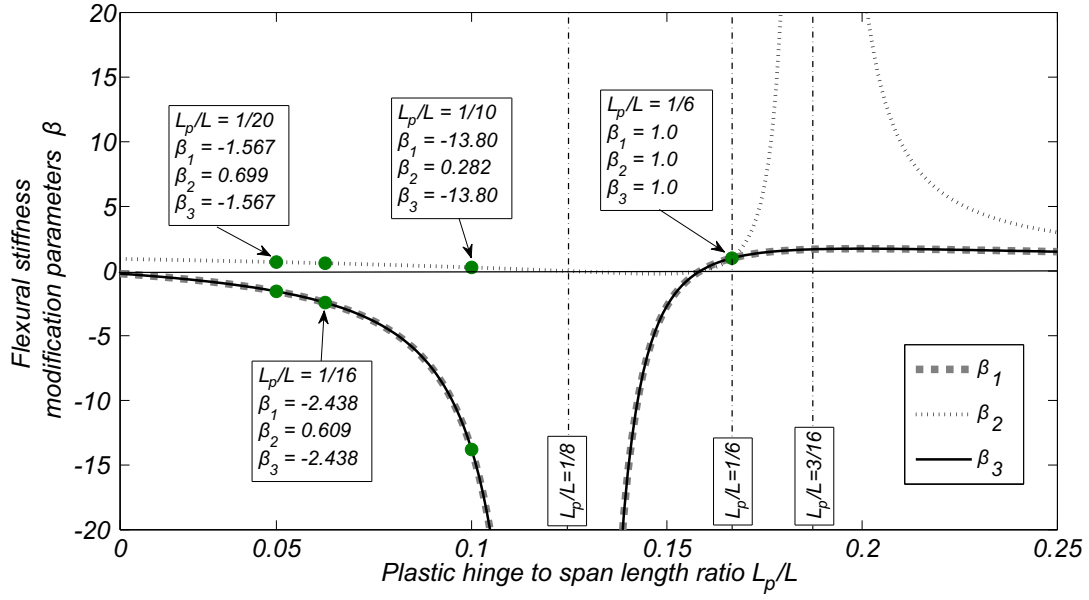

Figure 2.6: Flexural stiffness modification parameters β_1, β_2 and β_3 as a function of the plastic hinge length to span ratio L_p/L

a j^{th} degree of freedom (DOF). Furthermore, the displacement U_f and pseudo-time λ are initialized to zero, and the displacement increment dU_f for the control DOF and the reference load pattern P_{ref} are also initialized. The stiffness matrix K_S is computed in the *form stiffness matrix* procedure (see Figure 2.8) at the beginning of each analysis step and each Newton-Raphson (NR) iteration. In this procedure, the parameters α_1 and α_2 are calculated based on the committed (converged in a previous step) element forces and deformations, as well as the tangent stiffness. In the first analysis step, the section stiffness modification parameters β_1, β_2 and β_3 are computed, as shown in Figure 2.8. Once the stiffness modification parameters are computed, the stiffness matrix is computed through inversion of the flexibility matrix. The stiffness matrix is obtained considering the integration points (IPs) of the *modified* Gauss-Radau integration scheme shown in Figure 2.5. Transformation from the basic to the local coordinate system is performed with the matrix A_f. From this point onward a traditional NR algorithm is used, repeating the above procedure at the beginning of each analysis step and at each NR iteration. Different strategies can be used in updating the model state determination, namely: (i) update state of the model domain (displacements, pseudo-time, forces) using the residual tangent displacement from the previous iteration; (ii) decrease the displacement increment and update the model domain trying to overcome convergence problems; (iii) change the numerical method used (either for this analysis step only or for all remaining steps); and (iv) change the tolerance criteria (if that is admissible for the case being analyzed). In case the NR method is not able to converge after a user-defined maximum number of iterations, i_{max}, the analysis is stopped, and is considered not to have converged. Illustrative examples are presented in the following sections. Different solution algorithms may be used to solve the nonlinear residual equations [125,126]. The (NR) algorithm is one of the most widely used and is a robust method for solving nonlinear algebraic equations of equilibrium. In this figure (Figure 2.7) the flowchart for the calibration procedure is exemplified using the NR algorithm.

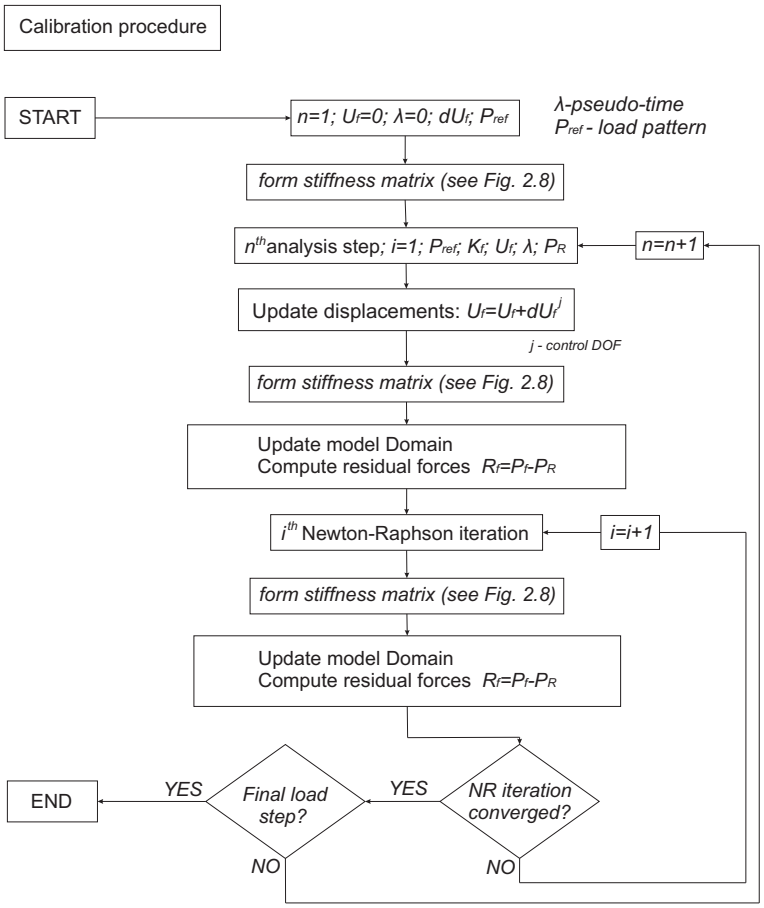

Figure 2.7: Calibration procedure for a nonlinear static structural (pushover) analysis

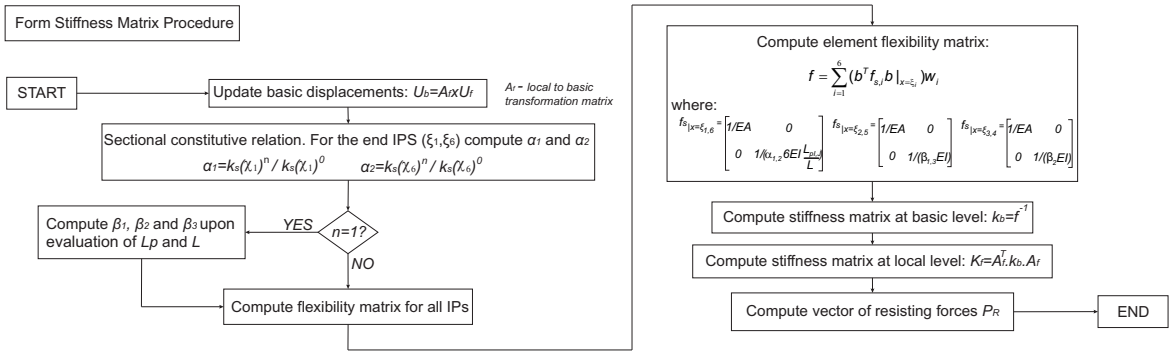

Figure 2.8: Flowchart for computation of element stiffness matrix

2.5 Numerical Examples

The proposed calibration procedure was applied to a set of simply supported beams subjected to end moments and considering different plastic hinge lengths, as well as a simple steel frame structure. The beams are analyzed considering a pushover analysis, where rotations are incremented until reaching an ultimate rotation. For the first beam, equal moments are applied at each support, while in the second case, the moment applied at the left support is half of that applied to the right support.

In these examples the flexural member behavior is defined through the multi-linear empirical model proposed by Lignos and Krawinkler [4]. This model allows for defining the moment-rotation relationship of steel members based on geometrical and physical properties. This is possible after an extensive calibration performed by Lignos [127] of hundreds of experimental test results. The model is based on a backbone curve, shown in Figure 2.9, that defines the behavior for monotonic loading and defines the boundaries for cyclic response. The backbone curve is characterized by: yielding moment and rotation (M_y and θ_y); capping moment (M_c); plastic rotation capacity (θ_p); post-capping rotation capacity (θ_{pc}); residual moment ($M_r = \kappa \times M_y$); and ultimate rotation (θ_u). The model parameters used in these examples are presented in Table 2.1.

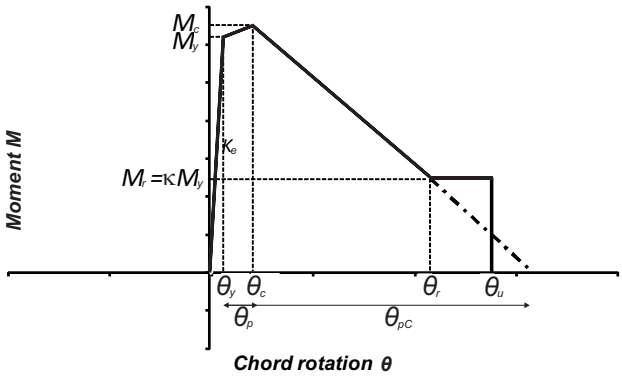

Figure 2.9: Moment-rotation model proposed by Lignos and Krawinkler [4]

Table 2.1: Element properties for numerical examples

	Geometric parameters		Moment-rotation model parameters			
	Inertia (m^4)	Area (m^2)	M_y (kNm)	M_c/M_y	θ_p (rad)	θ_{pc} (rad)
Example 1 and 2	0.0002	0.0073	320.78	1.05	0.0692	0.168
Frame Beams	0.0111	0.0551	1911.0	1.05	0.025	0.25
Frame Columns	0.0111	0.0551	969.0	1.05	0.03	0.35

2.5.1 Example 1

A simply supported beam is analyzed considering equal moments and rotations applied at both ends. Three models, corresponding to three different plastic hinge lengths, $L_p = \{L/16, L/10, L/6\}$, are tested. Figures 2.10(a), 2.11(a), and 2.12(a) show the element end

moment plotted against the element end rotation. A local response, corresponding to the rotation of a section at a distance L_p from the support is also plotted against the end moment in Figures 2.10(b), 2.11(b), and 2.12(b). The rotation at a distance L_p from the support, in the CPH model, must consider the rotation of the zero-length spring and the deformation of the elastic segment of length L_p. In these figures, the plastic rotation of the CPH model is computed obtained by adding the rotation of the zero-length spring to the rotation of the elastic element over a length of L_p. The former is obtained by multiplying the curvature (χ) of the end section of the element by L_p.

The *CPH* curve denotes the results obtained using a concentrated plastic hinge model, following the procedure employed by Lignos and Krawinkler [128], and serves as a benchmark. Figure 2.10(a) shows that end rotations obtained using the *CPH* model present an initial linear elastic response up to the yielding point, defined by the yielding moment-rotation pair $M_{y,CPH} - \theta_{y,CPH}$. Then, a linear hardening region connects the yielding point to the capping point ($M_{c,CPH} - \theta_{c,CPH}$) and a linear softening region links the capping point to the residual moment-rotation point ($M_{r,CPH} - \theta_{r,CPH}$), which is followed by a plastic region that extends to θ_u. The second model considered (*FLPH S*) corresponds to the use of finite length plastic hinge elements, defining the moment-curvature relation through direct scaling of the rotation parameters (θ_y, θ_c, θ_{pc}, θ_r, and θ_u) by the plastic hinge length L_p and no further calibration. The results show that this approach leads to erroneous results, as the elastic stiffness obtained is significantly lower than the target, and higher rotations are obtained in the softening branch. If the moment curvature is calibrated (curve *FLPH M*) using the proposed method, it is possible to reproduce the *CPH* behavior of the beam exactly for the entire analysis. Although the global response is in perfect agreement, Figure 2.10(b) shows that the local response is different when the *CPH* or the *FLPH M* models are used. For the *FLPH* models, local response in Figure 2.10(b) corresponds to the integration of the end section curvature (χ) over the plastic hinge length L_p ($\chi \times L_p$). This result is equal for the *FLPH S* and the *FLPH M* models since the end sections of both models are defined in a similar manner (only the interior sections are affected by the flexural modification parameters).

Figure 2.11, which is associated with a plastic hinge length $L_p = L/10$, shows similar results. In turn, Figure 2.12 shows that in case plastic hinge length is $L/6$ the correct moment-rotation response is obtained. This is in accordance with the findings of Scott and Ryan [123] for elasto-plastic behavior. In this case no calibration is required as the relationship between moment-rotation and moment-curvature is direct. Due to this fact, the local response in Figure 2.12(b) is also similar for both models.

Figure 2.16(a) shows the errors associated with the different models and different plastic hinge lengths. The errors are defined as the ratio between the computed slopes of the elastic, hardening, and softening branches, and the respective target moment-rotation defined in Lignos and Krawinkler [4]. The results show that: (i) the *FLPH M* calibration procedure provides accurate results when compared to the results obtained using *CPH* for the elastic, hardening and softening ranges of the response; (ii) the *FLPH S* procedure, where a scaled moment-curvature relation is used without further calibration, results in significant errors. It is worth noting that only for $L_p/L = 1/6$ does the *FLPH S* model result in the exact moment-rotation at yielding and at the capping point, as previously shown by Scott and Ryan [123]. The results from this example highlight the the advantages of the calibration procedure proposed herein, namely showing that accurate results can be achieved for varying lengths of the plastic hinge and for cases considering softening.

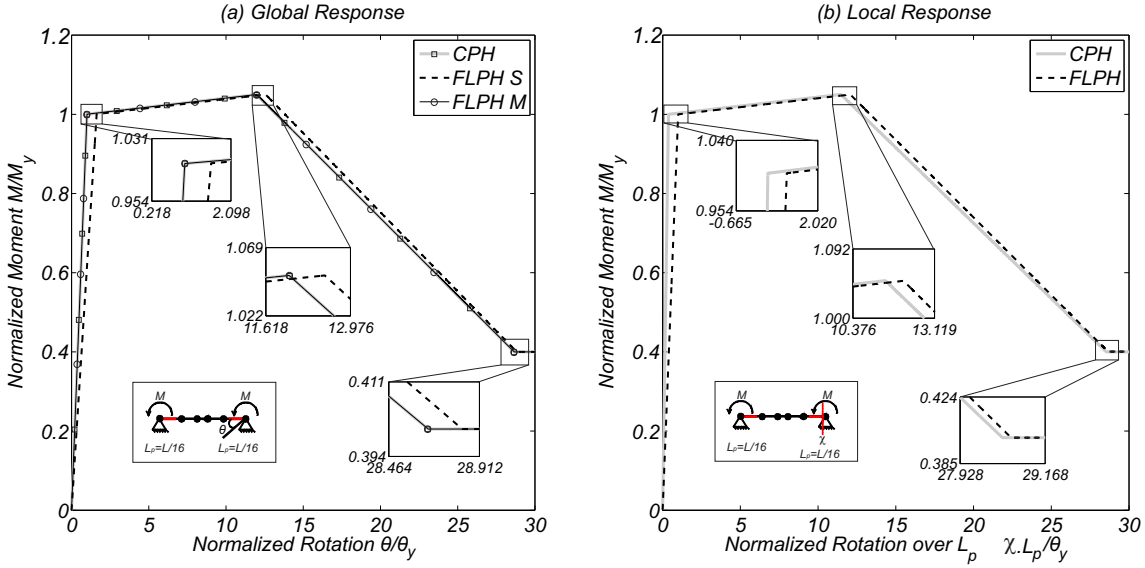

Figure 2.10: Example 1 - basic system with equal moments at both ends and plastic hinge length $L_p/L = 1/16$

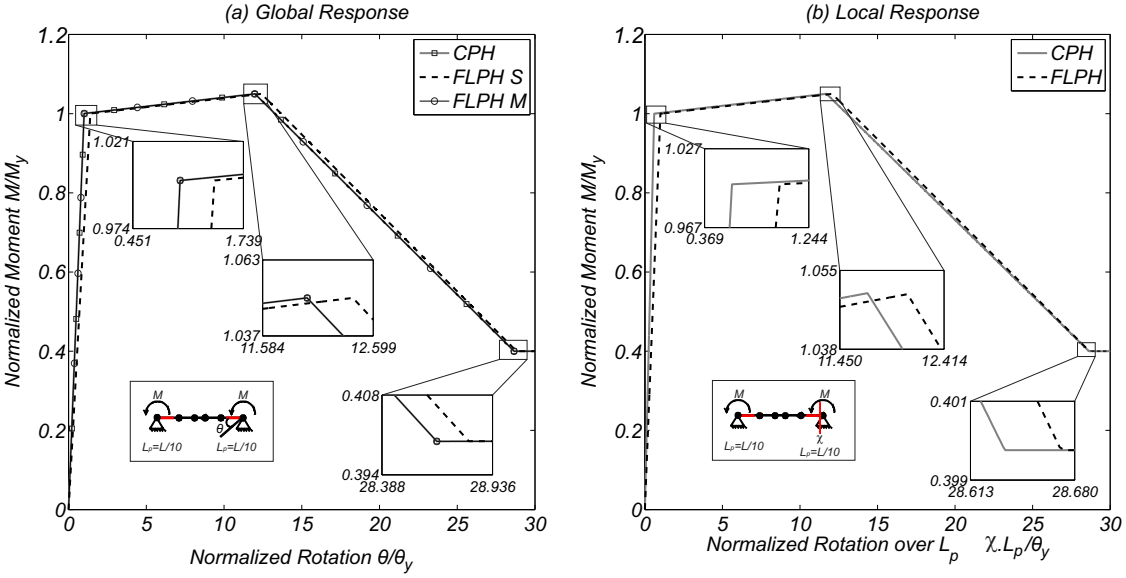

Figure 2.11: Example 1 - basic system with equal moments at both ends and plastic hinge length $L_p/L = 1/10$

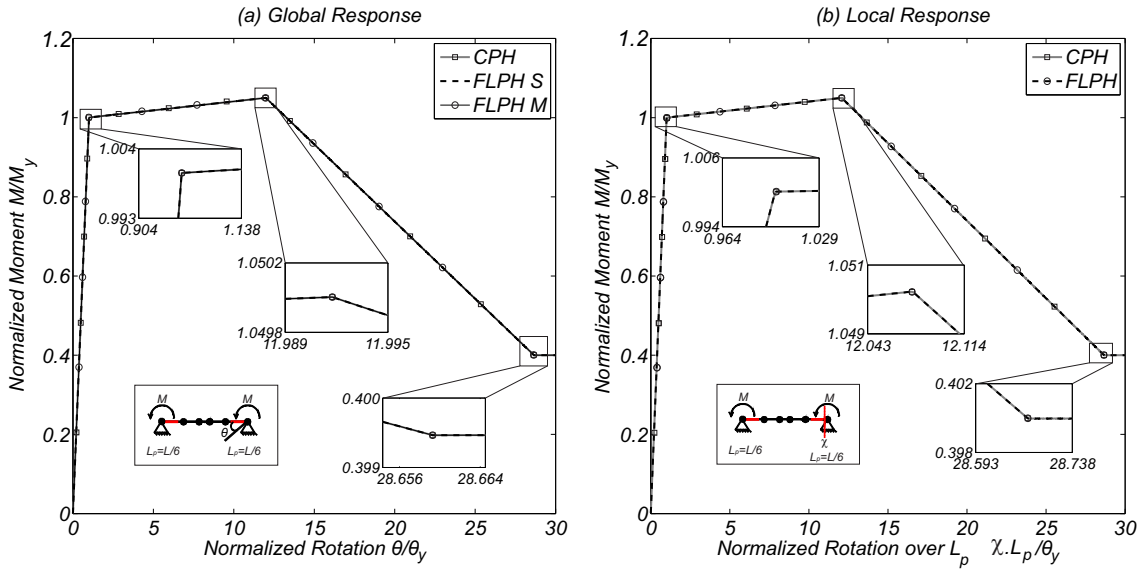

Figure 2.12: Example 1 - basic system with equal moments at both ends and plastic hinge length $L_p/L = 1/6$

2.5.2 Example 2

To show calibration for other moment gradients in the beam element, an identical beam to that from the previous example is analyzed considering the left moment equal to half of the right moment. As a result the left end of the beam is always in the elastic range, and the beam does not deform in double curvature. However, as shown in Figures 2.13, 2.14, and 2.15, the results obtained for these three plastic hinge lengths ($L_p/L = \{1/16, 1/10, 1/6\}$) are consistent with those obtained in Example 1. In fact, the results obtained with the scaled moment curvature relation without calibration (*FLPH S*) show significant errors from the elastic range, propagating over the entire range of analysis. When calibration is considered (*FLPH M*) the results are corrected and perfect agreement is found between *CPH* and *FLPH M* models. Figure 2.16(b) shows the results obtained considering several plastic hinge lengths. The errors are computed by comparing the slopes of the elastic, hardening and softening branches of the two $FLPH$ elements with the *CPH* model. Results show that the analysis presented for $L_p/L = 1/16, 1/10, 1/6$ is valid for all values of the plastic hinge length. Furthermore, the results show that the proposed calibration procedure is applicable to different moment gradients besides anti-symmetric bending.

2.5.3 Frame Structure

A single-bay three-story frame with uniform stiffness and strength over its height (see Figure 2.17) is used to illustrate the application of the calibration procedure described above. A dead load of 889.6kN is applied to each story, giving a total structure weight W of 2669kN. The flexural stiffness EI is identical for beams and columns with values given in Table 2.1. Plastic hinges form at beam ends and at base columns. The other columns are assumed to remain elastic. Pushover analyses of the frame are conducted in the OpenSees framework [129] using a P-Delta geometric transformation for the columns. Results obtained with model *FLPH M* are compared to results obtained using the *CPH* models. It is worth

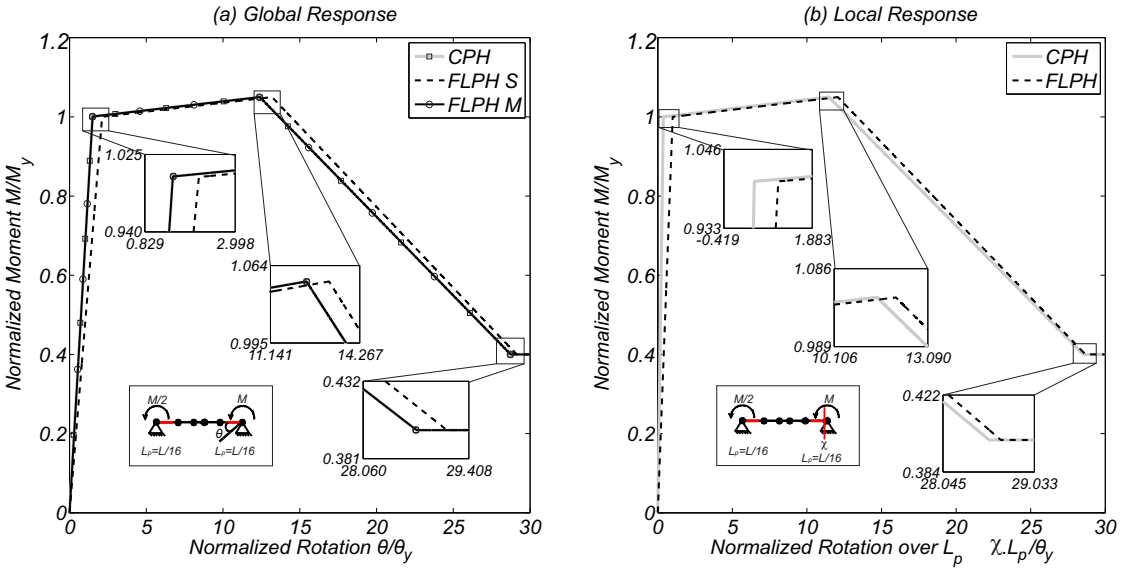

Figure 2.13: Example 2 - basic system with different moments at both ends and plastic hinge length $L_p/L = 1/16$

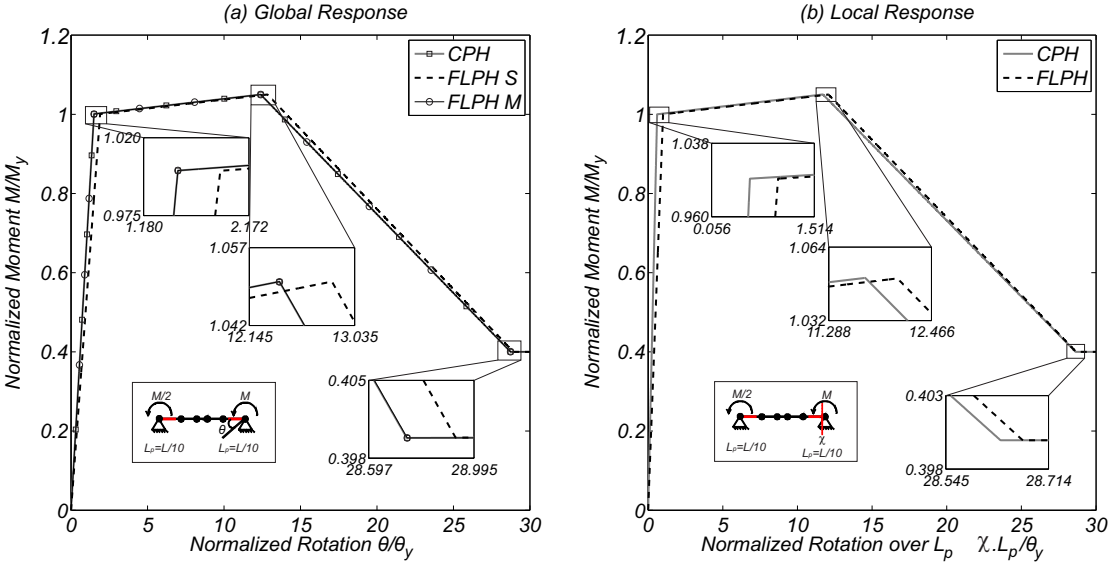

Figure 2.14: Example 2 - basic system with different moments at both ends and plastic hinge length $L_p/L = 1/10$

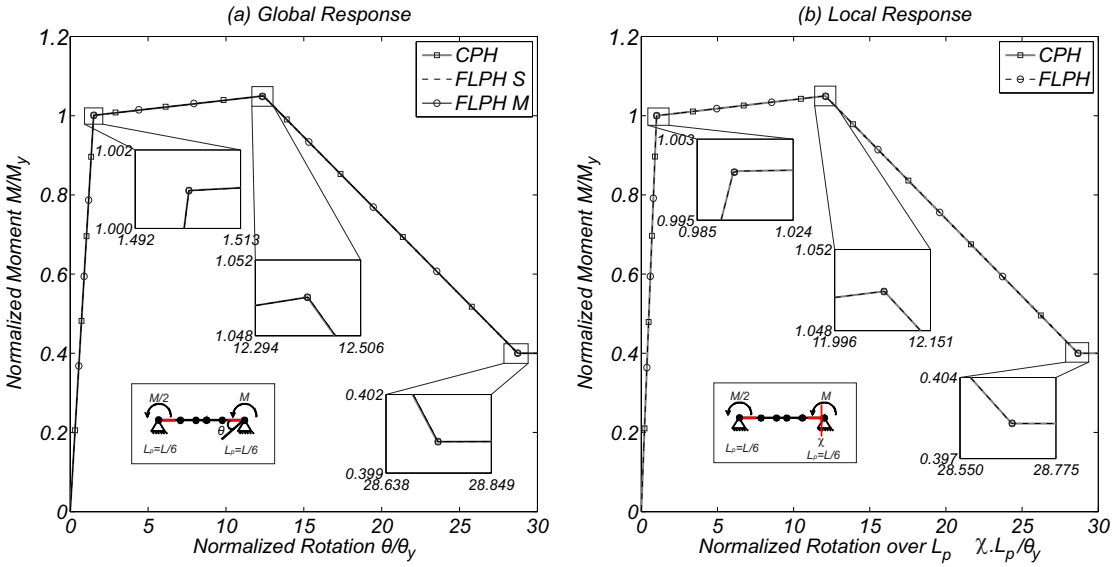

Figure 2.15: Example 2 - basic system with different moments at both ends and plastic hinge length $L_p/L = 1/6$

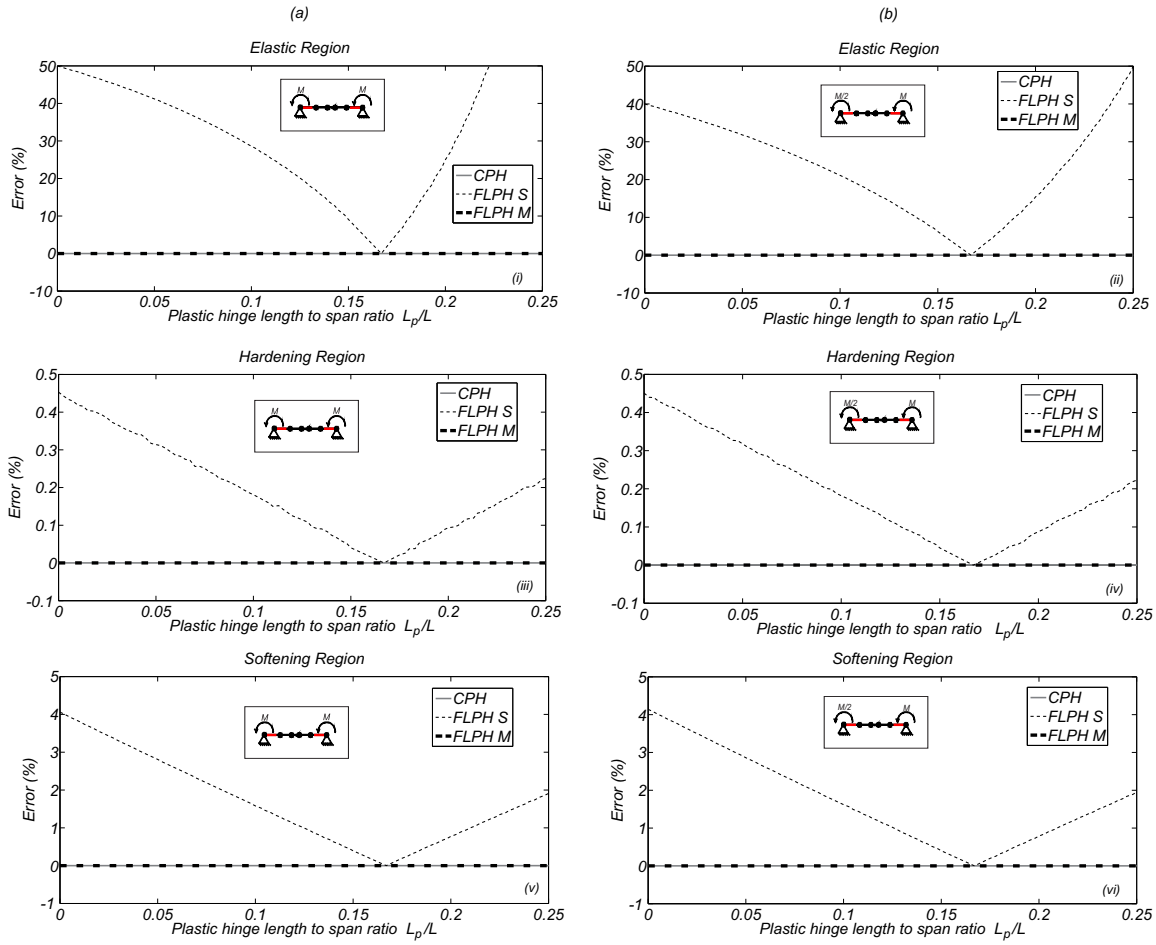

Figure 2.16: Errors in the slopes of the elastic, hardening and softening regions for the *CPH*, *FLPH S* and *FLPH M* models during a monotonic analysis

noting that in steel W-shape beams with shape factors ($k = M_p/M_y$) of approximately 1.12, the plastic hinge length is taken as 10% of the distance between the point of maximum moment and the inflection point [130]. This value is slightly larger, approximately 12.5%, at the center of beams that are subjected to distributed loads. Thus, for members in a state of anti-symmetric double curvature, it is suggested that a plastic hinge length between $L/20$ and $L/16$ be used.

Figure 2.18(a) shows the normalized base shear (V/W) versus roof drift ratio for the three models and Figure 2.18(b) illustrates the beam moment-rotation response. The results obtained for this frame show that the conclusions drawn for the two previous examples hold, namely *FLPH S* should not be used as a procedure for converting from empirical moment-rotation relations to moment-curvature relations when *FLPH* elements are used, and *FLPH M* is an adequate procedure that produces objective results without computationally expensive iterative/updating procedures.

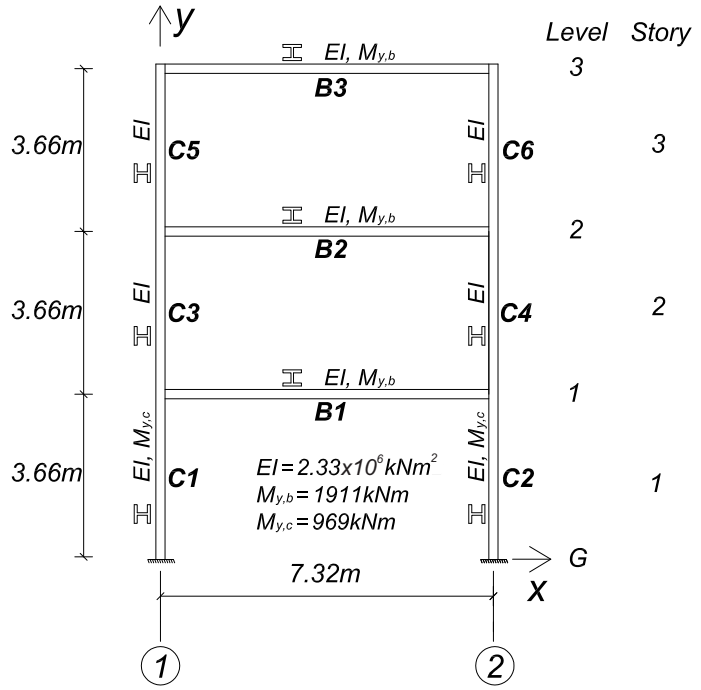

Figure 2.17: Steel moment frame

2.6 Conclusion

The present Chapter presented a calibration procedure for the use of finite-length plastic hinge (*FLPH*) force-based beam-column elements with empirically calibrated moment-rotation relationships describing the entire range of response. This allows for accurate modeling of steel moment frames that exhibit softening response at the section and element levels. The use of scaled but uncalibrated moment-curvature relationships in *FLPH* elements leads to significant errors in both local and global responses and is therefore not adequate for structural analysis. The new calibration procedure is performed at the element level through the introduction of section flexural stiffness modification parameters (β), which are computed at the beginning of the analysis as a function of the user defined plastic hinge lengths.

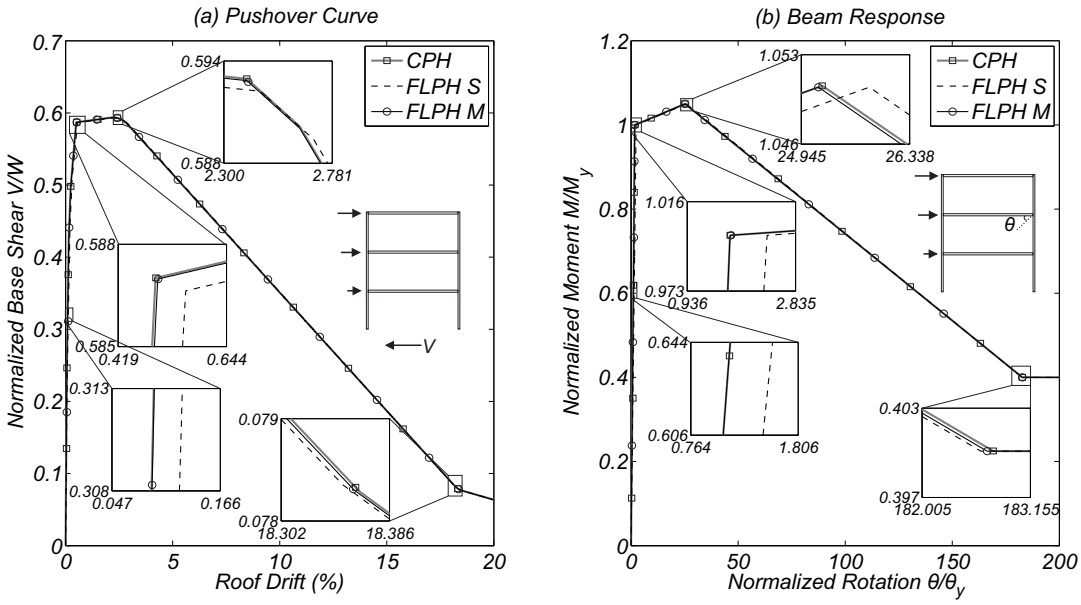

Figure 2.18: Example three-story frame used to demonstrate the proposed calibration procedures

The modification parameters are obtained by equating element flexural coefficients of the flexibility matrix and a target flexibility matrix, where the latter is given by the user-defined moment-rotation relation and is computed in this work using a *CPH* model.

Nonlinear static analyses of two simply supported beams and pushover analysis of a steel moment-resisting frame were performed considering different plastic hinge lengths. The results illustrate that the exact linear elastic stiffness can be recovered for linear problems while ensuring objective response after the onset of deterioration. The cases studied as well as error analysis based on analytical expressions show that the calibration procedure is valid for any moment gradient. Even though the proposed calibration procedure has only been validated for multi-linear moment-rotation relationships, it is, in principle, possible to use it with other constitutive laws, where moment-rotation can be related to moment-curvature by a user-defined plastic hinge length.

The calibration procedure was validated at the section level for bending moments and rotations only, but similar approaches may be used for cases in which the interaction between bending and axial deformations is considered. The accuracy and stability of the proposed calibration procedure remains to be studied for nonlinear dynamic time-history analysis of steel moment frame buildings.

2.7 Dissemination

This part of the research program resulted in the following outputs.

1. Scientific paper published in the Journal of Structural Engineering

   Scope: Presentation of the plastic-hinge calibration approach that allows for simulation of structures using FLPH elements that use the modified Gauss-Radau integration scheme and make use of recent multilinear moment-rotation constitutive laws

that have been derived from experimental results. The proposed methodology was applied to a set of simply supported beams subjected to end moments and considering different plastic hinge lengths, and a simple steel frame structure.

Complete reference: Ribeiro, F., Barbosa, A., Scott, M., and Neves, L. (2015). "Deterioration Modeling of Steel Moment Resisting Frames Using Finite-Length Plastic Hinge Force-Based Beam-Column Elements." Journal of Structural Engineering, 141(2), 04014112.

Chapter 3

Development of Enhanced Finite Element Models for Seismic Analysis. Part II: Implementation

3.1 Scope

Due to the importance of using empirical models in the simulation of member response for seismic analysis of building structures, a calibration procedure was proposed in Chapter 2 making use of multi-linear moment-rotation constitutive laws. In this Chapter, the implementation of that calibration procedure is performed based on recently developed phenomenological relationships. . For example the Modified Ibarra-Medina-Krawinkler (ModIMK) [4,131] deterioration model that have been derived from experimental results. The general ModIMK model is versatile and has been applied to steel, reinforced concrete, and timber structures. The proposed implementation allows for the use of these recently proposed models in both finite-length plastic hinge elements and in concentrated plastic hinge models. The proposed unified implementation also overcomes additional accuracy issues related to the update of model parameters due to cyclic deterioration. Results from included examples validate the proposed algorithms, which were implemented in OpenSees. Additionally, results highlight that FPLH models avoid errors and convergence pitfalls of CPH models.

3.2 Introduction

Accurately modeling the behavior of structural members under large cyclic deformations is paramount for the quantification of the seismic performance of structures with some degree of confidence. However, the behavior of structural elements under these extreme loading conditions is extremely complex. As a consequence, several simulation approaches have been proposed which include models of varying complexity and computational cost.

The main objective of this chapter is to present a unified implementation algorithm of the ModIMK deterioration models for use in CPH and FLPH models. For the CPH model, new implementations are provided for updating the unloading stiffness and the post-yield hardening ratio, as well as, the computation of the committed member displacements and the updated spring displacements. For the FLPH models, the proposed calibration procedure

(see Chapter 2), which updates the flexural stiffness of the interior sections of the member, is implemented to provide objective and consistent element responses when empirically calibrated moment rotations rules are employed for cyclic analysis. The formulation and implementation proposed was included in a modified version of the Open System for Earthquake Engineering Simulation (OpenSees, [132] 2.4.3, r5695) framework. Results from included examples validate the proposed algorithms. Additionally, results highlight that FPLH models avoid errors and convergence pitfalls of CPH models.

3.3 Literature Review

3.3.1 Empirical Laws for Simulating Member Behavior

Many hysteretic laws have been proposed in the last decades to model the performance of different structural elements and structural materials subjected to large cyclic displacements. The main observed nonlinear phenomena include cyclic deterioration in stiffness [105] and strength [106,107], and pinching under load reversal [68]. Among these models, the Modified Ibarra-Medina-Krawinkler [127], denoted ModIMK, was selected herein for its versatility. The ModIMK model has been applied to RC [88], steel [4], and timber structures [84].

Based on a large database of experimental results, Lignos and Krawinkler [4] have developed and validated multi-linear moment-rotation relationships that can be used to capture plastic hinge behavior in simulating the deteriorating response of steel structures to collapse. The multi-linear moment-rotation relationships are based on the ModIMK model. This model is based on: (i) a backbone curve defining the reference monotonic behavior, (ii) a set of rules defining the hysteretic behavior between the positive and negative backbone curves; and (iii) a set of rules that define up to six modes of deterioration of the hysteretic behavior. Figure 3.1(a) illustrates the parameters that define the backbone curve of this model. This curve is defined by three strength parameters: effective yield strength (or basic strength), F_y, capping strength, F_C (or post-yield strength hardening ratio F_C/F_y), and residual strength, F_r; and four deformation parameters: yield deformation, d_y, pre-capping plastic deformation for monotonic loading, d_p, post-capping plastic deformation, d_{pc}, and ultimate deformation capacity, d_u. The six modes of cyclic strength and stiffness deterioration: (i) basic strength, (ii) post-yield hardening ratio, (iii) post-capping strength, (iv) unloading stiffness, (v) reloading stiffness, and (vi) pinching behavior. Figures 3.1(b) to 3.1(d) illustrate three models that have been proposed in the literature based on different combinations of these six modes of deterioration. All three models share the same backbone curve. The models are:

- Bilinear hysteretic response (Bilin) model with strength deterioration (Figure 3.1(b));
- Peak-oriented model with strength and stiffness deterioration (Figure 3.1(c));
- Pinching model with strength and stiffness deterioration (Figure 3.1(d)).

In the ModIMK models, the rates of cyclic deterioration are controlled by a characteristic total hysteretic energy dissipation capacity E_t and an energy based rule developed by Rahnama and Krawinkler [133]. The characteristic total hysteretic energy dissipation capacity E_t is obtained from experimental results.

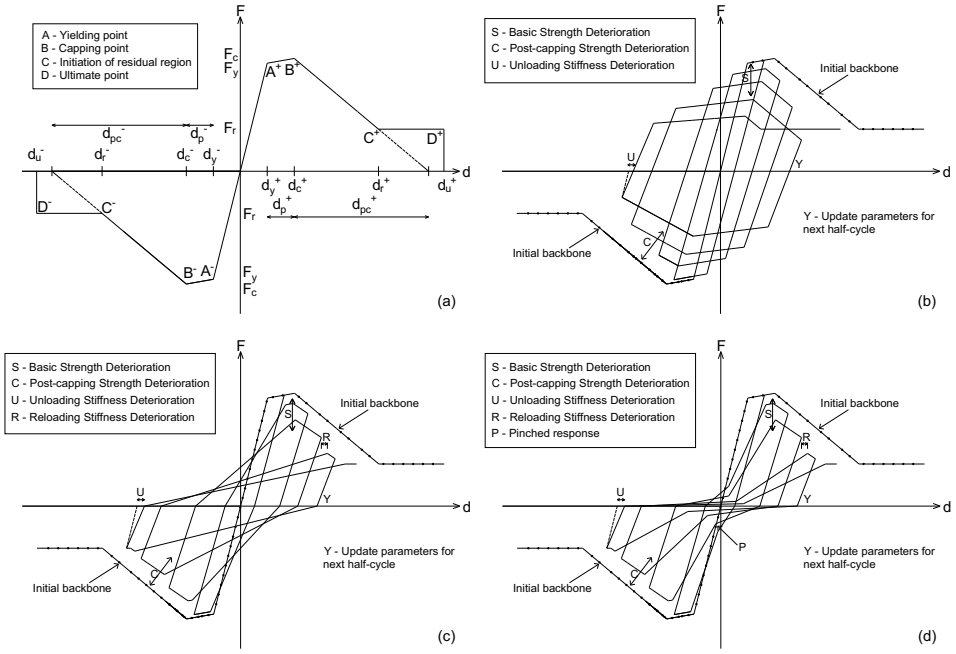

Figure 3.1: Modified Ibarra-Medina-Krawinkler deterioration models: (a) backbone curve, (b) Bilin model, (c) Peak-oriented model, and (d) Pinching model.

The energy based rule developed by Rahnama and Krawinkler [133] expresses the cyclic deterioration in excursion i, β_i, as:

$$\beta_i = \left(\frac{E_i}{E_t - \sum_{j=1}^{i} E_j} \right)^c \leq 1 \tag{3.1}$$

where E_i is the hysteretic energy dissipated in excursion i, and $\sum E_j \leq E_t$ is the hysteretic energy dissipated in all previous excursions in both positive and negative directions. The exponent c defines the rate of deterioration. According to Rahnama and Krawinkler [133], a reasonable range of values for c is between 1.0 and 2.0. β_i ranges between 0 and 1.

The generalized stiffness or strength parameter, X, can be updated through:

$$X_i = (1 - \beta_k) \times X_{i-1} \tag{3.2}$$

where X_i is the value of the parameter in excursion i and β_k is the value of deterioration parameter.

3.3.2 Using Empirical Laws in CPH and FLPH Models

CPH models are used herein as a reference modeling approach, considering the vast experience on the use of these in the modeling of buildings under seismic loads [84,88,108,109]. In these models, each structural element is modeled as the association of a linear elastic beam element and a nonlinear spring at each member end. The correct linear-elastic solution for the entire member is only obtained if the end rotational springs are approximated as rigid-plastic. This is usually achieved using an ad-hoc stiffness modifier parameter, n_{Factor}, for the zero-length springs. However, the definition of the ideal value n_{Factor} is not trivial, as a low value leads to erroneous results and a high value results in numerical instability and convergence issues. As discussed in detail in this work, the use of n_{Factor} also increases significantly the complexity of the implementation of nonlinear deterioration models.

The moment-rotation $(M - \theta)$ relationships described in the previous section can be used directly in concentrated plastic hinge (CPH) elements following approaches presented in Ibarra and Krawinkler [84]. In this case, moment-rotation relationships are employed to define the nonlinear zero-length springs that control element flexural response. Although approaches to avoid the use of ad-hoc penalty functions (n_{Factor}) in zero-length spring elements exist (e.g., [134]), the methodology proposed herein allows for consistency with the reference modeling approach for design and assessment of building structures under seismic actions defined in ATC-72 [109].

Otherwise, in what concerns finite-length plastic hinge elements, plastic hinge behavior can be defined through explicit fiber sections or by assigning moment-curvature and axial force-deformation (and shear force-distortion) relationships. When compared to the CPH approach, this model has been shown to be advantageous, namely in what concerns modeling effort, computational cost, clear separation between member and connection nonlinearity, and more realistic modeling of yielding progression and hinge rotations. Despite the enumerated advantages, the FPLH models assume that the plastic hinge length is constant throughout the analysis, which past experimental studies have demonstrated not to be accurate. In addition, when empirically calibrated deterioration models are used to define FLPH hinge sections flexural behavior, a moment-curvature relationship should be defined. The direct scaling of the moment-rotation relationship by the plastic length L_p in order

to obtain a moment-curvature $(M - \chi)$ relationship (i.e., by dividing each rotation by L_p ($\chi_i = \theta_i / L_p$)), at first may seem a logical approach. However, this leads to erroneous results when no further calibration is performed, as shown by Scott and Ryan [123] for the common case of elasto-plastic behavior with linear strain hardening under anti-symmetric bending. As a consequence, a calibration procedure is needed in FLPH models. A calibration procedure was proposed in Chapter 2 for sections exhibiting softening response under monotonic loading.

The ModIMK is used herein to model the behavior of plastic hinges. However, the implementation of this model within a finite element framework is complex and dependent on the type of finite element used. In the following sections the details regarding a consistent and unified implementation of these models is provided for CPH and FLPH models. This work focuses on description of the flexural behavior of the finite length plastic hinges. For certain problems, axial-flexure-shear coupling is important, such as in reinforced-concrete columns and several authors proposed finite element models combining axial force-shear-flexure interaction (e.g., Saritas and Filippou [135,136], Elwood and Moehle [137])). However, often these are not considered in state-of-practice modeling efforts and guidelines.

3.4 Implementation of ModIMK Models for Cyclic Analysis

Figure 3.2 shows the general procedure used to update the ModIMK model parameters. This procedure is a direct application of the proposal by Ibarra *et al.* [131], and it is detailed here for completeness of the discussion on the new implementation that follows in the next subsections. At the beginning of the analysis, the model parameters are initialized. In the elastic range, no change in these parameters occurs and no update of the deterioration model law is required. The unloading stiffness is the only parameter which is updated when a load reversal takes place in the inelastic range. In a finite element implementation, the stiffness must be known before the reversal, requiring the updating of the unloading stiffness in all steps in the inelastic range. Furthermore, this is the only deterioration mode for which a common deterioration parameter, β_i, is used in both loading directions.

The remaining parameters are updated at the end of the unloading branch ($F_{n-1} \times F_n < 0$), denoted by point Y in Figure 3.1. At this point, dissipated energy in the previous excursion is computed. This allows for updating of the reloading stiffness, the basic strength, the strain hardening ratio, the capping point, and the pinching parameters for the current excursion. The procedure is then repeated for each excursion reaching the nonlinear range.

3.4.1 Implementation in CPH Models

As referred in Chapter 2, in CPH models, to guarantee the rigid plastic behavior of the springs, the initial stiffness is given by:

$$k_{s,m} = (n_{Factor} + 1) \times K_{mem}, \qquad m = I, J \tag{3.3}$$

where K_{mem} is the elastic stiffness of the member. In the case of double curvature, $K_{mem} = 6EI/L$, where EI the is cross-section flexural stiffness, and L is the member length. Since the elastic stiffness of the member is related to the elastic stiffness of the rotational springs

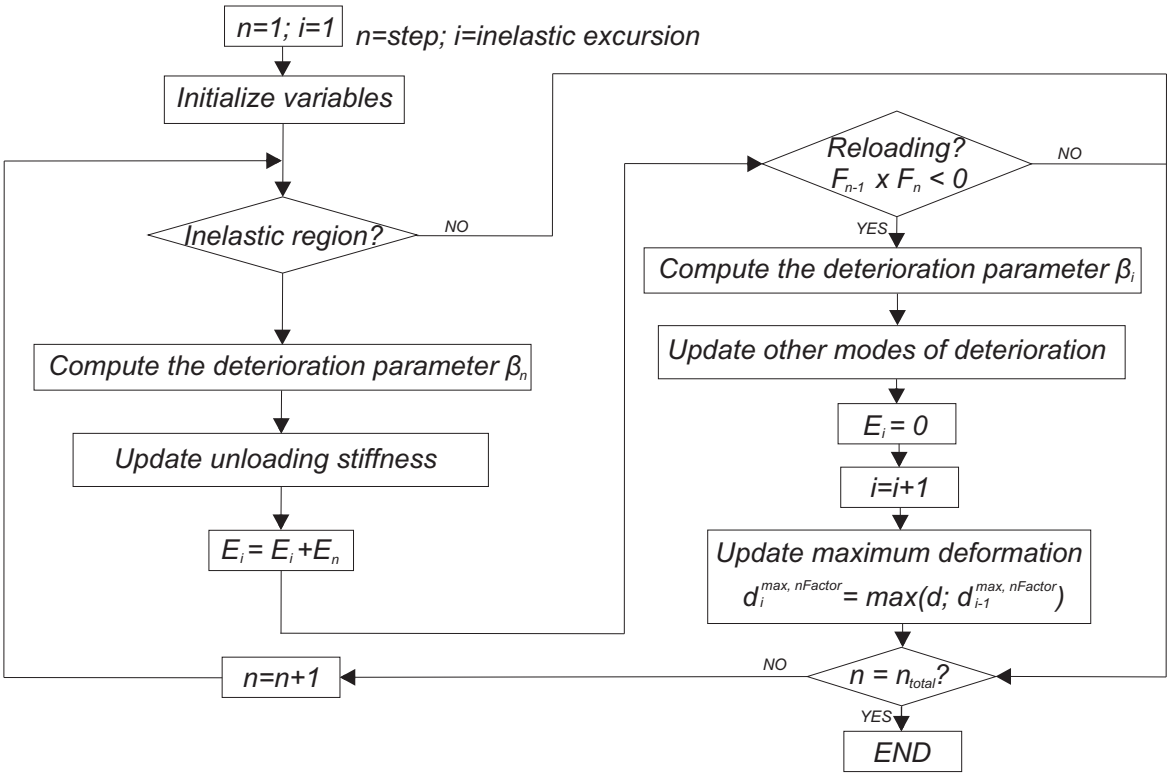

Figure 3.2: General procedure for updating model parameters during cyclic analysis

and the interior elastic element, which are connected in series, the stiffness of the interior element, k_{int}, is also affected by n_{Factor}, as:

$$k_{int} = \frac{n_{Factor}+1}{n_{Factor}} \times K_{mem} = \frac{6EI_{mod}}{L} \tag{3.4}$$

where $EI_{mod} = \frac{n_{Factor}+1}{n_{Factor}} EI$ is the modified elastic stiffness of the element interior.

In the post-yielding region, member stiffness is computed by multiplying the elastic stiffness by the post-yielding ratio, α. Since the elastic stiffness of the zero-length spring is affected by the n_{Factor}, an adjusted post-yielding ratio of the spring, α' (ratio of the tangent stiffness, k_{Ts}, to the linear elastic stiffness, k_s) is given by:

$$\alpha' = \frac{k_{Ts}}{k_s} = \frac{\alpha}{1 + n_{Factor} \times (1-\alpha)} \tag{3.5}$$

The introduction of an n_{Factor} in the definition of the zero-length springs requires that several modifications are considered in the ModIMK implementation and general deterioration model given in Equation 3.2. The adjusted implementation details when defining moment-rotation empirical relations in CPH models are presented next for each of the six deterioration modes. For comparison purposes, a simplified implementation, where the effect of n_{Factor} is not considered in the updating of model parameters, is denoted as CPH-original. In general, two main adjustments are made. First, the stiffness of the nonlinear spring is updated so that the stiffness of the entire element is equal to the objective stiffness. Second, the displacements of the springs need to be updated so that the correct target displacements (rotations) of the element are achieved. In what regards strengths, since the force (moment) in the spring is equal to the force (moment) in the element ends, no adjustment

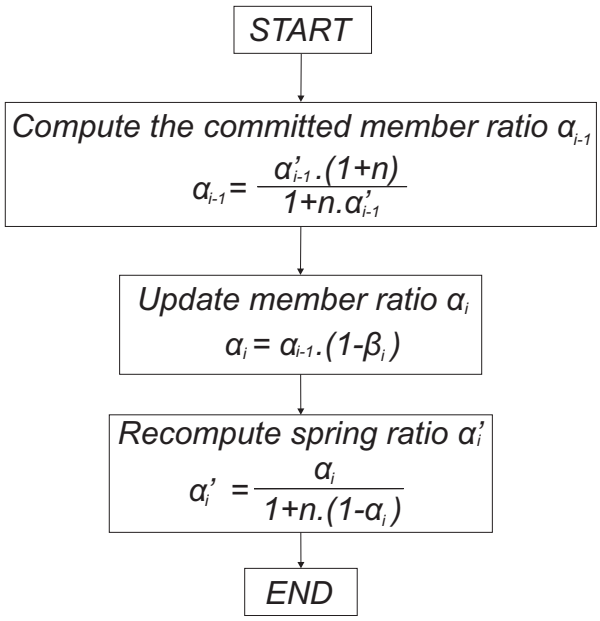

Figure 3.3: Procedure for updating post-yielding ratio during cyclic analysis for Concentrated Plasticity Hinge model

is required. Therefore, the basic and post-capping strength deterioration follows the general form of Equation 3.2. Thus, the update of the yielding moment is performed by:

$$M_{y,i} = M_{y,i-1} \times (1 - \beta_i) \tag{3.6}$$

Post-yielding stiffness update implementation

The zero-length spring stiffness is affected by the n_{Factor} and the post-yielding ratio of the spring defined in Equation 3.5 is used. When computing the deterioration of the post-yielding hardening ratio the general model described in Equation 3.2 is not applicable. Instead, the deterioration of the post-yielding hardening ratio is computed using the new procedure shown in Figure 3.3. In this procedure, first, the member hardening ratio of the previous excursion is computed using the inverse of Equation 3.5. Second, given β_i, the member post-yielding stiffness is updated. Lastly, Equation 3.5 is used to compute the updated hardening ratio of the nonlinear springs.

Unloading stiffness update implementation

Since the unloading stiffness deterioration depends on the energy dissipated up to the beginning of the unloading branch rather than that dissipated in a complete excursion, an implementation different from that proposed by Ibarra and Krawinkler [84] is used herein for this parameter. Equation 3.2 is thus replaced by:

$$K_{u,n}^{member} = \left[\prod_{j=1}^{i-1}(1 - \beta_{k,j})\right] \times (1 - \beta_{k,n}) \times K_0 = \gamma_k \times K_0 \tag{3.7}$$

where i is the total number of inelastic excursions up to load step n, $\beta_{k,j}$ is the deterioration parameter associated with completed inelastic excursion j, $\beta_{k,n}$ is the deterioration param-

eter computed considering the energy dissipated in excursion i up to load step n, γ_k is the cumulative deterioration of the unloading stiffness and K_0 is the member initial elastic stiffness. The procedure starts by computing the residual energy dissipation capacity, $E_t - \sum E_j$ and the damage parameter β_k. Equation 3.7 is then used to update the unloading stiffness of the element based on its elastic stiffness. The unloading spring stiffness is thus given by:

$$K_{u,n}^{spring} = \left(\frac{\gamma_k}{1 + n_{Factor} \times (1 - \gamma_k)} \right) \times K_0 \tag{3.8}$$

where K_0 and $K_{u,n}^{spring}$ are the original member elastic stiffness and updated unloading stiffness of the zero-length spring in loading step n.

Reloading stiffness and target displacement update implementation

The reloading stiffness deterioration is modeled by increasing the absolute value of the target displacement of the member, d_i, corresponding to the horizontal coordinate of point Y in Figure 3.1c, in each direction as:

$$d_i = (1 + \beta_i) \times d_{i-1}^{max} \tag{3.9}$$

where d_{i-1}^{max} is the maximum displacement observed up to the $i-1$ excursion in the same direction. The implemented algorithm for computing the reloading stiffness deterioration in CPH models is presented in Figure 3.4. Firstly, the maximum displacement of the member in previous excursions, $d_{i-1}^{max,member}$, is computed using the general relation between spring and member rotations:

$$d^{spring} = d^{member} - d^{elastic} = d^{member} - F(d^{member}) \times K_{member} \tag{3.10}$$

where $F(d^{member})$ is the force associated with the displacement d^{member}, obtained with the backbone curve computed for the current step of the analysis. $F(d^{member}) \times K_{member}$ is thus the elastic deformation of the member, associated with the force $F(d^{member})$ under the assumption of double curvature.

The updated member maximum displacement is then updated using Equation 3.9. Then, the updated backbone curve for this excursion is defined, based on the updated basic strength, post-yielding ratio, and post-capping strength. This is then used to compute the force $F(d_i^{max,member})$. The maximum deformation of the zero-length spring can then be calculated using Equation 3.10. Finally, the reloading stiffness is defined using point Y in Figure 3.1 and the new maximum deformation point ($d_i^{max,spring}$; $F^i(d_i^{max,member})$). The maximum deformation is monitored in each load step.

Pinching parameters update implementation

The implementation of updates of the pinching parameters is similar to that described for the reloading stiffness. The additional notable point in reloading (see point P in Figure 3.1(d)) is computed by multiplying the yielding displacement and the corresponding force by parameters A_{pinch} and $F_p^{\pm}$, respectively. Firstly, the maximum deformation in the member is calculated, using the relationship presented in Equation 3.10. Then, the intermediate point for pinching response is computed for the member by multiplying factors A_{pinch} and F_p^+ (for positive loading direction) to the maximum deformation and associated force, respectively. Once this intermediate point is found, the corresponding intermediate point for the

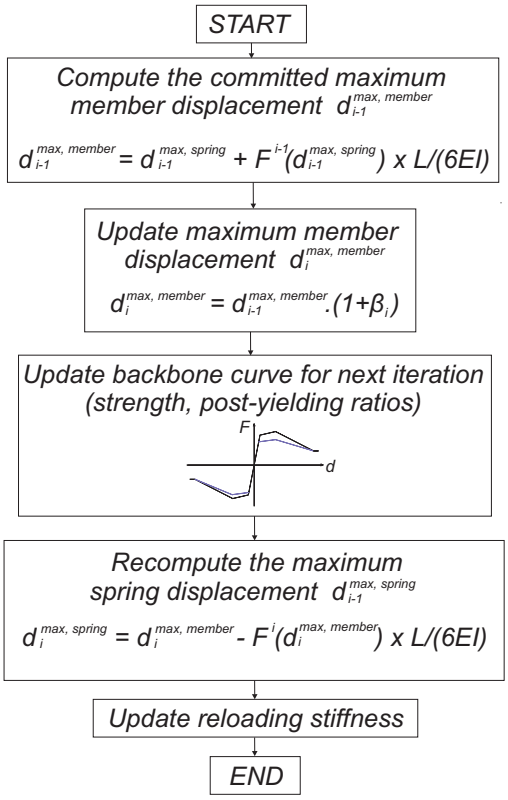

Figure 3.4: Procedure for updating reloading stiffness during cyclic analysis for Concentrated Plasticity Hinge model

zero-length spring is computed using Equation 3.10. Finally, the stiffness associated with the two branches that characterize pinching response can be computed for the CPH member.

3.4.2 Implementation and Calibration in FLPH elements

If the deteriorating models described herein are applied to $FPLH$ elements, the implementations developed by Ibarra and Krawinkler [84] do not require modifications, as the objective stiffness and displacements can be directly assigned to the member. This results in a much simpler implementation based on the general algorithm presented in Figure 3.2 and the general updating Equation (Eq. 3.2). This is one of the main advantages of using FLPH models, i.e. that the original hysteretic laws do not need adjustments as is the case when CPH models are used.

As shown by Scott and Ryan [123], employing a moment-rotation deterioration model law dividing the rotations by the plastic hinge length to obtain a moment-curvature relation produces inconsistent results and the objective moment-rotation response is not recovered. Thus, Scott and Ryan [123] proposed a calibration procedure to address this issue. However, the calibration procedure was developed for hardening responses only. An alternate calibration procedure developed in Chapter 2 was proposed for both hardening and softening responses under monotonic loading.

The flexural stiffness modification parameters ($\beta_i,\ i = \{1, 2, 3\}$) that were obtained in the previous chapter are independent of the assigned section behavior, as they are computed based on the comparison between the FLPH flexibility matrix and a reference flexibility

matrix provided by the CPH model. Therefore, these parameters are constant during the analysis and Equation 2.22 only needs to be applied once at the beginning the analysis, implying a very limited computational cost.

For the $FPLH$ model, in terms of calibration, the only other parameter that needs adjusting is the total energy dissipation capacity E_t. This term is defined empirically for the moment-rotation relation, and can be defined, for moment-curvature, as:

$$E_t^{M-\chi} = E_t^{M-\theta}/L_p \tag{3.11}$$

All other parameters follow the general models developed and implemented by Ibarra and Krawinkler [84]. Since the proposed calibration of the FLPH elements is done for the various segments of the force-deformation section response, the objectivity between target empirical energy dissipation modeled by the CPH models and the energy dissipation modeled using FLPH elements is achieved, regardless of the plastic hinge length considered.

3.5 Numerical Examples

In this section a simple structure subjected to a set of cyclic pushover analyses is used to evaluate the accuracy and stability of the proposed implementations. The algorithms and procedures discussed were implemented in a modified version of the Open System for Earthquake Engineering Simulation (OpenSees [132], v2.4.3, r5695) framework.

3.5.1 Example 1 - Validation

As examples, a set of simply supported beams and a plane frame are analyzed under cyclic pushover analyses. The beam, subjected to different end moments (see Figures 3.5 to 3.13), is analyzed under cyclic displacement control considering the three material models discussed. The beam has a 24 feet ($7.33m$) span and the model parameters for all material models are presented in Table 3.1. The ultimate rotation, θ_u and the plastic hinge length, L_p, were taken equal to 0.4 rad and $L/16$, respectively, for all cases. For the Pinching model, three additional parameters that define the mid-point in the reloading branch are assumed to be equal to 0.4.

Figures 3.5, 3.6, and 3.7 show results for analyses performed using the pinching model for moment gradients defined with one end moment, two anti-symmetric end moments, and two symmetrical end moments. The first set of results compares the results obtained using the CPH model, both considering direct application of Equation 3.2 (CPH-original) and using the proposed implementation (CPH-updated), with those obtained with the finite length plastic hinge model (FLPH) and an analytical solution. For the CPH-original, n_{Factor} was taken equal to 10 to reduce numerical instabilities, following recommendations in Ibarra and Krawinkler [84] and Zareian and Medina [121]. For CPH-updated n_{Factor} was taken equal to 10 and 1000. Results show that all implementations lead to acceptable results. However, the CPH-original and CPH-updated, considering a n_{Factor} equal to 10, lead to a noticeable over-estimation of the elastic stiffness. This error propagates to the entire analysis, as can be seen at the end of the unloading branch. Moreover, as a result of not updating the stiffness of the elastic element interior during analysis, the CPH-original also leads to significant errors in the unloading and reloading stiffness. The analysis using the FLPH elements provide the results closest to the theoretical results, being clearly the most accurate model. Figures 3.5,

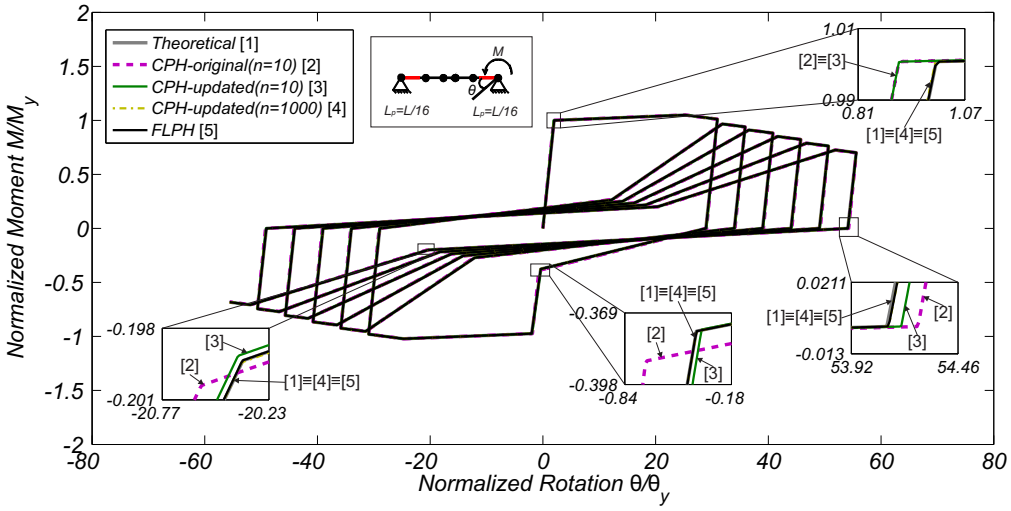

Figure 3.5: Pinching model - cyclic analysis considering a single end moment

3.6, and 3.7 show that the amplitude of observed errors decrease with increase in the moment gradient along the element length, being smaller for the anti-symmetric loading and larger for the symmetric loadings. In addition, it is clear that the use of the CPH-original model does not allow for obtaining accurate results as the direct application of Equation 3.2, i.e. not considering the implementation procedures proposed herein, is not enough for correctly updating model parameters during the analysis. For the three examples studied, the errors between the energy dissipated using the calibrated FLPH elements and the CPH elements (considering a $n_{Factor} = 1000$) are: 8.9×10^{-5} for the symmetric end moments, 8.6×10^{-5} for the anti-symmetric end moments, and 8.7×10^{-5} for the single end moment. Figures 3.10 to 3.13, which show the results obtained for the Peak-oriented and Bilin models indicate that the conclusions drawn for the pinching model hold for the other material models.

Table 3.1: ModIMK model parameters used in the numerical examples

Model	EI (kN.m^2)	M_y^+ and M_y^- (kN.m)	M_c/M_y	θ_p (rad)	θ_{pc} (rad)	κ	$E_t^{M-\theta}$ (kN.m)
All models	2.33×10^6	1911	1.05	0.233	0.156	0.4	2255

3.5.2 Example 2 - Stability and Numerical Errors

In Figure 3.14 the errors in the elastic stiffness are plotted for the FLPH model and for the CPH-updated implementation with n_{Factor} values between 10 and 1000. Results show convergence of the error when the CPH-updated implementation is used. However, even for large $n_{factors}$ the CPH-updated produces the largest errors when estimating the elastic stiffness. It is clear that the FLPH model results in very small errors, only comparable with those obtained for the CPH-updated with an n_{Factor} equal to 1000. The results presented refer to the Bilin model, but conclusions hold for all implemented models.

To compare the numerical stability of different implementations, results of an elementary

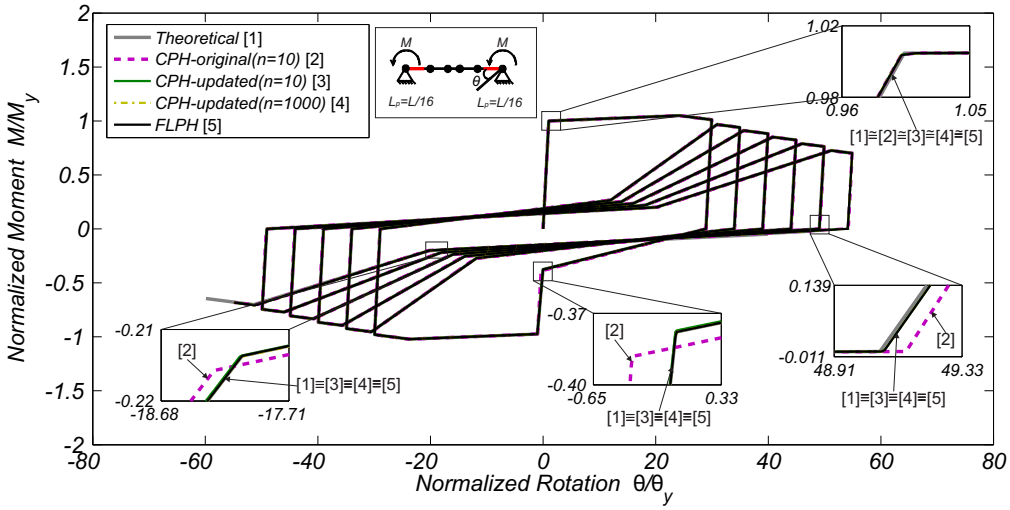

Figure 3.6: Pinching model - cyclic analysis considering anti-symmetric end moments

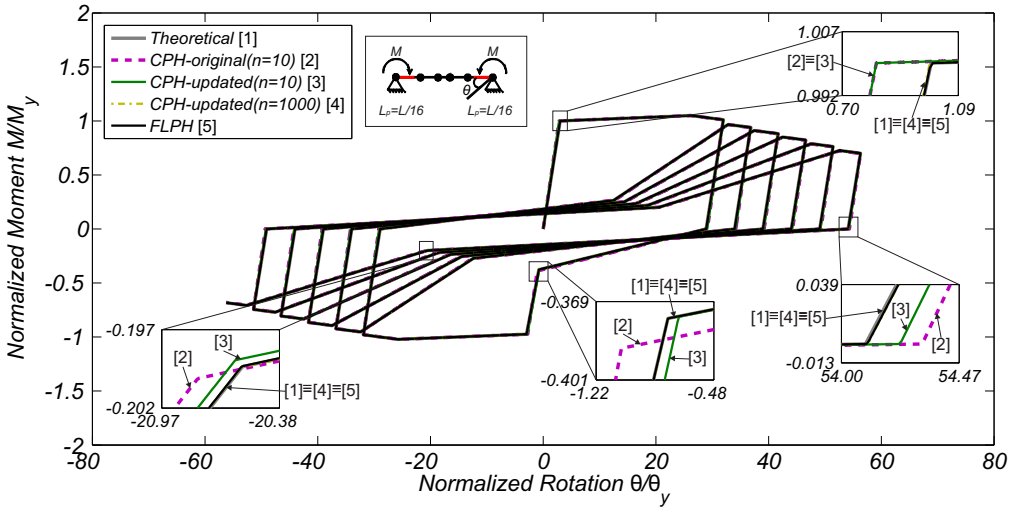

Figure 3.7: Pinching model - cyclic analysis considering symmetric end moments

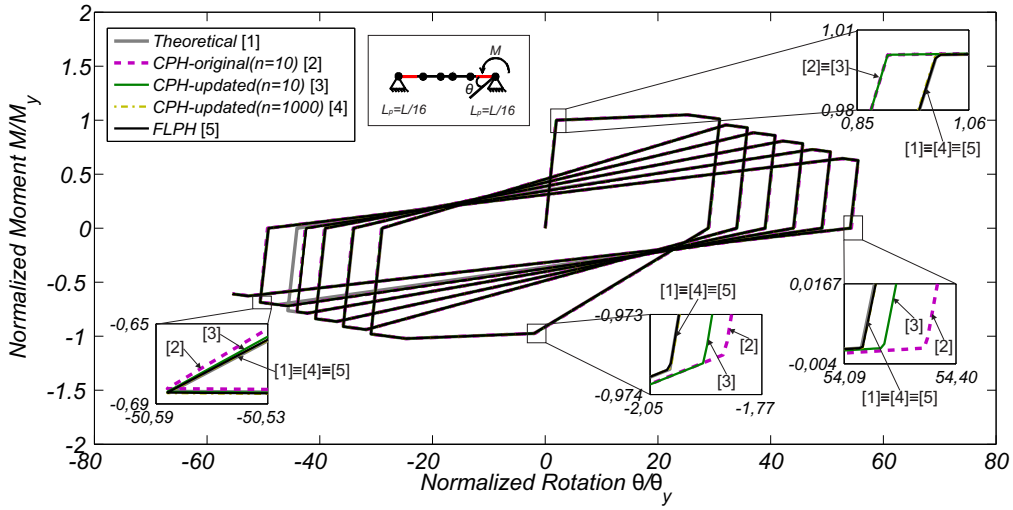

Figure 3.8: Peak-oriented model - cyclic analysis considering a single end moment

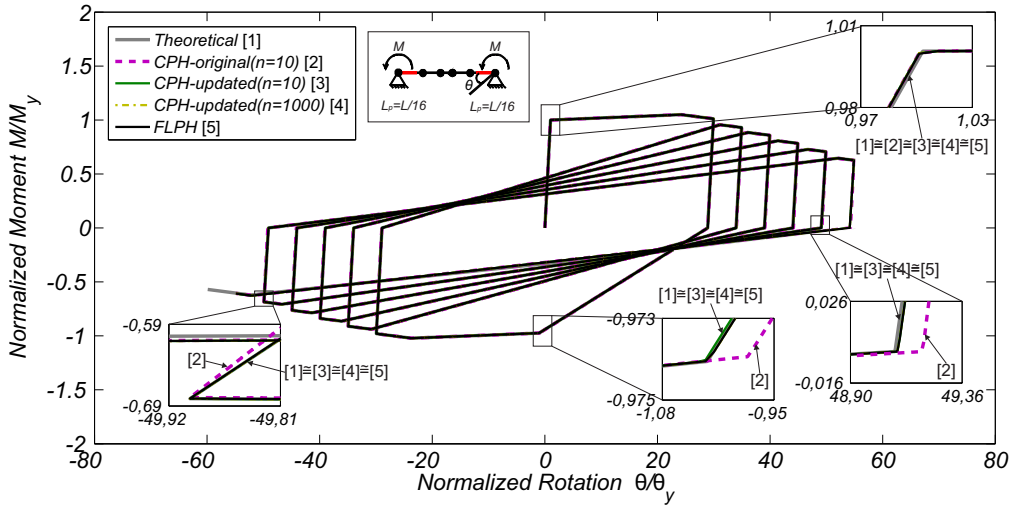

Figure 3.9: Peak-oriented model - cyclic analysis considering anti-symmetric end moments

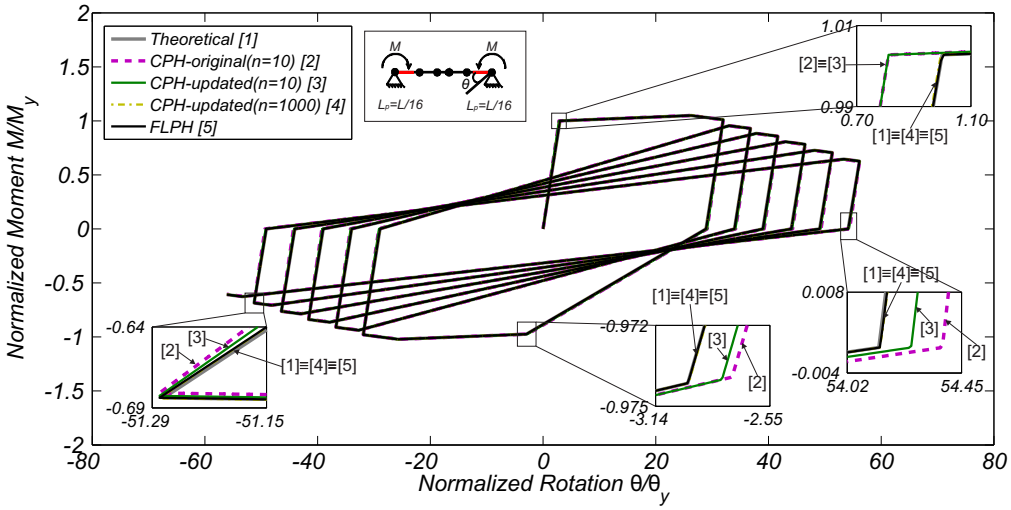

Figure 3.10: Peak-oriented model - cyclic analysis considering symmetric end moments

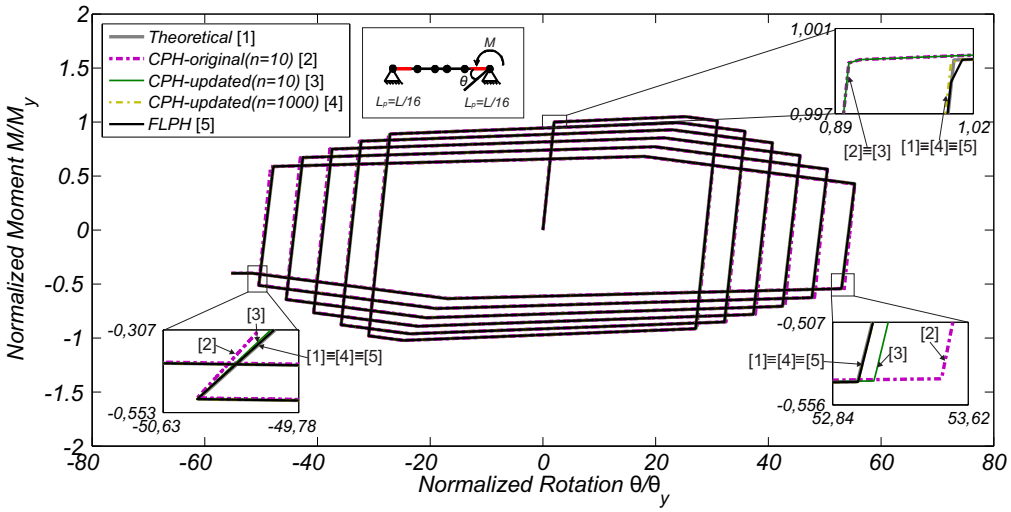

Figure 3.11: Bilin model - cyclic analysis considering a single end moment

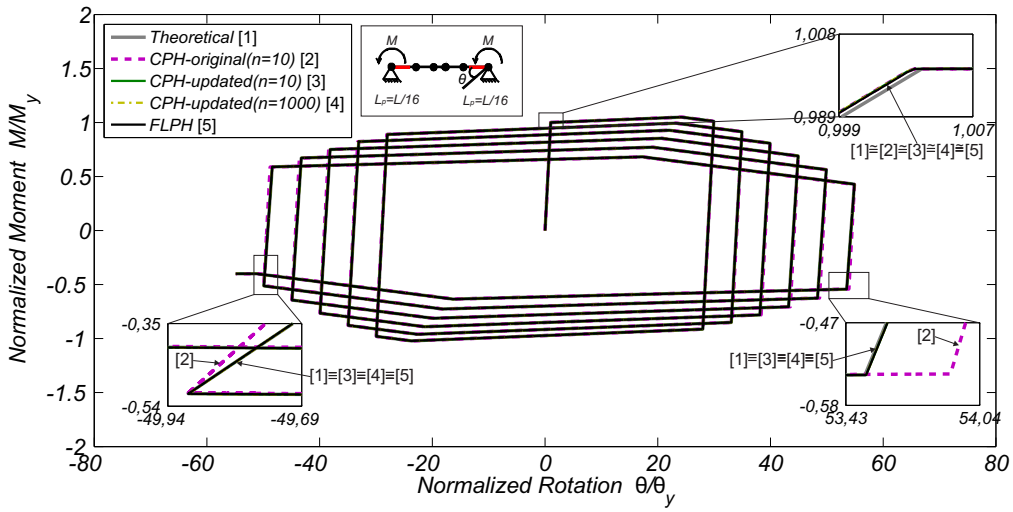

Figure 3.12: Bilin model - cyclic analysis considering anti-symmetric end moments

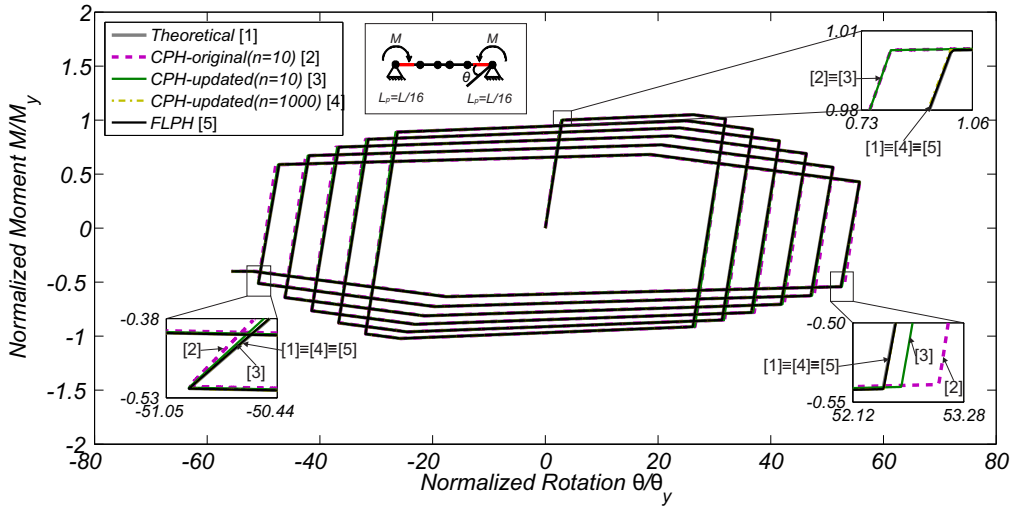

Figure 3.13: Bilin model - cyclic analysis considering symmetric end moments

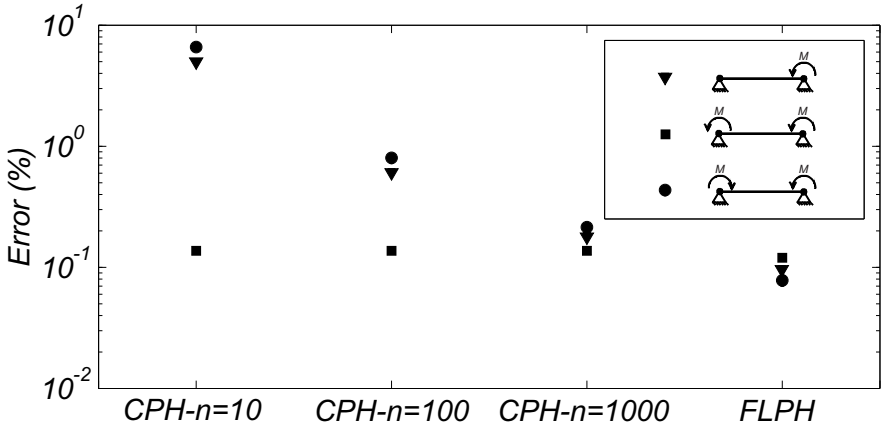

Figure 3.14: Comparison of error in the elastic stiffness for CPH-updated with different values of n_{Factor} and FLPH

assessment are shown in Figure 3.15. The models were analyzed considering the Krylov-Newton algorithm [126] under displacement control analyses. Pseudo-time steps between 1×10^{-7} and 1×10^{-3} are used in the analyses. The norm of the displacement increment convergence test is used with a threshold of 1×10^{-8}. Figure 3.15 shows that FLPH and the CPH-original with n_{Factor} equal to 10 converged for all time steps. However, n_{Factor} values between 100 and 500 required a pseudo-time step smaller than 1×10^{-5} for achieving convergence. For a n_{Factor} equal to 1000, a pseudo-time step of 1×10^{-7} was necessary to achieve convergence. Although this is not an exhaustive convergence stability analysis, the results indicate that the FLPH is significantly more stable. Similar stability is obtained for the CPH-original model only if n_{Factor} is taken equal to 10 which, as shown above, leads to significant overestimation of the elastic stiffness.

3.5.3 Example 3 - Frame Structure

The implemented models were also used to simulate the response of a 3-story steel moment resisting frame, represented in Figure 3.16, which was designed for Los Angeles by using pre-Northridge codes [138]. A detailed description of the building is presented in [77,139]. In this work, a two-dimensional centerline model of the external frame of the building is developed and used for structural analysis. The structural building model was developed considering columns modeled as distributed plasticity beam-column elements and a set of four different cases are considered for capturing the nonlinear behavior of the beams. For the first two cases, the CPH model is used, whereas the other two cases make use of the FLPH model. These alternatives are described in Table 3.2. For each case, the three Mod-IMK deterioration models implemented herein are used, resulting in a total of 12 different analyses. A n_{Factor} equal to 10 is used for all CPH models following suggestions by [121]. A cyclic lateral load pattern proportional to the first mode is applied to all cyclic pushover analyses.

Figures 3.17 to 3.19 show results associated with the global response of the building using the Pinching, Peak-Oriented, and Bilin models, respectively. Figures 3.20 to 3.22 show local results for the three models, in terms of the moment-rotation behavior of the left end of the beam B1 (see Figure 3.16).

Global results indicate that the use of a CPH model without employing the updated im-

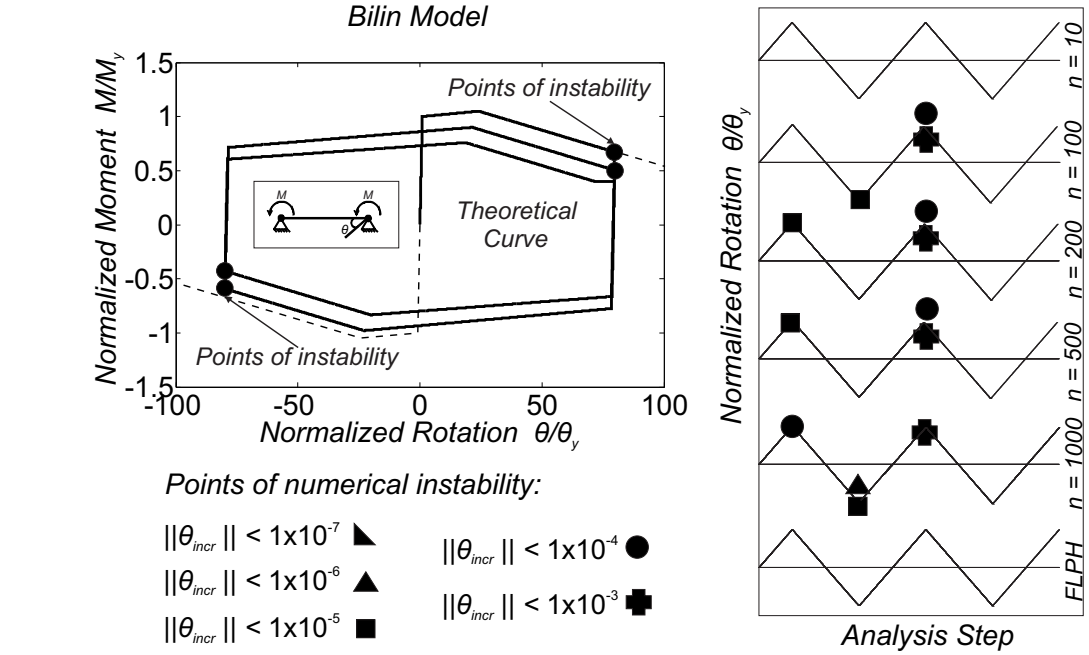

Figure 3.15: Convergence stability analysis using the Bilin model

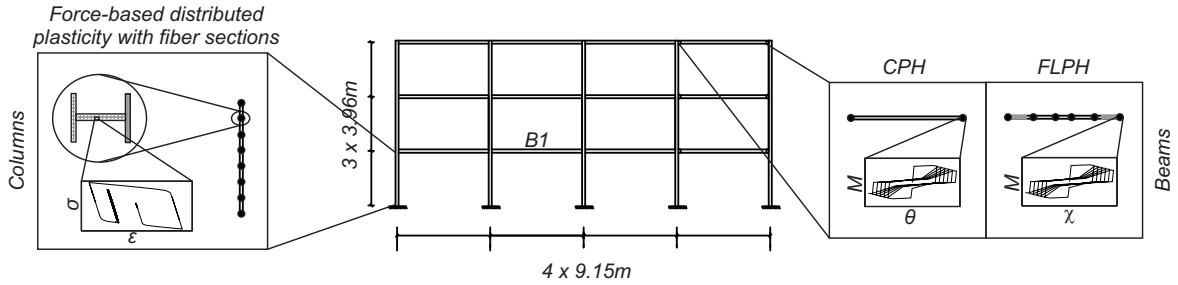

Figure 3.16: Three-story steel moment frame analyzed with the implemented models

Table 3.2: 3-Story frame numerical models description

Model	Columns	Beams		
	Element formulation and Material	Element formulation	Implementation	Plastic Hinge Length
CPH-original	Force-based fiber-section distributed plasticity	CPH	Original	-
CPH-updated			Proposed	
FLPH-$L_p = L/6$		FLPH		L/6
FLPH-$L_p = L/16$				L/16

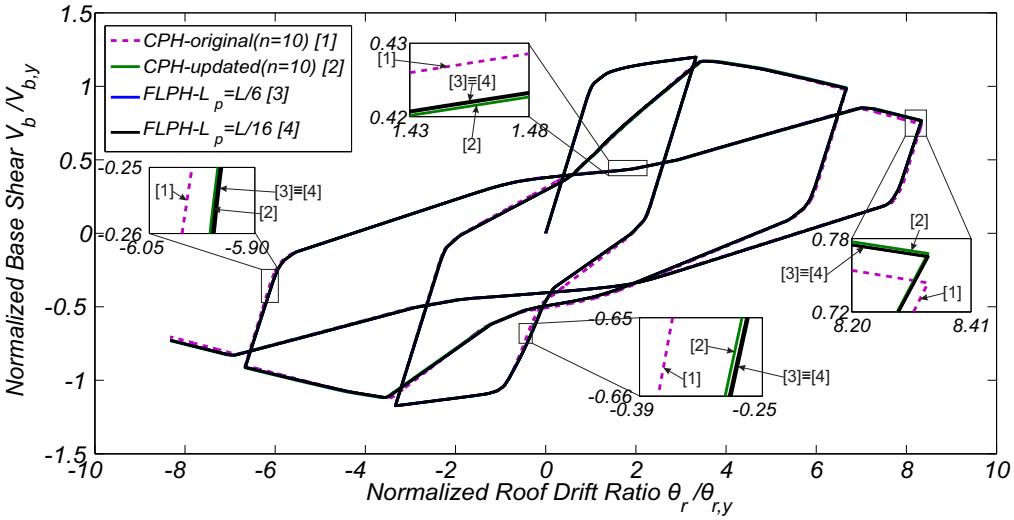

Figure 3.17: Cyclic pushover analysis of the 3-story frame with the ModIMK Pinching model

plementation of the ModIMK models that do not explicitly take into account the n_{Factor} (CPH-original) lead to noticeable differences in the unloading regions. Moreover, both updated CPH and calibrated FLPH models, that make use of the proposed implementation lead to very similar results and performance. The observed differences are expected when a low value, as $n_{Factor} = 10$, is used. This value is used to avoid numerical convergence problems as shown here and also in [121]. Finally, it should be highlighted that FLPH models with plastic hinges of $L/6$ and $L/16$ provide identical results. It is observable that models CPH-updated and FLPH (either with plastic hinge length equal to L/6 or L/16) lead to similar results. Figures 3.20 to 3.22 show that a similar performance is observed at a local level. A reduction of 10% in the computation time associated with FLPH models was recorded, when compared to that associated with the CPH models, even for a small problem. This value is expected to increase as the number of elements increase.

3.6 Conclusion

Within the member modeling approaches available in the literature, concentrated plastic hinge (CPH) models have been the reference model for earthquake engineering studies during the last decade. However, finite-length plastic hinge (FLPH) models have been recently shown to be advantageous over the CPH models on some points. A significant reduction in modeling effort, as well as in computational cost, a clear distinction between member and connection nonlinearities, and more realistic modeling of yielding progression and hinge rotations are the most important advantages of the FLPH models.

In this work, results obtained for cyclic analysis using implementation and calibration of the FLPH models are discussed and compared to those resulting from two implementations used for updating parameters of the unloading stiffness and other deterioration modes in the CPH models. All implementations were performed in the Open System for Earthquake Engineering Simulation (OpenSees) making use of the ModIMK material models, which have been widely used for simulating steel, RC, and timber frame structures.

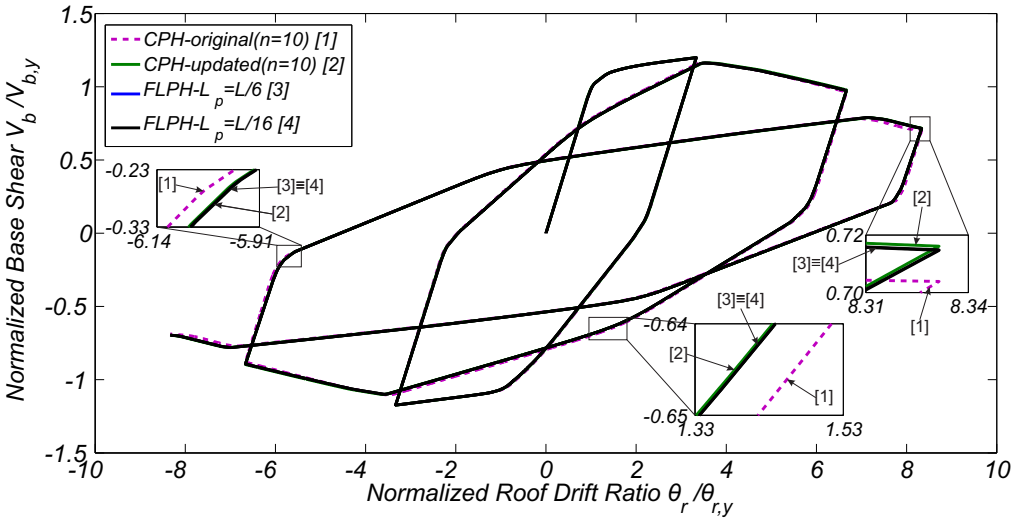

Figure 3.18: Cyclic pushover analysis of the 3-story frame with the ModIMK Peak-oriented model

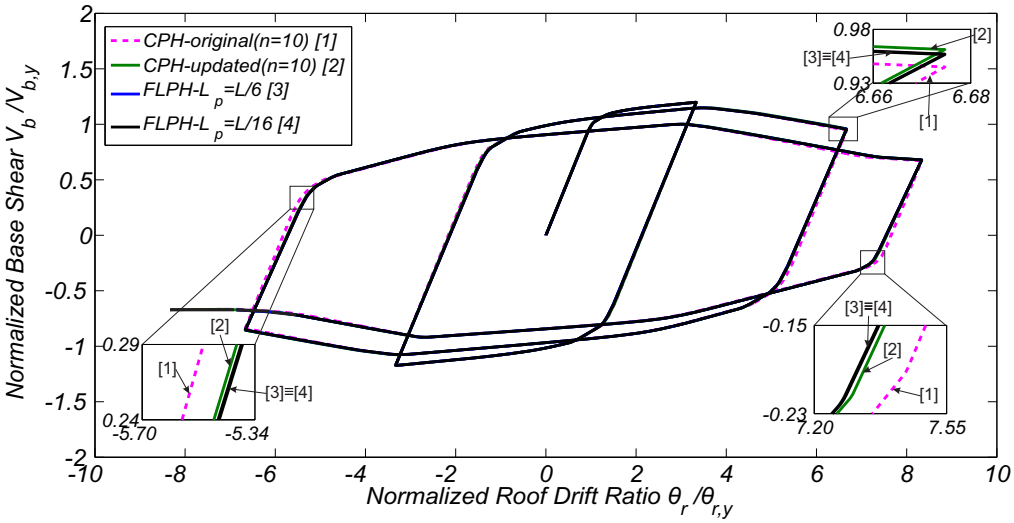

Figure 3.19: Cyclic pushover analysis of the 3-story frame with the ModIMK Bilin model

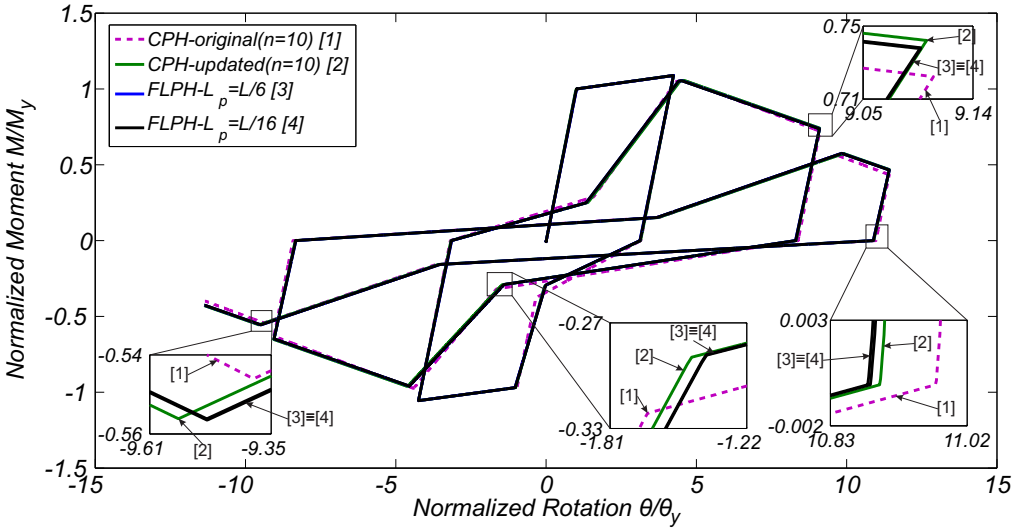

Figure 3.20: Beam response during the cyclic pushover analysis of the 3-story frame with the ModIMK Pinching model

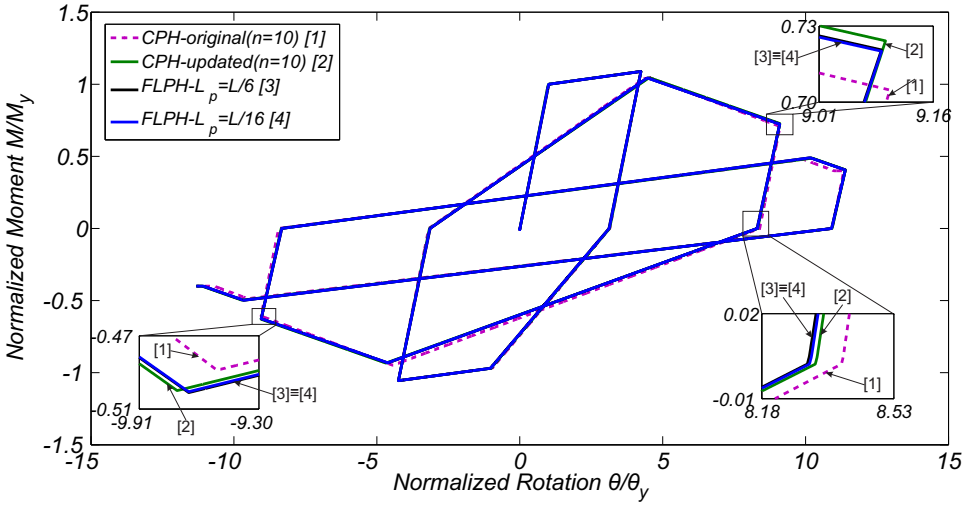

Figure 3.21: Beam response during the cyclic pushover analysis of the 3-story frame with the ModIMK Peak-oriented model

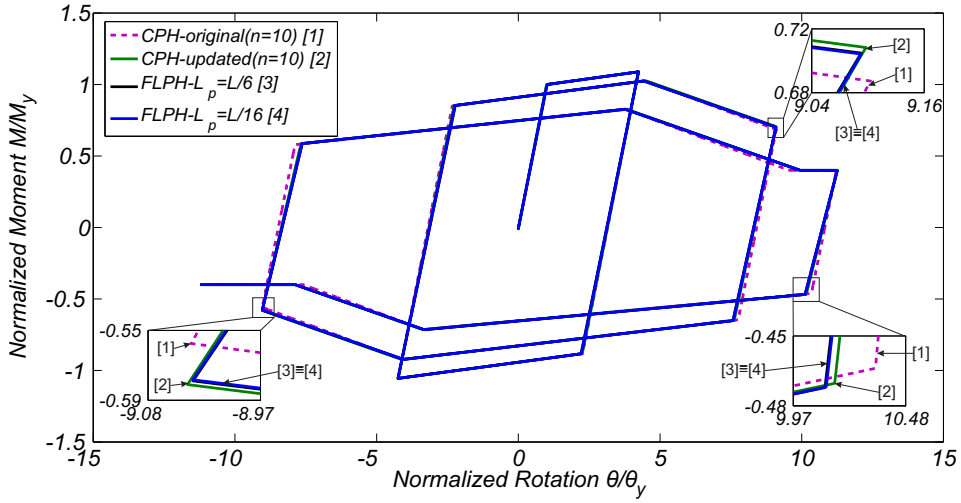

Figure 3.22: Beam response during the cyclic pushover analysis of the 3-story frame with the ModIMK Bilin model

In terms of the implementation, the main conclusions of this chapter are:

1. a new unified implementation was developed in the OpenSees framework, where the ModIMK material models can now be used in both CPH and FLPH models;

2. the implementation of the ModIMK in the CPH models proved to be significantly more complex than that done for FLPH models. This results from the use, in this case, of three separate components, two zero-length springs and an elastic beam-column interior element. In addition, the elastic stiffness of the zero-length springs needs to be amplified in order to obtain the correct member flexibility matrix, which requires further adjustments in the updating procedure of all parameters of the springs;

3. in FLPH models, the main difficulty lies, not on the implementation of the ModIMK material models, but in the need to calibrate the element to consider empirical moment-rotation relationships;

4. although a calibration procedure is required for the FLPH elements, this procedure can be used independently of the deterioration model law. For the CPH models, custom implementations are required if different deterioration model laws are to be used;

5. for FPLH models, once the formulation of the calibration is defined, the implementation procedure is significantly simpler and applicable to a wide range of deterioration model laws, thus not restricted to the ModIMK relationships;

6. the FLPH calibration proposed was validated for nonlinear cyclic analysis.

Based on the numerical results shown:

1. in general, CPH and FLPH models can provide reasonable results for nonlinear cyclic analysis;

2. for a beam element with anti-symmetric end moments, CPH models provide accurate results independently of the n_{Factor} that is used to amplify the elastic stiffness of the zero-length springs;

3. for a beam element with other moment gradients, non-negligible errors are obtained for the elastic stiffness if the n_{Factor} in CPH models is not large enough (e.g., approximately 5% error is obtained for symmetric bending moments for $n_{Factor} = 10$); these errors propagate throughout the analysis;

4. CPH models with large n_{Factor} values give rise to numerical instabilities;

5. calibrated FLPH models provided the most accurate results.

In summary, even though the use of FLPH models in large numerical studies requires more investigation, the results presented in this work indicate that these models are suitable for being used in large numerical simulations, being more stable, accurate, and versatile.

3.7 Dissemination

This part of the research program resulted in the following outputs.

1. Scientific paper published in the Journal of Earthquake Engineering (in press)

   Scope: Presentation of the unified implementation for use of ModIMK relationships in CPH and FLPH models. Results from included examples validate the proposed implementation, which were implemented in OpenSees. Additionally, results highlight that FPLH models avoid errors and convergence pitfalls of CPH models.

   Complete reference: Ribeiro, F., Neves, L., and Barbosa, A. (2015). "Implementation and calibration of finite-length plastic hinge elements for use in seismic structural collapse analysis." Journal of Earthquake Engineering (in press).

2. Oral presentations made at the OpenSees Days workshops in Portugal (2014) and Italy (2015)

   Scope: This part of the research program resulted in the release of the proposed unified implementation of the ModIMK models for FLPH and CPH elements in the OpenSees framework as new models. These new models are entitled Bilin02, ModIMKPeakOriented02, and ModIMKPinching02. The source code of the OpenSees framework can be download from "svn://peera.berkeley.edu/usr/local/svn/OpenSees/trunk". The wiki pages associated with these new models will be released soon and will be available at "http://opensees.berkeley.edu/wiki/ index.php/Command_Manual". In this context, the candidate presented these new implementation for the ModIMK models at the OpenSees Days Portugal 2014 and OpenSees Days Italy 2015. The presentation made at the last workshop was entitled "General Implementation of Modified Ibarra-Medina-Krawinkler Models for Concentrated Plasticity Models and Finite-Length Plasticity Models".

Chapter 4

Influence of Connections Brittle Fractures on Structural Fragility

4.1 Scope

The present chapter builds on Chapters 2 and 3 that proposed a formulation and implementation of finite element models for simulating member behavior under seismic loading. Not less important in steel construction is the simulation of the connections between structural elements. Beam-column connections in steel moment resisting frame are particularly sensitive and their behavior must be accounted for when assessing structural response. Pre-Northridge steel moment resisting frame buildings, which represent a large fraction of the existing steel buildings in the US, have been shown to be susceptible to brittle connection failures. Even though several experimental and numerical studies have been developed, the modeling approach proposed in this chapter adds to the current state of the art on two main points: (i) a new modeling approach for the beam-column and connections is proposed, which allows for aggregation at the member level of the connection and the beams; and (ii) the influence of uncertainty of the connection drift capacity and earthquake ground motion record-to-record (RTR) variability are separately considered on the estimation of building damage and loss assessment.

A probabilistic assessment of the performance of the 3- and the 9-story Los Angeles SAC buildings is performed. The drift demands for each structure modeled with brittle beam-column connections are compared with the results for the structure modeled with perfectly rigid connections. In this case, nonlinearities are concentrated on members. Comparison includes median drift results obtained for the various intensity levels, fragility analysis, and the repair cost ratio (RCR) with brittle and rigid connection response. New fragility curves that account for the brittle connections and the uncertainty in connection capacity are proposed. Results obtained in this chapter show that the consideration of brittle beam-column connection leads to significantly larger drift demands and, consequently, to higher repair costs.

4.2 Introduction

Prior to the 1994 Northridge earthquake, welded steel construction was widely accepted in seismic regions and was especially common in the U.S. west coast. Most steel moment

resisting frames (SMRF) were designed and constructed using welded-flange-bolted-web (WFBW) connections [140]. Figure 4.1 shows an example of this type of connection, which uses complete joint penetration groove welds connecting the beam flanges to the column flanges and a shear tab connecting the beam web to the column flange. The shear tab was typically shop welded to the column with fillet or groove welds and then bolted to the beam web.

Following the 1994 Northridge and 1995 Kobe earthquakes, brittle fractures in or around the groove weld between the beam bottom flange and the column flange were observed, resulting in extreme losses [141]. Based on experimental work developed in recent years to characterize the behavior of WFBW pre-Northridge connections, the impact of connection uncertainty on damage and loss assessments has been assessed by Xu and Ellingwood [140] and Luco and Cornell [142], among others.

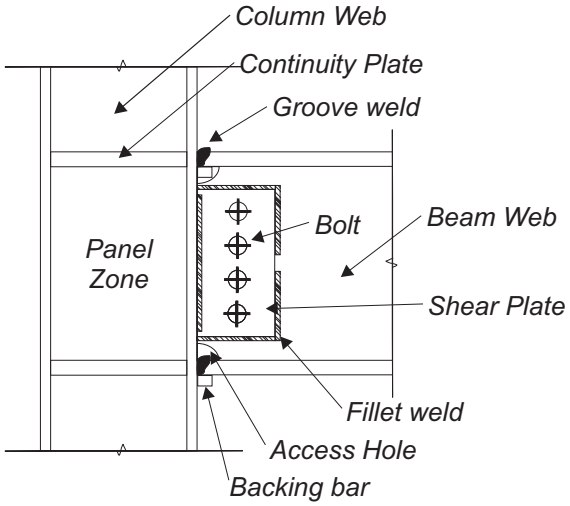

Figure 4.1: Typical pre-Northridge WFBW connection detail [143]

In this work, a new modeling approach that uses finite-length plastic hinge (FLPH) models to simulate member behavior and concentrated plastic hinge (CPH) springs as fracture elements is used. This modeling approach allows for separation between member and connection response. This is important as member empirical laws and connection fracture models can now be applied together and used in probabilistic studies. Moreover, this model allows for more realistic modeling of the fracture, such as the relationship between the rotation of the connection itself and the rotation of the member plastic hinge. In fact, when a connection fails, as the connection rotation increases, the member rotation remains unchanged and equal to the fracture rotation. This phenomenon is accurately simulated with the proposed model. Connection model parameters are based on experimental data. In addition, the sensitivity of the building response to connection rotation capacity is explored and the associated consequences on structural fragility are computed, thus allowing for estimating the impact of connection uncertainty on the performance. This topic is still not sufficiently studied as most of the studies developed to date have either neglected the uncertainty in connection rotation capacity or considered it together with the RTR variability (e.g., [142,144]). The isolated assessment of uncertainty in connection rotation capacity is important for performance-based engineering methods. The proposed modeling approach is implemented in the Open System for Earthquake Engineering Simulation (OpenSees) [132] framework.

In order to validate the proposed connection model, numerical analysis are executed to compare results obtained with the proposed modeling approach and force-displacement response obtained in four experimental tests conducted as part of the SAC Steel Project. After validating the model, a probabilistic assessment of the performance of two SMRF buildings subjected to various earthquake ground motions is performed. The 3- and the 9-story Los Angeles SAC buildings, which were designed according to pre-Northridge codes [138] are used in this work. Following Xu and Ellingwood [140], the rotation capacity associated with each connection of the buildings is defined through a log-normal distribution with parameters defined based on the experimental tests performed in SAC Project using WFBW connections. A correlation factor of 0.7 is considered between connections within each building [145]. Latin Hypercube Sampling [146,147] is used to generate two-hundred building samples. The building's performance is analyzed at ten different intensity levels. These are obtained by scaling ten ground motion records from the SAC Steel Project 10/50 (10% in 50 years probability of exceedance) ground motion set. The drift demands for each structure modeled with brittle beam-column connections are compared with the results for the structure modeled with perfectly rigid connections. In this case, nonlinearities are concentrated on members, thus leading to a ductile member response. Comparison includes median drift results obtained for the various intensity levels, fragility analysis, and the repair cost ratio (RCR) with brittle and rigid connection response.

Results obtained in this chapter show that the consideration of brittle beam-column connection lead to significantly larger drift demands. This increase in drift demands leads to an increase in the computed probability of exceedance of predefined damage states and to higher repair costs. The statistical measures derived in this work can be used on the development of future probabilistic studies.

4.3 Literature Review

During the 1994 Northridge earthquake extensive damage and local failures at the beam-to-column welded joints in SMRF buildings were observed. However, there have been very limited visible signs of inelastic action in the joints, such as local flange or web buckling. If undetected, local failures at the beam-to-column joints are critical, increasing the vulnerability of the structure during post-earthquakes events.

Experimental research performed after the Northridge earthquake confirmed that WFBW are prone to brittle fracture with little ductility, namely on the bottom beam-flange. In fact, Bonowitz and Youssef [141] state that, based on a post-Northridge damage survey, about 70 to 80% of the reported damage occurred in the beam bottom flange. Damage to the shear connections that could affect gravity load capacity, was quite rare. Additionally, column web fracture occurred in less than 10% of location already damaged at the beam-column weld [141,148]. Thus, Maison and Bonowitz [144] state that for these types of connections it suffices to model the frames with fracture elements at the beams ends in the beam-column flexural connection.

Based on the research developed in the SAC project numerous numerical models were proposed to simulate brittle connection fractures. The model proposed by Luco and Cornell [142] has been widely used in the simulation of pre-Northridge connections and is the modeling approach suggested in FEMA355C [77]. In this model, the fracture element is modeled as a rotational spring that is placed at each end of an elastic beam in order to emulate plastic

hinging (concentrated plasticity) of the beam and possible fracture of the connections. The moment-rotation hysteretic behavior of the fracture reproduces that observed in the experimental testing program of moment-resisting beam-column connections that experienced top and/or bottom beam flange fracture. The multi-linear moment-rotation hysteretic behavior proposed by Luco and Cornell [142] was calibrated based on experimental results obtained in the SAC project.

The typical moment-rotation hysteresis for a fracture element is shown in Figure 4.2(a). This model consists, in a first phase, in a common elasto-plastic behavior, where a ductile yielding, characterized by a hardening branch starting at the plastic moment M_p, is observed. Then, in a second phase, which starts when the plastic rotation θ_f is reached a sudden drop in strength is observed and the bending moment drops to its residual value M_r. The main parameter related to the fracture of the connections is the plastic rotation θ_f. In addition, this model also considers the possibility of fracture before reaching the nominal plastic moment M_p, designated as "pre-yield" (also known as "early" or "premature") fracture of the bottom beam flange. This phenomenon is represented in Figure 4.2(b). In this case after "early" fracture the moment drops immediately to the residual value M_r.

This model was implemented first in the DRAIN-2DX [149], and further development and improvement were proposed by Uang *et al.* [150]. The model was also implemented in the IDASS software [151]. Preliminary studies developed by Hall [152] and Song [153] made use of these models to assess the response of steel buildings with damaged welded connections. After that, several numerical studies were developed in order to study the SMRF buildings designed for Los Angeles, California, specifically for the SAC project. In this context, Luco and Cornell [142] and Lee and Foutch [154] used numerical models that included the effects of brittle connections, panel zone deformation, and interior gravity frames to compute the expected damage at two hazard levels (probability of exceedance of 10% in 50 years and 2% in 50 years).

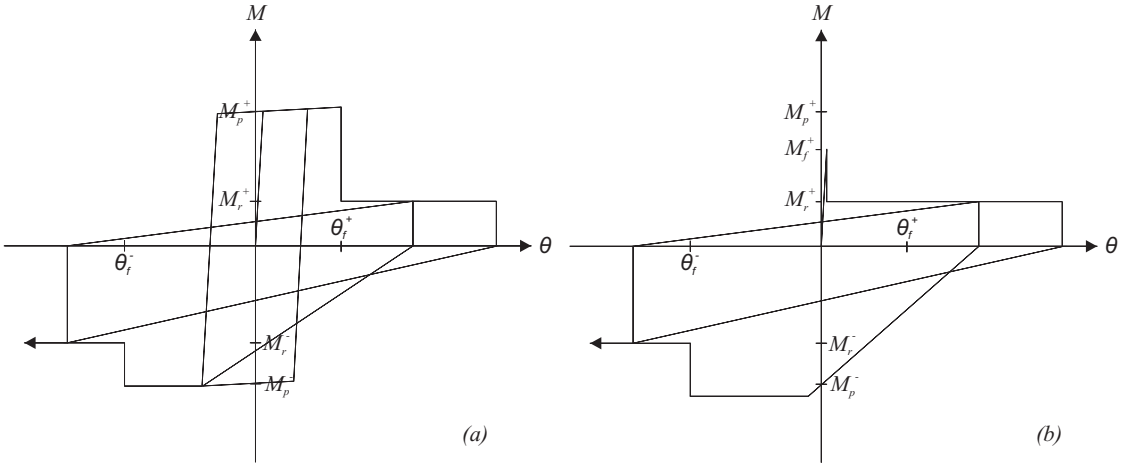

Figure 4.2: Fracture model developed by Luco and Cornell (2000)

Maison and Bonowitz [144] studied the Los Angeles 9-story building considering the fracture rotations associated with each connection as random variables. Wang and Wen [155] also used the model proposed by Luco and Cornell [142] and proposed a method for evaluating structural reliability and redundancy of steel buildings under earthquakes in terms of maximum column drift ratio. The seismic hazard is expressed in terms of annual exceedance probability of biaxial spectral displacement. A power law relationship between

MCDR and BSD is then established from regression analyses of building response under SAC ground motions for a wide range of intensities. A redundancy factor is developed for calculating the required design force for structures of different degrees of redundancy such that a uniform reliability requirement is satisfied.

Finally, Xu and Ellingwood [140] investigated the robustness of pre-Northridge steel moment frames under column removal, by using a model developed in OpenSees. In this model, columns and beams are both modeled using nonlinear beam-column elements with fiber sections, with a bilinear elastic-plastic material model with a 3% strain hardening ratio. The strength demands obtained with this model were used to determine the probability of fracture of connection in two three-story buildings. The probability of failure is estimated based on a model developed and calibrated with experimental results from the SAC project. Xu and Ellingwood [140] noted that panel zone deformations could be neglected in their collapse simulations due to the small imbalance of beam moments due to gravity loads after loss of columns. In what concerns the explicit modeling of panel zones, Li and El-Tawil [156] also stated that these deformations did not contribute substantially to the behavior of the macro-model and, consequently, may be ignored in the simulations. A list of works that have studied pre-Northridge type buildings are summarized in Table 4.1 as well as the obtained peak interstory drift ratio (IDR) and percentage of fractured connections (PFC), when available. These studies have analyzed the influence of connection fracture on the seismic performance of pre-Northridge buildings. Some of them consider probabilistic distributions of the rotation fracture. However, fracture rotation is assumed to be equal throughout the building. In this work, connection fracture uncertainty is considered in the development of numerical models able to reproduce the behavior of pre-Northridge SMRF structures. A new model that is able to simulate both member nonlinearity and connection fracture is presented.

Table 4.1: Results obtained by other works on the response assessment of WFBW Pre-Northridge buildings

Reference	Stories	Spectral Acc. (g)	Peak IDR (%)	PFC (%)
Luco and Cornell [142]	3	SAC 2/50	7.1	
Maison and Bonowitz [144]	9	SAC 10/50	1.5	35
Luco and Cornell [142]	9	SAC 10/50	2.4	20
Maison and Bonowitz [144]	9	SAC 2/50	4	65
Luco and Cornell [142]	9	SAC 2/50	5.1	
Islam [157]	11	0.09	1.1	28
SAC [158]	11	0.12	0.3	16
Uang *et al.* [150]	13	0.2	1.7	14
Luco and Cornell [142]	20	SAC 2/50	6.0	

4.4 Model Development

4.4.1 Beam and Connection FE Model

The developed model is based on: (i) the Finite-Length Plastic Hinge (FLPH) formulation [102], discussed in Chapter 2, for simulating member response including nonlinear behavior,

as well as strength and stiffness deterioration; and (ii) zero-length springs to model the connections. The zero-length springs are placed at both ends of the FLPH element and are assigned a rigid-plastic behavior, where the plastic strength is abruptly reduced to simulate connection fracture. This model allows for holistically considering empirical models in simulating member response at the same time that considers the possibility of connection fracture.

The Modified Ibarra-Medina-Krawinkler (ModIMK [127]) moment-rotation relations are used for their versatility. In Chapter 3 a consistent implementation of the ModIMK model was developed in order to be used in both FLPH and in concentrated plasticity (zero-length springs) models. These models were implemented by the authors in the OpenSees framework. Details of these models and the corresponding implementation are given in Chapter 3.

The Bilin model is used to model plastic hinges of the member. The moment-curvature relationship is obtained by scaling (by the plastic hinge length) the moment-rotation relationship provided by the empirical laws proposed by Lignos and Krawinkler [4] and described in Chapter 3. The parameters of the model are obtained from empirical laws proposed by Lignos and Krawinkler [4]. The Pinching model is used to model the moment-rotation behavior of connections. This model includes strength and stiffness deterioration mechanisms. Connections may fracture at different rotation amplitudes in positive and negative bending. Different positive fracture rotations, θ_f^+, and negative fracture rotations, θ_f^-, are typically defined in positive and negative bending corresponding to bottom and top beam-flange fracture, respectively, which is mainly due to the influence of a slab, a backup bar, or an access hole [143]. The moments associated with the rotation values at which fracture takes place depend on the model stiffness used to simulate member behavior. These rotation values are calibrated based on experimental results obtained in the SAC project, which include the beam rotation as well as the panel zone rotation at first fracture. After fracture the behavior of the connection model includes a softening branch over a rotation of 0.002 rad. The softening branch models the flange or weld tear´ing completely through, and thus the moment capacity decreases. Even after fracture in the top or bottom beam-flange, the strength capacity in the other flange of the beam remains intact. Thus the behavior of the connection has a pinched reloading branch, which is defined by three parameters ($F_{r,p}$, $F_{r,n}$, and A_{pinch}) defining the point at which reloading starts, and a residual strength capacity defined as a fraction of the fracture moment. The Λ parameter that controls the cyclic deterioration is set a large number because, apart from the pinched behavior, no cyclic deterioration is considered in the connections. Figure 4.3 shows an illustration of the developed model.

The modeling approach described above is exemplified through an example of a simply supported beam with anti-symmetric end moments. In this example, connection fracture rotation is set a value larger than the member yielding rotation. A cyclic pushover analysis is performed by controlling the rotation at the right-end node. Seven complete cycles of increasing rotation (see Figure 4.4(d)) are executed and three responses are tracked: (a) global response (Figure 4.4(a)); (b) member response (Figure 4.4(b)); and (c) connection response (Figure 4.4(c)). In this example, results in the figures indicate that during the first two cycles the connection has not fractured, even though the beam element goes into a nonlinear range. During the third cycle, the connection fractures, which is associated with an abrupt decrease in strength in the positive moment region. Subsequently, after load reversal (fourth cycle) the fracture closes, which occurs during the segment with lower slope (below point 3). After fracture closure, the initial strength remains intact for negative bending. As

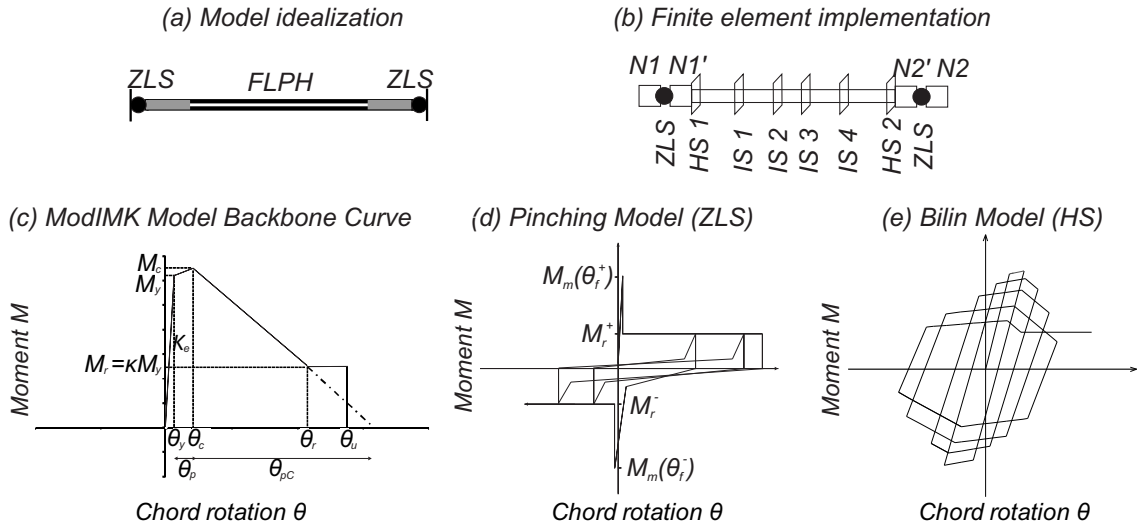

Figure 4.3: Conceptual description of the proposed modeling approach

a consequence, the connection remains rigid. However, after significant member yielding, connection fails for negative bending moments and a decrease in strength for negative moment is also recorded. During the following cycles (fifth, sixth, and seventh) the moment varies between the residual moment of the connection. When this value is reached, the connection rotation increases, while the member rotation remains the same. The segments with lowest slopes correspond to the closing of the fractures. The described model behavior presents improvements to the behavior of the model proposed by Luco and Cornell (see Figure 4.2(a)), namely in what concerns differentiation between fracture closing and reloading, which is not possible in the former model. Moreover, this model fits well data driven from experimental tests of welded connections, as shown in the next section.

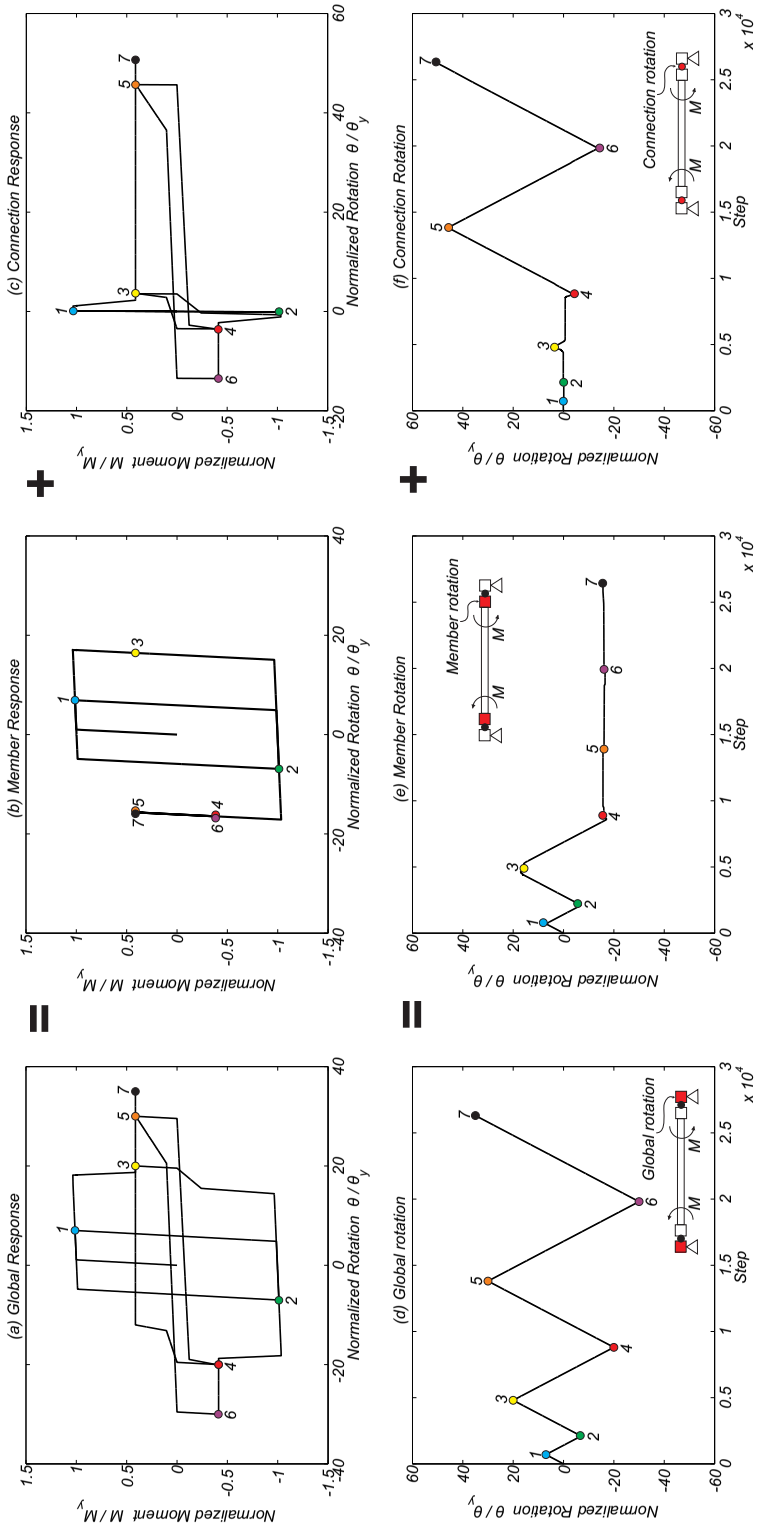

Figure 4.4: Illustrative example of the modeling approach behavior

4.4.2 Beam and Connection Model Validation

Four beam-column connection tests are used in the validation of the proposed modeling approach. These correspond to two tests carried out during Phase I and two tests performed during Phase II of the SAC project. The two Phase I tests are essentially used to validate the modeling approach and fracture rotation parameters. However, these tests were stopped after the first weld fracture, which hinders its usefulness to perform post-fracture validation. Tests carried out during Phase II were continued after weld fracture, and are thus used to validate post-fracture behavior. However, very few tests are available. Additional tests, performed in other research projects were used to assess the post-fracture accuracy of the model. Nevertheless, further work is needed in order to confirm the preliminar validation carried out in this work.

Figure 4.5 shows the experimental results obtained in the four tests plotted against the numerical results obtained with the model implemented in OpenSees. The main goal of these analyses is to verify that the proposed model is functional and to assess the accuracy of the results for these reference tests. Figures 4.5(a), 4.5(b), and 4.5(d) correspond to tests carried out by Bertero et al. and Popov et al. [5] as part of the SAC Project Phase I, whereas Figure 4.5(c) corresponds to a test carried out in SAC Project Phase II - Task 7 [159]. The tests setup are represented in the figures. The model corresponds to two perpendicular frame elements, connected at the base of the vertical element. The horizontal member is simply supported at both ends. Member sizes and geometrical properties of the test set up are represented at the figures. The beam and column nonlinear properties, namely plastic rotation capacity and deterioration parameters are obtained through the empirical expressions proposed by Lignos and Krawinkler [4]. A cyclic pushover is performed by applying displacements at the top of the vertical element. Material properties are considered following characterization provided in the test reports. The plastic hinge lengths are assumed to be equal to $L_p = L/16$. The connection fracture rotation is obtained after calibration of the proposed modeling approach, which serve as sensitivity analysis and validation of the considered fracture rotations. In these examples, the Krylov-Newton algorithm [126] is used to solve the nonlinear system of equations. Table 4.2 presents the main observations of these analyses.

In conclusion, the numerical model results fit well the experimental results. However, it depends on the definition of the fracture rotation for the accurate assessment of the global response. Even though the proposed model is not able to capture low-cycle fatigue induced fractures, the model shows a great ability to reproduce post-fracture behavior. It is worth noting that the reloading branches are very close, as are the residual segments. The residual strength capacity is estimated to be 25% of the full member capacity. The pinching parameters were considered to be $F_{r,p} = F_{r,n} = 0.3$ and $A_{pinch} = 0.8$.

4.4.3 Fracture Model Probabilistic Definition

In this Section, the rotation at which fracture occurs, θ_f, is defined as a random variable. Based on the limited tests available, θ_f is defined to follow a log-normal distribution. Top and bottom beam-flange fracture rotations are considered to be different.

The probabilistic model used to model the fracture rotation at the bottom beam-flange weld is based on tests performed in FEMA/SAC Steel Project Phase I, on a total of 12 exterior pre-Northridge steel moment connections designed to simulate the design practice

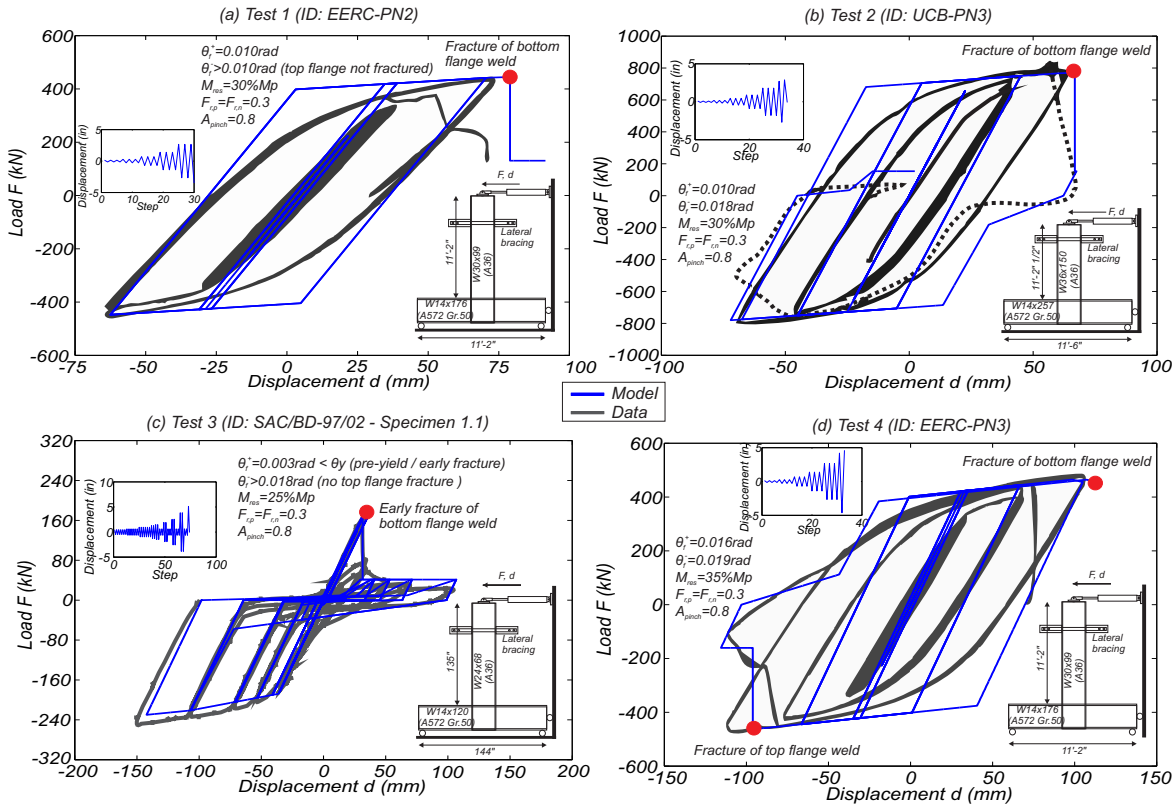

Figure 4.5: Numerical analyses performed to validate the modeling approach using four SAC Project tests

prevalent prior to the Northridge earthquake.

Fracture is assumed to take place at the bottom beam-flange when the plastic rotation reaches $\theta_f^+ = 0.015$ rad (positive bending). Note that the average (total) plastic rotation capacity of all the bottom beam-flange connections, including those which early fracture, is only 0.011 rad. This average value of plastic rotation capacity compares well to the average total (beam plus panel zone) plastic rotations at first fracture observed in the SAC Phase I laboratory tests [160]. The 12 tests of pre-Northridge type connections with 30- and 36-in.-deep beams (without slabs) yielded (total) plastic rotation capacities ranging from 0.0 to 0.021 rad, with an average of 0.010 rad. Also based on these tests, the standard deviation of the probability distribution is assumed to be 0.007rad.

Fracture at the top beam-flange is characterized through laboratory tests of full-scale beam-column connections that were continued beyond first (bottom) beam-flange fracture [161], that prompted the consideration of $\theta_f^- = 0.030$rad as a sensitivity case. Due to the lack of data on top beam-flange fracture, a deterministic factor of 2 is considered to define the ratio between fracture rotation for negative and positive bending moments ($\theta_f^- = 2 \times \theta_f^+$). This consideration is supported by Maison and Bonowitz [144].

Once fracture occurs, the bending moment (positive or negative) capacity is reduced to 30% of M_y, whereas the connection retains its full moment capacity in opposite bending direction (based on Anderson *et al.* [162]). This value is considered to be deterministic in this study. A sensitivity study performed by Luco and Cornell [142] showed that variation of the residual strength from 30% to 10% lead to an increase in the drift demands of less than 20%. FEMA 273 suggests 20% and SAC studies used 30%, which proved to fit well

Table 4.2: Observations of the numerical analyses performed to validate the modeling approach using four SAC Project tests

Model	Fracture		Post-fracture	Experimental
	Type	Rotation		
1 (Figure 4.5(a))	Fracture of the connection for positive moments (bottom flange)	$\theta_f^+ = 0.010$ rad	-	Low-cycle fatigue of the beam bottom flange weld at a rotation of 0.010 rad
2 (Figure 4.5(b))	Fracture of the connection for positive moments (bottom flange)	$\theta_f^+ = 0.010$ rad $\theta_f^- = 0.018$ rad	Post-fracture strength decay in positive and negative loading directions	Low-cycle fatigue of the beam bottom flange weld at a rotation of 0.010 rad and post-fracture strength decrease - the numerical results fit well the experimental ones
3 (Figure 4.5(c))	Fracture of the connection for positive moments (bottom flange)	$\theta_f^+ = 0.003$ rad $\theta_f^- > 0.018$ rad	No fracture for negative moments	Pre-yield fracture at the bottom beam-flange weld, no fracture was recorded at the top flange - a good accuracy in simulating post-fracture behavior is found
4 (Figure 4.5(d))	Fracture of the connection for negative moments (top flange)	$\theta_f^+ = 0.019$ rad $\theta_f^- > 0.016$ rad	No fracture for positive moments	Fracture of the top flange weld followed by fracture of the bottom flange weld - both fractures occurred, in fact, due to fatigue phenomena

the experimental tests.

The possibility of pre-yield fracture is neglected in this model for two reasons: (i) there is a lack of available data on this phenomenon and, consequently, modeling it would not be feasible; and (ii) results obtained by Luco and Cornell [142] showed that consideration of pre-yield fractures have almost no effect on story drift demands.

The inter-component correlation, namely the correlation between fracture rotations among the different beams of a building plays an important role in the probabilistic assessment of building performance. The correlation must take into account that the workmanship and material quality among different connections is expected to be similar. Data from actual structures, which are scarce, is required to assess the actual impact of inter-component correlation [163]. Data on this regard have been provided by Idota *et al.* [145] who tested coupons from each production lot of steel members and then tracked them to their actual positions in a six-story six-bay steel frame. They suggested a correlation coefficient of 0.65

for the yield strength of beams or columns belonging to the same production lot. A correlation coefficient of 0.70 is considered in this work among the distribution probabilities of the different connections based on the values used by Kazantzi *et al.* [163] and Idota *et al.* [145], as to take into account workmanship quality.

Three pinching parameters also need to be defined in the post-fracture connection behavior, which control the point at which reloading starts. Two of them correspond to the ratio of moment at which reloading starts in positive and negative direction, respectively. These are taken equal to 0.3. The remaining parameter, which corresponds to the ratio of rotation at which reloading starts is considered to be equal to 0.8. The sensitivity of the structural response to variation in these parameters is studied in Section 4.8.

4.5 Analysis Methodology

The building's performance is analyzed at ten different intensity levels. These are obtained by scaling ground motion records, which are part of the SAC Steel Project 10/50 (10% in 50 years probability of exceedance) ground motion set, with factors ranging from 0.3 to 1.8. For reference, the records scaled by 1.0 and 1.5 correspond to the DBE and MCE intensity levels, respectively.

The drift demands for each structure modeled with brittle beam-column connections (brittle connection model) are compared with the results for the structure modeled with perfectly rigid connections (rigid connection model). It is important to highlight that the consideration of rigid connections leads to a concentration of nonlinearities in the members only and, consequently, to a ductile member behavior. For the rigid connection model, three additional intensity levels (with scale factors 2.3, 2.6, and 3.0) are analyzed in order to allow for more accurate computation of the fragility curves, as the rigid connection model needs larger intensity ground motions to induce drifts similar to those attained by the brittle connection model.

In order to assess the influence of connection fracture uncertainty in building performance assessment, a sufficiently large number of analyses is required. Latin Hypercube Sampling [146,147] is used to generate two-hundred building samples. Each building differs from the other in what concerns fracture rotations, which are generated through the defined log-normal probabilistic distribution. Following the approach by Dolsek [164], the number of LHS samples was decided so that the correlation between random variables is equal to the objective correlation, i.e. 0.70. Recall that the median connection fracture rotation for positive bending moments is $\mu_{\theta_f^+} = 0.015$rad, and for negative bending moments is $\mu_{\theta_f^-} = 2 \times \mu_{\theta_f^+}$. The standard deviation of the probability distribution is taken as $\sigma_{\theta_f^+} = 0.007$rad. The LA3 building has 18 WFBW connections, while the LA9 building has 90 WFBW connections (see Figure 4.8). Figures 4.6(a) and 4.6(b) show the median and the standard deviation of the fracture rotations for the LA3 and LA9 buildings for the two-hundred different samples, respectively.

A reference model that neglects brittle connections is also used to allow for response comparison and evaluation of the influence of connections uncertainty.

The peak IDR is taken as the engineering demand parameter that best describes the structural response as it offers a compromise between local and global structural behavior [165]. For each analysis, the Newton-Raphson method is used to solve the nonlinear system of equations at each time step. An adaptive scheme was implemented to overcome possi-

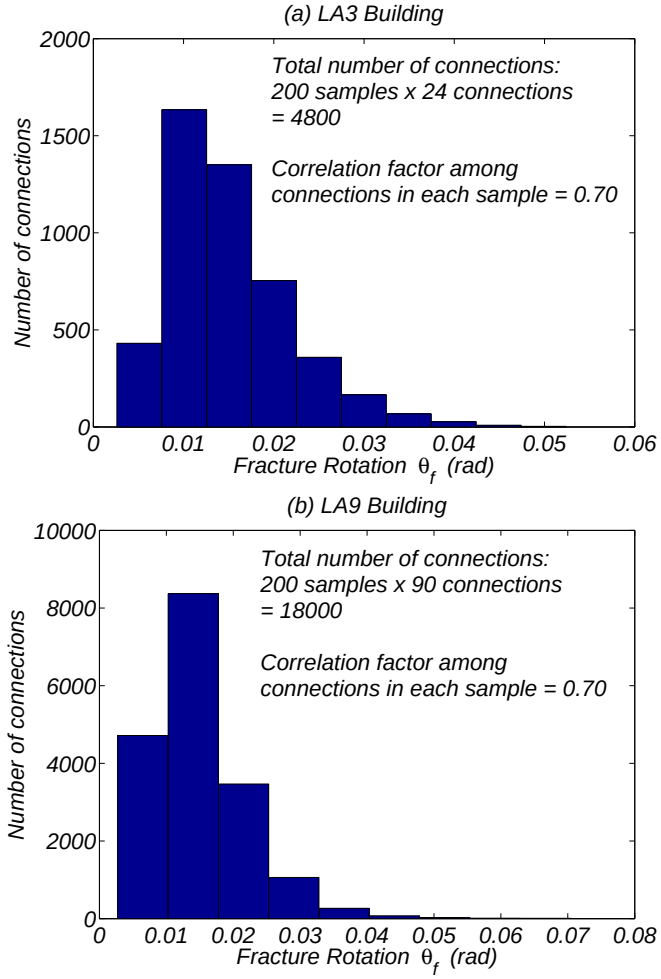

Figure 4.6: Median and standard deviation of the fracture rotation of the connections for the two hundred samples of: (a) LA3 building; and (b) LA9 building

ble convergence problems. The analysis time-step was determined following a convergence study where the accuracy of roof acceleration time-history response due to large intensity shaking was studied using five time steps between 0.01 sec and 0.00005 sec. To reduce the computational time required to perform the analyses, a high-throughput distributed computing framework based on HTCondor [166], available at Oregon State University was used.

4.6 Case Study Description

4.6.1 Buildings and Site Description

The SMRF buildings studied in this chapter are a subset of the models developed as part of the SAC steel project. These buildings are three (3-) and 9-story buildings (denoted LA3 and LA9, respectively), which were designed for Los Angeles by using pre-Northridge codes [138]. In both buildings, external frames were designed to resist the lateral seismic loads and interior frames were designed as gravity frames. Figure 4.8 shows one of the moment resisting frames in the N-S direction. As represented, all buildings have spans of 9.15 m in both directions. The 3-story building presents no basement, whereas the 9-story building

has one basement level. The height of the frames is constant and equal to 3.96 m, except for the first level of the taller building, which has a height of 5.49 m. The member sizes are indicated in Figure 4.8. A detailed description of the buildings is presented in FEMA355C [77] and Luco [139].

4.6.2 Ground Motion Records

Ten ground motion records from the SAC Steel Project are used Somerville *et al.* [167]. The records are part of the 10/50 (10% in 50 years probability of exceedance) ground motion set. This set consists in twenty record pairs corresponding to ten earthquakes. These records are based on real and simulated ground motions, scaled so that their mean response spectra matches the 1997 National Earthquake Hazards Reduction Program (NEHRP) design spectrum, as reported by Somerville *et al.* [167]. The acceleration time histories for Los Angeles are all derived from recordings of shallow crustal earthquakes on Soil Category D. As only one ground motion from each pair is used in this chapter, a total of ten different ground motion records are used. In each pair, the ground motion with the largest PGA is used.

The median pseudo-acceleration response spectra of the ground motions is presented in Figure 4.7. This figure also shows the ASCE 7-10 design spectrum. The two are very close and similar spectral acceleration values are obtained at the fundamental periods of both buildings.

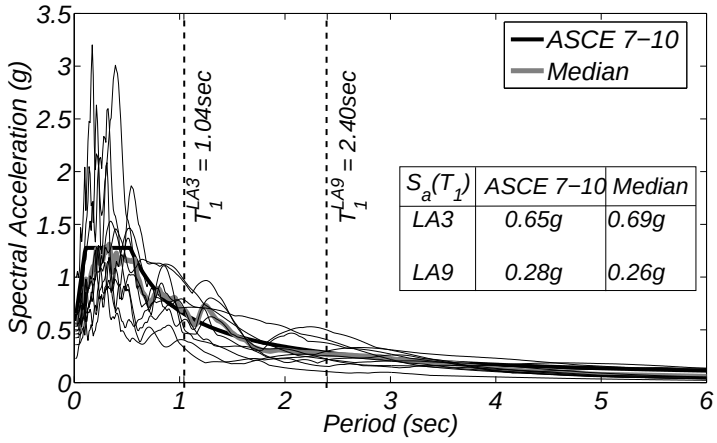

Figure 4.7: Median response spectra of the 10/50 SAC ground motion set

4.6.3 Model Definition

A centerline model of each of the SMRFs is defined for each building. Geometric nonlinearities are accounted for during the analysis by considering a $P-\Delta$ leaning column carrying half of the building's weight. A rigid diaphragm is assumed at each floor level. Soil-structure interaction is not considered. Masses and loads are applied to beam-column joints. Similarly to the approach in FEMA355C [77], Rayleigh damping is assigned to the models. As described by Erduran [168], a damping ratio of 2% is assigned to the first mode ($T_1^{LA3} = 1.04s$ and $T_1^{LA9} = 2.40s$) and a higher mode. Following FEMA355C [77], the

higher mode under consideration is a mode with period of 0.2s (a period close to LA3's third modal period and LA9's fifth modal period).

The modeling approach presented in Figure 4.3 is employed here to simulate beam behavior. The connections are defined according to the fracture model presented in section 4.4.3. Member plastic hinge flexural behavior is simulated through the Bilin model, whose properties are obtained using Lignos and Krawinkler [4] empirical expressions. The main parameters are summarized in Figure 4.8. All other model parameters are defined as proposed by Lignos and Krawinkler [4] and Lignos and Krawinkler [128]. A plastic hinge length of $L_p = L/16$ is considered. The columns are modeled using a force-based fiber-section distributed plasticity beam-column finite elements with six integration points and an elasto-plastic constitutive law with a 3% hardening rate assigned to each fiber. For beams, cyclic deterioration and connection fracture are considered to be the most relevant phenomena. For columns, the most important phenomenon to simulate is the interaction between axial force and bending moment.

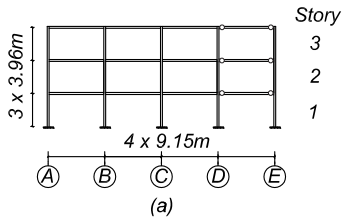

(a)

Story	Columns			Beams					Mass (kg)
	Exterior	Interior	Model	Section	Model	θ_p (rad)	θ_{pc} (rad)	$\Lambda=E_{tot}/M_y$	
1	W14x257	W14x311	NL-FB-H	W33x118	NL-FMRB	0.026	0.114	0.740	$9.75x10^5$
2	W14x257	W14x311		W30x116		0.031	0.152	1.001	$9.75x10^5$
3	W14x257	W14x311		W24x68		0.038	0.130	0.792	$1.06x10^6$

(b)

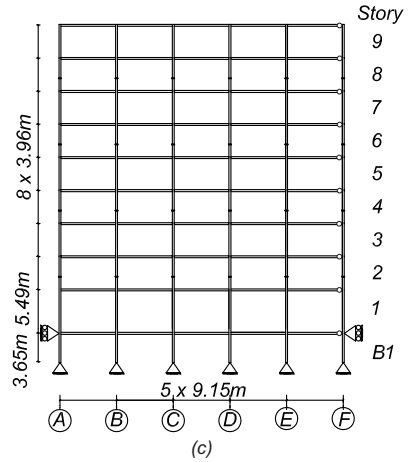

(c)

Story	Columns			Beams					Mass (kg)
	Exterior	Interior	Model	Section	Model	θ_p (rad)	θ_{pc} (rad)	$\Lambda=E_{tot}/M_y$	
B1	W14x370	W14x500	NL-FB-H	W36x160	NL-FMRB	0.025	0.146	0.978	$1.03x10^6$
1	W14x370	W14x500		W36x160		0.025	0.146	0.978	$1.03x10^6$
2	W14x370/ W14x370	W14x500/ W14x455		W36x160		0.025	0.146	0.978	$1.01x10^6$
3	W14x370	W14x455		W36x135		0.024	0.115	0.757	$1.01x10^6$
4	W14x370/ W14x283	W14x455/ W14x370		W36x135		0.024	0.115	0.757	$1.01x10^6$
5	W14x283	W14x370		W36x135		0.024	0.115	0.757	$1.01x10^6$
6	W14x283/ W14x257	W14x370/ W14x283		W36x135		0.024	0.115	0.757	$1.01x10^6$
7	W14x257	W14x283		W30x99		0.029	0.120	0.783	$1.01x10^6$
8	W14x257/ W14x233	W14x283/ W14x257		W27x84		0.033	0.123	0.768	$1.01x10^6$
9	W14x233	W14x257		W24x68		0.038	0.130	0.793	$1.09x10^6$

(d)

NL-FB-H *- **N**onlinear **F**orce-**B**ased Beam-Column Element with Fiber Section with 3% strain-**H**ardening*
NL-FMRB *- **N**onlinear **F**inite-**L**ength **M**odified Gauss-**R**adau Beam-Column Element with **B**ilinear Flexural Hinge Model*

Figure 4.8: (a) LA3 building; (b) LA3 Sections, Model Parameters, and Floor Masses; (c) LA9 building; and (d) LA9 Sections, Model Parameters, and Floor Masses.

4.7 Deterministic Performance Assessment

This Section presents two different analysis. In the first part, the building's response is analyzed under the ten earthquake ground motions considering that all connections in the buildings are characterized by the median fracture rotation, i.e. $\theta_f^+ = 0.015$rad. In the second part, the connections fracture rotations are randomly assigned using the defined probabilistic distributions and the results of two specific analysis, one for each building, are shown.

In the first part of the Section, a first estimation of the building response and the corresponding influence of brittle connections is obtained by performing the analysis for all ground motions at the DBE and MCE intensity levels. The results obtained for the DBE and MCE intensity levels are summarized in Table 4.3, namely the median peak IDR, the median PFC, and the increase in the median peak IDR (relatively to the rigid connection case).

Table 4.3: Preliminary results obtained considering brittle connections with $\theta_f^+ = 0.015$rad for all connections

	LA3		LA9	
	DBE	MCE	DBE	MCE
Median Peak IDR	4.41 %	9.34 %	2.41 %	3.87 %
Median PFC	69 %	97 %	0 %	5 %
Increase in Peak IDR	80 %	146 %	1 %	17 %

The obtained results indicate that a minimal increase in peak IDR is obtained for the DBE intensity level for the LA9 building and a relatively small increase (17% increase) is recorded for the MCE level. For the LA3 building, a large increase is observed for both intensity levels. The increase in peak IDR correlated well with the PFC of both buildings. In fact, considering the four points defined by the obtained median peak IDRs and PFCs, the computed linear correlation coefficient is 0.86.

In the second part of the Section, results of individual analysis for the LA3 and LA9 buildings are presented. Two building samples, one for the LA3 and other for the LA9 bulding, are randomly selected, among the total number of generated samples, to be shown here. A single ground motion, scaled to the MCE intensity level, is used to assess the response of the building. Results obtained with the rigid connection model are also represented. Figure 4.9 shows the response of the LA3 building under the third SAC earthquake ground motion (termed as "la03"). Results indicate that peak IDR associated with the brittle connection model is approximately twice as large as the one associated with the rigid connection model (5.53% for the brittle connection model and 2.75% for the rigid connection model). During this analysis 72% of the connections failed (13 out of 18, as represented in Figure 4.10(a)). Figure 4.10(a) also shows that the floor with most fractures recorded a larger drift. Furthermore, Figure 4.9 also indicates that due to the connections fracture (such as the one represented in Figure 4.9(e)) the vibration properties of the structure are significantly different at the end of the ground motion (observe the difference in the vibration cycles when almost no ground motion movement exists). In order to investigate this fact, Figure 4.10(b) shows that ratio between the structural periods of vibration of the intact structure (i.e., before ground motion starts) and after the ground motion (considering a 30s free vibration period after the end of the ground motion). The obtained results indicate that a significant increase (ratio of 2.03) is obtained for the first period. The ratio associated with the second period is 1.41, while for the third period a slight increase is also recorded (ratio of 1.07). For the rigid connection model, the increase is residual (maximum ratio of 1.01 for the first mode). This is due to the fact that no stiffness deterioration is considered in the member modeling.

Figure 4.11 shows the response of the 9-story building when subjected to the eleventh SAC ground motion (termed "la11") scaled to the MCE intensity. For this example, results indicate that peak IDR associated with the brittle connection model is almost twice as large as the one associated with the rigid connection model (4.82% for the brittle con-

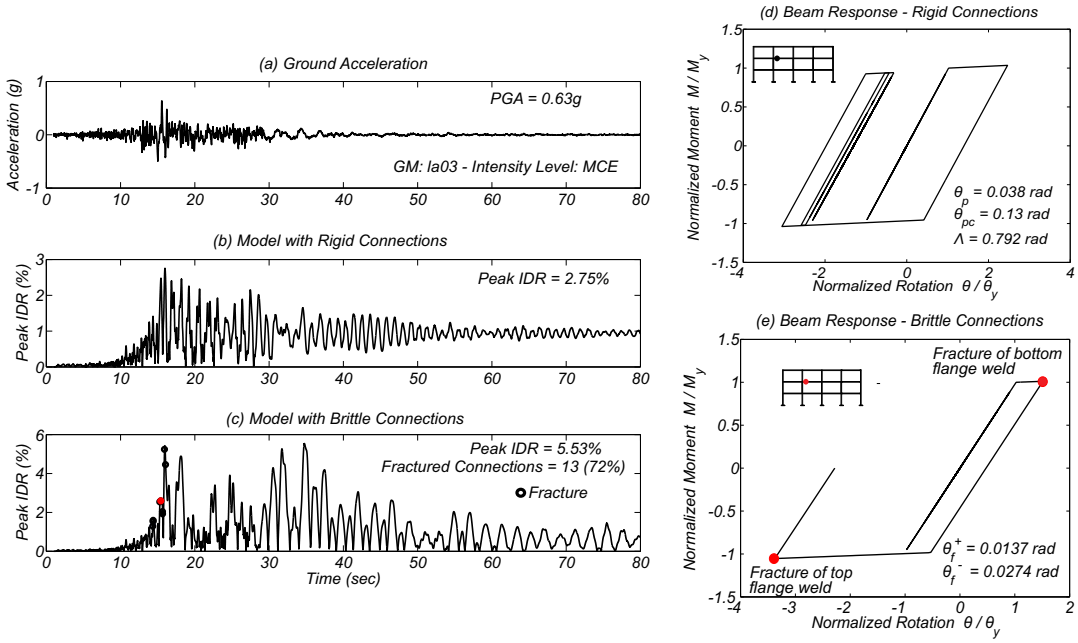

Figure 4.9: LA3 building - Time-history response: (a) ground motion acceleration; (b) peak IDR obtained with the rigid connection model; (c) peak IDR obtained with the brittle connection model; (d) beam moment-rotation response obtained with the rigid connection model; and (e) beam moment-rotation response obtained with the brittle connection model.

nection model and 2.88% for the rigid connection model). During this analysis 33% of the connections failed (30 out of 90 as shown in Figure 4.12(a)). Connections fracture induces a concentration of nonlinearities in the lower stories, i.e. larger peak IDR's are recorded at lower stories. This concentration of large drifts in the lower stories may be due, in part, to $P-\Delta$ effects and/or to the near-source nature of some of the SAC earthquake records for Los Angeles. In addition, the model with brittle connections show elongation of period. Figure 4.12(b) shows the ratio between the structural periods of vibration of the intact structure (i.e., before ground motion starts) and after the ground motion (considering a 30s free vibration period after the end of the ground motion). It is worth noting that for this building the increase in the first period of vibration of the brittle connection model is much larger than the increase in the other periods. In what concerns the rigid connection model, no change in the rigid connection model periods is observed. High correlation was found between the floor with larger number of fractured connections and the mode shape after the ground motion. Similar observations were made for the LA3 building.

4.8 Sensitivity Assessment of Fracture Model Parameters

A preliminary sensitivity study is carried out in order to assess the influence of variation in the fracture model parameters on the performance of the buildings. This study is based on simple variation of the fracture rotation θ_f^+ and pinching parameters ($F_{r,p}$, $F_{r,n}$, and A_{pinch}) and the comparison of the obtained peak IDR.

Figure 4.13 shows pushover analyses carried out with four different connection fractures rotations. All connections in each model are assigned the same fracture rotation. For θ_f^+ =0.020 rad the maximum base shear that the structures withstand is close to the rigid

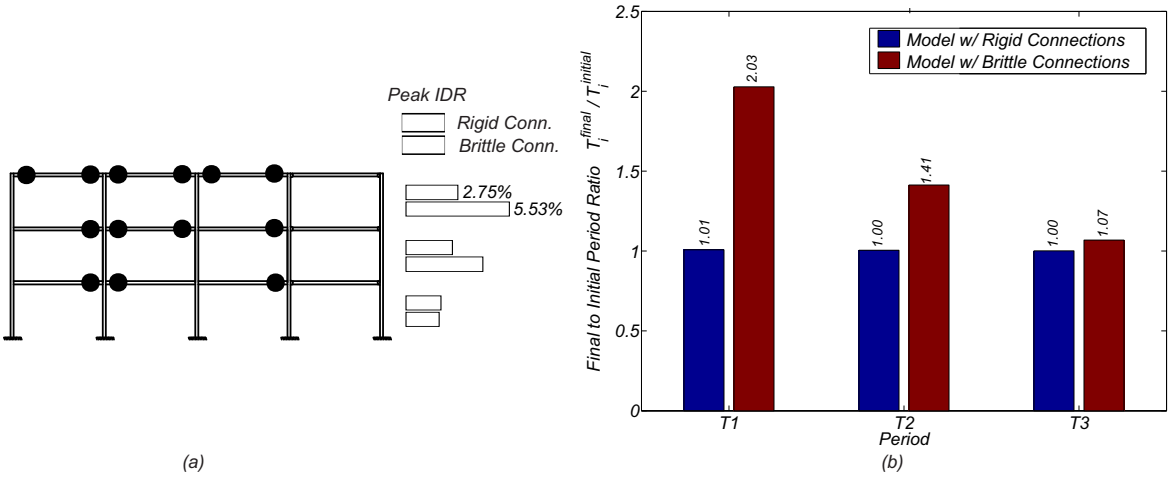

Figure 4.10: LA3 building - (a) Fractured connections; and (b) variation in the periods of vibration.

connection case. However, a brittle collapse occurs due to the fracture of several connections at the same time and, consequently, the generation of a collapse mechanism. When the value of the fracture rotation decreases the base shear associated with collapse also decrease but the type of brittle collapse remains.

Figure 4.13 also shows results when the fracture rotation is randomly assigned to the connections among the buildings, using the considered probabilistic distribution ($\mu_{\theta_f^+} = 0.015$rad; $\sigma_{\theta_f^+} = 0.007$rad) and the inter-component correlation coefficient of 0.7, the base shear associated with collapse is lower than the one associated with θ_f^+ =0.020 rad and larger than the one associated with θ_f^+ =0.007 rad. In this case the capacity curve is characterized by several steps, corresponding to the failure of different connections. This is the normal behavior of a structure with brittle connections. This is clearly seen in the LA9 building (Figure 4.13(b)) but not evident in the LA3 building (Figure 4.13(a)) due to the reduced number of connections. In the LA3 building after failure of some of the connections, convergence problems are found which hinders the prosecution of the analyses.

Figure 4.14 shows results of the nonlinear dynamic analysis performed by varying connection fractures rotations. The ground motion LA04 at DBE intensity level is used in this analysis. It is worth noting that for both buildings, if θ_f^+ =0.020 rad, no connections fail and, as a consequence, the peak IDR is equal to that obtained with the rigid connection model. When the value of the fracture rotation decreases, the peak IDR increases by more than twice for some cases. For the LA3 building the peak IDR associated with θ_f^+ =0.010 rad is larger than the one obtained with θ_f^+ =0.007 rad, which is due to particular ground motion acceleration history and the time at which connections fractured, which is a function of the fracture rotation. For the LA3 building three analyses were also performed by randomly assigning the fracture rotations. Peak IDR are, as expected, within the interval defined by the results of the deterministic samples.

Finally, the sensitivity of the peak IDR of the LA9 building to the variation of the pinching parameters was analyzed. In this analysis the fracture rotation is taken as $\theta_f^+ = \theta_f^- = 0.010$ rad. The three pinching parameters, which may assume values in the interval [0,1] (if these are equal to 0 or 1 the model is equivalent to the peak-oriented model, i.e. no pinched reloading is obtained). Five different values of each parameter are considered. Moreover, it

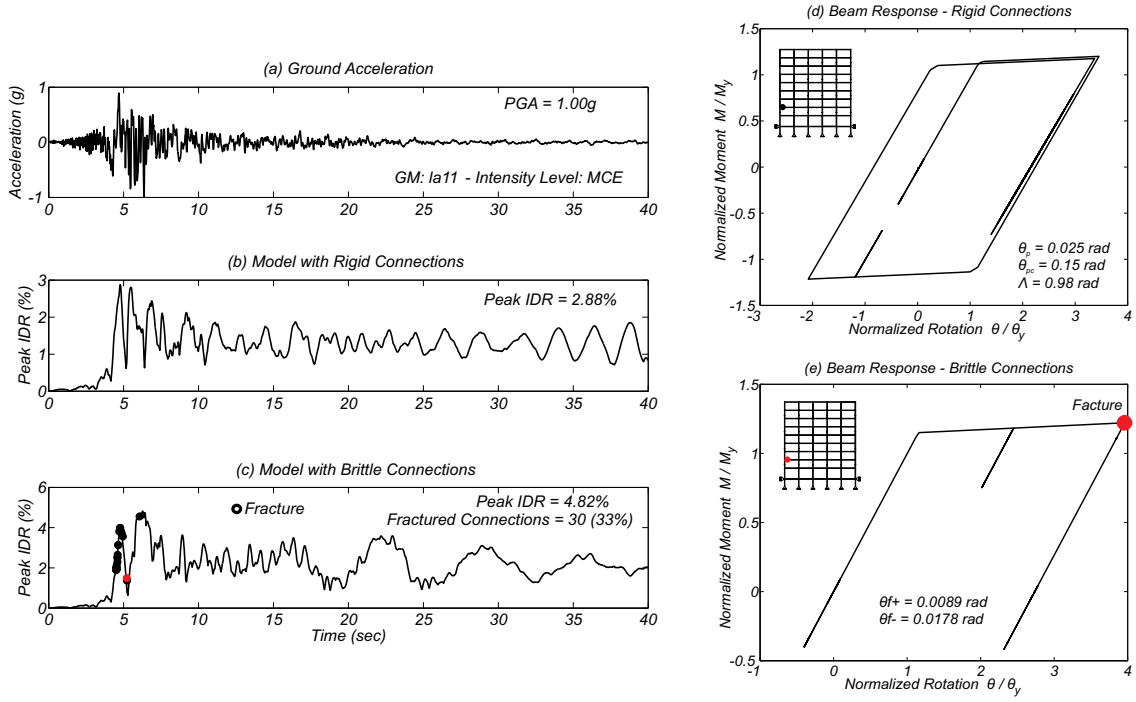

Figure 4.11: LA9 building - Time-history response: (a) ground motion acceleration; (b) peak IDR obtained with the rigid connection model; (c) peak IDR obtained with the brittle connection model; (d) beam moment-rotation response obtained with the rigid connection model; and (e) beam moment-rotation response obtained with the brittle connection model.

is considered that the parameters related to fraction of strength at which reloading starts are assumed to be the same in both positive and negative bending directions, i.e. $F_{r,p} = F_{r,n}$. Results obtained indicate that variation in F_r does not introduce significant variation in peak IDR. A_{pinch} (i.e. the rotation fraction at which reloading starts) does influence the peak IDR, although with small variations. Thus confirms the validity of the deterministic consideration of these parameters.

Table 4.4: LA9 Building - Sensitivity analysis to pinching reloading parameters

Peak IDR (%)		A_{pinch}				
		0.2	0.5	0.8	0.9	1
$F_{r,p} = F_{r,n}$	0.2	6.11			6.27	
	0.3		6.06	6.30		
	0.5		6.05	6.26		
	0.9	6.11			6.29	
	1					6.11

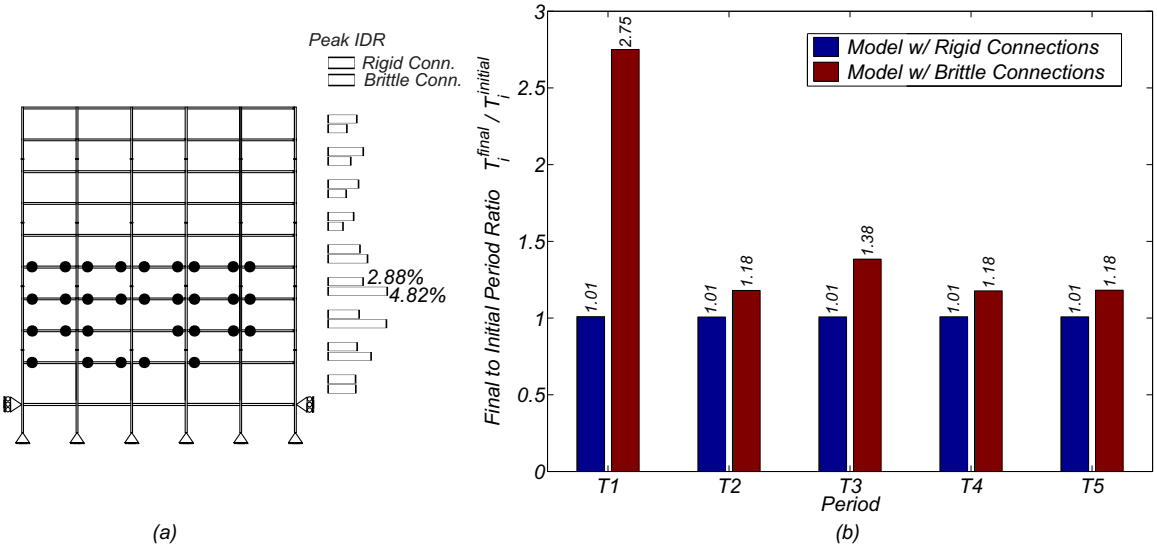

Figure 4.12: LA9 building - (a) Fractured connections; and (b) variation in the periods of vibration.

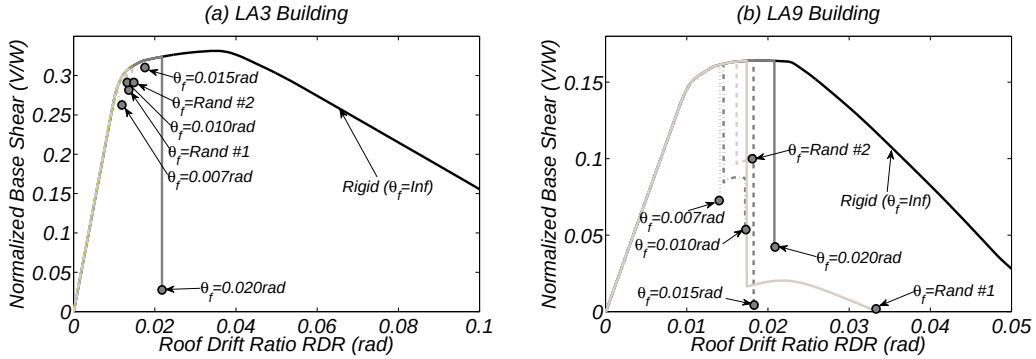

Figure 4.13: Pushover analysis with different connection fractures rotations: (a) LA3 building; and (b) LA9 building

4.9 Probabilistic Analysis

4.9.1 Performance Assessment of the LA3 Building

The probabilistic results of the complete set of analyses are presented in this section for the LA3 building. First, the median peak IDR of the structure under the ten intensity level, for the brittle connection model, and the thirteen levels, for the rigid connection model, is presented in Figure 4.15. Each intensity level is associated with a box, in which statistical measures of the results are represented. On each box, the central mark is the median, the edges of the box are the 25th and 75th percentiles, the whiskers extend to the most extreme data points not considering outliers. The range of the whiskers are $2.7 \times \sigma$ assuming a normal distribution. The outliers are plotted individually (red dots). The median peak IDR obtained for the DBE and the MCE intensity levels are 4.31% and 8.14%, respectively. These values represent an increase, relatively to the rigid connection case, of 76% and 114%, respectively. The ratio between the peak IDR's obtained with the brittle and rigid connection models are represented in Figure 4.16. Moreover, the results associated with the brittle connection

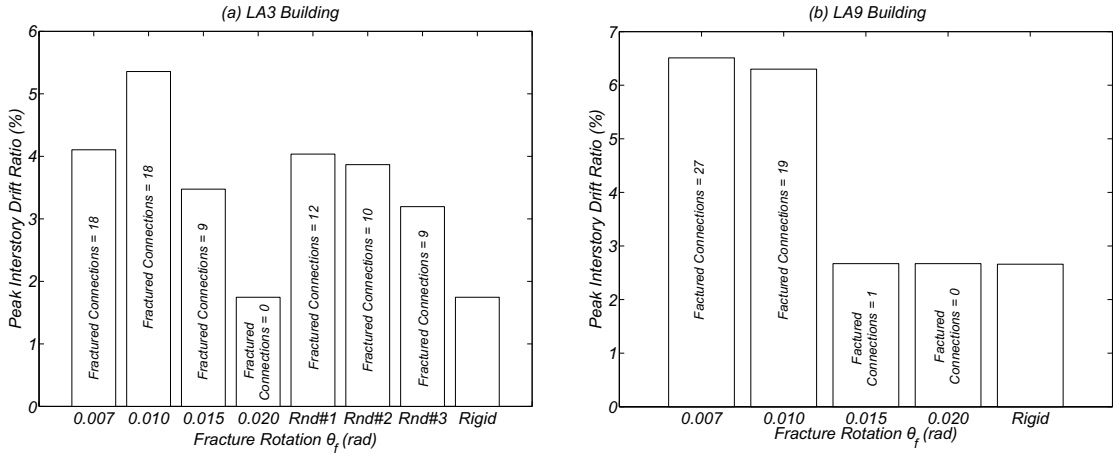

Figure 4.14: Nonlinear dynamic analysis with different connection fractures rotations: (a) LA3 building; and (b) LA9 building

model have a much larger dispersion, namely for intensity levels up to the MCE intensity levels. Above that, the dispersion, measured for example through the standard deviation of the obtained results (see Figure 4.16(b)), is approximately the same between the two modeling approaches.

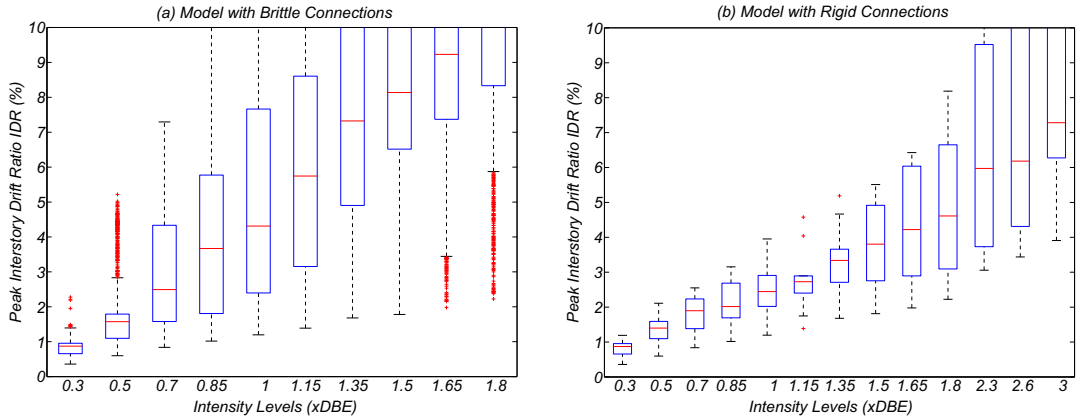

Figure 4.15: LA3 building - peak IDR associated with: (a) brittle connection model; and (b) rigid connection model

In Figure 4.17 the PFC associated with the LA3 building is represented. For the DBE intensity level the median PFC is 66%, while for the MCE level is 100%. Figure 4.18 shows the histogram of the PFC for each intensity level. For the lower intensity levels almost all analysis recorded low values of PFC. The increase in the intensity level increases the PFC. For intermediate intensity levels (e.g., the DBE) the PFC is either very large or very low for most of the analysis. This behavior will be analyzed in further detail in the LA9 building.

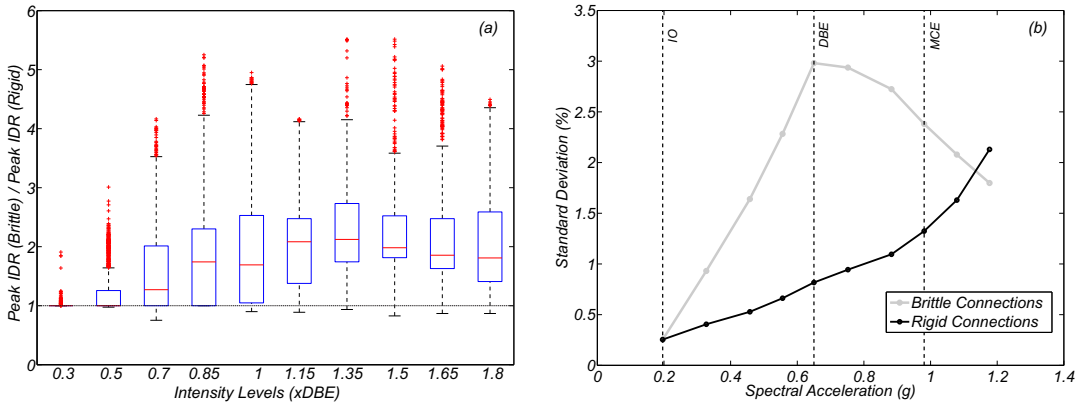

Figure 4.16: LA3 building - (a) Ratio of the peak IDR obtained with the brittle connection model and the rigid connection model; and (b) standard deviation of the peak IDR at each intensity level for the two models

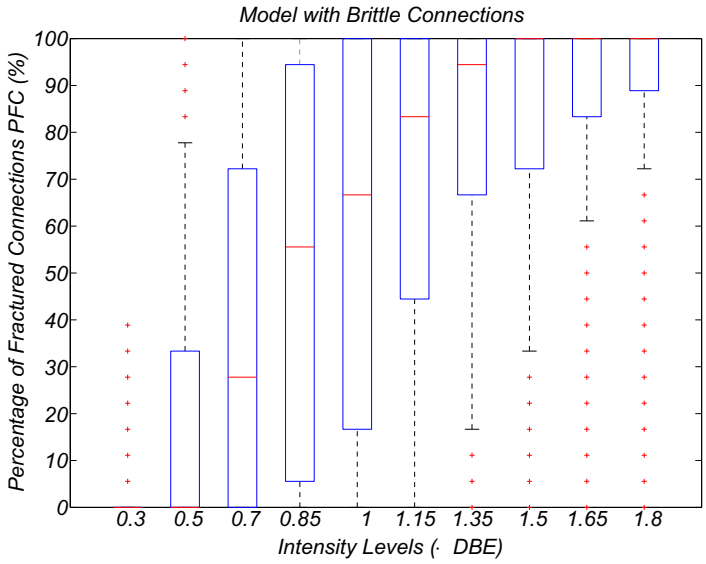

Figure 4.17: LA3 building - percentage of fractured connections (PFC)

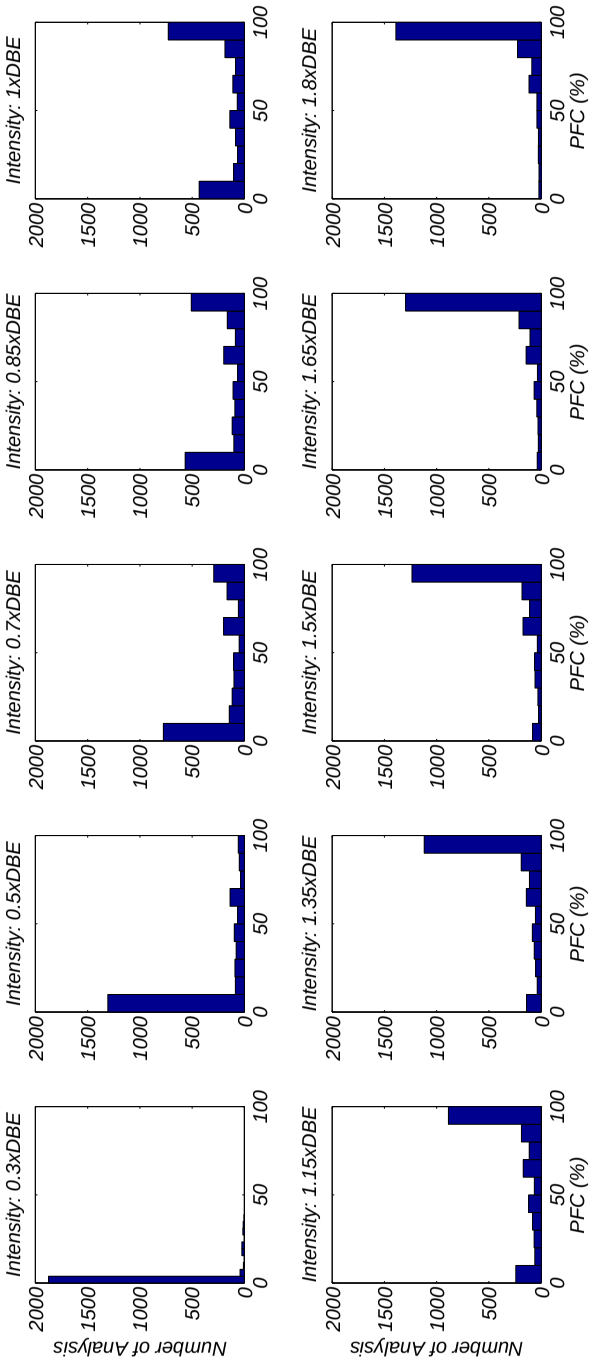

Figure 4.18: LA3 building - percentage of fractured connections histogram

The distribution of fractured connections along the building is represented as a function of the intensity level and as a function of the peak IDR in Figures 4.19 and 4.20. These figure show the most important modes of collapse for the various ground motion intensities and recorded response. The size of the circles are associated with the number of times each connection failed. In addition, the rectangles on the right side of each floor correspond to the median peak IDR attained at that floor. For the LA3 building, the observed patterns does not vary significantly due to the low number of connections. Nevertheless, except for the lower intensity level, the upper floor of the building record the largest number of fractures. This is due to the use of smaller sections in the upper floors, which results in larger drift demands for most of them, as can be observed in the IDR profiles represented on the right side of the building.

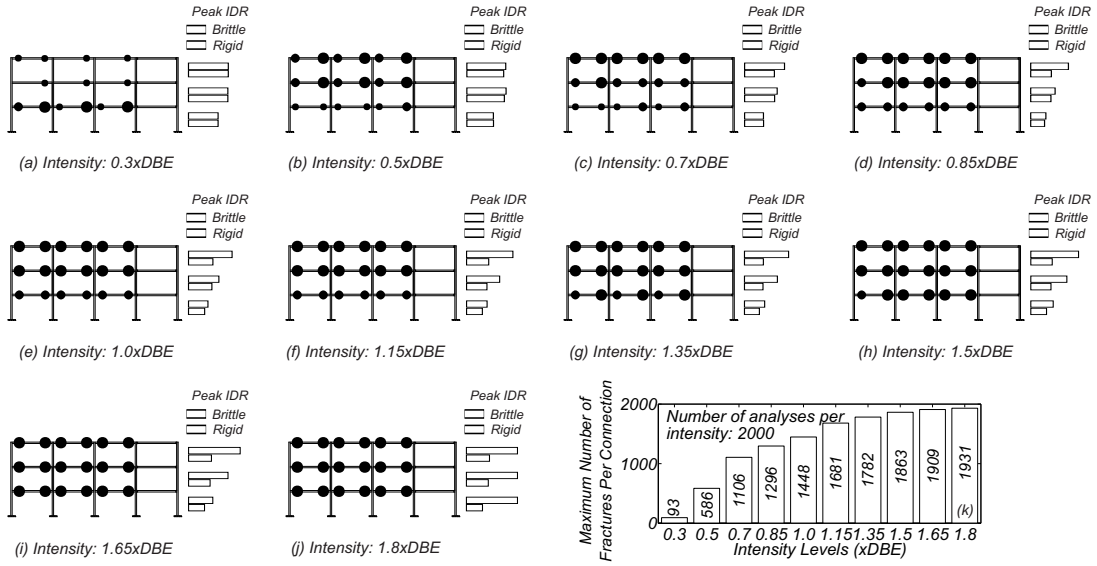

Figure 4.19: LA3 building - distribution of fractured connections in the building as a function of intensity level

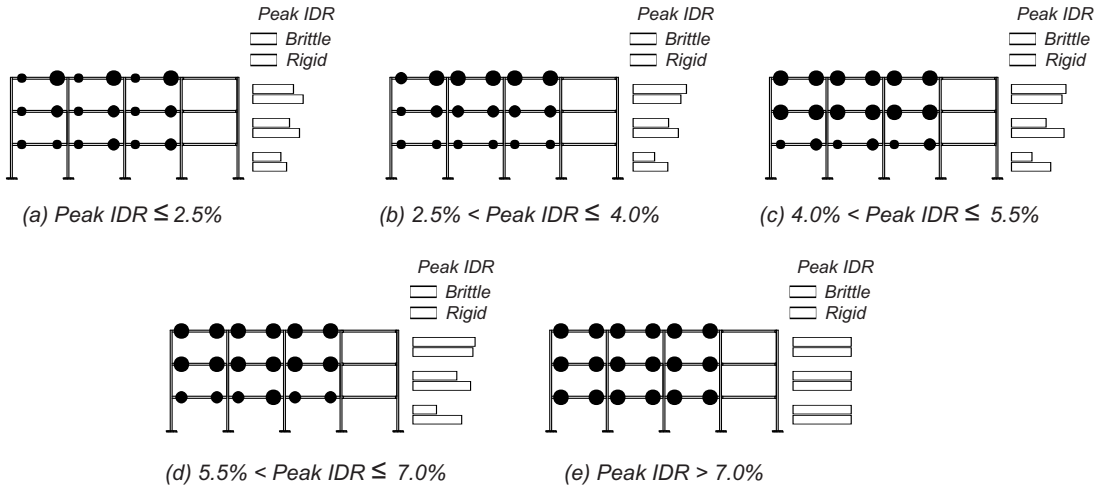

Figure 4.20: LA3 building - distribution of fractured connections in the building as a function of peak IDR

Finally, Figure 4.21 shows the relationship between the peak IDR and the PFC. Is is

worth noting the large dispersion in the obtained results. Again, this is mainly due to the small number of connection of this building. However, it is clear that for peak IDR's larger than 5% almost all analysis led to the fracture of all beam-column connections.

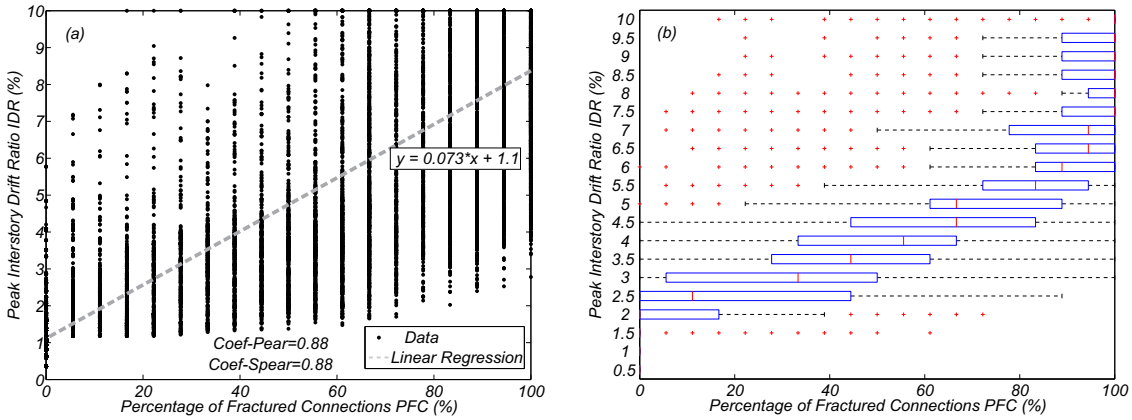

Figure 4.21: LA3 building - peak IDR as a function of the percentage of fractured connections (PFC)

4.9.2 Performance Assessment of the LA9 Building

In what concerns the LA9 building, the median, the 25th and 75th percentiles, and the computed outliers of the peak IDR are presented in Figure 4.22 for the various intensity levels. The median peak IDR obtained for the DBE and the MCE intensity levels is 2.47% and 3.84%, respectively. These values represent an increase, relatively to the rigid connection case, of 4% and 16%, respectively. The ratio between the peak IDR's obtained with the brittle and rigid connection models are represented in Figure 4.23. For the LA9 building, the increase in the peak IDR due to the consideration of brittle connections is much lower than that associated with the LA3 building. This is believed to be due to the capacity of the LA9 building to redistribute damage across the structure in an efficient way.

Luco and Cornell [142] and Prakash *et al.* [149] also observed a less than anticipated effect of connection fracture on overall building response. Shi and Foutch [169] stated that, although buildings with fractured connections experience larger story displacements than buildings with connections that do not fail, this effect is smaller than expected indicating that most existing steel buildings are safe during large earthquakes.

In Figure 4.24 the PFC associated with the LA9 building is represented. Although some analysis record a large number of fractured connections, the median value of the PFC associated with the DBE intensity level is 0%, which, would indicate, that for this building at this intensity level the connections present low risk. For the MCE level the PFC is 8%, which is still a low value.

Figure 4.25 shows the histogram of the PFC for each intensity level. For the lower intensity levels, very few fractures are recorded. For the intermediate intensity levels, the PFC seems to be low, which indicates that the fractured connections might be concentrated in a defined area of the structure. Then, when the ground motion intensity increases a different trend is observed. Two different regions are clearly observable, for example for the $1.8\times$DBE level, one is associated with low values of PFC and the other with large values of

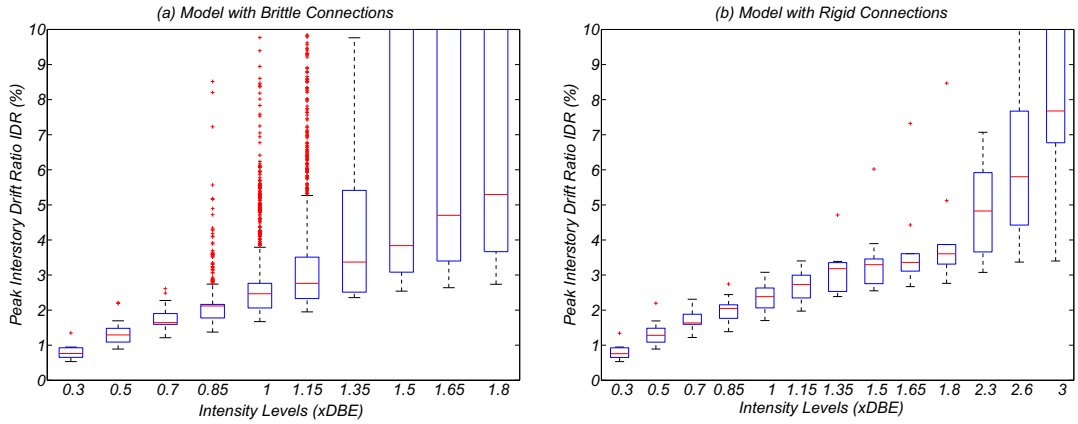

Figure 4.22: LA9 building - peak IDR associated with: (a) brittle connection model; and (b) rigid connection model

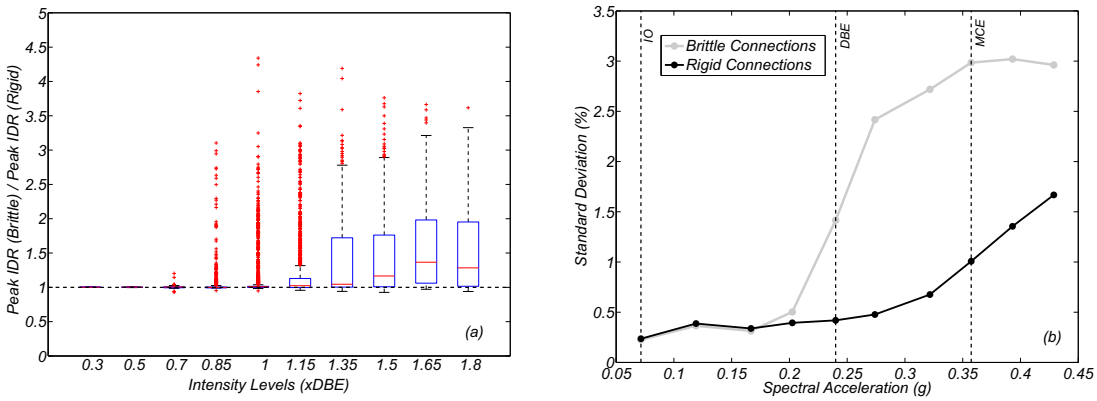

Figure 4.23: LA9 building - (a) Ratio of the peak IDR obtained with the brittle connection model and the rigid connection model; and (b) standard deviation of the peak IDR at each intensity level for the two models

PFC. This indicates that wither the building has few fractured connections or the building has almost all connections damaged. This bi-modal behavior indicates, once again, the capacity of this building to redistribute damage.

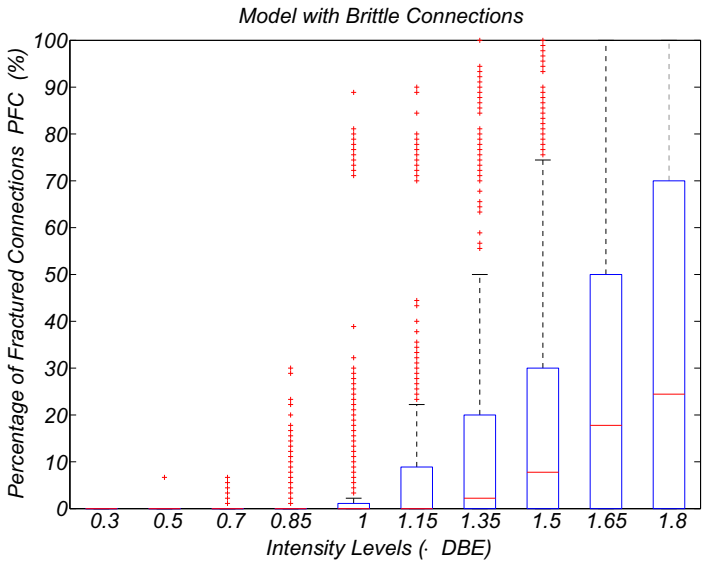

Figure 4.24: LA9 building - percentage of fractured connections (PFC)

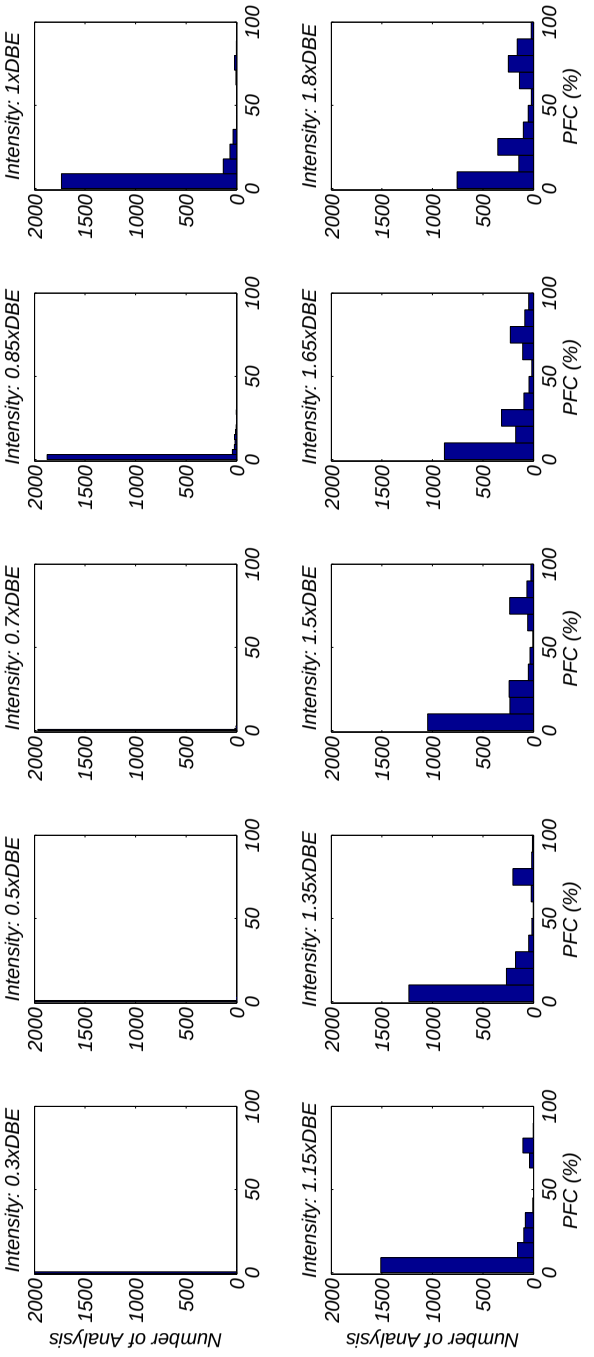

Figure 4.25: LA9 building - percentage of fractured connections histogram

In order to further investigate the distribution of damage across the building, the distribution of fractured connections is represented as a function of the intensity level and as a function of the peak IDR in Figures 4.26 and 4.27. In what concerns the fourth lower intensity levels, most fractured connections are concentrated in the 7^{th} and 8^{th} floors. For the intermediate intensity levels, the fractures are divided into two main areas, one that ranges from the 1^{st} to the 3^{rd} floors and the other from the 7^{th} floor to the top. For the larger intensities the fractures seem to be concentrated at the lower levels. Moreover, a good correlation is observed between fractured connections and IDR. Despite that, the IDR's tend to be quite uniform along building height, which confirm the hypothesis of good capacity of damage redistribution.

The analysis of the distribution of fractured connections as a function of the peak IDR indicates that for peak IDR's lower than 2.5% very few connections failed and these are mainly at the lower floors. For peak IDR's between 2.5% and 4.0% the fractured connections are mainly at the 7^{th} and 8^{th} floors. For peak IDR's ranging from 4.0% to 7.0% the lower floors concentrate most the damaged connections. Finally, for peak IDR's larger than 7.0% the fractured connections are uniformly distributed over the building. Once again, the IDR are in good correlation with the number of fractured connections at each floor.

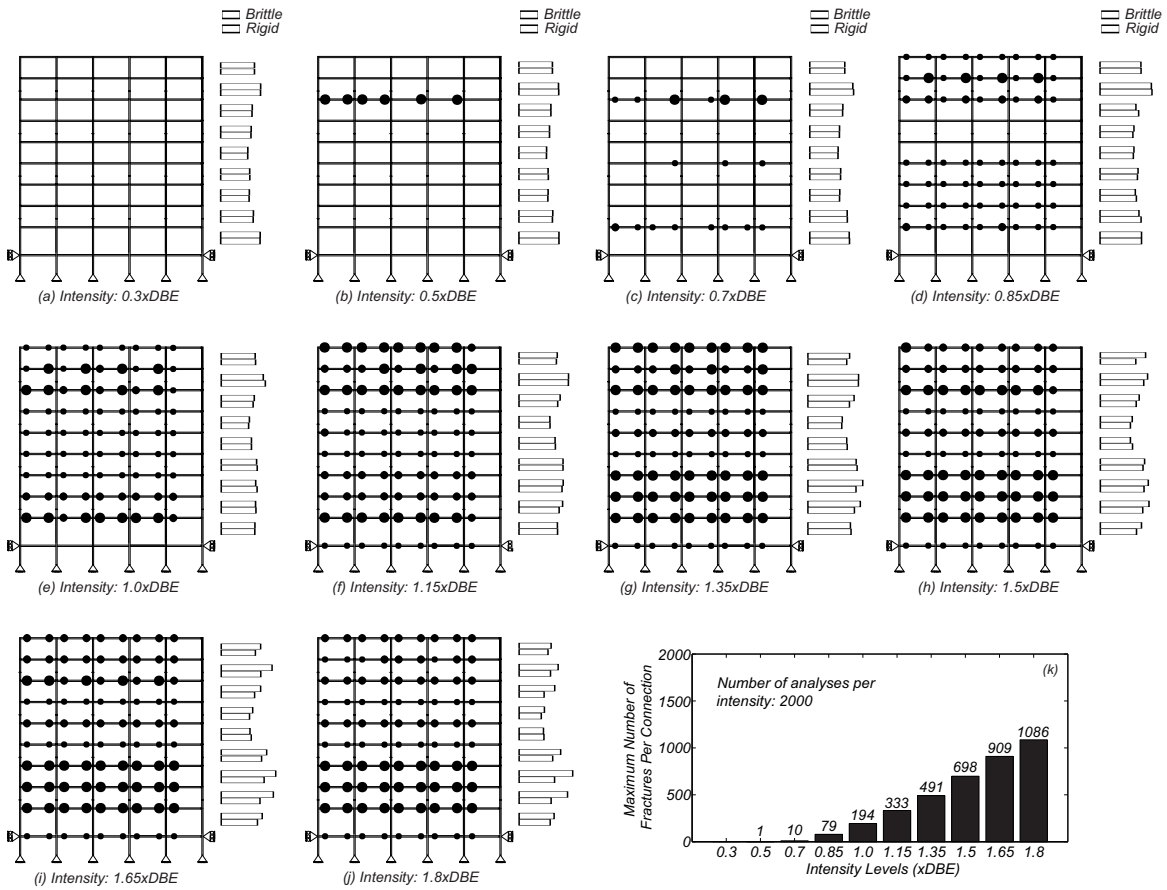

Figure 4.26: LA9 building - distribution of fractured connections in the building as a function of intensity level

At last, Figure 4.28 shows the relationship between the peak IDR and the PFC. A clear trend is observable and a linear regression fits very well the results. For peak IDR lower than 9.5% no more than 40% of fractures are expected in this building.

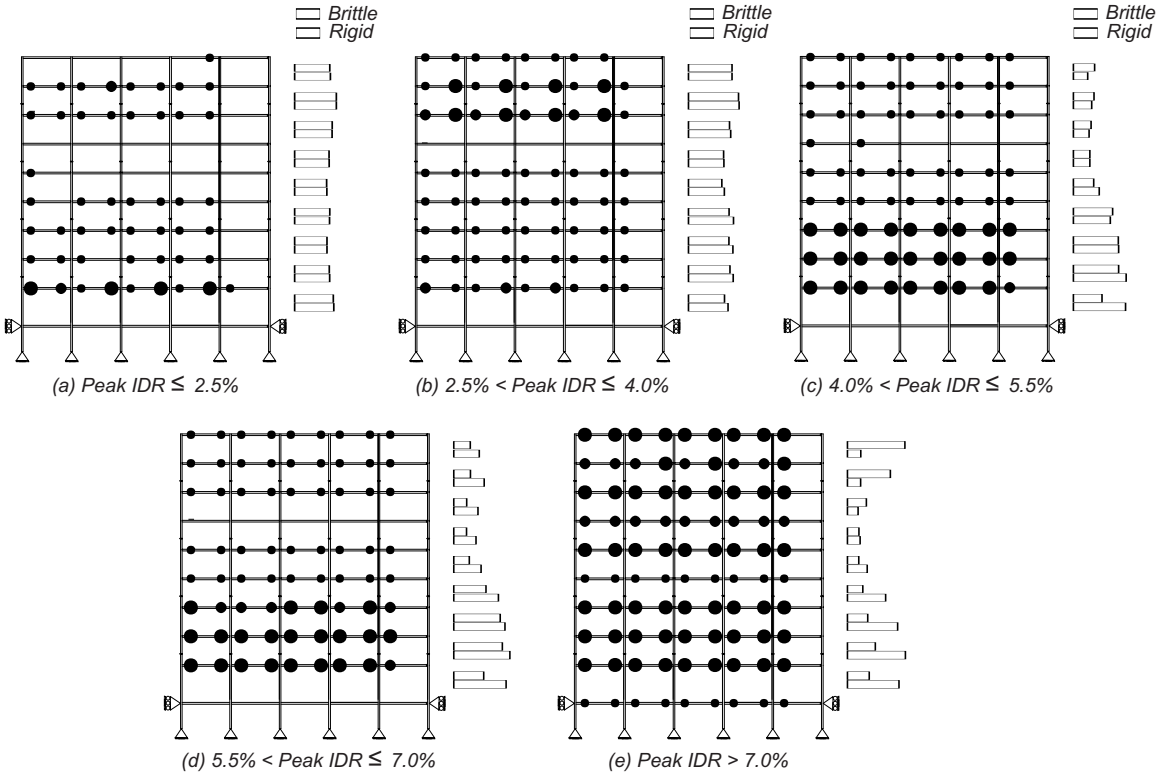

Figure 4.27: LA9 building - distribution of fractured connections in the building as a function of peak IDR

4.9.3 Fragility Analysis

The last part of this chapter consists in the risk analysis. Computation of the fragility curves is executed and the RCR of the damaged buildings is estimated using both the rigid and brittle connection models. The fragility curves and the RCR computation allows for the assessment of the influence of connection fracture on building response but also for analyzing the influence of connection fracture uncertainty on the risk assessment.

Fragility curves are computed using the maximum likelihood parameter estimates method proposed by Baker [55]. Four different damage states (DS) are considered as defined in FEMA351 [170]. The values of the peak IDR thresholds defining the different DS are listed in Table 4.5. These values are also supported by other studies, such as Maison and Bonowitz [144]. Table 4.5 lists the RCR associated with each DS as well. The average RCR of the building at a given intensity level IL is given by:

$$\mu_{RCR} = \sum_{i=1}^{4} RCR_i \times P(DS = ds_i|IL) \tag{4.1}$$

The values of the RCR for each DS and the total cost of the buildings are estimated following FEMA351 [170]. The total costs are 1.6M$ and 5M$ for the LA3 and LA9 buildings, respectively.

Figure 4.29(a) shows the fragility curves obtained for the LA3 building. These curves indicate that for the first two DS (Slight and Moderate damage states) the influence of connection fracture is negligible. This is due to the low number of fractures that occur at this level of deformation. For the Extensive DS the influence of connection fracture is clearly

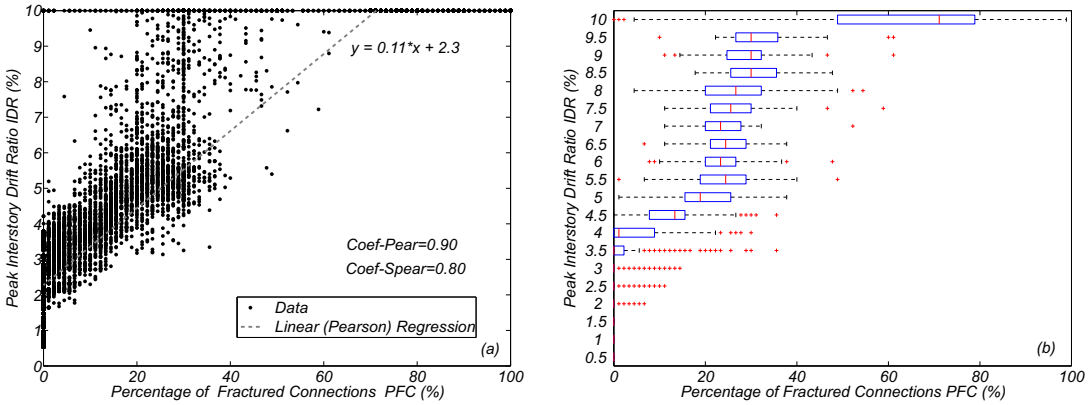

Figure 4.28: LA9 building - peak IDR as a function of the percentage of fractured connections (PFC)

Table 4.5: Maximum values defining Damage States thresholds

Damage State	Peak IDR (%)	RCR (FEMA Pre-Northridge)
Slight	1	8
Moderate	1.5	20
Extensive	2.5	80
Complete	4	100

visible, increasing the probability of exceeding the threshold value of peak IDR defining this DS. Finally, for the Complete DS the difference between the fragility curves associated with the brittle connection model and the rigid connection model is very significant. These differences have repercussions on the costs associated with the rehabilitation of the building after the earthquake, which are represented in Figure 4.29(b). In fact, the RCR's computed with the brittle connection model and the rigid connection model are significantly different. For the DBE intensity level a difference of approximately 35% exists, which leads to a difference of $560k in the total repair cost.

Table 4.6 shows the fragility curves parameters as defined by Baker [55]. These are useful for use in performance-based studies. This tables also lists the difference in the β parameter, which is associated with the uncertainty in the results, between the brittle connection model and rigid connection model. The uncertainty in the rigid connection model arises from the RTR variability. Whereas the uncertainty in the brittle connection model is related to the RTR variability and the connection fracture uncertainty. Thus, the difference between the two provides the uncertainty in the results due to the connection fracture uncertainty. The obtained results indicate that only for the Complete DS there is an increase in the uncertainty due to connection fracture uncertainty ($\beta_{Conn} = 0.05$). For the Moderate DS a negative difference is observed. This is probably due to the low number of intensity levels analyzed.

Figure 4.30(a) shows the fragility curves obtained for the LA9 building. These curves indicate that for the first three DS (Slight, Moderate, and Extensive damage states) the influence of connection fracture is negligible. This is due to the low number of fractures that occur at this level of deformation. For the Complete DS the influence of connection fracture is clearly visible, increasing the probability of exceeding the threshold value of peak

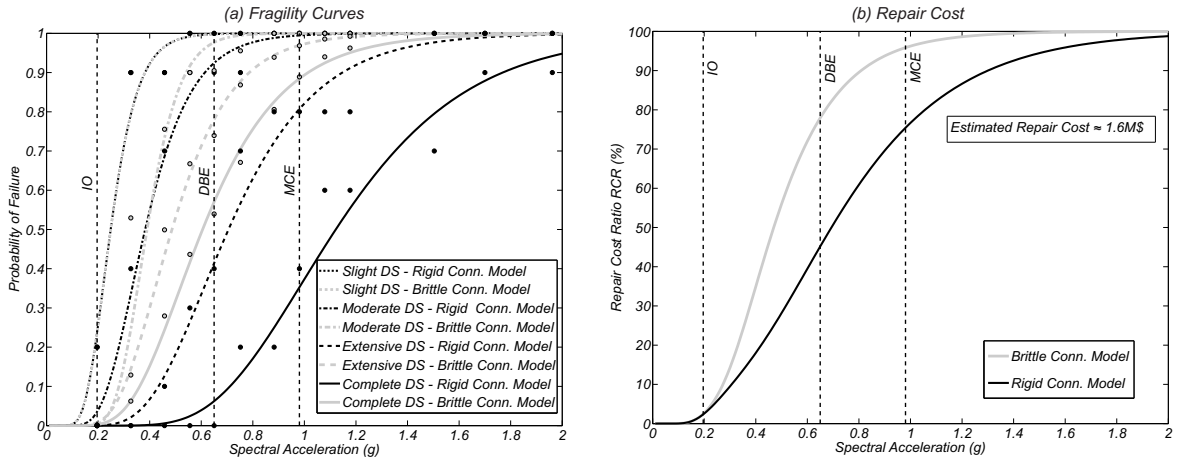

Figure 4.29: LA3 building - fragility curves and repair cost ratio (RCR) estimation

Table 4.6: Fragility curves parameters associated with LA3 building

	Brittle Conn. Model		Rigid Conn. Model		Uncertainty Summary	
Damage State	θ	β	θ	β	β_{RTR}	β_{Conn}
Slight	0.25	0.33	0.25	0.33	0.33	0.00
Moderate	0.39	0.26	0.38	0.37	0.37	-0.11
Extensive	0.49	0.37	0.71	0.38	0.38	0.00
Complete	0.61	0.40	1.12	0.36	0.36	0.05

IDR defining this DS. Due to the fact that only the Complete DS is affected by the connections fractures, the differences in the RCR, which are represented in Figure 4.30(b), are much smaller than the ones associated with LA3 building. At the MCE intensity level, the difference 8%, which yields a difference in the total cost of repair of 400k$.

Table 4.7 shows the fragility curves parameters and the difference in the β parameter. The obtained results indicate that for the Complete DS there is an increase in the uncertainty due to connection fracture uncertainty ($\beta_{Conn} = 0.04$). For the other DS's the influence of connection fracture uncertainty is negligible.

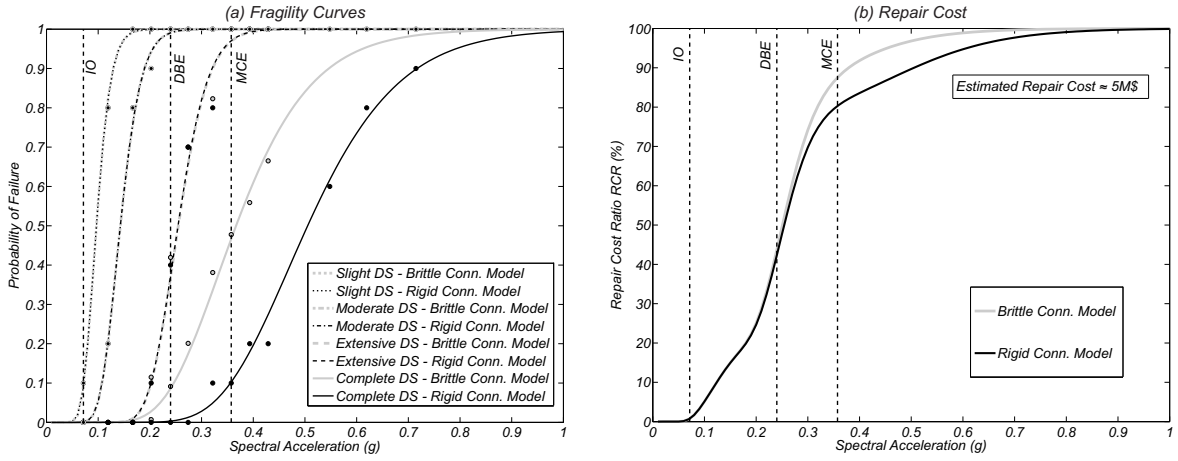

Figure 4.30: LA9 building - fragility curves and repair cost ratio (RCR) estimation

Table 4.7: Fragility curves parameters associated with LA9 building

	Brittle Conn. Model		Rigid Conn. Model		Uncertainty Summary	
Damage State	θ	β	θ	β	β_{RTR}	β_{Conn}
Slight	0.10	0.23	0.10	0.23	0.23	0.00
Moderate	0.14	0.22	0.14	0.22	0.22	0.00
Extensive	0.25	0.18	0.25	0.18	0.18	0.00
Complete	0.37	0.31	0.51	0.27	0.27	0.04

4.10 Conclusion

This chapter is focused on the response assessment of steel moment resisting frames (SMRF) designed according to pre-Northridge codes. During the 1994 Northridge and 1995 Kobe earthquakes many brittle fractures were observed, indicating that these type of structures may be vulnerable to this type of failure. Pre-Northridge buildings represent a large fraction of the existing buildings in the US. Although several experimental and numerical studies have been developed, this chapter adds on the current state of the art on two main points: (i) a new model, that uses finite-length plastic hinge (FLPH) elements to simulate member behavior and concentrated plastic hinge (CPH) springs as fracture elements, is proposed allowing for complete separation of member response and connection response; (ii) the influence of uncertainty on connection capacity on building performance is separated from that associated with earthquake record-to-record (RTR) variability.

In order to validate the proposed model, numerical analysis are executed in order to compare results obtained with the proposed modeling approach and force-displacement relationships obtained in five experimental tests. Although the significant capabilities of the proposed modeling approach, one main limitation is the fact that it is not able to capture low-cycle fatigue fractures. After validating the model, a probabilistic assessment of the performance of two SMRF buildings subjected to various earthquake ground motions is performed. The 3- and the 9-story Los Angeles SAC buildings, which were designed according to pre-Northridge codes [138] are used in this chapter. The drift demands for each structure modeled with brittle beam-column connections are compared with the results for the structure modeled with perfectly rigid connections. Comparison includes median drift results obtained for the various intensity levels, fragility analysis and the repair cost ratio (RCR) with brittle and rigid connection response.

Results obtained in this chapter show that the consideration of brittle beam-column connection lead to significantly larger drift demands. For the 3-story building, an increase of 100% is obtained for the Maximum Considered Earthquake intensity level, whereas for the for 9-story building this increase is much lower (around 20%) which is due to capacity to distribute damage among the building's connections. This increase in drift demands leads to an increase in the computed probability of exceedance of predefined damage states and, consequently, to higher repair costs. Although further work is needed, important numerical and statistical measures are provided in this chapter for the development of future probabilistic studies, which may or may not account for brittle connections.

Future work is also needed in estimating the fracture rotation of the top beam-flange connection, for example through laboratory tests of MRF connections with slabs.

4.11 Dissemination

This part of the research program resulted in the following outputs:

1. Oral presentation made at the National Conference on Seismology and Earthquake Engineering (Sismica 2016) held in Azores in May 2016

   Scope: In this paper, bilinear models accounting for strength and stiffness deterioration of both beams and beam-column connections of pre-Northridge steel moment frames are studied. Results obtained using OpenSees show that consideration of brittle beam-column connections leads to significantly different fragility functions and larger repair costs for intensities and damage beyond the design basis earthquakes.

   Complete reference: Ribeiro, F., Barbosa, A., and Neves, L. (2016). "Fragility and Loss Assessment of Pre-Northridge Steel Moment Frames Using the OpenSees Framework". In: National Conference on Seismology and Earthquake Engineering (Sismica 2016). Ponta Delgada, Azores.

Chapter 5

Influence of Ground Motion Duration on Structural Damage

5.1 Scope

The accurate assessment of structural response is of paramount importance in PBEE methodologies. Due to this fact, it is fundamental to develop numerical models able to simulate structural response, including deterioration mechanisms, is fundamental. In spite of this, accurate assessment of structural response also relies on the proper definition of the ground motion. Among the parameters involved in ground motion definition, ground motion duration is a key parameter for many regions of the globe. Developed studies have shown that ground motions with different duration may lead to significantly different structural performance, which may influence the residual structural capacity to face post-earthquake events. However, consensus has not been reached in what concerns the influence of ground motions duration on deformation and hysteretic energy dissipated.

This Chapter presents an analytical study evaluating the influence of ground motion duration on structural damage of 3-, 9-, and 20-story SAC steel moment resisting frame (SMRF) buildings designed for downtown Seattle, Washington, USA, using pre-Northridge codes. Results indicate that the duration of the ground influences, above all, the combined damage measures, although some effect on drift-based response measures is also observed for larger levels of drift. These results indicate that since the current assessment methodologies do not capture the effects of ground motion duration, both performance-based and code-based assessment methodologies should be revised to consider damage measures that are sensitive to duration.

5.2 Introduction

Ground motion records used in PBEE must be representative of the seismic hazard of the site. Although different hazard sources can significantly contribute to the seismic action, for decades, research focused on the effects of short duration shallow crustal ground motions on the response of structures since there was a lack of ground motion records from other sources. The study of structural performance under different hazard sources, for example under subduction zone ground motions, have been performed only in the last decade.

The objective of this Chapter is to better understand differences in structural damage

on 3-, 9-, and 20-story ductile steel moment resisting frames (SMRF) when subjected to long duration or short duration earthquake ground motions. The SMRFs are part of the SAC steel project and correspond to buildings located in Seattle, Washington, designed using pre-Northridge codes. These three buildings are representative of the design practice in the US for decades, and the conclusions of this work can be significant in the assessment/retrofit of thousands of buildings. Two-dimensional nonlinear finite element models of the buildings are developed in the Open System for Earthquake Engineering Simulation, OpenSees [132], are validated against data available in the literature [77].

A database of 44 ground motions was used to assess the combined influence of ground motion duration and spectral acceleration on structural response. To isolate the effects of duration, 10 spectrally equivalent ground motion pairs, where shallow crustal records are scaled to have approximately the same response spectra of the corresponding subduction zone records, are selected from the initial database following a procedure proposed in Chandramohan et al. [171]. Structural response is investigated in terms of deformation, energy dissipation, number of inelastic cycles, and damage state. Structural damage is assessed using incremental dynamic analysis for each ground motion and the results are compared at at least twenty intensity levels.To track damage, the Park and Ang [75] and Reinhorn and Valles [76] damage indices are used. The results show that buildings with different number of stories display different deformation and energy dissipation distributions that significantly affect their post-earthquake structural damage.

5.3 Literature Review

There are several subduction zones around the world [172], where megathrust earthquakes may occur (e.g., the US Cascadia region in the Pacific Northwest or the Gorringe Ridge close to Portugal in the Atlantic Ocean). Large subduction zones earthquakes have been responsible for generating long duration ground motions such as the 2011 Great East Japan Earthquake (Tohoku, Japan, Mw 9.0), the 2010 Chile earthquake (Maule, Chile, Mw 8.8), and the 2004 Sumatra-Andaman Earthquake (Mw 9.1, 2004). The damage induced by these earthquakes shows that the structural performance observed is significantly different from that predicted with crustal earthquakes.

As opposed to large subduction zone earthquakes, shallow crustal motions are typically shorter in duration and have higher frequency content when compared to the subduction zone motions. The effect of earthquake duration on civil engineering has been addressed only in the last decades, and consensus within the scientific community is yet to be reached [173]. For example, the effect of earthquake duration on liquefaction [174] and slope instability [175] has been shown to be significant, where the longer ground motions produce increased damage and larger collapse risks. However, previous studies on the sensitivity of structural response measures to ground motion duration reported mixed results [50,176,177]. For decades, research focused on the effects of shallow crustal ground motions on the response of structures since there was a lack of ground motion records for large magnitude subduction events. The results of the research on the structural response to shallow crustal motions, along with the mixed findings of some studies on ground motion duration, made its way into seismic design code provisions currently used in the design and assessment of building and bridge structures [178]. Thus, to date, since bridges and buildings have not been designed considering explicitly the effect of ground motion duration,

the response and expected damage under long duration (subduction) earthquakes is largely unknown, making this a very important topic that requires further investigation.

Among the works available in the literature that address the effect of duration on structural response, the main observations can be classified into two groups. First, studies that employ response measures based on peak displacement demands, such as peak drift ratios, generally do not find strong correlations between duration and the magnitude of the response (e.g., [173,179]). Iervolino et al. [179] concluded that duration of ground motion is statistically insignificant to displacement ductility and cyclic ductility demand. Hancock and Bommer [173] analyzed an 8-story RC wall-frame building that was subjected to 30 accelerograms with different durations. Results in Hancock and Bommer [173] indicate that duration has no influence on peak drift-based measures, such as peak inter-story drift ratio (IDR). However, results indicate a significant correlation exists between ground motion duration and cumulative response measures, such as fatigue damage. Second, studies that employ cumulative response measures, such as number of inelastic cycles, cumulative inelastic strains, and hysteretic energy dissipated, find a positive correlation between ground motion duration and structural response measures (e.g., [180–182]). Results in the second group of studies, indicate that larger energy demands are observed for longer duration ground motions, thus causing collapse at lower intensities [182]. These conclusions are also supported by Iervolino et al. [179], Ruiz-Garcia [183] and Song et al. [184].

Although these last three recent studies indicate that the usual approach for duration independent seismic design and assessment may lead to an overestimation of the structural capacity to withstand long duration strong ground motions, the cumulative damage induced by the ground motion has been shown to be dependent on the amplitude, source-to-site distance, fault type, as well as the duration of the ground motion, thus is not trivial to decouple the specific influence of duration. In addition, studies on the influence of ground motion duration on structural performance have been developed, until recently, using shallow crustal ground motions records [179,185], thus not explicitly considering long duration subduction zone motions. However, the difference between the subduction and crustal earthquakes lies, not only on the duration, but also on the frequency content. Even though the crustal ground motions are associated with a rapid and abrupt energy release [186], Tremblay [187] suggests that the longer duration, number of cycles, and energy dissipation, associated with subduction zone ground motions tend to induce more severe consequences. Due to the increase in available data from recent subduction zone earthquakes, mainly from Japan and Chile, ground motion records from large subduction zone megathrust earthquakes are now being used [182,188–190]. To isolate the effect of ground motion duration, Foschaar et al. [189] for example, selected ground motions with similar spectral shape and studied the relationship between the response and different intensity measures of ground motion duration.

A comprehensive study on the influence of ground motion duration on structural damage is developed in this work. The accurate simulation of the structural damage recorded during an earthquake is fundamental to capture the residual capacity of the structure to withstand cascading events.

5.4 Ground Motion Selection

Subduction earthquake motions were selected from databases that include earthquake records from the 2011 Great East Japan Earthquake [191], the 2010 Santiago, Chile earthquake

[192], the 1985 Valparaiso, Chile earthquake, the 2010 Southern Peru earthquake, and the 1989 Chi-Chi, Taiwan earthquake. It is worth noting that due to the high-frequency site effects, amplifications in the 2011 Great East Japan Earthquake records are expected to be greater than those adopted in the U.S. based on NEHRP site class [193]. Twenty-two ground motions obtained from these databases had to be filtered and baseline corrected [194]. For each of these long duration records a corresponding short duration record with significant duration, D_{5-75}, shorter than 25 s, and having a closely matching response spectrum was chosen from the PEER NGA-West2 database [195]. The spectral ordinates of each short duration record were then scaled, such that the mean spectral ordinates of the scaled record were similar to those of the long duration record. Among all candidate short duration records that had not already been selected, the one with the lowest sum of squared errors was chosen. The complete ground motion database is presented in Table 5.1. The characteristics of these ground motion records are shown in Figure 5.1, namely in terms of moment magnitudes and source-to-site distance for each ground motion, as well as, peak ground acceleration, PGA, and the significant duration, D_{5-75}, which are detailed in Kramer [196]. Figure 5.1(a) shows the distribution of earthquake ground motions as a function of the ground motion duration, D_{5-75}. Figures 5.1(b) to 5.1(d) show the relationship between D_{5-75} and ground motion magnitude, source-to-site distance, and PGA, along with the correlation coefficients. These are the linear Pearson correlation coefficient, which corresponds to the squared root of the determination coefficient (R^2), and the Spearman correlation coefficient, which is a ranks coefficient and thus independent of the type of distribution. These Figures show that, although determination coefficients are not very large, a correlation between ground motion duration and magnitude, distance and PGA exist.

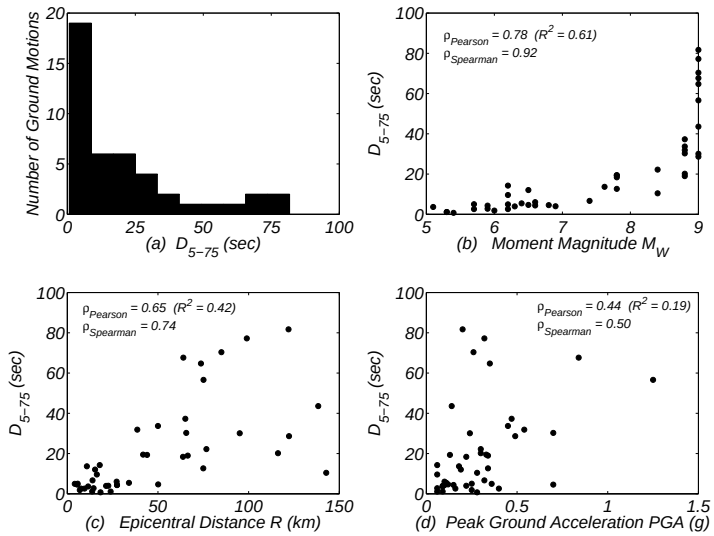

Figure 5.1: Ground motion records characteristics and correlation

Figure 5.2 shows the relationship between spectral acceleration at the fundamental period of the three buildings and ground motion duration. Figures 5.2(a) and 5.2(c) indicate that correlation between these two measures, although weak, can not be neglected as a trend can be observed graphically. In the interest of isolating duration effect on structural response, the comparison is based on ground motion pairs with similar response spectra.

The selecting and scaling procedure is independent of the hazard at any site. However, for reference the Seattle MCE values are shown in Figure 5.2 for each building.

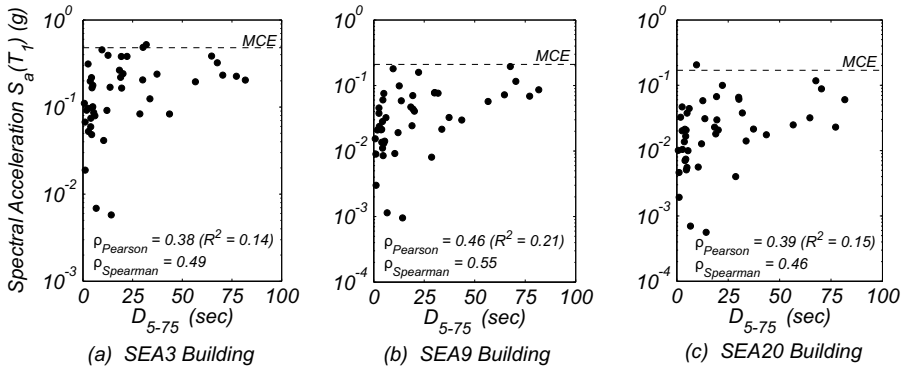

Figure 5.2: Ground motion spectral acceleration at the fundamental period of the intact structures versus significant duration for: (a) SEA3 Building; (b) SEA9 Building; and (c) SEA20 Building

These 44 ground motion records are used to first assess the influence of both ground motion intensity and duration in the structural response and attained damage. Second, in order to decouple effect of duration from that related to intensity, ground motion pairs were defined following Chandramohan *et al.* [171], to guarantee that both types of ground motions are spectrally equivalent. In this second analysis, 10 ground motion pairs are considered. Figure 5.3 shows the response spectra for the 10 crustal and 10 subduction zone motions. The 10 selected shallow crustal ground motions and subduction zone ground motions are underlined in Table 5.1. Table 5.1 also lists the scale factors SF applied to the crustal motions response spectra. These factors are computed as to minimize the mean squared error of the logarithmic 5%-damped linear response spectral acceleration associated with each pair of subduction and crustal motions in the period range of interest of each building. The ratio between the spectral accelerations ($S_a(T_i)$, where T_i are the list of discretized periods of the response spectra) for each of the ten pairs of subduction/crustal ground motion ranges between 0.44 to 2.46 (SEA3: 0.54-2.46, SEA9: 0.44-2.28, SEA20: 0.46-2.37) across the period range of interest for the spectral response. The period range of interest is defined as $0.2T_1$ to $1.5T_1$, where T_1 is the fundamental period of the structure after application of the gravity loads.

Figure 5.3 shows a comparison between the response spectra associated with the Subduction Zone and Shallow Crustal ground motions sets. Figures 5.4 and 5.5 show two ground motion pairs scaled to be used with SEA9 and SEA20 buildings, respectively. These figures show a very good agreement between the individual response spectra for the two types of ground motions. For other pairs of ground motion and buildings, similar results are obtained, but not shown here in the interest of brevity. Moreover, median spectra of the long duration and short duration sets are, consequently, very similar. The median spectrum of the two sets of ground motions associated with the SEA3 building is shown in Figure 5.6. This similarity between the response spectra of the two types of earthquake ground motions is key in this study so that the effects of duration can be isolated from ground motion spectral response parameters.

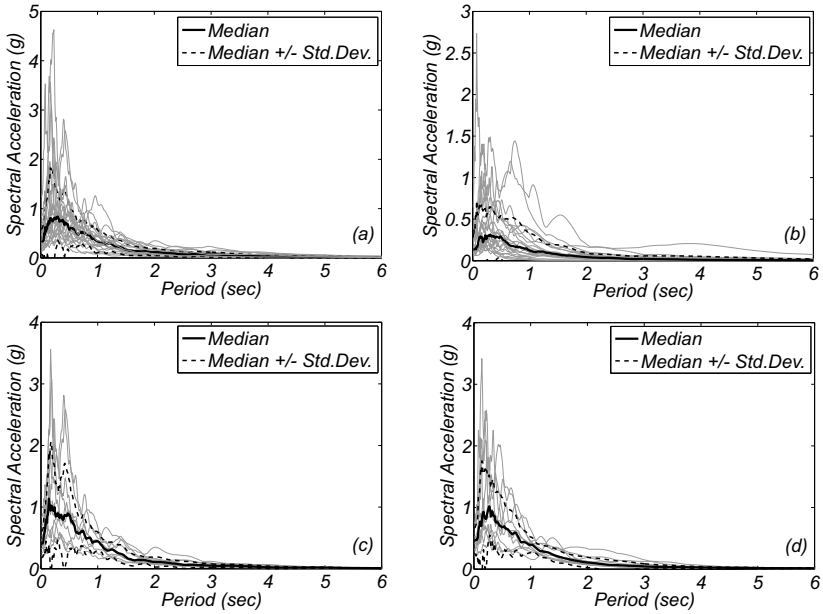

Figure 5.3: Comparison of the response spectra associated with the Subduction Zone and Shallow Crustal ground motion sets: (a) unscaled Subducton ground motions; (b) unscaled Crustal ground motions; (c) selected 10 Subduction ground motions (unscaled); and (d) selected and scaled Crustal ground motions.

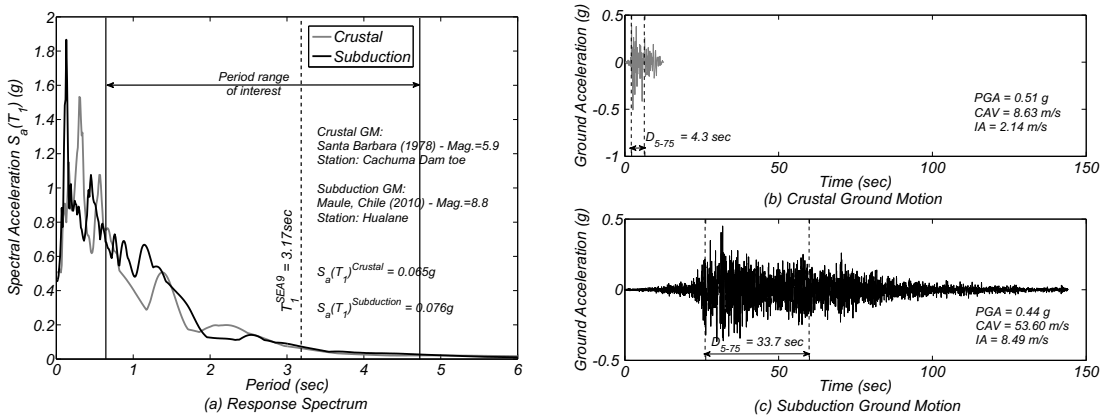

Figure 5.4: SEA9 Building: Comparison of the Suduction Zone and Shallow Crustal ground motion pair number 8: (a) Response Spectra; (b) Shallow Crustal Ground Motion; and (c) Subduction Zone Ground Motion

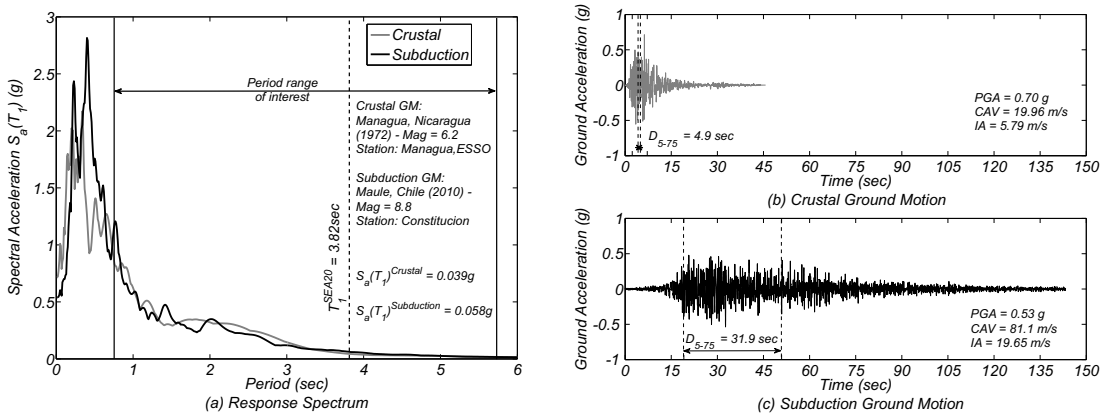

Figure 5.5: SEA20 Building: Comparison of the Suduction Zone and Shallow Crustal ground motion pair number 6: (a) Response Spectra; (b) Shallow Crustal Ground Motion; and (c) Subduction Zone Ground Motion

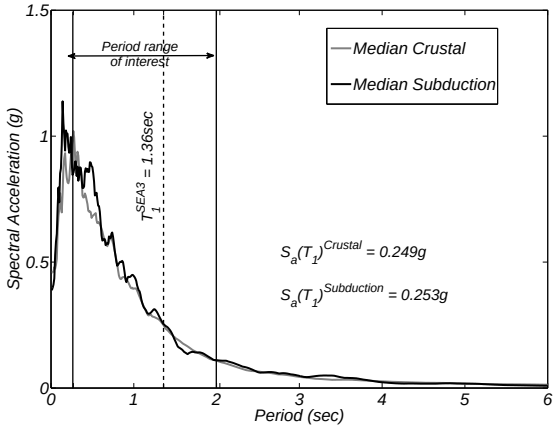

Figure 5.6: SEA3 Building: Comparison of the Median Acceleration Response Spectra of the Subduction Zone and the Shallow Crustal Selected Ground Motions

Table 5.1: Database of Shallow Crustal and Subduction Zone Earthquake Ground Motions

Pair	Subduction								Crustal										
	Earthquake	Year	Station	Comp.	Mag.	R (km)	PGA (g)	D5-75 (s)	Earthquake	Year	Station	Comp.	Mag.	R (km)	PGA (g)	D5-75 (s)	SF SEA 3	SF SEA 9	SF SEA 20
1	Valparaiso (Chile)	1985	El Almendral	L	7.8	63.8	0.22	18.3	Chalfant Valley-02	1986	Zack Brothers Ranch	360	6.2	7.6	0.40	2.6	0.73	0.68	0.58
2	Valparaiso (Chile)	1985	Llolleo	L	7.8	41.8	0.33	19.4	Livermore-02	1980	San Ramon-East. Kodak	180	5.4	18.3	0.28	0.7	1.47	2.04	1.92
3	Valparaiso (Chile)	1985	Laligua	200	7.8	44.0	0.13	19.3	Mammoth Lakes-02	1980	Convict Creek	90	5.7	9.5	0.16	2.6			
4	Valparaiso (Chile)	1985	San Fernando	EW	7.8	75.0	0.34	12.6	Gazli, USSR	1976	Karakyr	0	6.8	5.5	0.70	4.6			
5	Maule (Chile)	2010	Angol	EW	8.8	65.6	0.70	30.2	Irpinia, Italy-01	1980	Brienza	0	6.9	22.6	0.22	4.0	3.38	3.04	2.88
6	Maule (Chile)	2010	Constitucion	L	8.8	38.6	0.54	31.8	Managua, Nicaragua-01	1972	Managua, ESSO	90	6.2	4.1	0.36	4.9	1.99	1.94	1.92
7	Maule (Chile)	2010	Curico	NS	8.8	65.1	0.47	37.2	Coalinga-01	1983	Parkfield - St. Corral 3E	90	6.4	34.0	0.11	5.4	5.00	5.00	5.00
8	Maule (Chile)	2010	Hualane	T	8.8	50.0	0.45	33.7	Santa Barbara	1978	Cachuma Dam Toe	250	5.9	27.4	0.10	4.3	5.00	5.00	5.00
9	Maule (Chile)	2010	Papudo	L	8.8	116.2	0.30	20.1	Lytle Creek	1970	Cedar Springs Pmp.	126	5.3	23.9	0.06	1.1			
10	Maule (Chile)	2010	Vina del Mar	EW	8.8	66.4	0.34	18.9	San Fernando	1971	Lake Hughes No.1	21	6.6	27.4	0.15	4.4			
11	Tohoku (Japan)	2011	Miyakoji	EW	9.0	64.0	0.84	67.6	Parkfield-02, CA	2004	Parkfield-Cholame 5W	90	6.0	6.9	0.25	1.8	2.79	2.38	2.43
12	Tohoku (Japan)	2011	Takahata	EW	9.0	122.0	0.20	81.7	Coyote Lake	1979	Gilroy Array No4	360	5.7	5.7	0.25	5.0	0.83	0.87	1.03
13	Tohoku (Japan)	2011	Fukushima	EW	9.0	99.0	0.32	77.2	Friuli, Italy-02	1976	San Rocco	0	5.9	14.5	0.06	2.8	3.82	3.93	3.99
14	Tohoku (Japan)	2011	Iwanuma	EW	9.0	85.0	0.26	70.3	L'Aquila, Italy	2009	Celano	NS	6.3	21.4	0.09	3.9	3.42	2.95	2.76
15	Tohoku (Japan)	2011	Tsukidate	EW	9.0	75.1	1.25	56.6	Imperial Valley-06	1979	Compuertas	15	6.5	15.3	0.19	12.1			
16	Tohoku (Japan)	2011	Sakura	NS	9.0	122.3	0.49	28.6	Tabas, Iran	1978	Dayhook	L	7.4	13.9	0.32	6.7			
17	Tohoku (Japan)	2011	Haga	EW	9.0	95.1	0.24	30.0	Parkfield	1966	Cholame-Shandon No.12	50	6.2	17.9	0.06	14.3			
18	Tohoku (Japan)	2011	Chiba	EW	9.0	138.4	0.14	43.6	San Francisco	1957	Golden Gate Park	10	5.3	13.7	0.09	1.1			
19	Tohoku (Japan)	2011	Hirata	NS	9.0	73.7	0.35	64.7	Hollister-03	1974	Hollister City Hall	181	5.1	11.5	0.09	3.7			
20	Southern Peru	2010	Moquegua	EW	8.4	76.7	0.30	22.2	San Fernando	1971	Pasadena-CIT Ath.	0	6.6	27.2	0.10	6.0			
21	Southern Peru	2010	Arica Casa	NS	8.4	142.8	0.28	10.4	Imperial Valley-06	1979	Coachella Canal No.4	L	6.5	50.1	0.12	4.7			
22	Chi-Chi (Taiwan)	1999	CWB ALS	NS	7.6	10.8	0.18	13.6	Irpinia, Italy-02	1980	Bisaccia	0	6.2	16.3	0.06	9.6			
μ								36.8								4.8	2.77	2.78	2.69
σ								22.6								3.4	1.63	1.60	1.57
min								10.4								0.7	0.46	0.34	0.28
max								81.7								14.3	5.00	5.00	5.00

5.5 Building Models

5.5.1 Modeling Description

The steel moment resisting frame (SMRF) buildings studied are a 3-, a 9-, and a 20-story building (denoted SEA3, SEA9, and SEA20, respectively), which were designed for Seattle, WA, as part of the SAC steel project [77] using pre-Northridge codes [138], considering a site class S2 similar to site class D [101]. In the buildings under analysis, the external frames were designed to resist the lateral (seismic) loads and the interior frames were designed as gravity frames. As shown in Figure 5.7, the three-story building presents no basement, while the nine- and 20-story buildings have one and two basement levels, respectively. The height of the frames is constant and equal to 3.96m, except for the two taller buildings, which have a first level with a height of 5.49m. A detailed description of the buildings is available in Gupta and Krawinkler [101].

Two-dimensional centerline nonlinear finite element models of a N-S external frame of each of the three buildings are developed in the Open System for Earthquake Engineering Simulation (OpenSees) [132] and used for the structural analysis. A strong-column weak-beam ductile behavior is assumed for all structures. Brittle mechanisms and connection fracture modes are not considered. Geometric nonlinearities are accounted for during the analysis by considering a P-Δ leaning column. A rigid diaphragm is assumed for each floor. Soil-structure interaction is not considered. Floor masses are applied to beam-column joints whereas loads are applied to beam-columns joints and beam spans following the distribution of loads used by Luco [139]. Rayleigh damping proportional to the mass and to committed stiffness is assigned to the models considering a damping ratio of 2% at the fundamental period T_1 of the intact structure of each building (shown in Table 6.2) and at $T = 0.2$ sec for SEA3 and SEA9 buildings, and the fifth mode ($T_5 = 0.43$ sec) for SEA20.

Two variations of a nonlinear finite element model are developed in OpenSees for the buildings. In both models, columns are modeled using nonlinear force-based fiber-section beam-column elements in which an elasto-plastic constitutive law with a 3% kinematic hardening is assigned to each fiber. Beams are modeled using the force-based finite length plastic-hinge beam-column formulation presented in Chapters 2 and 3, which models plastic hinge length explicitly and separates the behavior of beam in the span from that of beam-column connections. Both models use the modified Gauss-Radau integration scheme.

The difference between the two models lies in the modeling of the plastic-hinge employed for beams, which can be: (i) an elasto-plastic with hardening constitutive law; or (ii) bilinear model with strength deterioration (Bilin model presented in Chapter 3). Here the first model is labeled FMRH (Finite-length Modified Gauss-Radau with Hardening), while the second model is labeled FMRB (Finite-length Modified Gauss-Radau with Bilin Model).

Axial and shear behavior is assumed to be linear elastic. Joint shear deformations and connection fracture are not considered in this chapter.

5.5.2 Model Validation

The model validation performed here includes the comparison of results of nonlinear static pushover analysis and periods of the buildings models developed here using OpenSees with the FEMA355 M1 models [77]. The building periods available associated with the FEMA355 M1 models correlate well with the ones obtained in the FE models developed

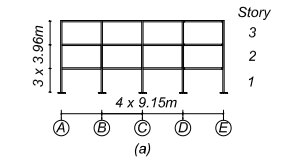

Story	Columns			Beams					Mass (kg)
	Exterior	Interior	Model	Section	Model	θ_p (rad)	θ_{pc} (rad)	$\Lambda=E_{sc}/M_y$	
1	W14x159	W14x176	NL-FB-H	W24x76	NL-FMRB	0.019	0.116	0.889	$9.58x10^5$
2	W14x159	W14x176		W24x84		0.021	0.131	1.029	$9.58x10^5$
3	W14x159	W14x176		W18x40		0.030	0.149	0.852	$1.04x10^6$

(b)

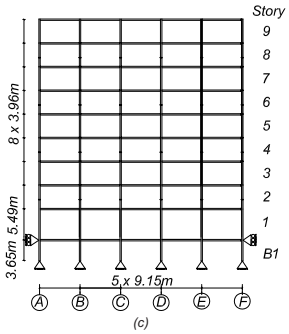

Story	Columns		Beams					Mass (kg)
	Section	Model	Section	Model	θ_p (rad)	θ_{pc} (rad)	$\Lambda=E_{sc}/M_y$	
B1	W24x229	NL-FB-H	W30x108	NL-FMRB	0.017	0.110	0.871	-
1	W24x229		W30x108		0.017	0.110	0.871	$1.01x10^6$
2	W24x229/ W24x229		W30x116		0.018	0.122	0.978	$9.92x10^5$
3	W24x229		W30x108		0.017	0.110	0.871	$9.92x10^5$
4	W24x299/ W24x207		W27x94		0.018	0.112	0.873	$9.92x10^5$
5	W24x207		W27x94		0.018	0.112	0.873	$9.92x10^5$
6	W24x207/ /W24x162		W24x76		0.019	0.116	0.887	$9.92x10^5$
7	W24x162		W24x76		0.019	0.116	0.887	$9.92x10^5$
8	W24x162/ W24x131		W24x62		0.122	0.019	0.889	$9.92x10^5$
9	W24x131		W24x62		0.122	0.019	0.889	$1.07x10^6$

(d)

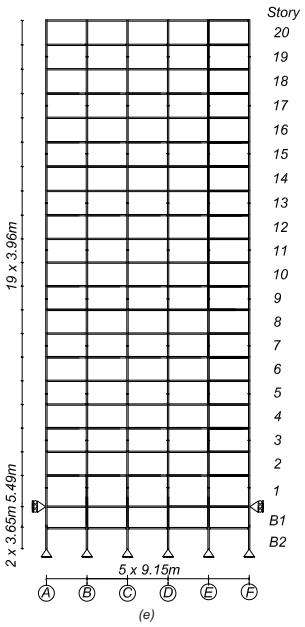

Story	Columns		Beams					Mass (kg)
	Section	Model	Section	Model	θ_p (rad)	θ_{pc} (rad)	$\Lambda=E_{sc}/M_y$	
B2	W24x229	NL-FB-H	W12x14	NL-FMRB	0.038	0.114	0.602	-
B1	W24x229		W30x132		0.019	0.150	1.252	-
1	W24x229/ W24x229		W30x132		0.019	0.150	1.252	$5.64x10^5$
2	W24x229		W30x132		0.019	0.150	1.252	$5.52x10^5$
3	W24x229/ W24x229/		W30x132		0.019	0.150	1.252	$5.52x10^5$
4	W24x229		W30x132		0.019	0.150	1.252	$5.52x10^5$
5	W24x229/ W24x192		W30x132		0.019	0.150	1.252	$5.52x10^5$
6	W24x192		W30x132		0.019	0.150	1.252	$5.52x10^5$
7	W24x192/ W24x192		W30x132		0.019	0.150	1.252	$5.52x10^5$
8	W24x192		W30x116		0.018	0.127	1.026	$5.52x10^5$
9	W24x192/ W24x192		W30x116		0.018	0.127	1.026	$5.52x10^5$
10	W24x192		W27x114		0.020	0.151	1.264	$5.52x10^5$
11	W24x192/ W24x192		W27x114		0.020	0.151	1.264	$5.52x10^5$
12	W24x192		W27x94		0.017	0.118	0.927	$5.52x10^5$
13	W24x192/ W24x162		W27x94		0.017	0.118	0.927	$5.52x10^5$
14	W24x162		W27x94		0.017	0.118	0.927	$5.52x10^5$
15	W24x162/ W24x162		W27x94		0.017	0.118	0.927	$5.52x10^5$
16	W24x162		W24x62		0.019	0.128	0.953	$5.52x10^5$
17	W24x162/ W24x131		W24x62		0.019	0.128	0.953	$5.52x10^5$
18	W24x131		W21x57		0.022	0.151	1.125	$5.52x10^5$
19	W24x131/ W24x131		W21x57		0.022	0.151	1.125	$5.52x10^5$
20	W24x131		W21x57		0.022	0.151	1.125	$5.52x10^5$

(f)

NL-FB-H - ***N***onlinear ***F***orce-***B***ased Beam-Column Element with Fiber Section with 3% strain-***H***ardening
NL-FMRB - ***N***onlinear ***F***inite-***L***ength ***M***odified Gauss-***R***adau Beam-Column Element with ***Bi***linear Flexural Hinge Model

Figure 5.7: Two-Dimensional Models of Steel Moment Resisting Frames Buildings in Seattle : (a) SEA3 Building; (b) SEA3 Sections, Model Parameters, and Floor Masses; (c) SEA9 Building; (d) SEA9 Sections, Model Parameters, and Floor Masses; (e) SEA20 Building; (f) SEA20 Sections, Model Parameters, and Floor Masses

here, as shown in Table 5.2. The FEMA355 models were developed using *DRAIN-2DX* [149]. The elements used in the *DRAIN-2DX* models correspond to concentrated plastic hinge models with a linear P-M interaction surface for compressive axial loads greater than $0.15P_{max}$. $P-\Delta$ effects were considered through modeling of a leaning column. Thus, the main differences between the FEMA355 models and the ones developed here are: (i) columns are now modeled using fiber section distributed plasticity elements and therefore account explicitly for the P-M interaction; and (ii) finite-length plastic hinge are modeled in two different ways: (a) similar to the FEMA models, assuming that the hinges do not have strength and stiffness degradation (FMRH models); and (b) considering degradation through use of the ModIMK model (FMRB model).

Table 5.2: Periods of Vibration for OpenSees Models and FEMA355 Model

	SEA3 Building		SEA9 Building		SEA20 Building	
	OpenSees	FEMA355	OpenSees	FEMA355	OpenSees	FEMA355
1^{st} Mode	1.36	1.36	3.15	3.17	3.82	3.92
2^{nd} Mode	0.43	0.43	1.12	1.13	1.37	1.40
3^{rd} Mode	0.22	0.22	0.60	0.61	0.81	0.82

In all buildings the nonlinear static pushover analyses were performed assuming that the lateral load pattern applied is proportional to the 1^{st} mode of vibration of each structure.

Figure 5.8 shows the pushover curves for each of the three buildings and three finite element models (FMRH, FMRB, and FEMA355 M1 models). For reference, figures also show the design base shear quantified according to the allowable stress design method of the 1994 Uniform Building Code [138]. In Figure 5.8, for the SEA3 building, it can be observed that the pushover curve of the model that does not consider strength deterioration (FMRH) matches relatively well the pushover curve of the FEMA model. For the SEA9 building, a good match is also found up to approximately 6% of roof drift ratio (RDR). At this RDR, the moment gradient of the columns is substantially reduced due to simplified axial force-bending moment $P-M$ interaction surface considered in FEMA 355 M1 models, leading to a faster decrease in base shear. At this level of RDR (6%), the peak base shear has reduced by more than 80%, allowing for a validation of the model up to failure, if failure is described to correspond to the drift at which the strength capacity is reduced by 20% or more, as commonly assumed in earthquake engineering analyses. For the SEA20 building, significant differences are observed over the entire range. Such differences are expectable as a consequence of alternative modeling assumptions such as beam-column joint modeling.

In Figure 5.8(b), it can also be observed that the model FMRB, which considers the strength degradation in beams, has considerably greater strength deterioration. Note that the model has zero residual strength at about 6% RDR. Therefore, the results indicate that this model is valid until collapse, since it is only at this level of RDR that the column bending moment gradient would start playing an important role.

In summary, the model validation performed here is considered to be sufficient for the FMRH models. Although no direct validation of the FMRB models with experimental or numerical results is possible, the definition of component degradation is consistent with experimental results from a large database of component tests and P-M interaction is explicitly considered.

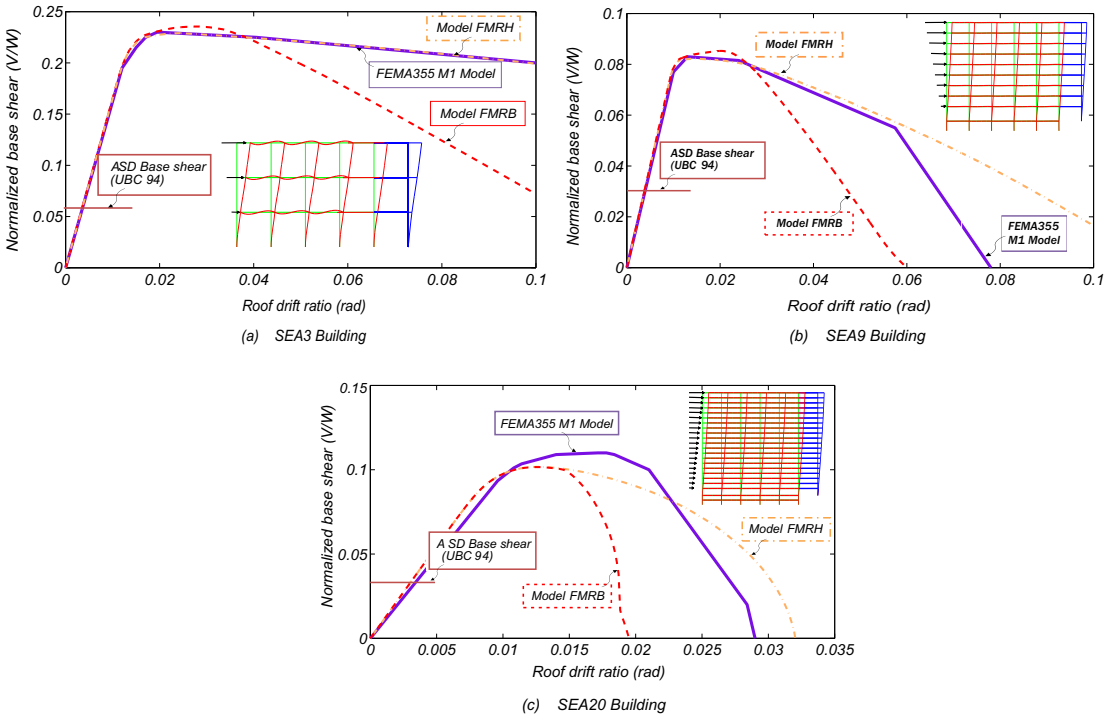

Figure 5.8: Nonlinear Static Pushover Capacity Curves Considering a 1^{st} Mode Lateral Load Pattern: (a) SEA3 Building; (b) SEA9 Building; (c) SEA20 Building

5.6 Analysis Methodology

Following model validation, first, the buildings are analyzed under all forty-four (44) ground motions described in Table 5.1 without considering any ground motion scaling. The objective of this first analysis is to evaluate the importance of duration on damage indices. However, results obtained in this first analysis are both dependent of duration, D_{5-75}, and ground motion intensity, $S_a(T_1)$. Then, a second analysis is performed in which two groups of ten (10) ground motions are scaled to identical intensities in IDA analysis [54] . This second analysis isolates the effect of ground motion duration, as for each intensity considered in the IDA analysis, the ground motions are selected to have identical response spectral values and shapes. IDA is performed at at least twenty intensity levels. Response measures recorded are the peak drift, residual drift, energy dissipated, and number of inelastic excursions at every beam section. The spectral acceleration at the fundamental period of the intact structure is taken as the intensity measure of the ground motions.

In this study, the damage indices are computed at the section level for each beam hinge and at the global level by aggregating the damage data for all beams. Structural damage is computed based on the performance of beams only, since these provide the largest contribution to the damage, as the design of these buildings was based on a strong column-weak beam concept. The section damage index is computed considering the curvature (χ) and moment (M) as the deformation (d) and strength (F) in Equations 1.10 and 1.11. The element damage index is taken as the maximum of the section damage index of both hinges in a beam element, which is modeled as a FLPH element.

If some conditions are met, namely a regular distribution of mass, strength and stiffness in plan and height, such as the case of the buildings considered herein, a global value of

the damage indices can be used to characterize damage in ductile members of steel frames [197]. Following the approach in IDARC2D [76], the damage index of the global structure is defined as the average of the element's damage indices weighted by their hysteretic energy dissipated, as:

$$DI^{structural} = \sum_{i=1}^{n_{element}} \lambda_{element,i} \times DI^{element,i} \tag{5.1}$$

where $DI^{element,i}$ is the damage index associated with element i and $\lambda_{element,i}$ is the ratio of the energy dissipated by element i to total element energy dissipated by all elements, given by:

$$\lambda_{element,i} = \frac{\int E_h^{element,i}}{\sum_{j=1}^{n_{element}} \int E_h^{element,j}} \tag{5.2}$$

where $\int E_h^{element,i}$ is the hysteretic energy dissipated by element i. If an element remains on an elastic state, its hysteretic energy dissipated is zero and according to Equations 5.1 and 5.2 it does not affect the structural damage index. On the other hand, if a single member has a damage index of 1.0 locally, the global index may not reach 1.0.

Using definitions in Equations 1.10 to 5.2, the following damage indices are recorded during the analysis: (i) damage index for each element, (ii) maximum element damage index over all floors, and (iii) structural damage index obtained through Equation 5.1. The second damage measure corresponds to the maximum among the damage indices computed for all beams and all floors. This value is intended to represent the damage state of the beam in worst condition. The value is saved regardless of the beam/floor where it was attained. The third and last measure corresponds to a hysteretic energy dissipated weighted average of the observed damage over all beams at all floor levels. For each of the twenty ground motion intensities considered in this study, median values are computed for each damage measure.

It is worth noting that, when the hysteretic energy dissipated, $\int E_h$, exceeded the reference low inelastic cyclic energy dissipation capacity defined by Reinhorn and Valles [76] (Equation 1.11) as $4 \times (d_u - d_y) \times M_y$, it is assumed that $DI_{RV} = 1.0$. Although non-converged analyses can be incorporated in the collapse risk assessment when a fragility/collapse analysis is performed [41], the scope of this study is to compare the structural damage due to shallow crustal and subduction zone earthquakes, thus non-converged analyses are ignored.

In all analyses, the Newmark average acceleration method was employed. A maximum time step of 0.002 sec was used during analysis. This time step was deemed sufficient following a convergence study where the accuracy of roof acceleration time-history response due to large intensity shaking was studied using five time steps between 0.01 sec and 0.00005 sec. It was observed that a time step of 0.002 sec produces negligible errors (when compared to a time step of 0.00005 sec) and no significant changes in the response are observed when smaller time steps are used. The Newton-Raphson method is used to solve the nonlinear system of dynamic equations of equilibrium at each time step. An iterative scheme, which reduces the time-step, changes the solving algorithm, or slightly increases the tolerance criterion when a convergence issue was found, was implemented in the OpenSees analysis procedure.

5.7 Preliminary Results and Damage Assessment Calibration

5.7.1 Unscaled Ground Motions

The structural response of the three buildings was initially evaluated using all the unscaled records present in the database. Figures 5.9 and 5.10 show the structural response in terms of peak interstory drift ratio and Park and Ang structural damage index $DI_{PA}^{structural}$ for the three buildings as a function of the spectral acceleration and significant duration. Figure 5.11 shows similar plots for the remaining damage indices ($DI_{RV}^{structural}$, $DI_{PA}^{max-member}$, and $DI_{RV}^{max-member}$) for the SEA3 building. In these figures forty-four points, associated with each performed analysis, are represented together with a multiple linear regression surface that best fits the data. Spectral acceleration is transformed so that the corresponding axis is in log-scale. In all figures a black line is also shown representing the maximum recorded response.

Figure 5.9 shows that there is a clear trend throughout all buildings. At first, for low values of spectral acceleration, there is no visible influence of ground motion duration on peak IDR. This is expected due to the existence of very few structural nonlinearities introduced by ground motions. Second, for intermediate spectral acceleration values the influence of ground motion duration increases as longer duration motions tend to induce larger peak IDR. Finally, for large intensity ground motions, long duration motions lead to significantly larger peak IDR. The coefficients of determination indicate that the performed multiple linear regression fit reasonably well the recorded data.

Figure 5.10 indicates that the trends identified in the previous figure hold for the case of this damage index for the three buildings. Since the obtained regression surfaces associated with the Park and Ang structural damage indices are similar for the three buildings, in Figure 5.11 results for the remaining damage indices are only represented for the SEA3 Building. In this Figure similar trends are identified. Comparison between $DI^{structural}$ and $DI^{max-member}$ shows that the influence of duration seems to be more relevant for the members.

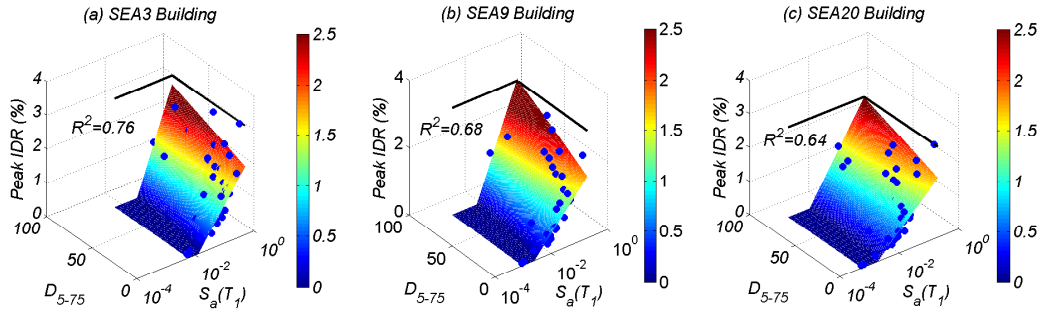

Figure 5.9: Peak interstory drift ratio as a function of the significant duration D_{5-75} and spectral acceleration $S_a(T_1)$ for the 44 unscaled ground motions for: (a) SEA3 Building; (b) SEA9 Building; and (c) SEA20 Building

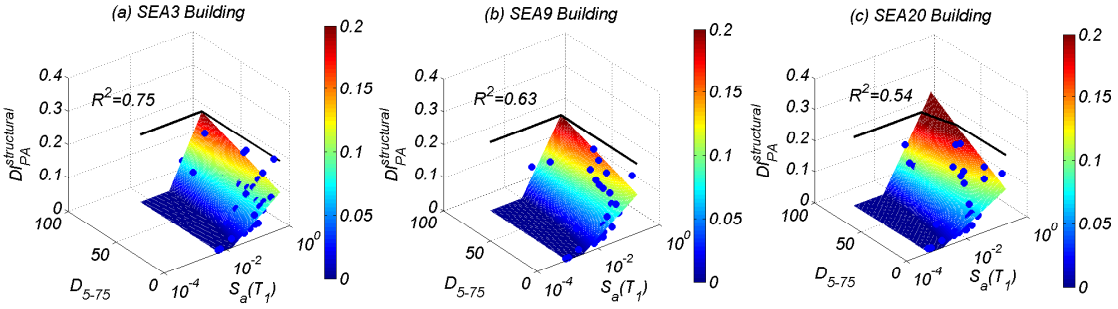

Figure 5.10: Park and Ang Structural Damage index $DI_{PA}^{structural}$ as a function of the significant duration D_{5-75} and spectral acceleration $S_a(T_1)$ for the 44 unscaled ground motions for: (a) SEA3 Building; (b) SEA9 Building; and (c) SEA20 Building

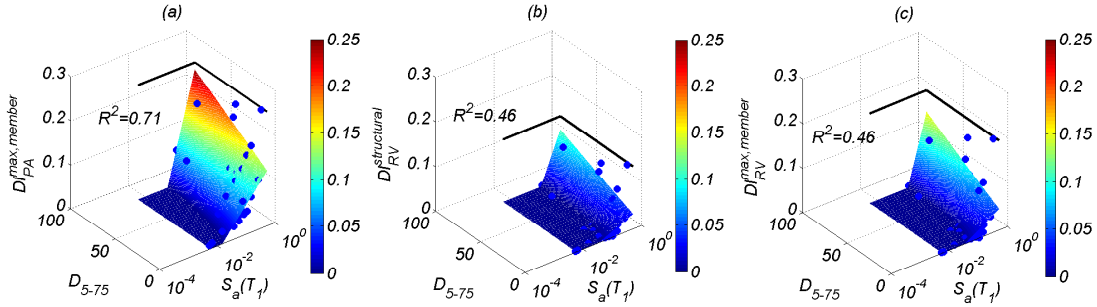

Figure 5.11: SEA3 Building: Damage indices as a function of the significant duration D_{5-75} and spectral acceleration $S_a(T_1)$ for the 44 unscaled ground motions: (a) Park and Ang maximum damage index $DI_{PA}^{max,element}$; (b) Reinhorn and Valles Structural Damage index $DI_{RV}^{structural}$; and (c) Reinhorn and Valles maximum damage index $DI_{RV}^{max,element}$

5.7.2 Scaled Ground Motions

The structural response of the three buildings was then evaluated using selected scaled ground motion pairs. Results of the spectrally equivalent earthquake pair number 6 for SEA3 and SEA20, and pair number 8 for SEA9 building are shown next. Figure 5.12 shows the time-history results for the SEA3 building in terms of IDR and ratio between energy dissipated and total energy dissipation capacity (E_h/E_{tot}) for a left most plastic hinge at each story level. This figure shows that the difference in the peak IDR is not significant, where 2.95% is observed for the shallow motion against 3.09% for the subduction motion. However, the difference in terms of energy dissipation in the beam of the upper floor is significant, being 5.6% for the shallow motion and 20.4% for the subduction motion. Figure 5.13 shows results for SEA9 building. Only results of floors 1, 7, 8, and 9 are shown as these are the most critical floors, where higher IDRs are attained and more energy is dissipated. This figure shows that a peak IDR of 3.17% is induced by the subduction motion, while a peak IDR of 1.65% is induced by the crustal motion. Simultaneously, energy dissipated is considerably different for all the beams. Energy dissipation ratio is 12.0% for the subduction motion, while only 2.11% is attained for the crustal motion for the upper floor beam. Finally, results for SEA20 building are shown in Figure 5.14, in which only the response of the most critical floors is presented. For the SEA20 building these are floors 1, 17, 18, and 19. This figure shows that a peak IDR of 2.35% is induced by the subduction motion, while a peak IDR of 2.14% is induced by the crustal motion. Moreover, the larger energy dissipation ratio is 14.95% for the subduction motion, while only 4.46% is attained for the crustal motion.

In summary, results in Figures 5.12 to 5.14 indicate that ground motion duration may be an important factor that needs to be considered. Moreover, in the next subsection, structural response of the three buildings is evaluated using IDA.

5.8 Deformation and Energy Demands

The results in this section were obtained using 10 ground motions pairs underlined in Table 5.1. In Figure 5.15 results for Incremental Dynamic Analysis (IDA) are shown for the three buildings. The intensity levels are chosen to guarantee that IDA structural failure is observed in all cases. This required twenty (20) intensity levels for SEA9 and SEA20 and twenty four (24) for SA3. In each figure, the median response is represented for the crustal and subduction ground motion sets. Overall, the median response is similar until approximately 4% peak IDR, up until which both types of earthquakes induce similar peak IDRs. Above the 4% peak IDR, the subduction ground motions seem to induce larger deformations than the crustal ground motions, for the same level of intensity, resulting in smaller spectral accelerations that cause collapse. This can be explained due to the concentration of damage, which is discussed in detail in the next paragraphs. It is worth noting that a similar trend was obtained by Tirca *et al.* [198] for concentrically braced steel frames.

The residual interstory drift ratio (RIDR) has been referred as a good measure of the cumulative damage achieved by the structure and, consequently, a good indicator of the post-earthquake resistant capacity [183]. Figure 5.16 shows the incremental dynamic analysis (IDA) curves for the RIDR. Obtained results indicate that, for low intensities of shaking, shallow crustal ground motions tend to induce larger RIDRs than long duration subduction zone ground motions. The tendency of the longer duration motions to reduce the RIDR

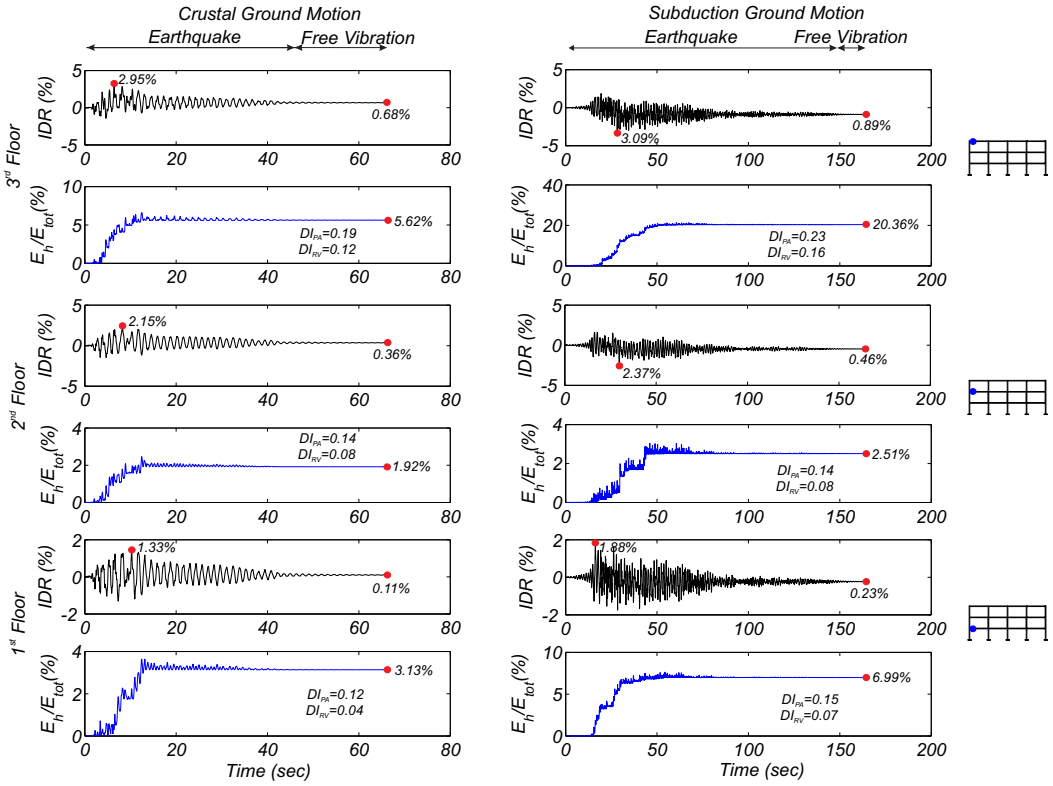

Figure 5.12: SEA3 Building: Response obtained with ground motion pair number 6 (with scaled crustal ground motion) in terms of Interstory Drift Ratio and ratio between energy dissipated and total energy dissipation capacity (E_h/E_{tot}) for a specific plastic hinge at each story level

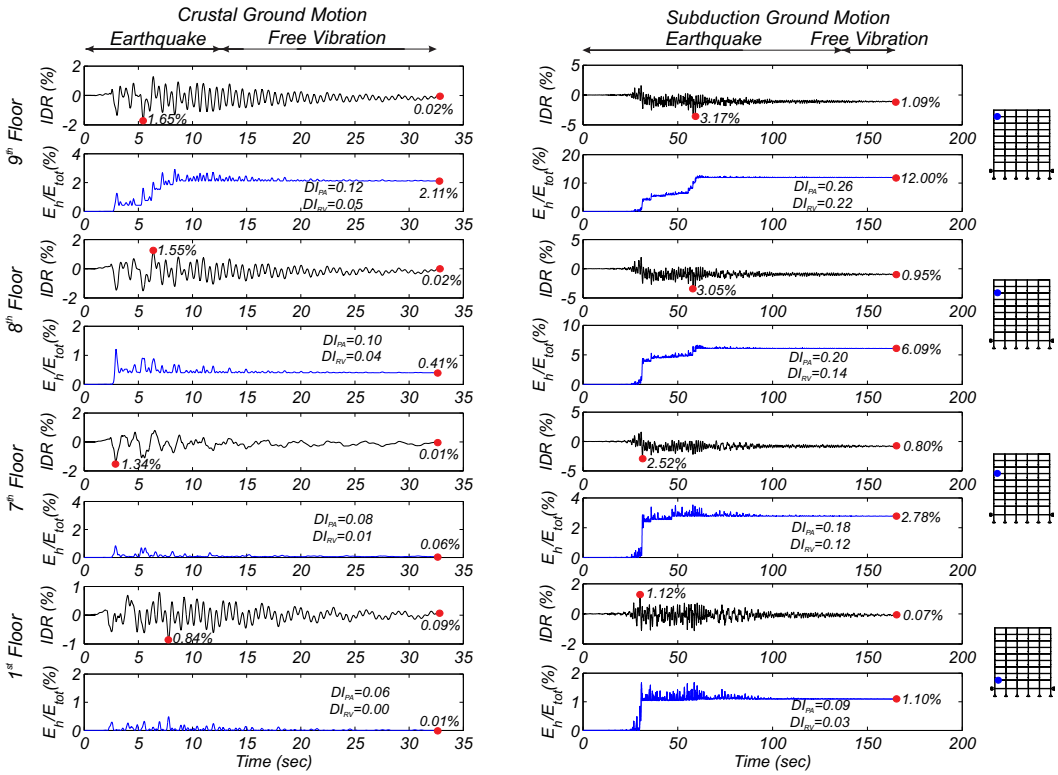

Figure 5.13: SEA9 Building: Response obtained with ground motion pair number 8 (with scaled crustal ground motion) in terms of Interstory Drift Ratio and ratio between energy dissipated and total energy dissipation capacity (E_h/E_{tot}) for a specific plastic hinge at each story level

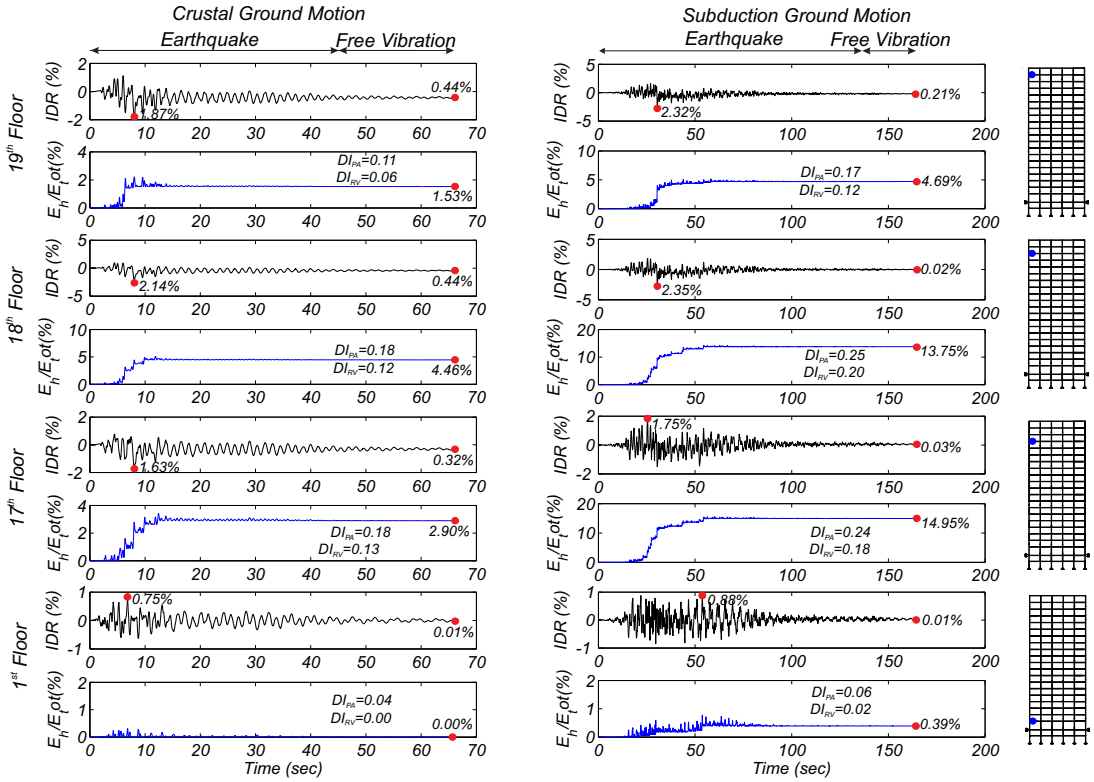

Figure 5.14: SEA20 Building: Response obtained with ground motion pair number 6 (with scaled crustal ground motion) in terms of Interstory Drift Ratio and ratio between energy dissipated and total energy dissipation capacity (E_h/E_{tot}) for a specific plastic hinge at each story level

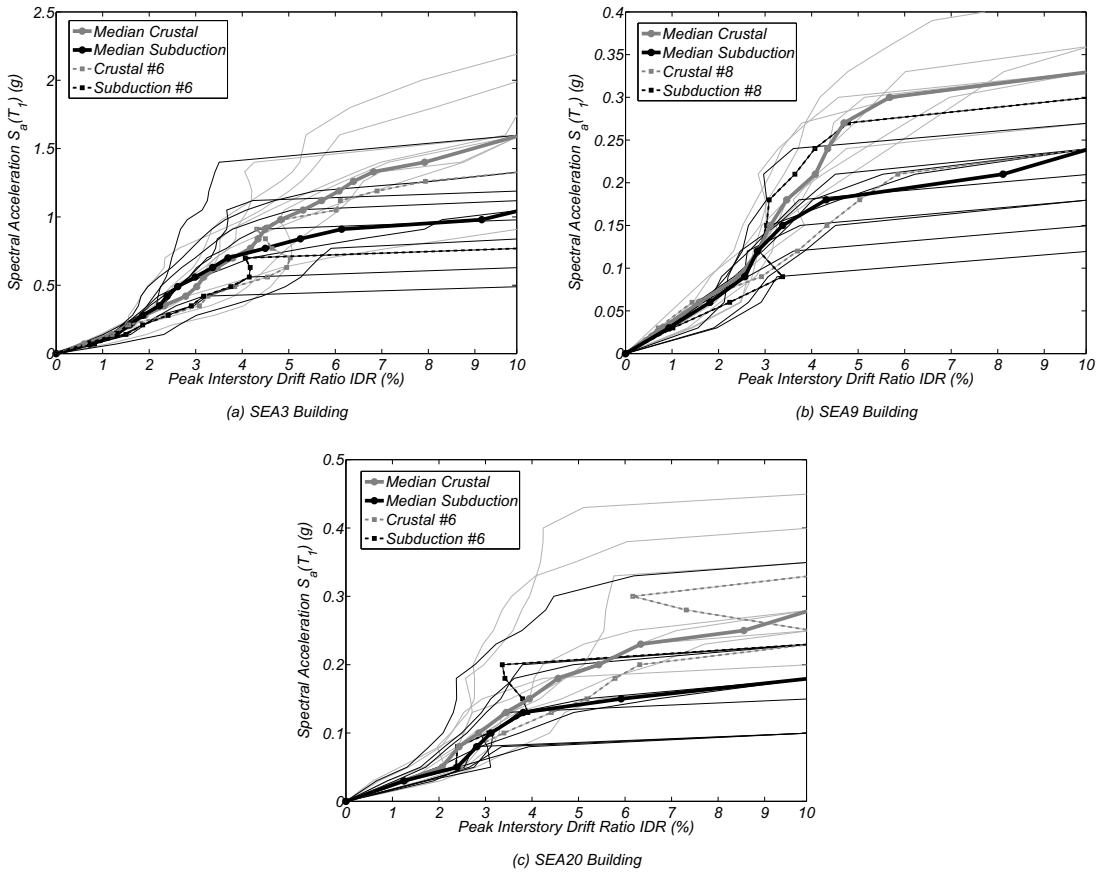

Figure 5.15: Peak Interstory Drift Ratio (Peak IDR) obtained through Incremental Dynamic Analysis: (a) SEA3 Building; (b) SEA9 Building; and (c) SEA20 Building

for lower intensities is thought to be related to the self-centering nature of the model.As the earthquake ground motion intensity increases, subduction ground motions induce larger residual deformations due to the increase in cumulative damage that is sustained by the structural members. It is worth noting that RIDR is affected by the modeling approach used, especially when modeling structures to collapse. However, in the interest of the length of this Chapter, and because damage indices do not account for the RIDR, detailed discussion of the RIDR is left for future works.

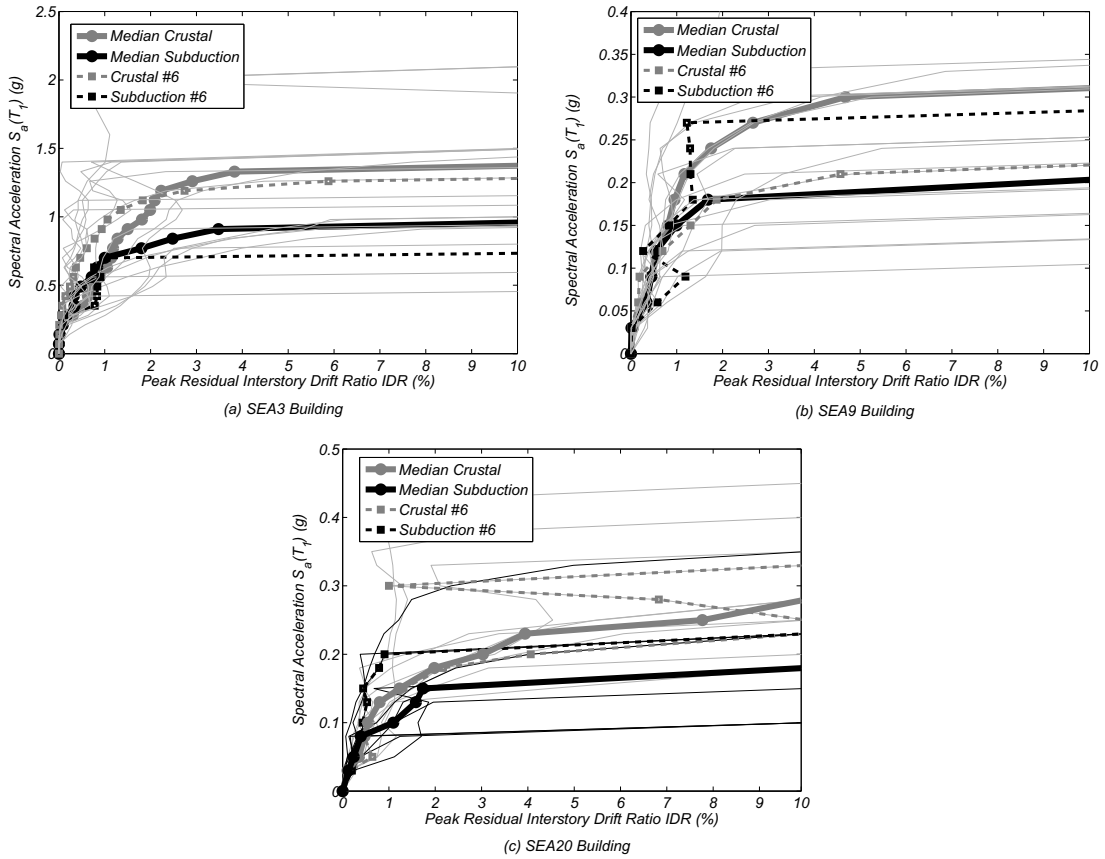

Figure 5.16: Residual Interstory Drift Ratio (RIDR) obtained through Incremental Dynamic Analysis: (a) SEA3 Building; (b) SEA9 Building; and (c) SEA20 Building

Figure 5.17 shows the median ratio between E_h and E_{tot} in each plastic hinge at floor levels for each building. Results are shown for $S_a(T_1) = 0.56$g for the SEA3 building, for $S_a(T_1) = 0.21$g for the SEA9 building, and $S_a(T_1) = 0.15$g for the SEA20 building. These values correspond to the spectral acceleration at the fundamental period of vibration of the buildings, based on Seattle MCE response spectrum. Note that an increase in the E_h/E_{tot} ratio corresponds to a reduction in the residual structural resistant capacity of the members. Figure 5.17 also shows the median IDR at each story for the same ground motion intensity levels, on the right side of each building. For the three buildings, it can be seen that the energy dissipated during subduction zone ground motions is significantly greater than that dissipated in shallow crustal ground motions, as a result of longer durations. In Figure 5.17(a), for the SEA3 building, the maximum E_h/E_{tot} ratio is reached at level 3, with a value of 16%. In Figure 5.17(b) it can be seen that building SEA9 is capable of redistributing deformations across a wide range of floors, where the peak ratios tend to be

similar at multiple floors. In this building, the maximum ratio E_h/E_{tot} is 65%. Figure 5.17(c), for the SEA20, shows that the maximum energy dissipated in a plastic hinge is achieved in the SEA20 building, where the energy dissipation is concentrated in the 18^{th} and 19^{th} floors. For this building, the maximum ratio E_h/E_{tot} is 68%. For each ground motion type, a strong correlation between the energy dissipated at each floor and the interstory drift ratio is found. Building SEA20, in particular, presents a high concentration of energy dissipated in higher floors, where peak interstory drift ratios are also recorded, thus showing that this building may be more vulnerable after the earthquake. Possible reasons for the concentration of damage in higher floors are: (1) contribution of higher modes, and (2) smaller cross-sections of the beams in the upper two to three stories (see Figures 5.7(c) and 5.7(d) for building SEA9 and Figures 5.7(e) and 5.7(f) for building SEA20). It is worth noting, however, that even though a greater demand is expected from subduction events, the distribution of the demand over the building height is similar for both groups of earthquakes.

In conclusion, at these levels of intensity, although subduction zone ground motions do not significantly influence peak interstory drift ratios, they impose a greater energy dissipation demand, that can negatively impact the performance of the structures. This highlights the importance of considering damage indices that account for the effect of energy dissipation.

5.9 Damage Assessment

As mentioned before, three groups of results are obtained for each damage index (DI_{PA} and DI_{RV}): (i) median damage index for each beam; (ii) median maximum beam damage index (regardless of the beam at which the maximums were recorded); and (iii) median structural damage index. The results for each damage index shown noext were obtained using 10 ground motion pairs underlined in Table 5.1.

Figure 5.18 shows the median DI_{PA} damage index recorded at three different intensities, $S_a(T_1) = 0.56$ g, $S_a(T_1) = 0.21$ g, and $S_a(T_1) = 0.15$ g for SEA3, SEA9, and SEA20 buildings, respectively. The subduction ground motions consistently lead to higher damage indices, thus proving to be more damaging than crustal ground motions. The maximum damage index is achieved in the SEA20 building, which is consistent with conclusions drawn from Figure 5.17. At the elements where the maximum damage index is recorded in SEA9 and SEA20 buildings, the index associated with crustal ground motions is, at most, 60% of the corresponding value for subduction ground motions.

Figure 5.19(a) shows the median structural damage indices obtained for subduction ground motions plotted versus the indices obtained for the crustal ground motions for all IDA intensity levels. Every pair of results for ground motion types were obtained at the same ground motion intensity levels, as can be seen for an example pair of the IDA results in Figure 5.15. A similar plot is presented in Figure 5.19(b) but here considering the median maximum damage index recorded. In both figures, damage indices associated with subduction ground motions are always greater than the ones associated with crustal ground motions. Damage indices associated with building SEA20 are consistently larger than the ones associated with the other two buildings, namely for the structural damage index. In addition to this, damage index DI_{RV} is always greater than DI_{PA}, showing that building response presents high sensitivity to energy dissipation, which can be considered as a proxy for cumulative damage. For the subduction zone ground motions, a large number of elements

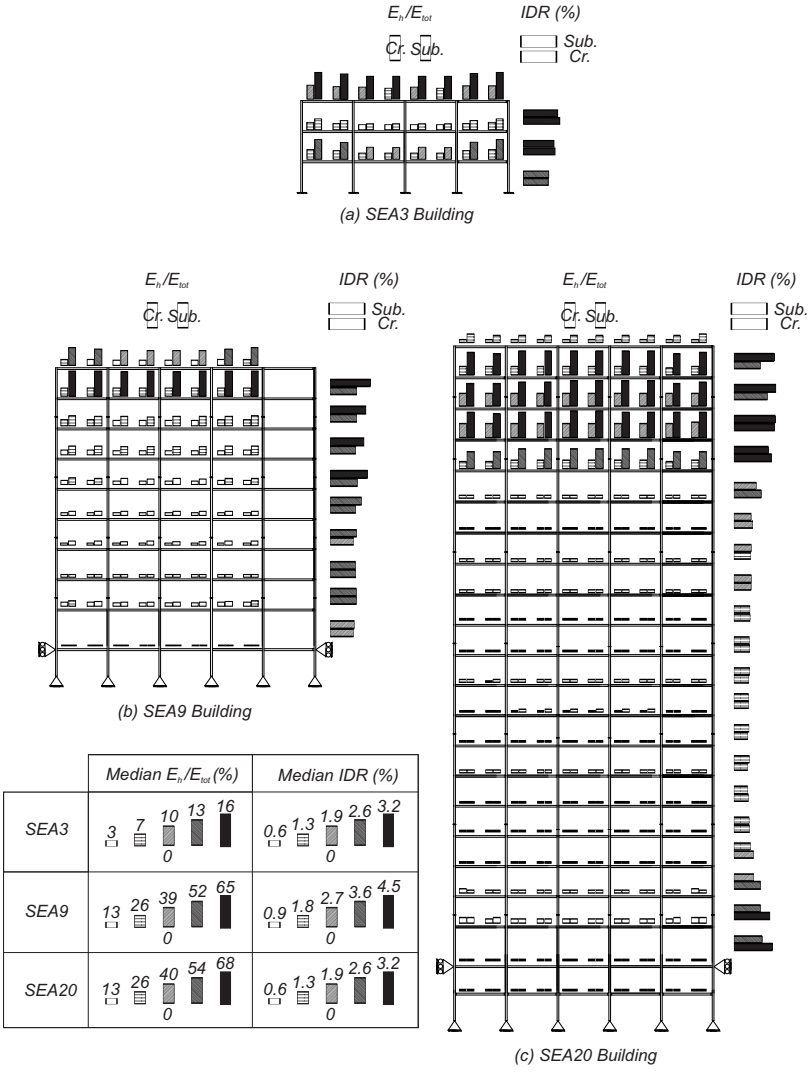

	Median E_h/E_{tot}(%)	Median IDR (%)
SEA3	3 7 10 13 16 / 0	0.6 1.3 1.9 2.6 3.2 / 0
SEA9	13 26 39 52 65 / 0	0.9 1.8 2.7 3.6 4.5 / 0
SEA20	13 26 40 54 68 / 0	0.6 1.3 1.9 2.6 3.2 / 0

Figure 5.17: Median Ratio of the Energy Dissipated to the Total Energy Dissipation Capacity (E_h/E_{tot}) at Each Plastic Hinge Section and Median Interstory Drift Ratio (IDR) at Each Story for a Spectral Acceleration Corresponding to the Seattle MCE intensity levels: (a) SEA3 Building at $S_a(T_1) = 0.56$ g; (b) SEA9 Building at $S_a(T_1) = 0.21$ g; and (c) SEA20 Building at $S_a(T_1) = 0.15$ g

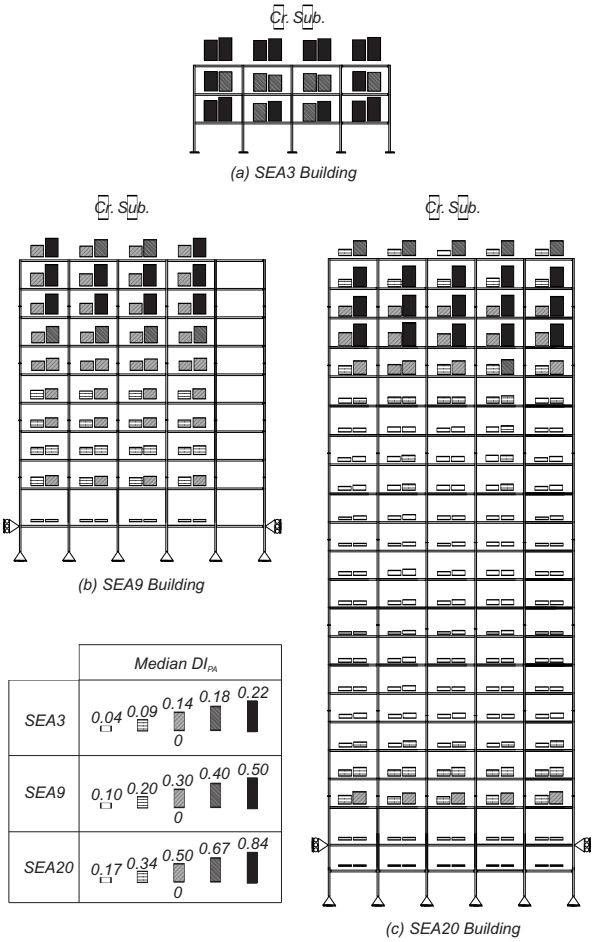

Figure 5.18: Median Park and Ang Damage Index at Each Element for a Spectral Acceleration Corresponding to the Seattle MCE Intensity Levels: (a) SEA3 Building at $S_a(T_1) = 0.56$ g; (b) SEA9 Building at $S_a(T_1) = 0.21$ g; and (c) SEA20 Building at $S_a(T_1) = 0.15$ g

exceeds the threshold value of $DI_{PA} = 0.4$, which according to Park et al. [81] indicates a non-repairable damage state. For the shallow crustal ground motions this threshold is only exceeded in the SEA20 building.

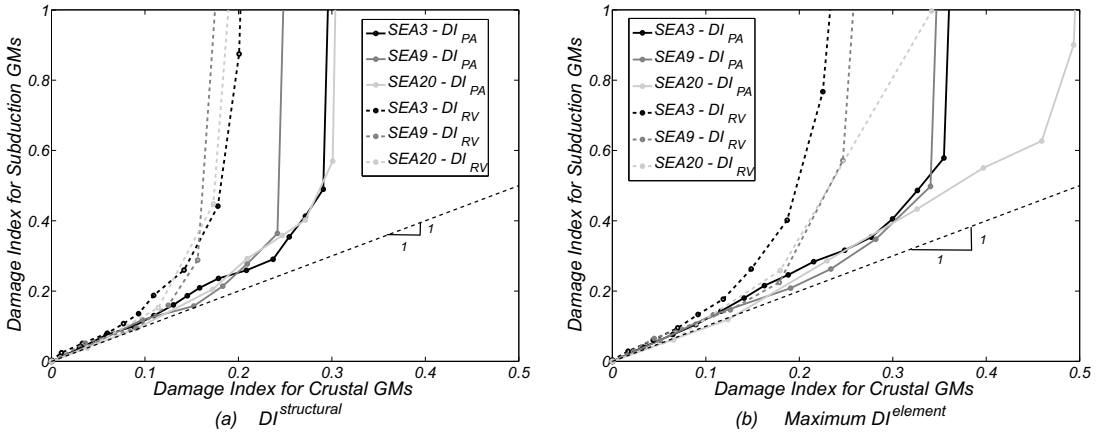

Figure 5.19: Comparison of the Median Damage Indices Recorded in the Analyses Carried Out With Shallow Crustal and Subduction Zone Ground Motion: (a) Structural Index; and (b) Median Maximum Element Value

5.10 Influence of Duration on Deformation-Damage Relationships

Figures 5.20 to 5.25 show the damage indices associated with subduction and crustal ground motions plotted as a function of the peak IDR, for the 10 ground motion pairs underlined in Table 5.1. Figures 5.20, 5.22, and 5.24, show the computed median results of the four different damage indices, namely the structural DI_{PA} index, maximum DI_{PA} index, structural DI_{RV} index, and maximum DI_{RV} index, for the SEA3, SEA9, and SEA20 buildings, respectively. Figures 5.21, 5.23, and 5.25 show the individual results of the same damage indices, associated with ground motion pair number 6 for the SEA3 and SEA20 buildings, and ground motion pair 8 for the SEA9 building. The coefficients of variation (CoV) of the IDRs for two definitions of the damage index, and at two levels of damage (DI = 0.2 and 0.4), are also shown in the tables presented in Figures 5.20, 5.22, and 5.24.

Similar trends are observed throughout these figures, i.e. similar damage indices are obtained for both subduction zone and shallow crustal motions for peak IDR lower than 2.0%, in terms of the median but also for individual pairs of ground motions. Up to this point, in most cases, subduction ground motions induce slightly larger damage indices, but the differences are not significant. However, beyond 2.0% IDR, the differences are significant and results clearly show that longer durations impose much larger damage indices at similar levels of peak IDR. For example, for a peak IDR of 4.0%, the damage index associated with subduction ground motion is at least 50% higher than that associated with crustal ground motions. Moreover, it is worth noting that smaller IDR tend to lead to smaller damage indices. However, in some cases larger IDR can be associated with lower damages (as seen at the top right of Figure 5.25(a). This phenomenon, denoted "resurrection from death", was first identified by Vamvatsikos and Cornell [199] when analyzing IDR under IDA. Results

in Figures 5.20, 5.22, and 5.24 indicate that the CoV for the subduction records are always greater or equal to that of crustal records. Results also show that the same damage index can be expected from a subduction earthquake with an intensity significantly lower than the corresponding crustal earthquake intensity. This difference tends to increase as the peak IDR increases because the slope of the two lines, corresponding to the two types of earthquakes, is significantly different. This highlights the limitations of the IDR as a surrogate for quantifying damage for subduction earthquakes.

As a conclusion, it can be stated that damage measures based on the peak IDR underestimate the potential consequences of long duration earthquakes. To accurately compute structural damage, it is paramount to define more accurate performance measures to use with both crustal and subduction earthquakes.

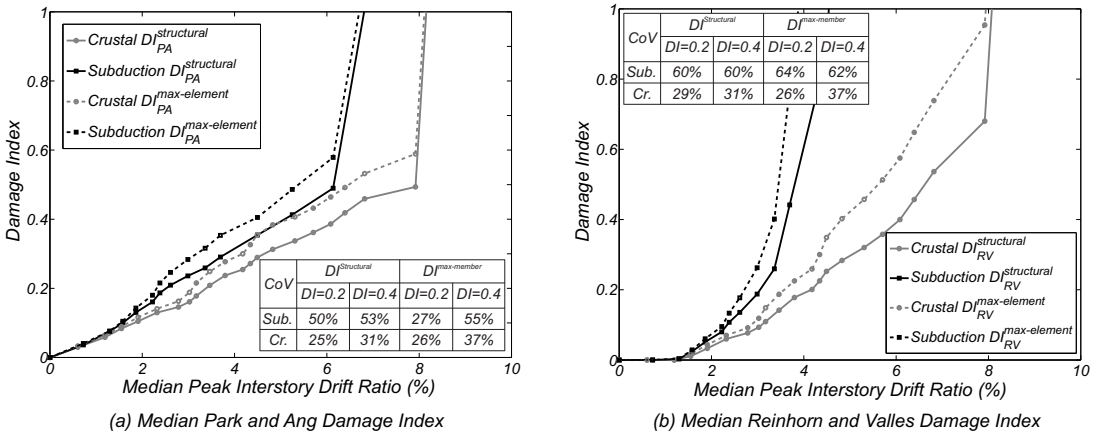

(a) Median Park and Ang Damage Index

(b) Median Reinhorn and Valles Damage Index

Figure 5.20: SEA3 Building: Median Damage Indices as a Function of the Median Peak Interstory Drift Ratio for Shallow Crustal and Subduction Zone Ground Motions: (a) Park and Ang Damage Index (DI_{PA}); and (b) Reinhorn and Valles Damage Index (DI_{RV})

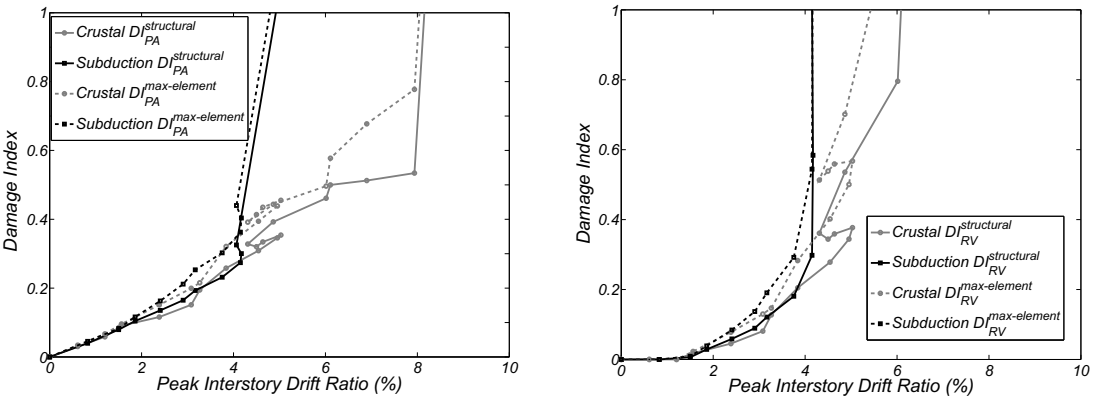

(a) Park and Ang Damage Index - GM Pair #6

(b) Reinhorn and Valles Damage Index - GM Pair #6

Figure 5.21: SEA3 Building: Damage Indices as a Function of the Peak Interstory Drift Ratio for Ground Motion Pair Number 6: (a) Park and Ang Damage Index (DI_{PA}); and (b) Reinhorn and Valles Damage Index (DI_{RV})

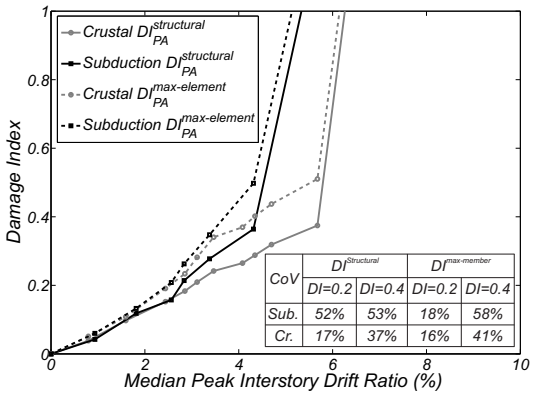

(a) Median Park and Ang Damage Index

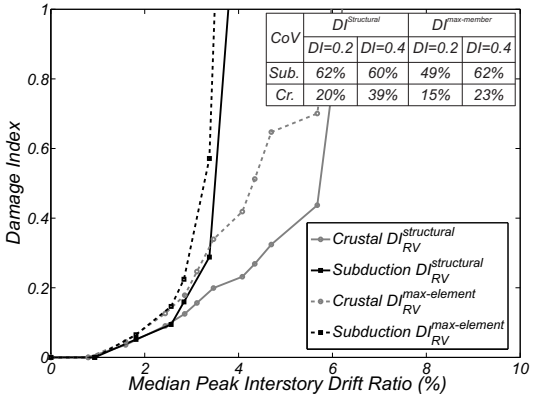

(b) Median Reinhorn and Valles Damage Index

Figure 5.22: SEA9 Building: Median Damage Indices as a Function of the Median Peak Interstory Drift Ratio for Shallow Crustal and Subduction Zone Ground Motions: (a) Park and Ang Damage Index (DI_{PA}); and (b) Reinhorn and Valles Damage Index (DI_{RV})

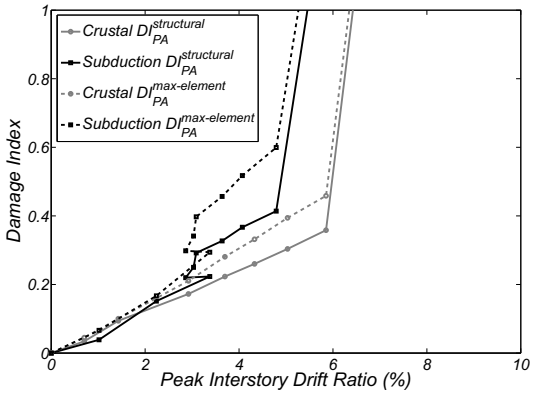

(a) Park and Ang Damage Index - GM Pair #8

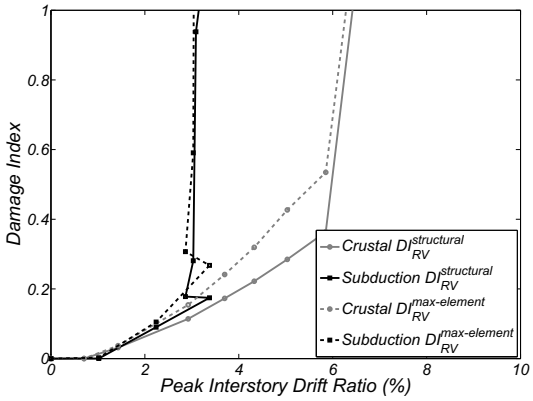

(b) Reinhorn and Valles Damage Index - GM Pair #8

Figure 5.23: SEA9 Building: Damage Indices as a Function of the Peak Interstory Drift Ratio for Ground Motion Pair Number 8: (a) Park and Ang Damage Index (DI_{PA}); and (b) Reinhorn and Valles Damage Index (DI_{RV})

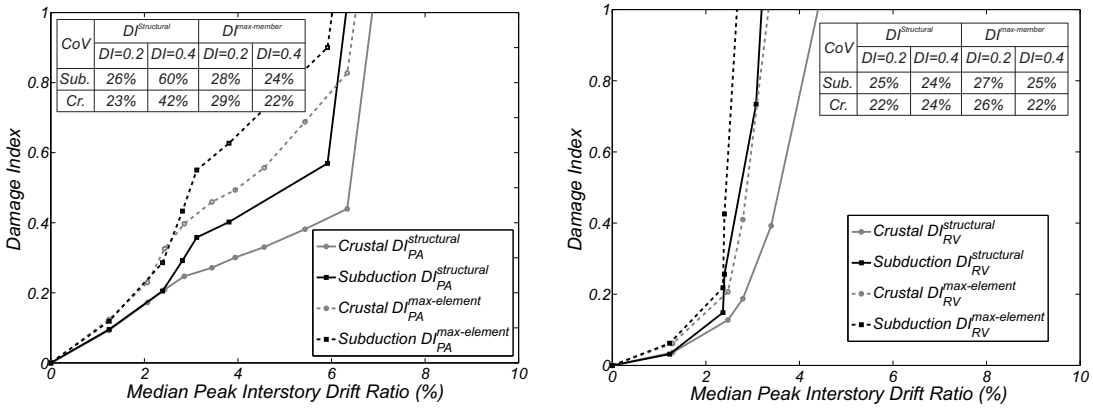

(a) Median Park and Ang Damage Index

(b) Median Reinhorn and Valles Damage Index

Figure 5.24: SEA20 Building: Median Damage Indices as a Function of the Median Peak Interstory Drift Ratio for Shallow Crustal and Subduction Zone Ground Motions: (a) Park and Ang Damage Index (DI_{PA}); and (b) Reinhorn and Valles Damage Index (DI_{RV})

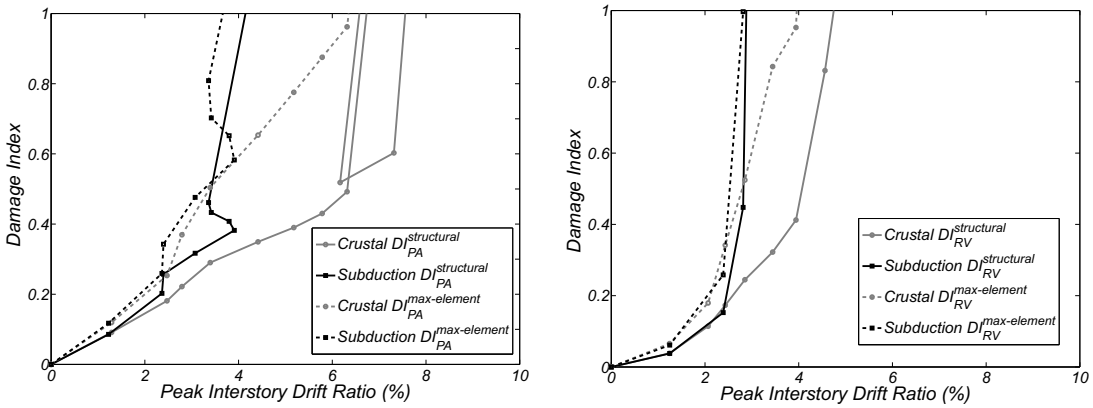

(a) Park and Ang Damage Index - GM Pair #6

(b) Reinhorn and Valles Damage Index - GM Pair #6

Figure 5.25: SEA20 Building: Damage Indices as a Function of the Peak Interstory Drift Ratio for Ground Motion Pair Number 6: (a) Park and Ang Damage Index (DI_{PA}); and (b) Reinhorn and Valles Damage Index (DI_{RV})

5.11 Conclusion

Structural damage estimation in civil engineering infrastructure due to long duration ground motions has received less attention than short duration earthquakes. As a result, present codes as well as performance-based design methodologies are typically based on response and damage measures calibrated to short duration shallow crustal earthquakes. Subduction zone earthquakes are responsible for developing ground motions longer than those expected to develop due to shallow crustal earthquakes. Even though some recent studies have shown that longer duration ground motions may lead to greater collapse risk, an extensive assessment of the influence of ground motion duration on structural damage is still lacking in the earthquake engineering literature. This Chapter aims at partially bridging that knowledge gap.

In the present Chapter, the performance of steel moment resisting frames under sets of 22 short duration and 22 long duration earthquakes is compared in terms of the expected level of damage caused by the earthquakes, to evaluate the combined influence of ground motion duration and spectral acceleration. Subsequently, 10 ground motion pairs are selected from the initial sets and are used to investigate the influence of duration on structural response in terms of deformation, energy dissipation, number of inelastic cycles, and damage state. Crustal ground motions are scaled so that spectrally equivalence is guaranteed in each pair. Incremental dynamic analysis are then performed at at least 20 intensity levels.

The obtained results for short and long duration earthquakes indicate that:

- for low values of spectral acceleration, there is no visible influence of ground motion duration on deformations and damage; for large spectral accelerations, longer duration motions tend to induce larger peak IDRs and damage indices;

- in terms of deformation, the median response between the two sets of ground motions is similar until approximately 4% peak IDR; above this, the long duration ground motions tend to induce larger deformations under the same values of spectral acceleration;

- the relationship between the peak inter-story drift ratio and damage indices was found to be nonlinear; this level of nonlinearity increases with ground motion duration;

- the 3- and the 9-story buildings presented a relatively homogeneous distribution of damage over the height, while the 20-story building presented a concentration of damage in the top three floors; this damage concentration was enhanced for the longer duration motions;

- largest damage indices were obtained for the 20-story building as a consequence of the concentration of damage; on the other hand, the design of the 9-story building efficiently distributed deformations over the height;

- although further work is needed, residual interstory drift ratio (RIDR) was found to be different for the two ground motion earthquake types; for the structural modeling approach used here, similar levels of RIDR are obtained only for smaller intensities.

The observations in this Chapter on damage accumulation in structural members and on the relationship between deformation and damage are expected to be similar when studying

new buildings designed with current codes, for example, when considering connection fracture. Nonetheless, further work will be necessary to evaluate the performance of different building types under long duration earthquakes and to assess the validity of this statement. In addition, results in this work indicate that regions affected by subduction zone earthquakes, such as the Cascadia Subduction Earthquake Zone, should be subjected to an extensive probabilistic assessment of the seismic performance of structures subjected to ground motions due to all potential sources. Such a study should account for the relative contribution of the various seismic sources, for example following the approach presented in FEMA P-695 [83]. If the trends recorded in this work are maintained, these regions should have their design revised to account for the effects of duration. More research is required considering different types of buildings and different modeling assumptions, namely in what concerns modeling different failure mechanisms (e.g., low-cycle fatigue, shear failure, or connection failure) and materials (RC, timber, etc.). Further work is also required in order to develop accurate relationships between ground motion intensity measures and structural damage indices to be used within performance-based earthquake engineering frameworks.

5.12 Dissemination

This part of the research program resulted in the following outputs.

1. Scientific paper published in the Earthquake Engineering & Structural Dynamics Journal (in press)

   Scope: Presentation of analytical study evaluating the influence of ground motion duration on structural damage of 3-, 9-, and 20-story SAC steel moment resisting frame (SMRF) buildings designed for downtown Seattle,Washington, U.S.A..

   Complete reference: Barbosa, A., Ribeiro, F., and Neves, L. (2015). "Influence of Earthquake Ground-Motion Duration on Damage Estimation: Application to Steel Moment Resisting Frames." Earthquake Engineering & Structural Dynamics (in re-review).

2. Oral presentation made by Professor André R. Barbosa at the 10^{th} National Conference on Earthquake Engineering, Alaska, U.S.A. (2014)

   Scope: Presentation of preliminar results of the study on the influence of ground motion duration on damage of the 9-story building.

   Complete reference: Barbosa, A., Ribeiro, F., and Neves, L. (2014). "Effects of subduction zone earthquake motions on a 9-story SAC steel moment resisting Frame." In: 10th National Conference on Earthquake Engineering, Alaska, U.S.A.

Chapter 6

Robustness Assessment of Structures Considering Post-Earthquake Aftershocks

6.1 Scope

This Chapter presents a reliability-based framework for quantifying the structural robustness considering the occurrence of a major earthquake (mainshock) and subsequent cascading hazard events, such as aftershocks that are triggered by the mainshock. These events can significantly increase the probability of failure of buildings, especially for structures that are damaged during the mainshock.

The application of the proposed framework is exemplified through three numerical case studies. The case studies correspond to three SAC steel moment frame buildings of 3-, 9-, and 20- stories, which were designed for Los Angeles by using pre-Northridge codes and standards. Two-dimensional nonlinear finite element models of the buildings are developed using the Open System for Earthquake Engineering Simulation framework (OpenSees), using a finite-length plastic hinge beam model and the Modified Ibarra-Medina-Krawinkler model, and are subjected to multiple mainshock-aftershock seismic sequences.

For the three buildings analyzed herein, it is shown that the structural reliability under a single seismic event can be significantly different from that under a sequence of seismic events. The reliability-based robustness indicators used shows that the structural robustness is influenced by the extent by which a structure can distribute damage.

6.2 Introduction

Structures in earthquake prone regions are susceptible to being damaged due to intense ground motion shaking. Traditionally, design and analysis of building structures only considers one single earthquake event, also known as a mainshock. However, in reality, structures can be subjected to cascading events, defined as events likely to be triggered by a major earthquake, such as aftershocks, fires, explosions, or tsunamis. The focus of this chapter is placed on sequences of ground motions that include the mainshock as well as aftershocks. The magnitudes of aftershocks are usually lower than the mainshock, but an aftershock record may have higher peak ground acceleration (PGA), longer duration, larger intensity,

and different energy content than the mainshock [184]. The aftershocks have the potential to produce larger seismic demand for a specific building, e.g. due to larger spectral acceleration at the fundamental period of the building [200]. Structural damage is typically observed in the large intensity mainshocks. Since the typical time interval between mainshocks and aftershocks is small, structural repair or retrofit is not possible and the mainshock-damaged structures are thus more susceptible to failure when an aftershock occurs. The term failure, as used herein, is synonymous with exceeding a defined limit state that may render structures unfit for use [201].

In this chapter, a measure of structural robustness is used to characterize the effect of aftershocks on the seismic safety of structures. With respect to aftershocks triggered by mainshocks, a structure is said to be more or less robust depending on its capacity to sustain post-mainshock damage without reaching failure. Three main approaches for quantifying structural robustness have been proposed in the literature. In the first approach, measures of structural robustness are derived from probabilistic risk assessments [15]. Baker *et al.* [15] defined a measure for quantifying structural robustness as a function of direct and indirect risk. Even though this approach is very powerful, the complexity and subjectiveness in the quantification of the direct and indirect risk in large structural systems hinders the application of this approach. In the second approach, measures of structural robustness are quantified in terms of ratios of structural properties (e.g. damage, energy, or stiffness) between undamaged and damaged structures [20,24]. While these measures are useful in engineering practice, they fail to explicitly describe failures. Finally, in the last approach, measures of structural robustness are defined as a function of the probabilities of failure of the intact and damaged structure. Examples of such measures are the indices presented by Frangopol and Curley [27] and Lind [28]. It is worth noting that, as discussed in Starossek and Haberland [202], both these measures evaluate structural redundancy rather than robustness. However, for buildings, redundancy is provided by the existence of alternative load paths which is the main mechanism providing robustness, rendering these indicators an adequate indirect measure of structural robustness. Robustness assessment of structures for cascading hazards is currently lacking in the literature.

There are two main challenges in modeling the effects of aftershock events on structures for computing structural robustness. The first challenge is related to the accurate modeling of expected mainshock-aftershock seismic sequences. This has been discussed extensively in [52,203–208]. Luco *et al.* [207] and Ryu *et al.* [208] performed mainshock-aftershock incremental dynamic analyses (IDA [54]) on single-degree-of-freedom models subjected to artificial sequences of mainshock-aftershock "back-to-back" structural analyses. The second challenge is related to accurate modeling of the effects of damage introduced by the mainshock on structural performance. To this effect, state-of-the-art modeling for estimation of structural performance/damage can be found in ATC-72 [109]. In the ATC-72 report emphasis is placed on phenomenological models that capture the main effects of strength and stiffness deterioration.

In this study, a framework for the assessment of structural robustness under mainshock triggered aftershocks is developed. Emphasis is placed on the evaluation of the structural robustness as a function of the probability of failure (or the reliability index) under different damage scenarios. In the probabilistic methodology, nonlinear dynamic time-history analyses of structural computational models of buildings are used to estimate the recorded structural damage due to multiple mainshock-aftershock sequences. Mainshock and aftershock incremental dynamic analyses are carried out following the approach proposed by

Ryu *et al.* [208], where artificial mainshock-aftershock sequences are used in the "back-to-back" nonlinear dynamic time-history analyses. This approach is applied to multi-degree-of-freedom (MDOF) structural models of the 3-, 9-, and 20-story steel moment resisting frames (SMRFs) of the SAC steel project [77]. The analytical building models are developed using the Open System for Earthquake Engineering Simulation, OpenSees [132], and were validated using the numerical data available in the literature [77,139]. Important aspects of beam strength and stiffness degradation as damage progresses during the analysis were also included in the model. To quantify the damage due the mainshock and aftershock, the buildings are first subjected to a mainshock incremental dynamic analysis and for each level of the intensity of the mainshock, the mainshock-damaged structure is then subjected to incremental dynamic analysis due to the aftershocks.

6.3 Literature Review

Aftershock ground motions may cause weakening and/or collapse of structures already damaged by the mainshock, thus threaten life safety, and result in significant economic losses. As a consequence, even when minor damage is present from the mainshock, aftershocks affect decisions to evacuate (possibly damaged) buildings [42]. In this context, Bazzurro et al. [209] have developed guidelines for tagging damaged buildings that include nonlinear structural analyses performed prior to a mainshock to determine the residual capacity of a given building in several different states of potential damage. The elapsed time between the mainshock the largest aftershock can range from several minutes to months. It is not realistic that the damaged building is repaired to an intact state immediately after the mainshock or before the next aftershock [200]. According to Yeo and Cornell [210], it can take two or more years to reopen mainshock-damaged buildings, which lead to significant financial loss from business downtime.

Towards the probabilistic assessment of the aftershock ground motion hazard, Yeo and Cornell [42] proposed a methodology, entitled Aftershock Probabilistic Seismic Hazard Analysis (APSHA), to describe the likelihood of occurrence of aftershocks after a mainshock with specific characteristics. Then, the same authors [210] proposed stochastic financial loss estimation models over the structural life time due to mainshocks and their aftershock sequences. Jalayer et al. [211] applied these concepts in the L'Aquila earthquake, calculating the probability of exceeding a limit state in a given interval of time elapsed after the occurrence of the mainshock event, considering a simplified single degree of freedom model. There are also studies that present the aftershock hazard deduced from the aftershock earthquake occurrence rates obtained for California [212].

Recent research, developed during the last decade, has focused on the study of aftershock risk influence on structural safety, life-cycle losses, as well as the corresponding impact on design and assessment of building and bridge structures. Luco et al. [52] define the random residual capacity of buildings in a post-mainshock damage state i (DS_i) in terms of the minimum first-mode ground motion spectral acceleration, at the fundamental oscillatory period of the intact structure, T_1, and a damping ratio of ξ, that would induce localized or complete collapse due to an aftershock. The computation of the collapse probability can be accomplished by convolving the aftershock ground motion hazard (demand) at the site, e.g., [42], with the probabilistic residual capacity of the damaged building to withstand aftershock shaking [52]. Luco et al. [207,208] presented a methodology for evaluating the

fragility of mainshock damaged structures (i.e. aftershock fragility), by performing IDA [54] with a sequence of mainshock-aftershock back-to-back structural analyses.

Li et al. [213] investigated the collapse probability of mainshock-damaged steel buildings considering aftershocks with different fault types and spectral shapes. It was found that structural collapse capacity may reduce significantly when the building is subjected to a large intensity mainshock. Song et al. [184], in turn, studied the impact of earthquake ground motion characteristics, namely duration and frequency content on collapse risk of post-mainshock buildings considering aftershocks. The results indicate that post-mainshock structures with more serious damage states may be more fragile when subjected to the aftershocks with longer duration and lower frequency, thus highlighting the importance of accurately characterize aftershock ground motion.

Moreover, Yin and Li [214], and Yeo and Cornell [42] performed life-cycle cost analyses due to mainshock and aftershock occurrences on building structures, and showed that aftershocks and downtime are important contributors to total seismic loss. Song *et al.* [200] developed a framework for loss estimation of steel structures subjected to mainshock-aftershock sequences, and concluded that even if the aftershocks have little influence on structural behavior, they may still have a significant effect on the seismic loss due to the uncertainty in the damage states and in the cost estimation. Finally, Nazari et al. [215] developed a methodology that can quantify the changes that would be needed in the structural design of a building to account for aftershock hazards. The objective of the study was to calculate the difference in terms of structural properties (e.g., strength and stiffness) so that the same collapse probability was obtained for the mainshock-aftershock and the mainshock alone cases. An illustrative case study example showed that a 10% increase in both stiffness and strength would be required to keep the collapse probability equal in both cases.

Although the important works that have been developed recently, there is no established framework to assess the robustness of structures in post-earthquake scenarios considering cascading events. In this chapter a framework for quantifying the robustness of structures considering the occurrence of a major earthquake (mainshock) and the subsequent cascading hazard events, namely fire and aftershocks, is proposed.

6.4 Framework

6.4.1 General Formulation

This section presents the proposed methodology to assess the robustness of structures subjected to cascading hazards triggered by a mainshock. Figure 6.1 shows the event tree that illustrates the possible sequences of events that are considered in this methodology. In this event tree it can be seen that different combinations of hazard events may lead to system collapse. The first situation that may lead to system collapse is the mainshock itself. That possibility is analyzed in Step 1. If collapse does not occur, then three combinations of events are considered: (i) occurrence of a fire/blast following the mainshock; (ii) occurrence of an aftershock following the mainshock; and (iii) occurrence of a fire/blast and an aftershock following the mainshock. Both the fire/blast and the aftershock may lead to system collapse. If probabilities associated with the occurrence of each event are known, the total probability of system collapse can be computed. The probability of failure associated with the original hazard alone is computed in analysis step (1). In the subsequent analysis steps, the probabilities of failure due to the mainshock-fire/blast (1+2), mainshock-aftershock (1+3), and

mainshock-fire/blast-aftershock (1+2+3) are computed.

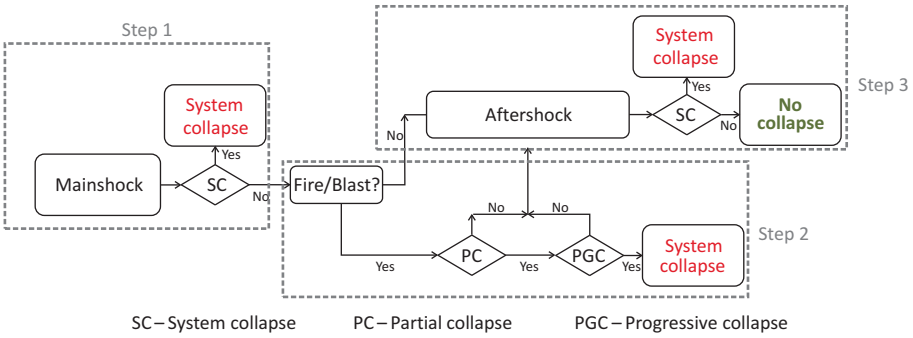

Figure 6.1: Event tree considering cascading hazard events following a mainshock

Considering the occurrence of a mainshock followed by a fire or blast and an aftershock, the probability of structural failure can be expressed as:

$$P(C) = \int_{IM^m}\int_{F}\int_{DS^m}\int_{DS^f}\int_{IM^a} P(C|im^a, ds^f, ds^m) \times dP(im^a|im^m) \times dP(ds^f|f, ds^m) \times dP(f|im^m) \times dP(ds^m|im^m) \times dP(im^m) \quad (6.1)$$

where im^m and im^a represent the intensity measures associated with the mainshock and the aftershock, respectively; f is the occurrence of a specific fire scenario or blast scenario following the mainshock; ds^m and ds^f corresponds to the damage state of the structure after the mainshock and after the fire/blast, respectively; IM^m, IM^a, DS^m, and DS^f represent the sample space of im^m, im^a, ds^m, and ds^f, respectively.

Equation 6.1 contains four conditional probability terms: $dP(im^m)$ corresponds to the probability of occurrence of a mainshock with intensity im^m; $dP(ds^m|im^m)$ is the conditional probability of a certain damage state ds^m being recorded after the mainshock; $dP(f|im^m)$ is the probability of occurrence of fire or blast following a mainshock characterized by im^m; $dP(ds^f|F, ds^m)$ is the conditional probability of a certain damage state ds^f being recorded after both the mainshock and fire/blast have occurred; $dP(im^a|im^m)$ is the conditional probability of occurrence of an aftershock with intensity im^a following a mainshock with intensity im^m; and $P(C|im^a, ds^f, ds^m)$ represents the probability distribution function of C (*structural collapse criteria*), defined herein through one or more structural damage indicators [216], conditional on im^a, ds^f, and ds^m. If the collapse event is defined as $IM^a \geq im^{a,c}$ which allows the simplification of Equation 6.1 by integrating out IM^a, resulting in:

$$P(C) = \int_{IM^m}\int_{f}\int_{DS^m}\int_{DS^f} P(C|ds^f, ds^m) \times dP(ds^f|f, ds^m) \times dP(f|im^m) \times dP(ds^m|im^m) \times dP(im^m) \quad (6.2)$$

where,

$$P(C|ds^f, ds^m) = \int_{IM^a} P(C|im^a, ds^f, ds^m) dim^a = P[IM^a \geq im^{a,c}|DS^f = ds^f, DS^m = ds^m] \quad (6.3)$$

and where $im^{a,c}$ represents the minimum ground motion intensity leading to collapse, which can be computed through IDA [54].

It is worth noting that not all ground motion intensities larger than $im^{a,c}$ lead to collapse as shown by Vamvatsikos and Cornell [54], who considered the spectral acceleration at the fundamental period of the intact structure as intensity measure, since the IDA curves are non-monotonic functions, i.e. exhibit twisting patterns. However, it is considered that $im^{a,c}$ corresponds to the minimum aftershock intensity leading to failure.

Furthermore, it is assumed that the uncertainties regarding mainshock, aftershock and damage introduced by fire/blast are of greater magnitude than that associated with the structural properties. Therefore, all parameters defining the structure are modeled as deterministic variables and are set equal to their expected values.

6.4.2 Application to Mainshock-Aftershock Sequences

The the presented methodology serves as basis for the development of a framework for the structural robustness assessment of buildings, which is schematically presented in Figure 6.2. The first step of the analysis corresponds to the definition of the engineering measures considered to define failure and the thresholds used to define the performance or limit states. The following step of the analysis corresponds to the definition of the mainshock hazard. This depends on the location of the building and the foundation soil. Extensive data exists on the seismic hazard of locations in Europe, North America, and Japan [e.g., 217]. From this, the mean annual rate of exceeding a ground motion intensity measure can be defined and, consequently, a probabilistic distribution of the mainshock intensity measure can be obtained. The most used ground motion intensity measure is the 5% damped linear elastic spectral acceleration at a fundamental period of the structure T_1, which is denoted as $S_a(T_1)$ [e.g. 218]. Herein, the notation S will be used to refer to a spectral acceleration at a fundamental period of the structure.

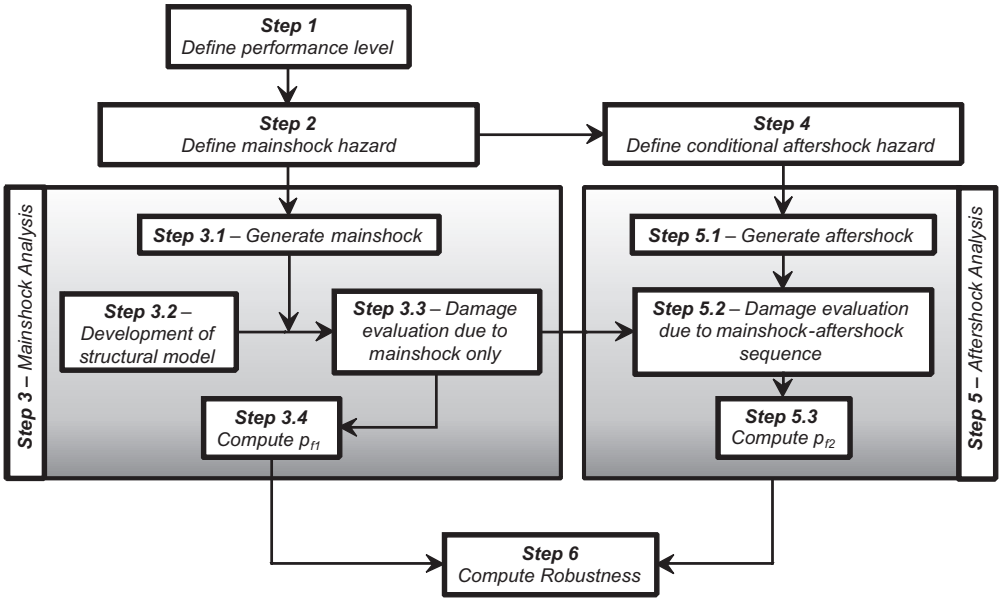

Figure 6.2: Flowchart for the robustness assessment of buildings subjected to cascading seismic events

Based on the definition of the hazard, a set of mainshock ground accelerograms can be defined (Step 3.1), considering either real or artificial accelerograms [e.g., 60]. Considering the uncertainty in the characteristics of the mainshock, several different accelerograms should be used and methods for estimating the structural response due to the mainshock are discussed in Baker [218], for example. When probabilistic simulation is employed, a set of mainshocks following the distribution of the spectral acceleration are used. In Step 3.2, finite element models are defined, leading at sufficient accuracy to characterize the nonlinear response to collapse, providing reliable estimates of the residual displacements and loss in stiffness and strength. Details on an example of models that can be employed to account for the strength and stiffness deterioration are described in the following section. In Step 3.3, the damage caused by the mainshock is evaluated for each of these samples. In the present chapter, this is done using an incremental dynamic analysis [54], but other methods for estimating the damage conditional on the mainshock ground motion intensity measure can be defined. Based on the results of these analyses, in Step 3.4, the probability of failure under mainshock alone (p_{f1}) can be estimated using:

$$p_{f1} = \int_{S^m} P(F|S^m = s^m) dP(S^m) \tag{6.4}$$

where S^m represent the ground motion spectral accelerations associated with the mainshock at the fundamental period of the intact structure, $P(S^m)$ corresponds to the annual probability of occurrence of a spectral acceleration associated with the mainshock, and $P(F|S^m = s^m)$ represents the probability of failure F conditional on S^m. The probabilities of exceedance of a given S^m are defined considering, for example, the data described in Petersen *et al.* [217]. According to Jayaram and Baker [219] the spectral accelerations follow lognormal distributions. The term F describes a failure event, which is defined as exceedance of a limit state. When considering a collapse limit state, for example, FEMA356 [220] reports 5% as a limiting value interstory drift ratio in buildings. It is worth noting that Eq.6.4 is applicable for any limit state.

Based on the properties of the mainshock, the conditional aftershock hazard can be defined in Step 4. The occurrence rate and the distribution of aftershocks have strong correlations with mainshock magnitude [42]. As a consequence, an aftershock hazard should be defined considering the mainshock amplitude, frequency content, and duration. Therefore, the simulation of mainshock-aftershock ought to be performed with real sequences whenever possible. However, for most sites such information in not available, and a general formulation cannot rely on existence of this data. Thus, artificial mainshock-aftershock sequences are used herein, following Luco *et al.* [207], Ryu *et al.* [208], Li *et al.* [221], and Song *et al.* [200]. In Step 5.1 a set of aftershock ground accelerations is defined. In Step 5.2, damage resulting from mainshock and aftershock is evaluated, following the tasks described above for the mainshock alone. The probability of failure due the aftershock conditional on the occurrence of a mainshock that does not lead to failure, p_{f2}, can be computed through:

$$p_{f2} = \frac{p_{f3} - p_{f1}}{1 - p_{f1}} \tag{6.5}$$

where the probability of failure considering both mainshock and aftershock, computed in Step 5.3, is given by:

$$p_{f3} = \int_{S^m} \int_{S^a} P(F|S^m = s^m, S^a = s^a) dP(S^a|S^m = s^m) dP(S^m) \tag{6.6}$$

and where S^a represent the ground motion spectral accelerations associated with the aftershock at the fundamental period of the intact structure, $P(S^a|S^m = s^m)$ is the conditional probability of occurrence of an aftershock with spectral acceleration S^a following a mainshock with spectral acceleration S^m, and $P(F|S^m = s^m, S^a = s^a)$ represents the probability of failure F conditional on S^m and S^a. S^a is also assumed to follow a lognormal distribution.

In Step 6, the robustness assessment is performed by using the reliability-based robustness indicator presented in Chapter 1, which is based on the comparison of the reliability index ($\beta = -\Phi^{-1}(p_f)$) of the undamaged structure β_{intact}, which accounts for the mainshock only, with the reliability index of the mainshock-damaged structure $\beta_{damaged}$ as:

$$\beta_R = \frac{\beta_{intact}}{\beta_{intact} - \beta_{damaged}} \tag{6.7}$$

where $\beta_{intact} = -\Phi^{-1}(p_{f1})$ and $\beta_{damaged} = -\Phi^{-1}(p_{f2})$. The main issue related to the use of this index is the fact that results do not vary within a defined limit. In fact, β_R may assume values from 0 to ∞, which hamper the comparison among different cases (e.g., buildings typologies, design methods, etc.).

To overcome this difficulty, a new index was developed in this work by manipulation of the index proposed by Frangopol and Curley [27]. This index, designated Robustness Factor (RF), is thus a robustness index based on comparison of reliability measures of the intact and damaged structural system. The RF is given by:

$$RF = \left(exp\left(\frac{P_{f(dmg)} - P_{f(int)}}{P_{f(int)}} \right) \right)^{-1} \tag{6.8}$$

where $P_{f(int)}$ and $P_{f(dmg)}$ are the probabilities of failure of the intact and the damaged system, respectively. The RF takes values in the interval $]0; 1]$. When a structure does not provide any robustness, the correspondent RF is 0. While, a very robust structure results in RF equal to 1. As shown in Figure 6.3 the variation of RF as a function of the failure probability of both the intact and the damaged structure is exponencial.

6.5 Building models

6.5.1 General Description

The steel moment resisting frame (SMRF) buildings studied in this chapter are a subset of the models developed as part of the SAC Steel project [77]. The buildings included in this study are a 3-, a 9-, and a 20-story buildings (denoted LA3, LA9 and LA20, respectively) which were designed for Los Angeles using pre-Northridge codes [138]. In all buildings, external frames were designed to resist the lateral seismic loads and interior frames were designed as gravity frames. As shown in Figure 6.4, all buildings have spans of 9.15m in both directions. The 3-story building presents no basement, while the 9- and 20-story buildings have one and two basement levels, respectively. The height of the frames is constant and equal to 3.96m, except for the first level of the two taller buildings, which have a height of 5.49m, as shown in Figure 6.4. A detailed description of the buildings can be found in FEMA 355C [77] and Luco [139].

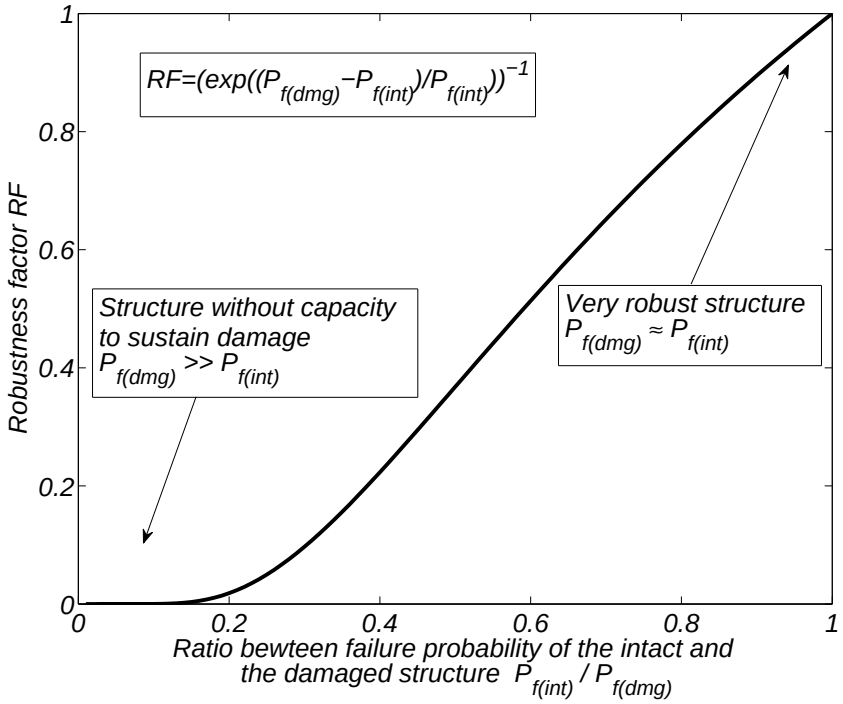

Figure 6.3: Variation of the proposed rosbustness factor (RF) as a function of the ratio bewteen the failure probability of the intact and the damaged structure

Two-dimensional centerline models of an external frame of each of the three buildings are used for the structural analysis. According to one of the modeling alternatives presented in Luco and Cornell [142], strong-column weak-beam ductile behavior is assumed for all structures. Brittle mechanisms and connection fracture modes are not considered.

Geometric nonlinearities are accounted for during the analysis by considering a $P-\Delta$ leaning column. A rigid diaphragm is assumed for each floor. Soil-structure interaction is not considered. Masses and loads are applied to beam-column joints. Similarly to what was defined in FEMA355C [77], Rayleigh damping is assigned to the models. As described in Erduran [168], a damping ratio of 2% is assigned to the first mode and a higher mode. Following FEMA355C [77] the higher mode considered is the fifth mode for LA20 and a mode with period 0.2s for buildings LA3 and LA9 (a period close to the LA3's 3rd modal period and the LA9's 5th modal period).

6.5.2 Component Modeling

The building's nonlinear behavior is modeled considering a set of four different models for each structure, as described in Table 6.1. The four models differ in the method used to simulate the beams. For the first two models, a zero-length plastic hinge element is used, considering elasto-plastic behavior with hardening and a bilinear model with deterioration (*Bilin* model in OpenSees). The third and fourth models used the same material models, but consider a finite-length plastic hinge element. In all four cases, the columns are modeled considering a distributed plasticity model and an elasto-plastic constitutive law with a 3% hardening rate assigned to each fiber. A moment-curvature section analysis shows that this corresponds to a section hardening of 3.0%, consistent with the assumptions used in

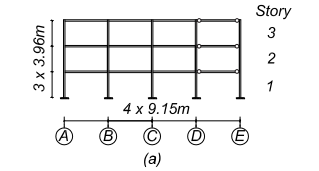

(a)

Story	Columns			Beams					Mass (kg)
	Exterior	Interior	Model	Section	Model	θ_y (rad)	θ_{pc} (rad)	$\Lambda=E_{so}/M_y$	
1	W14x257	W14x311	NL-FB-H	W33x118	NL-FMRB	0.026	0.114	0.740	$9.75x10^5$
2	W14x257	W14x311		W30x116		0.031	0.152	1.001	$9.75x10^5$
3	W14x257	W14x311		W24x68		0.038	0.130	0.792	$1.06x10^6$

(b)

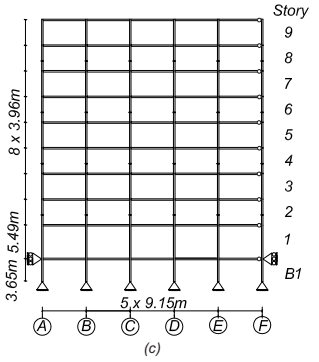

(c)

Story	Columns			Beams					Mass (kg)
	Exterior	Interior	Model	Section	Model	θ_y (rad)	θ_{pc} (rad)	$\Lambda=E_{so}/M_y$	
B1	W14x370	W14x500	NL-FB-H	W36x160	NL-FMRB	0.025	0.146	0.978	$1.03x10^6$
1	W14x370	W14x500		W36x160		0.025	0.146	0.978	$1.03x10^6$
2	W14x370/ W14x370	W14x500/ W14x455		W36x160		0.025	0.146	0.978	$1.01x10^6$
3	W14x370	W14x455		W36x135		0.024	0.115	0.757	$1.01x10^6$
4	W14x370/ W14x283	W14x455/ W14x370		W36x135		0.024	0.115	0.757	$1.01x10^6$
5	W14x283	W14x370		W36x135		0.024	0.115	0.757	$1.01x10^6$
6	W14x283/ W14x257	W14x370/ W14x283		W36x135		0.024	0.115	0.757	$1.01x10^6$
7	W14x257	W14x283		W30x99		0.029	0.120	0.783	$1.01x10^6$
8	W14x257/ W14x233	W14x283/ W14x257		W27x84		0.033	0.123	0.768	$1.01x10^6$
9	W14x233	W14x257		W24x68		0.038	0.130	0.793	$1.09x10^6$

(d)

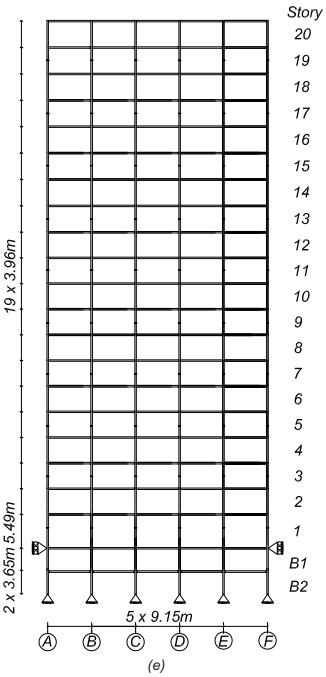

(e)

Story	Columns			Beams					Mass (kg)
	Exterior	Interior	Model	Section	Model	θ_y (rad)	θ_{pc} (rad)	$\Lambda=E_{so}/M_y$	
B2	15x15x2.0	W24x335	NL-FB-H	W14x22	NL-FMRB	-	-	-	-
B1	15x15x2.0	W24x335		W30x99		0.029	0.120	0.780	-
1	15x15x2.0	W24x335		W30x99		0.029	0.120	0.780	$5.76x10^5$
2	15x15x2.0/ 15x15x1.25	W24x335/ W24x335		W30x99		0.029	0.120	0.780	$5.76x10^5$
3	15x15x1.25	W24x335		W30x99		0.029	0.120	0.780	$5.63x10^5$
4	15x15x1.25	W24x335		W30x99		0.029	0.120	0.780	$5.63x10^5$
5	15x15x1.25/ 15x15x1.0	W24x335/ W24x229		W30x108		0.031	0.136	0.898	$5.63x10^5$
6	15x15x1.0	W24x229		W30x108		0.031	0.136	0.898	$5.63x10^5$
7	15x15x1.0	W24x229		W30x108		0.031	0.136	0.898	$5.63x10^5$
8	15x15x1.0/ 15x15x1.0	W24x229/ W24x229		W30x108		0.031	0.136	0.898	$5.63x10^5$
9	15x15x1.0	W24x229		W30x108		0.031	0.136	0.898	$5.63x10^5$
10	15x15x1.0	W24x229		W30x108		0.031	0.136	0.898	$5.63x10^5$
11	15x15x1.0/ 15x15x1.0	W24x229/ W24x192		W30x99		0.029	0.120	0.780	$5.63x10^5$
12	15x15x1.0	W24x192		W30x99		0.029	0.120	0.780	$5.63x10^5$
13	15x15x1.0	W24x192		W30x99		0.029	0.120	0.780	$5.63x10^5$
14	15x15x1.0/ 15x15x0.75	W24x192/ W24x131		W30x99		0.029	0.120	0.780	$5.63x10^5$
15	15x15x0.75	W24x131		W30x99		0.029	0.120	0.780	$5.63x10^5$
16	15x15x0.75	W24x131		W30x99		0.029	0.120	0.780	$5.63x10^5$
17	15x15x0.75/ 15x15x0.75	W24x131/ W24x117		W27x84		0.033	0.123	0.768	$5.63x10^5$
18	15x15x0.75	W24x117		W27x84		0.033	0.123	0.768	$5.63x10^5$
19	15x15x0.75/ 15x15x0.5	W24x117/ W24x84		W24x62		0.039	0.163	0.967	$5.63x10^5$
20	15x15x0.5	W24x84		W21x50		0.042	0.111	0.650	$5.97x10^5$

(f)

NL-FB-H - ***N****onlinear* ***F****orce-****B****ased Beam-Column Element with Fiber Section with 3% strain-****H****ardening*

NL-FMRB - ***N****onlinear* ***F****inite-****L****ength* ***M****odified Gauss-****R****adau Beam-Column Element with* ***B****ilinear Flexural Hinge Model*

Figure 6.4: Two-Dimensional Models of Steel Moment Resisting Frames Buildings in Los Angeles : (a) LA3 Building; (b) LA3 Sections, Model Parameters, and Floor Masses; (c) LA9 Building; (d) LA9 Sections, Model Parameters, and Floor Masses; (e) LA20 Building; (f) LA20 Sections, Model Parameters, and Floor Masses

the FEMA355C modeling. Thus, for the columns, the main phenomenon considered is the interaction between moment and axial load. This assumption is supported by recent testing [222], where it is shown that columns such as the ones being modeled do not exhibit deterioration in strength by more than 10% for $P/Py \leq 0.75$ even at 8% story drift ratios. For the buildings under analysis, which were designed using the strong-column-weak-beam assumption, only minor deterioration in stiffness and strength of columns is expected, and disregarding these effects will have no significant impact on the results. However, for buildings consisting of slender columns, this assumption may not hold and the effect of deterioration of the strength and stiffness of the columns should be evaluated.

Table 6.1: Models description

<table>
<tr><th rowspan="2">Model</th><th colspan="2">Columns</th><th colspan="2">Beams</th></tr>
<tr><th>Element formulation</th><th>Material</th><th>Element formulation</th><th>Material</th></tr>
<tr><td>FZLH</td><td rowspan="4">Force-based fiber-section distributed plasticity</td><td rowspan="4">Elasto-plastic with hardening</td><td rowspan="2">Zero-length (Concentrated plasticity)</td><td>Elasto-plastic with Hardening</td></tr>
<tr><td>FZLB</td><td>Bilinear with deterioration (Bilin)</td></tr>
<tr><td>FMRH</td><td rowspan="2">Finite-length plastic hinge (Modified-Radau)</td><td>Elasto-plastic with Hardening</td></tr>
<tr><td>FMRB</td><td>Bilinear with deterioration (Bilin)</td></tr>
</table>

Zero-Length vs. Finite-Length Plastic Hinge Elements

Based on what the work presented in Chapters 2 and 3, concentrated plastic hinge models are used herein as a reference, and the results obtained using the finite length plastic hinge models are compared with those to ascertain their accuracy.

Elasto-plastic Model with Kinematic Hardening vs. Bilinear Model With Deterioration

In the present chapter, a modified version of the Ibarra-Medina-Krawinkler [4,131] phenomenological model, applicable to any force-deformation relationship, is employed to simulate beam behavior and compared to a bilinear model with kinematic hardening. This model was used by Lignos and Krawinkler [4] to model the moment-rotation relationship of plastic hinges in steel elements. The description and implementation of this model was performed in Chapter 2 and 3.

Beams are simulated by using finite length plastic hinge elements with a plastic hinge length of $L_p = L/6$. All other model parameters are defined as proposed in Lignos and Krawinkler [4] and Lignos and Krawinkler [128]. Axial and shear behavior is assumed to

be linear elastic. Joint shear deformations [e.g. 101] and fracture due to low cycle fatigue [223] are not included in this chapter.

For the building examples analyzed, the axial load expected to develop in beams is very low and the interaction between axial load and bending moment in beams is significantly less relevant than the deterioration of stiffness and strength which is expected to occur in the beams. For this reason, the interaction between axial load and bending moment is disregarded for the beams. The modeling assumptions made in this chapter are intended to provide a relatively simple structural model and, at the same time, accurately simulate the deterioration of the steel members to collapse. Thus, the modeling of some building components was neglected in these models, such as beam-column joints, column base plate connections, and partially restrained connections. The influence of these components in the robustness of steel structures to cascading events is worth studying in future works.

6.5.3 Model Validation

The four models described were compared to those developed by Luco and Cornell [224], also designated as *Model M1* [77], for the same buildings. The models in Luco and Cornell [224] were developed using the software *DRAIN-2DX* [149]. The models implemented herein were developed in OpenSees. The elements used in the *DRAIN-2DX* models correspond to concentrated plastic hinge models and a linear P-M interaction surface was assumed for compressive axial loads greater than $0.15P_y$. While the model in FEMA355C [77] considered this simplified bilinear P-M interaction surface, the P-M interaction surface considered herein is obtained implicitly during the analysis since the columns are modeled using fiber-section nonlinear beam-column elements. A representation of the P-M interaction curve (at the section level) is presented in Figure 6.5.

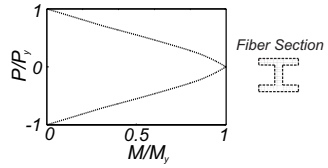

Figure 6.5: Fiber section P-M interaction curve

The model validation performed herein includes the comparison of results for both a nonlinear static pushover and nonlinear dynamic time-history analysis. Furthermore, the buildings periods available in the literature also correlate well with the ones obtained in the FE models developed in this chapter, as shown in Table 6.2.

Table 6.2: Periods of vibration for OpenSees models and FEMA355C model

	LA3 Building		LA9 Building		LA20 Building	
	OpenSees	FEMA355C	OpenSees	FEMA355C	OpenSees	FEMA355C
1^{st} Mode	1.04s	1.03s	2.40s	2.34s	4.10s	3.98s
2^{nd} Mode	0.34s	0.33s	0.90s	0.88s	1.40s	1.36s
3^{rd} Mode	0.18s	0.17s	0.52s	0.50s	0.81s	0.79s

Nonlinear Static Analysis

The nonlinear static analyses were carried out considering the four models described in Table 6.1 and compared to those presented in FEMA355C [77] and Luco [139]. The lateral load pattern applied is proportional to the first mode of vibration of each structure.

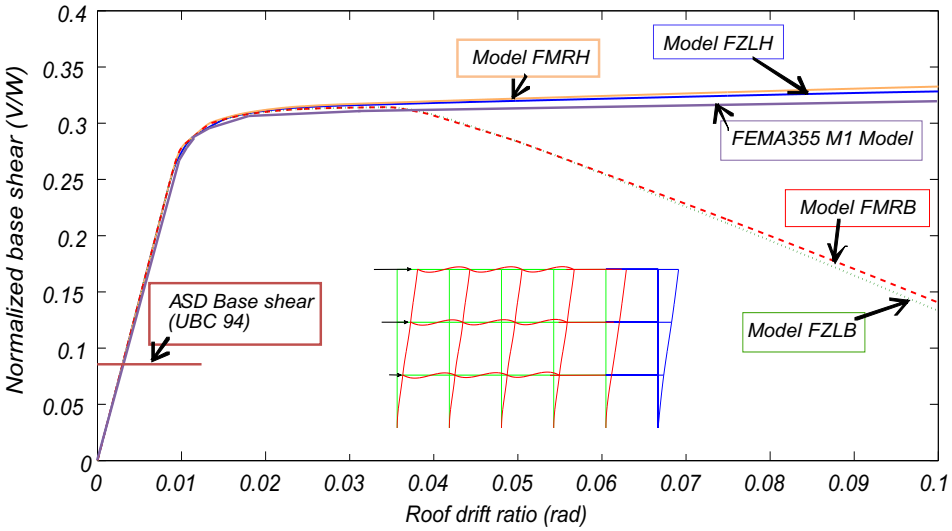

Figure 6.6: LA3 building - Nonlinear static (pushover) capacity curve considering a 1^{st} mode lateral load pattern

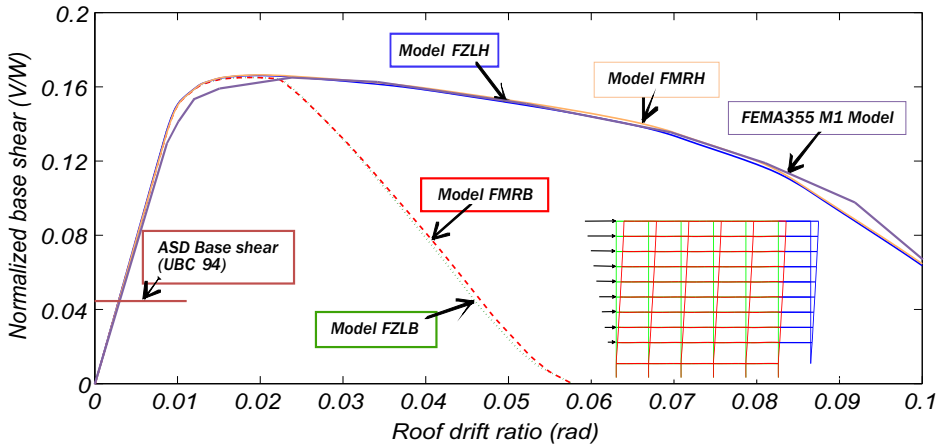

Figure 6.7: LA9 building - Nonlinear static (pushover) capacity curve considering a 1^{st} mode lateral load pattern

Figures 6.6, 6.7, and 6.8 show the pushover curves for each of the three buildings and the four finite element models used. For reference, these figures also show the design base shear quantified according to the allowable stress design method of the 1994 Uniform Building Code [138]. It can be seen from these figures that the overall match of the pushover curve are quite good for the models with hardening . In the elastic range the differences for all models to the results presented in FEMA355C [77] are small, increasing slightly with the increase in building height. In spite of the differences for the 20-story building being discernible in the elastic range, as shown in FEMA355C [77], such variations are expectable as

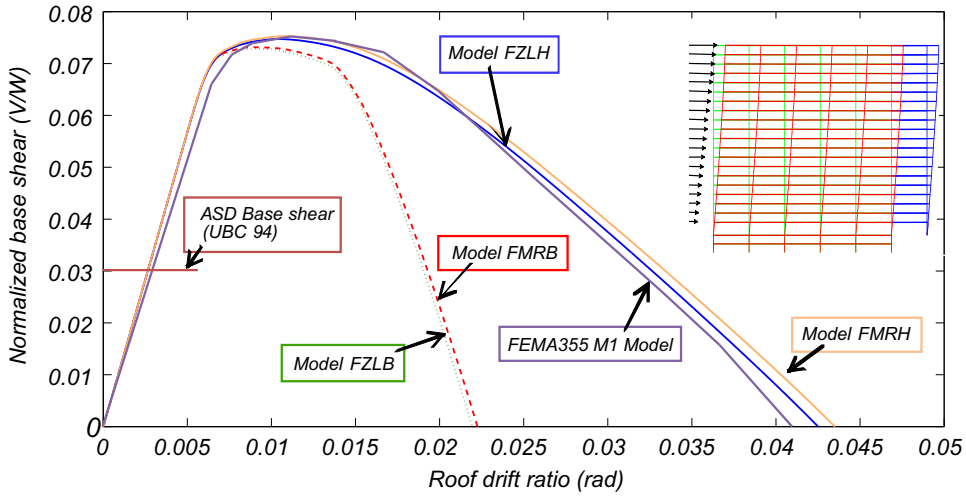

Figure 6.8: LA20 building - Nonlinear static (pushover) capacity curve considering a 1^{st} mode lateral load pattern

a consequence, for example, of alternative joints models. For all buildings, the models considering an elasto-plastic with hardening constitutive law (FMRH, FZLH, and FEMA355) presented a similar behavior, showing that the use of beam with hinges models does not affect significantly the results obtained. For the two taller buildings, a softening behavior is observable in all models, as a result of $P-\Delta$ effects. When the bilinear model with deterioration is considered (FMRB and FZLB) the post peak force decreases faster, as a result of the strength deterioration considered for the beams. As a consequence of the strong-column weak-beam design, plastic hinges form firstly in the beams. The use of the bilinear model with deterioration (FMRB and FZLB) leads to a faster decrease in the post peak base-shear force, as a result of softening in the beams and corresponding change in column moment gradient, once the plastic hinges form.

In summary, the results of the pushover analysis show that the models using an elastic-plastic constitutive law lead to results similar to those described in FEMA355C [77]. Secondly, the use of zero-length and beam with hinges does not affect the results significantly, allowing the use of the finite-length plastic hinges model in subsequent analysis. Finally, the use of the bilinear model with deterioration for the beams produced larger strength reduction.

Nonlinear Dynamic Time-History Analysis

To compare the results described in Luco and Cornell [142] with those resulting from the models used in this chapter, the structural response is evaluated considering forty (twenty two-component records) SAC Steel Project LA01-LA40 earthquake records. Forty nonlinear dynamic time-history response analyses are performed for each model and each of the three buildings. Obtained results are compared to those presented by Luco and Cornell [142] in terms of maximum interstory drift ratio. The results are presented in the Appendix. The mean relative errors obtained for each model and building are presented in Table 6.3. For the models considering an elastic-plastic behavior (FZLH and FMRH) the results are relatively close, with a maximum mean error of 7.4%. Larger errors are observed for models FZLB and FMRB, which are induced by the modes of cyclic deterioration included in these mod-

els. Correlation between the floor levels where these interstory drift ratios are observed for the models developed by Luco and Cornell [142] and the ones shown in this chapter is also quite good as shown in Figures 6.9 to 6.11, which presents the story where the maximum intertsory drift ratio is attained. The results obtained with models FZLH and FMRH are ploted against the results driven by Luco and Cornell [142] which serve as benchmark for this validation.

Table 6.3: Mean relative difference in peak interstory drift ratio to model M1 (FEMA355C 2000)

Building	Model			
	FZLH	FMRH	FMRB	FZLB
LA3	4.6%	4.0%	5.6%	8.7%
LA9	4.5%	5.1%	6.4%	8.4%
LA20	7.4%	6.3%	9.3%	9.8%

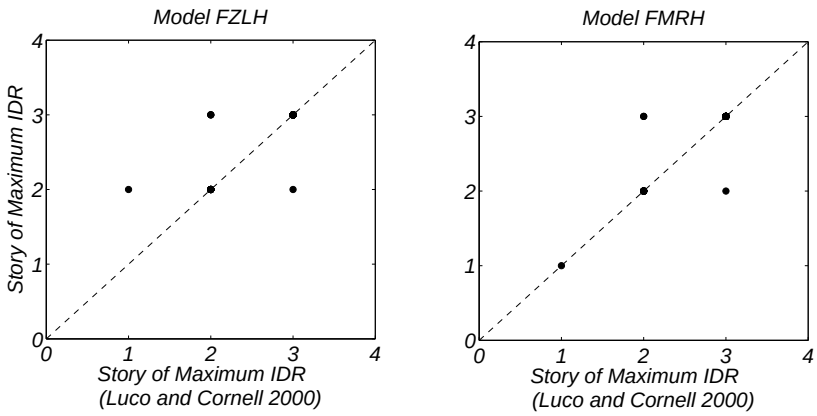

Figure 6.9: LA3 building - Correlation in the story of maximum interstory drift ratio between models $FZLH$ and $FMRH$, and FEMA355C (2000) models M1

The model validation performed is considered to be sufficient for the FZLH and FMRH models. Even though no direct validation of the FZLB and FMRB models with experimental results is possible, the definition of component deterioration is consistent with experimental results and P-M interaction is considered explicitly. Considering the advantages of the finite length model described in Chapters 2 and 3 and to include realistic effects of beam properties deterioration in the analysis, the FMRB model is used in the subsequent analyses.

6.6 Analysis Description

To evaluate the increased probability of failure associated with the occurrence of an aftershock following a major earthquake, a simulation procedure was employed that considered as random variables the spectral accelerations of the mainshock and the aftershock corresponding to the initial fundamental period of the structure. Although the occurrence rate and distribution of aftershocks are correlated to mainshocks magnitude [42], their amplitude,

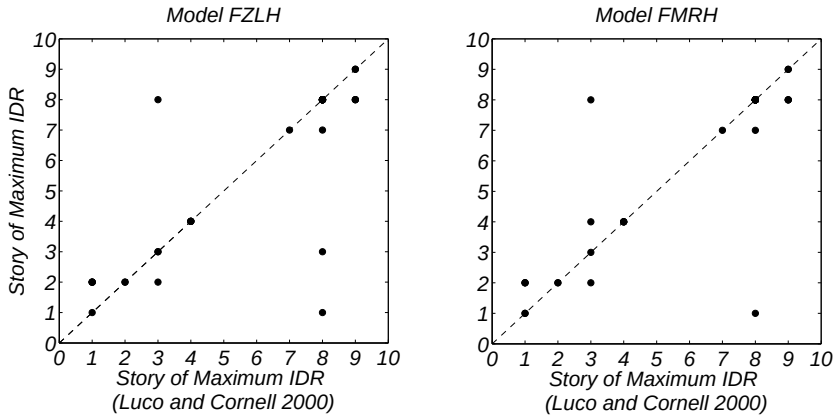

Figure 6.10: LA9 building - Correlation in the story of maximum interstory drift ratio between models $FZLH$ and $FMRH$, and FEMA355C (2000) models M1

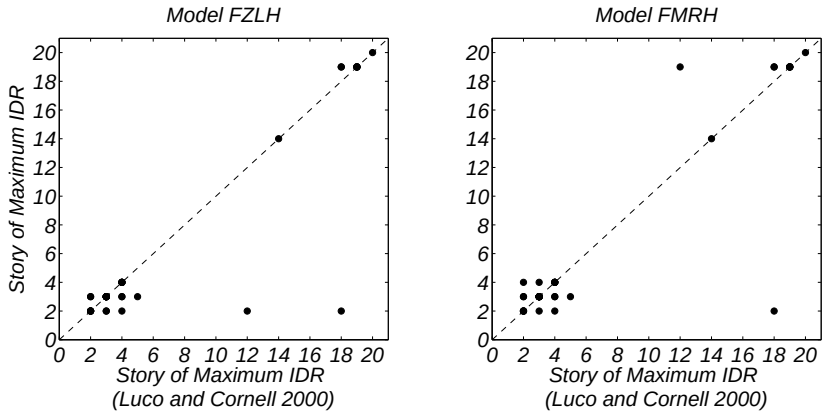

Figure 6.11: LA20 building - Correlation in the story of maximum interstory drift ratio between models $FZLH$ and $FMRH$, and FEMA355C (2000) models M1

frequency content, and duration are very complex to simulate. Thus, artificial mainshock-aftershock sequences are used herein, following Luco *et al.* [207], Ryu *et al.* [208], Li *et al.* [221], and Song *et al.* [200].

Herein, the reliability index for the mainshock β_{intact} is computed considering the spectral acceleration event space divided in 10 intervals for ten equally likely ground motion records each denoted as earthquake E_j using a technique known as Stratified Sampling [225]. The reliability index for the aftershock $\beta_{damaged}$ is computed using stratified sampling for the mainshock spectral acceleration and considering the conditional probability of failure due to aftershock as the probability of exceedance of the minimum aftershock spectral acceleration leading to failure. The probability of failure is computed considering the combination of 10 mainshock and 10 aftershock ground motion records. In this computation it is assumed herein that the mainshock and the aftershock ground motion spectral acceleration are uncorrelated.

6.6.1 Numerical and Computational Methods

The mainshock and aftershock are modeled considering a set of 10 accelerograms, each scaled independently, representing different shaking intensities. For performing incremental dynamic analysis (IDA), each of the 10 mainshocks considered is scaled 10 times, by multiplying the correspondent time-history record by the objective spectral acceleration, $S^m(T_1)$, divided by the original ground motion spectral acceleration, $S^{GM}(T_1)$, corresponding to a stratified sampling of the spectral accelerations. Each of the mainshocks can be followed by one of the 10 aftershocks. For each aftershock an IDA is also performed for at least 20 intensity levels. Thus, in this analysis the aftershock ground motion is incrementally scaled (by multiplying the time-history record by $S^a(T_1)/S^{GM}(T_1)$), similarly to the procedure of a regular IDA, performing a number of n back-to-back analysis, where n depends on the aftershock ground motion, the building being analyzed, and the damage state at the end of the mainshock. Each aftershock incremental dynamic analysis (AIDA) is computed considering the polarity of the aftershock (positive and negative directions). A 30s time interval of free-vibration is considered between the end of the mainshock and the application of the aftershock ground motion records. This duration is deemed sufficient after a preliminary study that showed that the maximum nodal velocity observed during the last second of this 30s interval was, for all buildings, smaller than 0.6% of the peak velocity observed for the mainshock leading to highest drifts short of collapse.

For each run, the Newton-Raphson method is used for solving the nonlinear system of equations at each time step. To analyze the structure up to interstory drift ratios of 20%, a convergence study of the horizontal roof peak displacement and horizontal peak floor absolute acceleration as a function of the integration time step was performed. Time-steps considered were 0.01s, 0.005s, 0.002s, 0.001s, 0.0005s, 0.0001s, and 0.00005s. It was observed that a time step of 0.002s was sufficiently small to produce negligible errors (when compared to the 0.00005s) and no significant changes in the response were observed when smaller time steps were used. In addition, other authors (e.g., Faggella *et al.* [226]) have observed that errors associated with accelerations are larger than the ones associated with structural displacements. As a consequence, it is recommended to analyze the errors associated with structural accelerations in order to guarantee stabilization of the error and convergence of the response. The root mean square errors (RMSE) obtained in these preliminary analyses are presented in Figure 6.12.

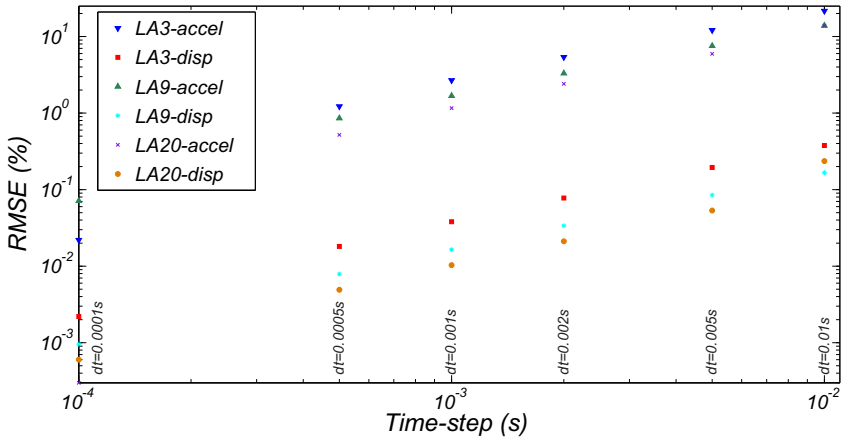

Figure 6.12: RMSE associated with roof acceleration and displacement as a function of the analysis time-step (considering 5×10^{-5} as reference time-step)

To reduce the total computational time required for obtaining all the results for these large number of runs, an embarrassingly parallel computing framework is implemented. The implemented framework makes use of the OpenSees (v2.4.0, release 5172) sequential version and a batch-queue system called HTCondor (v7.8.0) [166]. HTCondor is a specialized batch system for managing computational-intensive jobs. To make the most use of two student computer centers of Civil Engineering Departments at both Oregon State University (OSU) and Universidade Nova de Lisboa (UNL), two HTCondor pools are created, consisting of 464-cores at OSU and 96-cores at UNL. To minimize the time needed for simulation data transfer and post-processing of the numerical results, a OSU-UNL web shared folder is created using a commercial application.

6.6.2 Ground Motion Records

The ground motion records used in this study are selected from the set of forty SAC Steel Project LA01-LA40 earthquake records mentioned above, considering earthquakes with the highest peak ground acceleration. These records were obtained from real and simulated ground motions, scaled so that their mean response spectrum matches the 1997 NEHRP design spectrum, as reported by Somerville *et al.* [167]. The time histories for Los Angeles were all derived from recordings of shallow crustal earthquakes on soil category D. The ten SAC records selected for this study are characterized by a moment magnitude M_W between 6.0 and 7.4, duration between $29.9s$ and $59.9s$, and peak ground acceleration between $0.6g$ and $1.3g$. The ten E1 to E10 ground motion records used correspond to SAC earthquakes: LA11, LA18, LA19, LA21, LA26, LA28, LA30, LA31, LA36 and LA37.

In order to quantify the probability of failure of the structures, the spectral accelerations at Los Angeles are estimated from the hazard curves generated for the 2008 National Seismic Hazard Mapping Project (NSHMP) [217] for soil type D. These are approximated by a log-normal distribution, under the mild assumption that the findings of Jayaram and Baker [219] also hold for the modified ground motion records.

6.7 Deterministic Nonlinear Dynamic Time-History Response Analysis

This section presents results obtained for representative nonlinear dynamic time-history response analyses, selected from those described above. The performance of the LA3 building is assessed considering a mainshock ground motion spectral acceleration of $1.2g$ and $0.9g$ for the aftershock spectral acceleration. Earthquake ground motions E1 and E4 are used as the mainshock and aftershock, respectively.

Figures 6.13 and 6.15 show the time-histories response of the LA3 and LA9 buildings, respectively, in terms of floor acceleration, roof drift ratio, and interstory drift ratio during four identified time-periods (TP1-TP4): (i) TP1 - duration of the mainshock; (ii) TP2 - free vibration period of 30s after the mainshock; (iii) TP3 - duration of the aftershock; and (iv) TP4 - free vibration period of 30s after the aftershock. This figure also shows the floor accelerations and the interstory drift ratios at the instants when peak interstory drift ratio is attained during the mainshock and the aftershock, respectively. Regarding the response of the LA3 building, the peak interstory drift ratio during the mainshock is 4.1% at the 3^{rd} story. While, during the aftershock, the peak interstory drift ratio is approximately 5.7% also in the 3^{rd} story. In what concerns to the LA9 building, during the mainshock the peak interstory drift ratio is approximately 4.0% at the 4^{th} story, whereas during the aftershock the peak interstory drift ratio is 6.8% at the 2^{nd} story. In Figure 6.14 two moment-rotation responses are shown at two different elements of the LA3 building. It is important to note that during the aftershock the deformations are much larger, especially for beams, whose response go beyond the peak strength, i.e. a softening response is observable. Strength cyclic deterioration is also noticeable.

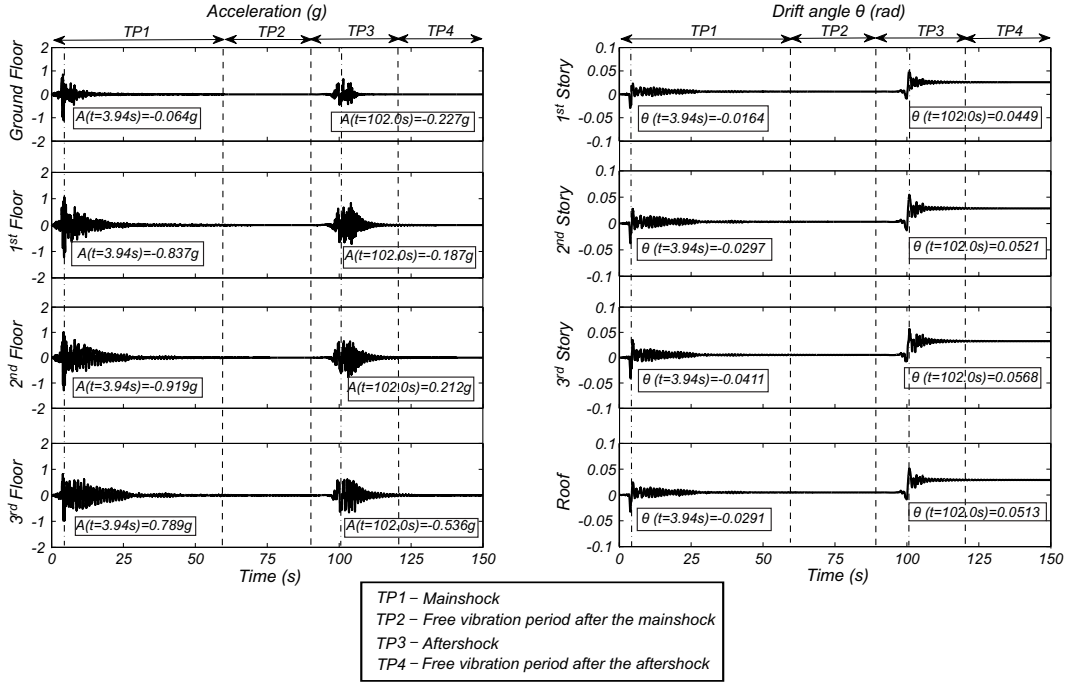

Figure 6.13: LA3 building - Example of a mainshock-aftershock back-to-back acceleration and drift response time-histories

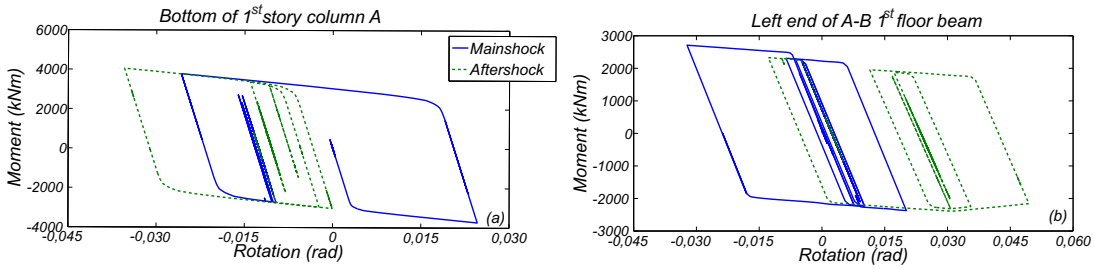

Figure 6.14: LA3 building hinge moment-rotation response at: (a) bottom of first story in grid line A; (b) left end of first floor level beam A-B

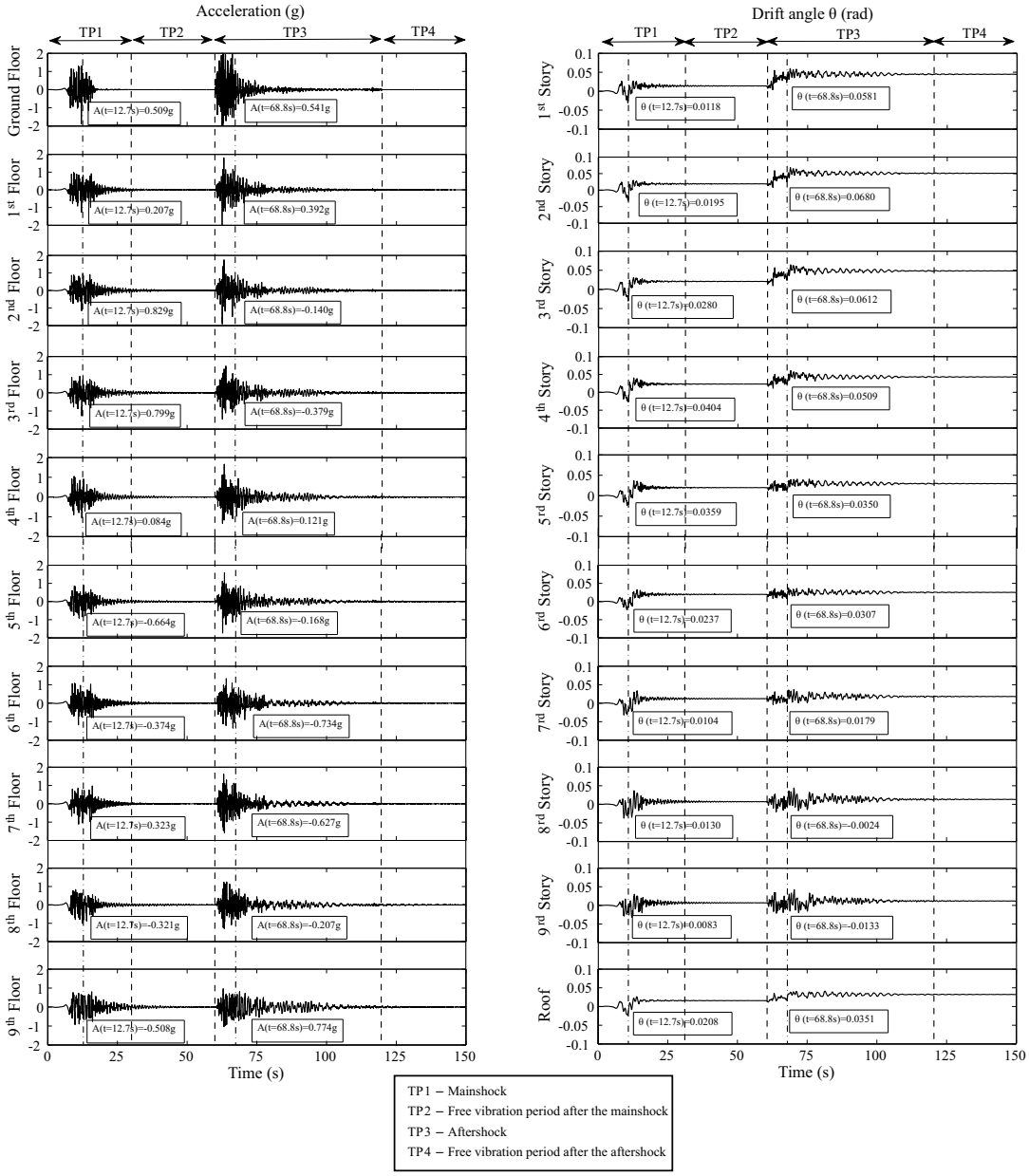

Figure 6.15: LA9 building - Example of a mainshock-aftershock back-to-back acceleration and drift response time-histories

The deformed shape of the LA3 building at the peak deformation instant is shown in Figure 6.16. This figure also shows the deformed shapes of the LA9 and LA20 buildings, in which, for representative analyses, the size of the circles illustrate the relative scales of rotations recorded at the end of each element. For the LA3 building, almost all beam ends had gone into the inelastic regime during the mainshock. Although the damage on the structure at the end of the mainshock is considerable, as it can be inferred through the number of plastic hinges formed during the mainshock, the residual deformation is not significant (see Figure 6.13). At the instant when the peak interstory drift ratio is recorded during the aftershock, columns on the first story have formed plastic hinges in both ends, which indicates that an undesirable soft story mechanism is formed. Four plastic hinges have also formed in second story columns and two in the third one. Effects of higher modes in the instants where peak interstory drifts are recorded can be observed in the LA9 and LA20 building response especially during the aftershock (see Figure 6.16).

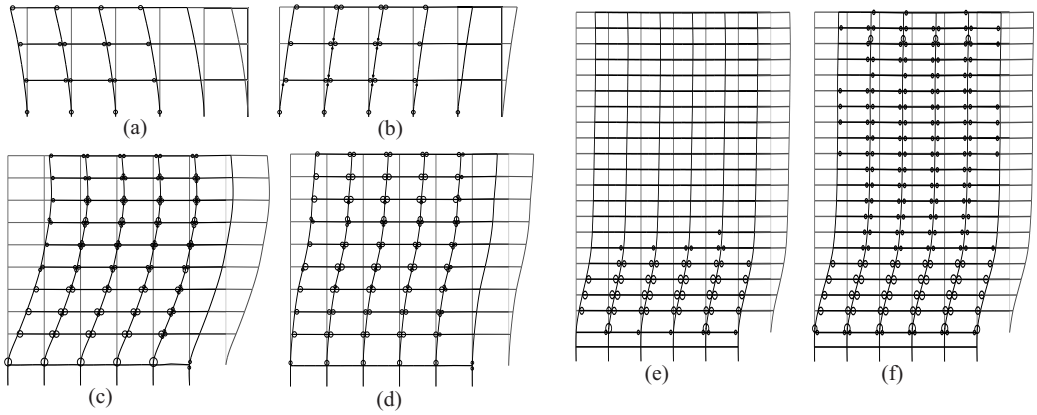

Figure 6.16: Deformed shapes of the buildings at two different instants: (a,c,d) - Peak interstory drift ratio during the mainshock; and (b,d,f) - Peak interstory drift ratio during the aftershock, for LA3, LA9 and LA20, respectively.

6.7.1 Aftershock Incremental Dynamic Analysis

For each mainshock-aftershock combination and each mainshock intensity, an AIDA is performed for increasing aftershock intensities in order to compute the failure probability under this sequence of events. In Figures 6.17 to 6.19, AIDA curves are shown for four mainshock ground motion spectral accelerations. Earthquakes E5, E7 and E10 are considered as mainshock for LA3, LA9, and LA20 buildings, respectively. Ten AIDA curves are then computed for the ten possible aftershocks. For each mainshock intensity, the results obtained show the variation of the peak IDR as a function of the aftershock ground motion spectral acceleration.

The value of 10% of interstory drift ratio is considered to be the threshold for failure [218]. Higher values of interstory drift ratio will lead to violation of the performance threshold and thus be considered as failure. Previous probability-based studies [e.g. 218] have concluded that 10% IDR is an adequate threshold to define collapse in a numerical framework. Although FEMA356 [220] defines 5% IDR for collapse prevention, to study the structural robustness (i.e., the capacity of the structure to sustain damage) this larger

value allows for the assessment of the nonlinear structural behavior under very large deformations, which contributes to the accurate evaluation of the reliability-based structural robustness by allowing for more accurate computation of the probability of failure.

The obtained AIDA curves illustrate the decrease in capacity with the increase in the mainshock intensity. For example for the LA3 building (see Figure 6.17), the aftershock E4 ground motion spectral acceleration that leads the structure to failure is $1.7g$ when the mainshock ground motion spectral acceleration is $1.2g$, whereas when the mainshock ground motion spectral acceleration is $2.4g$ the aftershock spectral acceleration that leads to failure is $1.1g$.

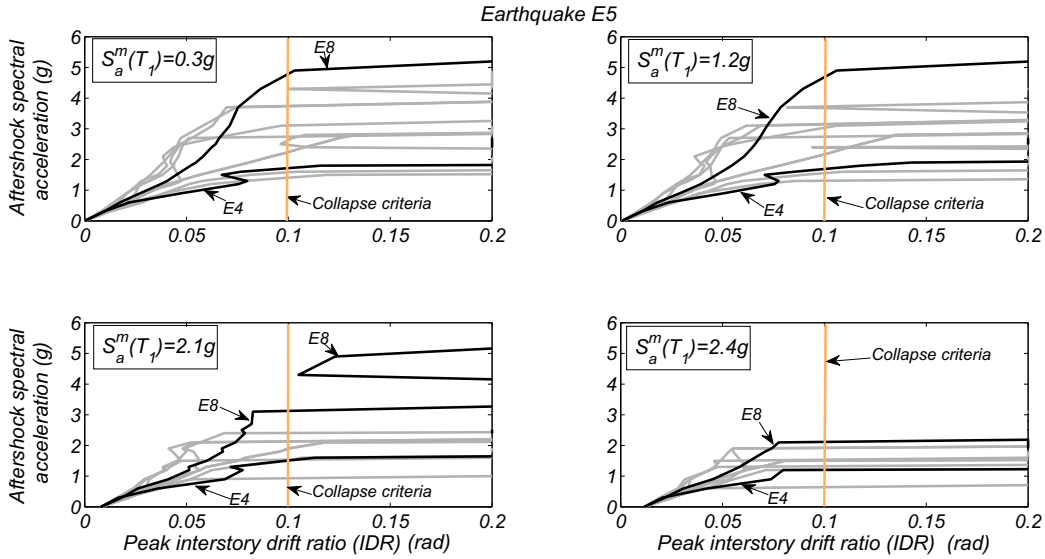

Figure 6.17: LA3 building - AIDA curves for ten earthquake records and four different mainshock ground motion spectral accelerations

An alternative approach for assessing the decrease in the post-mainshock building capacity would be to perform post-mainshock pushover analysis. Figure 6.20 shows examples of the capacity curves obtained with the LA3 building and three mainshock intensities. The intact capacity curve is also represented and serves as base for comparison. Although this approach is simple and provides useful results, important simplifications must be considered, namely in the type of lateral load distribution and the way mainshock damage is accounted for. In addition, this approach does not permit the computation of the probability of failure using the proposed methodology.

6.8 Robustness Assessment Results

Figure 6.21 shows the lowest aftershock spectral acceleration that leads the LA3 building to fail (Peak IDR = 10%) versus the mainshock spectral acceleration at the fundamental period of the intact structure (after gravity loads application). The figure corresponds to results obtained using earthquake E_5 for both the mainshock and the aftershock. It can be seen that for lower intensities of the mainshock there is little impact of mainshock induced damage on the aftershock spectral acceleration that leads to failure. Additionally, for increasing mainshock intensities, the aftershock spectral accelerations that lead to failure decrease, since

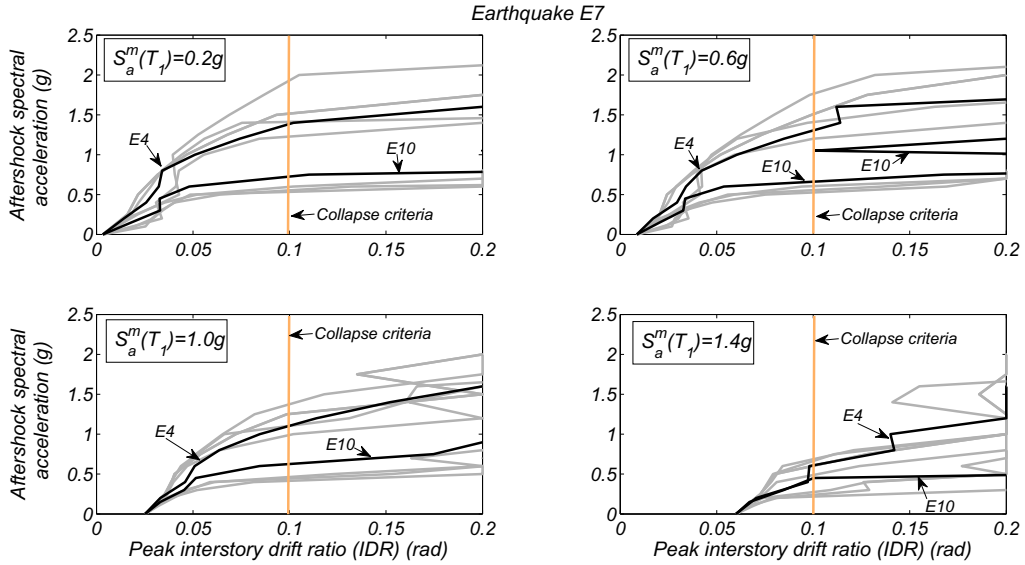

Figure 6.18: LA9 building - AIDA curves for ten earthquake records and four different mainshock ground motion spectral accelerations

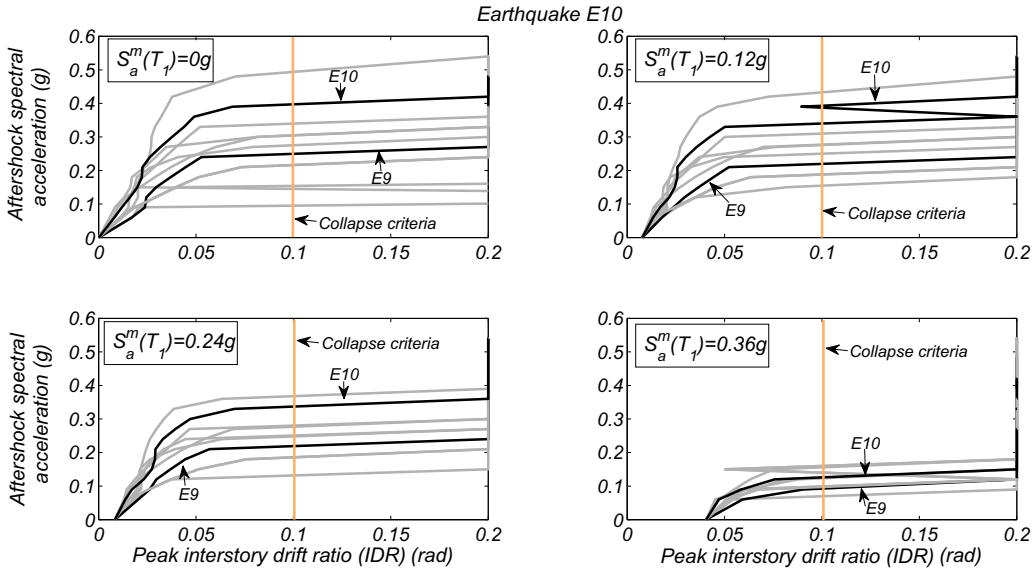

Figure 6.19: LA20 building - AIDA curves for ten earthquake records and four different mainshock ground motion spectral accelerations

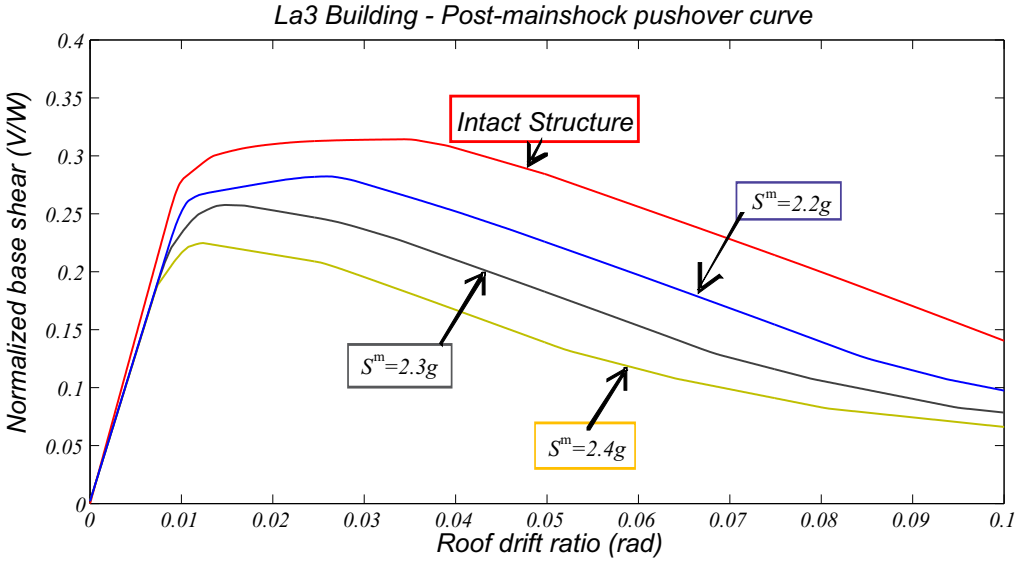

Figure 6.20: LA3 building - Post-mainshock pushover curves for three mainshock intensities

the mainshock induced damage reduces the capacity of the structure to sustain additional damage due to the aftershocks. Since the same accelerograms are used for generating both mainshock and aftershock, application of a mainshock only or an aftershock following a low intensity mainshock (i.e., causing no damage to the structure) are equivalent. Consequently, the lowest mainshock spectral acceleration leading to failure is identical to the (minimum) aftershock spectral acceleration that leads to failure for very low mainshock intensities.

In Figure 6.22 the median aftershock ground motion spectral acceleration that leads the structures to failure is represented as a function of the median mainshock ground motion spectral acceleration. A similar trend to that described for Figure 6.21 is observable here, but now for the entire set of AIDA analyses considered. Figure 6.22 also shows the median residual displacements after application of the mainshock. The results show a significant correlation between the increase in residual displacements and the reduction in the aftershock leading to failure, indicating that residual displacements could be used as a measure of damage.

In Table 6.4, the probabilities of failure and the corresponding reliability indices are presented considering mainshock, aftershock and mainshock+aftershock. The redundancy indicator, β_r, introduced by Frangopol and Curley [27], the vulnerability index proposed by Lind [28], V, as well as the robustness factor proposed in this work are used to compare robustness of the three buildings. The reliability indices obtained considering only the mainshock are very similar across structures, showing that the design procedure applied is consistent. However, the probability of failure considering aftershock and mainshock-induced damage increases much more significantly for buildings LA3 and LA20, than for LA9.

The results obtained for β_r, V, and RF, show that LA9, although less safe than LA3 and LA20 under a mainshock alone, is significantly more robust. These results can be correlated to the LA9 building ability to distribute damage over its entire height of the building as shown in Figure 6.16.

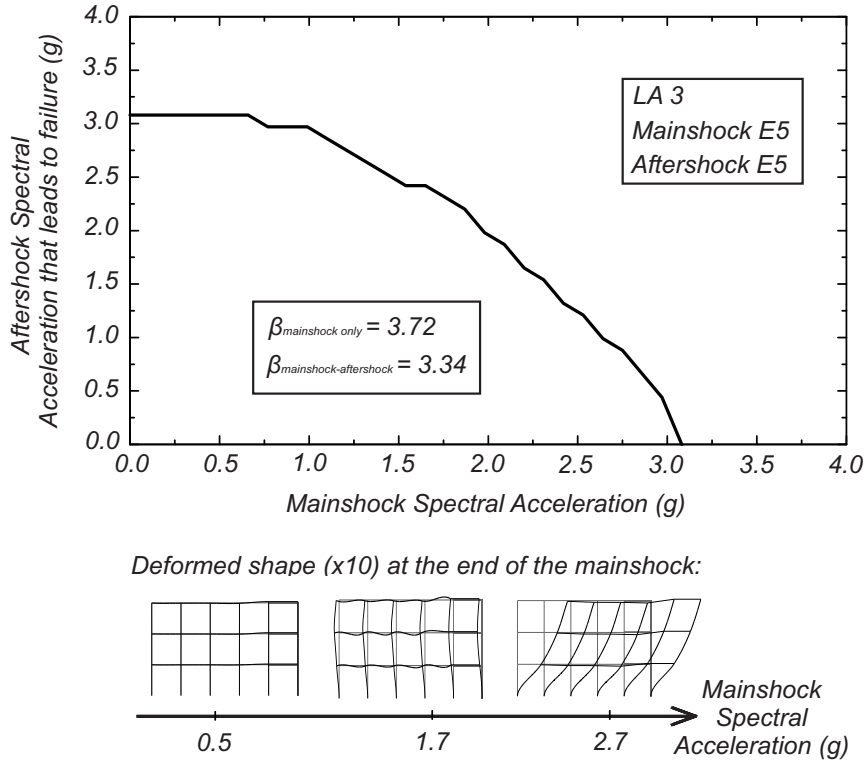

Figure 6.21: LA3 building - Aftershock ground motion spectral acceleration at the fundamental period of the intact structure that leads to failure as a function of the mainshock ground motion spectral acceleration for earthquake E5

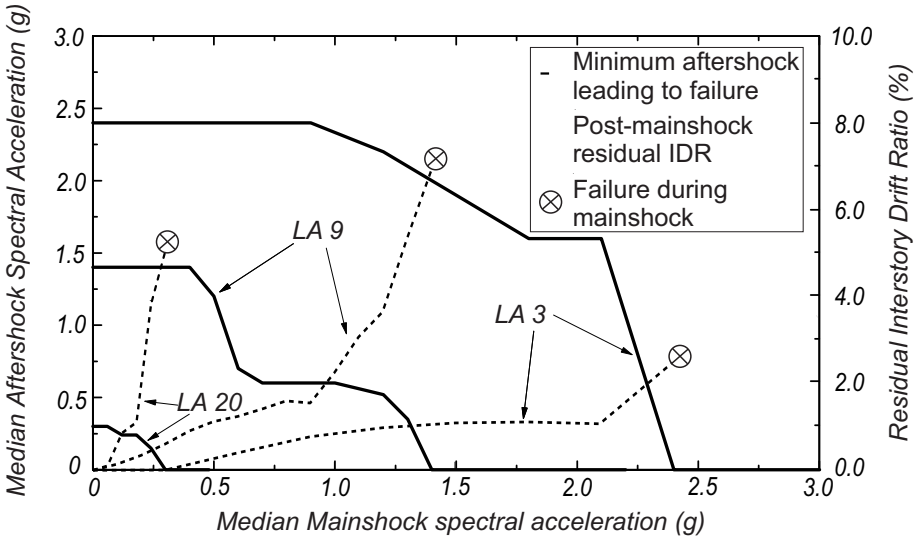

Figure 6.22: Median lowest aftershock ground motion spectral acceleration at the fundamental period of the intact structure that leads to failure (solid line and left vertical axis) and median residual interstory drift ratio after mainshock (dashed line and right vertical axis) as a function of the median mainshock ground motion spectral acceleration

Table 6.4: Probabilities of failure, reliability indexes and redundancy index associated with the scenarios considered

Scenario		LA3 Building	LA9 Building	LA20 Building
Mainshock	Probability of failure (p_{f1})	3.56×10^{-4}	7.22×10^{-4}	6.17×10^{-4}
	Reliability index (β)	3.38	3.19	3.23
Mainshock $\bigcup$ Aftershock	Probability of failure (p_{f3})	1.02×10^{-3}	1.66×10^{-3}	2.23×10^{-3}
	Reliability index (β)	3.08	2.94	2.84
Aftershock | Mainshock	Probability of failure (p_{f2})	6.64×10^{-4}	9.39×10^{-4}	1.61×10^{-3}
	Reliability index (β)	3.21	3.11	2.95
Redundancy index β_r		19.32	41.52	11.31
Vulnerability index V		1.87	1.30	2.61
Robustness factor RF		0.42	0.74	0.20

6.9 Fragility Curves and Repair Cost Estimation

Based on the results obtained in the performed aftershock IDA analysis, fragility curves are computed and the expected structural repair cost is estimated. The maximum likelihood method described in Section 1.6 and the FEMA-351 [170] threshold values presented in Section 4.9.3 (Table 4.5), defining the four Damage States (DS): (i) slight; (ii) moderate; (iii) extensive; and (iv) complete.

Figure 6.23 shows the aftershock fragility curves associated with the LA3 building. Each plot (i.e., Figures 6.23(a) to 6.23(d)) corresponds to one of the four DS. In each plot, eleven curves are represented, which correspond to the analyzed mainshock intensities. Each aftershock fragility curve is conditional on the mainshock intensity and the considered DS. Additionally, the fragility curve parameters, θ and β, whose derivation is explained in Section 1.6, are listed in the tables shown in the figure. The obtained fragility curves indicate that the probability of exceedance for a defined DS increases as the mainshock intensity increases. This is valid for the four considered DS, but the influence of the mainshock intensity on the probability of exceedance is much larger for the most critical DS's, namely for the extensive and complete DS. In these cases, the difference between the no-mainshock case (the same as mainshock only) and the case with the largest mainshock intensity, is considerable.

In order to investigate the variation of the fragility curves parameters, Figures 6.24(a) and 6.24(b) show the θ and β parameters as a function of the mainshock intensity, respectively. Figures 6.24(c) and 6.24(d) show the ratio between the fragility curve parameter associated with each aftershock fragility curve and the parameter associated with the fragility curve of the no-mainshock (or mainshock only) case. Figures 6.24(a) and 6.24(b) show similar

trends. First, a negligible variation is observed in the parameters associated the slight DS. Second, the curves associated with the remaining DS's have similar shapes and most of them tend to the same final value, namely for the θ parameter. It is important to note that with such low number of ground motions and performed analysis, parameter β may not be particularly accurate. Further investigation of the β parameter must be carried out. In this context, Figure 6.24(c) presents a very interesting trend for the variation of the ratio of the θ parameter. This plot shows that approximately the same ratio is obtained for the moderate, extensive, and complete DS's, as a function of the mainshock intensity. The slight DS yields different ratios as very small variation is recorded, regardless of the mainshock intensity. Finally, Figure 6.24(d) indicates that the aftershock β parameter associated with the largest mainshock intensity is much larger, namely for the complete DS, than the one associated with the no-mainshock case.

Finally, Figure 6.25 shows repair cost ratios (RCR) of the damaged building for mainshock-aftershock intensity pairs, which are computed following the basics mentioned in Section 1.6. Although RCR curves are computed for all mainshock-aftershock intensities, only six curves are shown in this figure for simplicity of visualization. As expected, based on the results of Figures 6.23 and 6.24, for the same aftershock spectral acceleration, the estimated RCR increases as the mainshock intensity increases. Is is worth noting that the approximate value of the total repair cost, shown in the figure is associated with only the structural components and is based on reference values provided by FEMA-351 [170] and are associated with the need to repair the building for the "complete" damage state.

Figures 6.26 to 6.31 show similar results for the LA9 and LA20 buildings, respectively. These results highlight the influence of the sequences of mainshock-aftershock events on the reduction of structural capacity and, consequently, the importance of the consideration of aftershock events in structural safety assessments. The fragility function parameter values, as well as the ratios computed by comparison with the no-mainshock case, can be useful for future works with these buildings.

6.10 Conclusion

In this chapter, a reliability-based robustness assessment methodology for steel moment resisting frame structures subjected to post-mainshock seismic events was proposed and exemplified. Robustness is computed through comparison of the structural reliability index under a mainshock, considering the undamaged structure, and under an aftershock applied to the mainshock-damaged structure. Probabilities of failure are computed through simulation, using nonlinear finite element models that explicitly reproduce damage induced by strong shaking. The methodology is exemplified using back-to-back mainshock-aftershock nonlinear dynamic time-history analyses.

For structures expected to form strong-column weak-beam failure mechanisms, a finite element modeling approach was presented in which columns were modeled using force-based fiber-section distributed plasticity elements and beams were modeled using a recently proposed phenomenological bilinear model with deterioration. The models used for the columns directly account for axial load- bending moment interaction. For the beams, the deterioration behavior defined for the plastic hinges is fundamental for accurate performance assessments under mainshock-aftershock sequences. The finite-length plastic hinge element is used due to its ability to model plastic hinge lengths explicitly and to separate the behavior

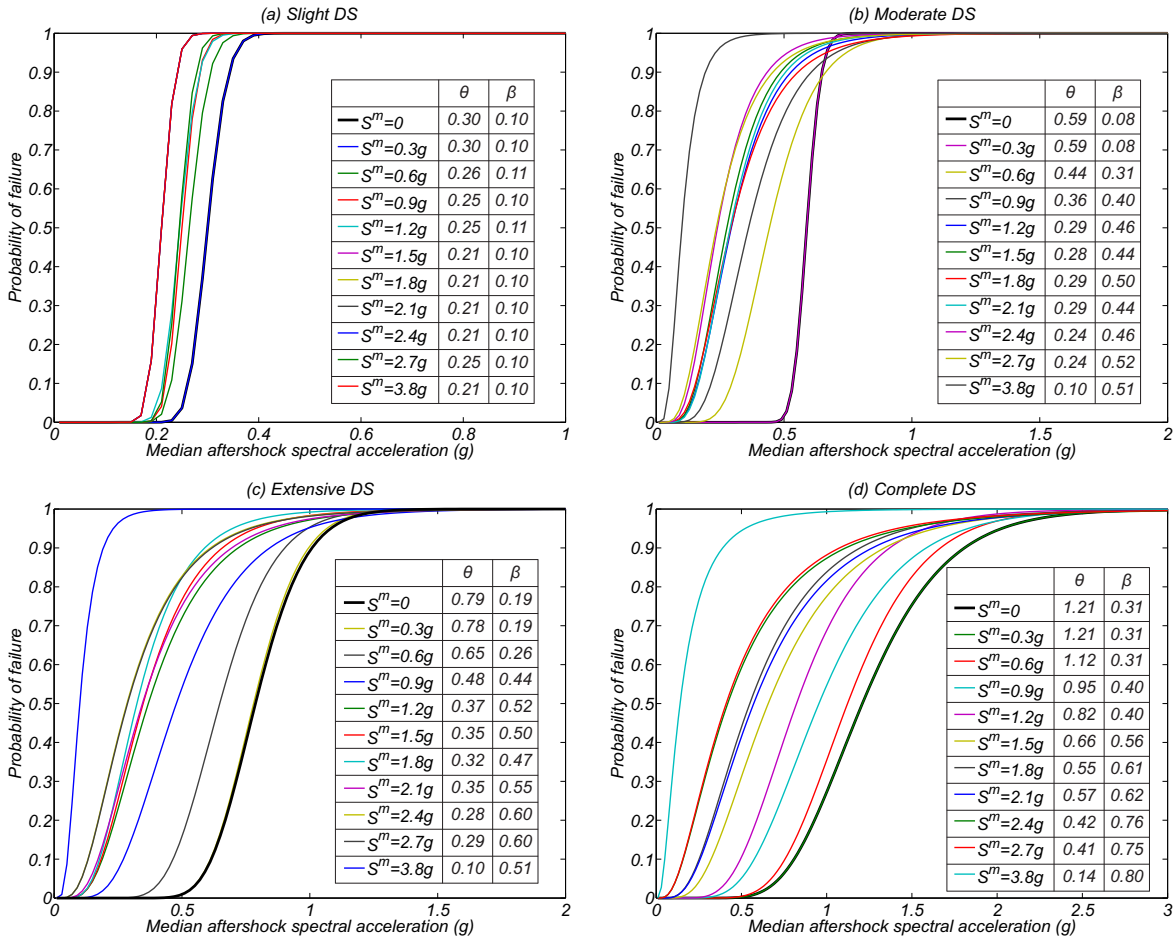

Figure 6.23: LA3 building - Aftershock fragility curves: (a) Slight DS; (b) Moderate DS; (c) Extensive DS; and (d) Complete DS

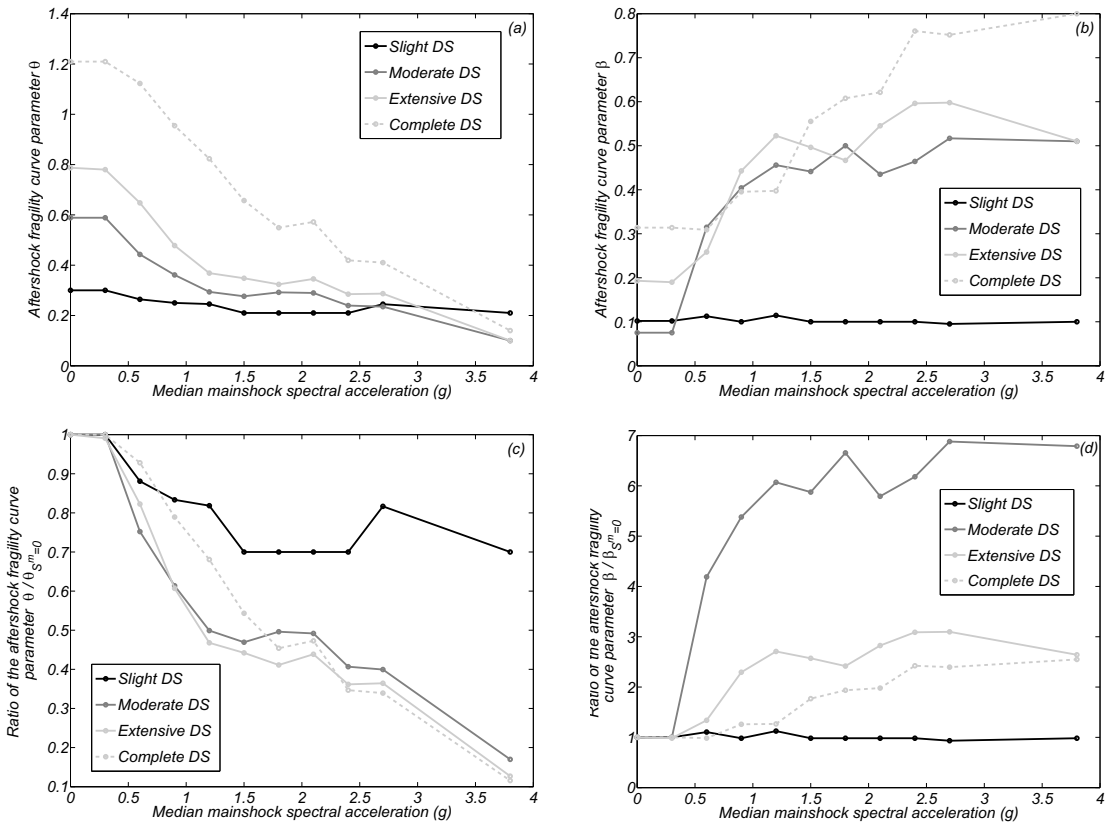

Figure 6.24: LA3 building - Variation of the aftershock fragility curve parameters as a function of the mainshock spectral acceleration: (a) variation of the θ parameter; (b) variation of the β parameter; (c) ratio $\theta/\theta_{S^m=0}$; and (d) ratio $\beta/\beta_{S^m=0}$

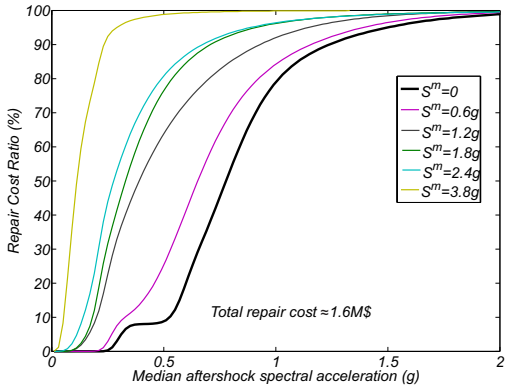

Figure 6.25: LA3 building - Estimated structural repair cost ratio as a function of the aftershock spectral acceleration

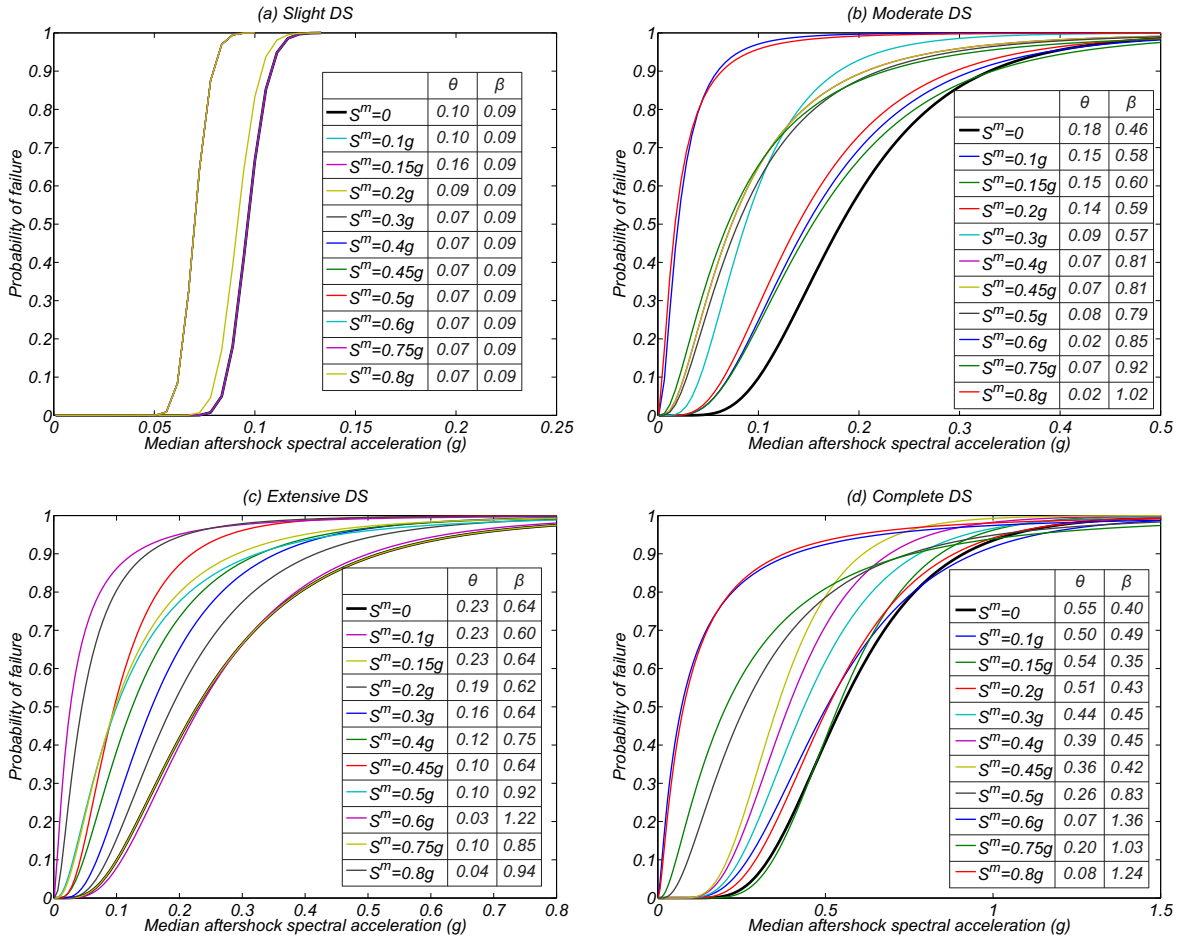

Figure 6.26: LA9 building - Aftershock fragility curves: (a) Slight DS; (b) Moderate DS; (c) Extensive DS; and (d) Complete DS

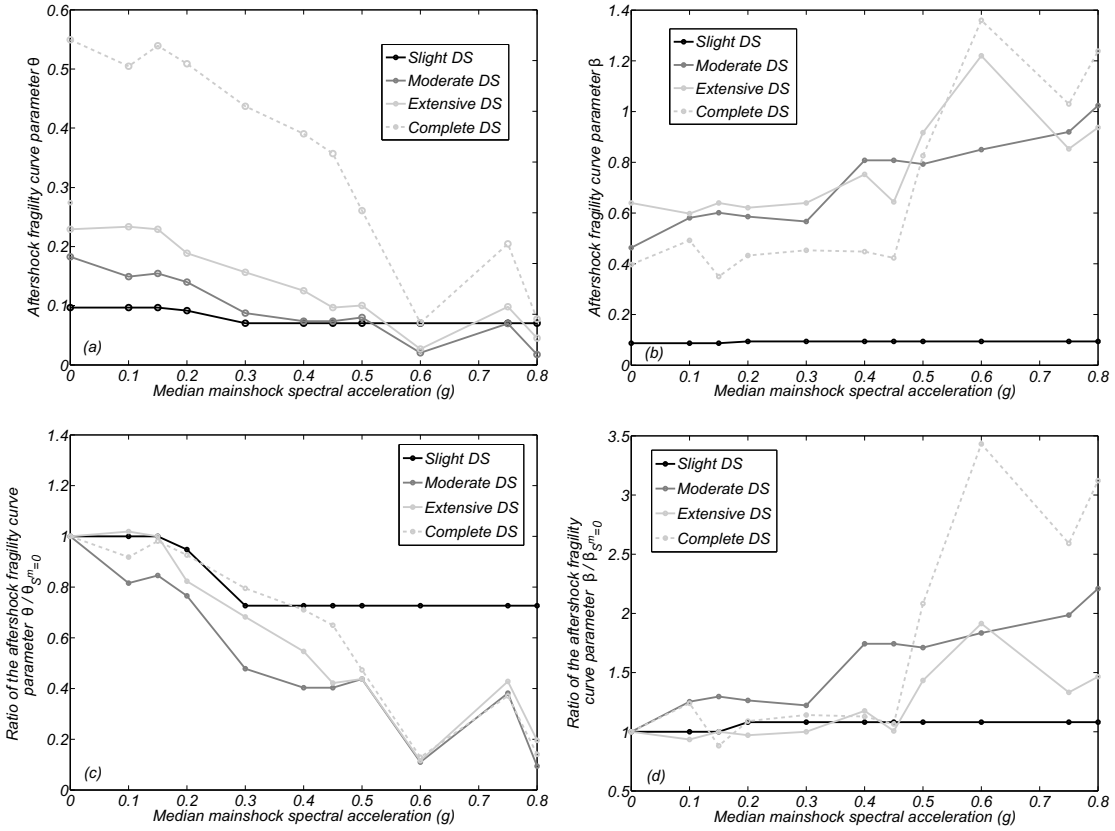

Figure 6.27: LA9 building - Variation of the aftershock fragility curve parameters as a function of the mainshock spectral acceleration: (a) variation of the θ parameter; (b) variation of the β parameter; (c) ratio $\theta/\theta_{S^m=0}$; and (d) ratio $\beta/\beta_{S^m=0}$

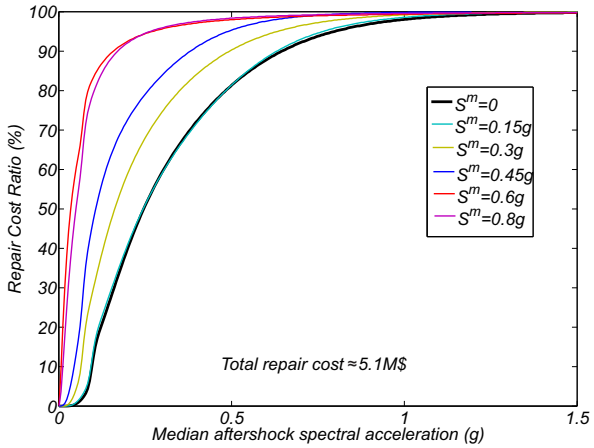

Figure 6.28: LA9 building - Estimated structural repair cost ratio as a function of the aftershock spectral acceleration

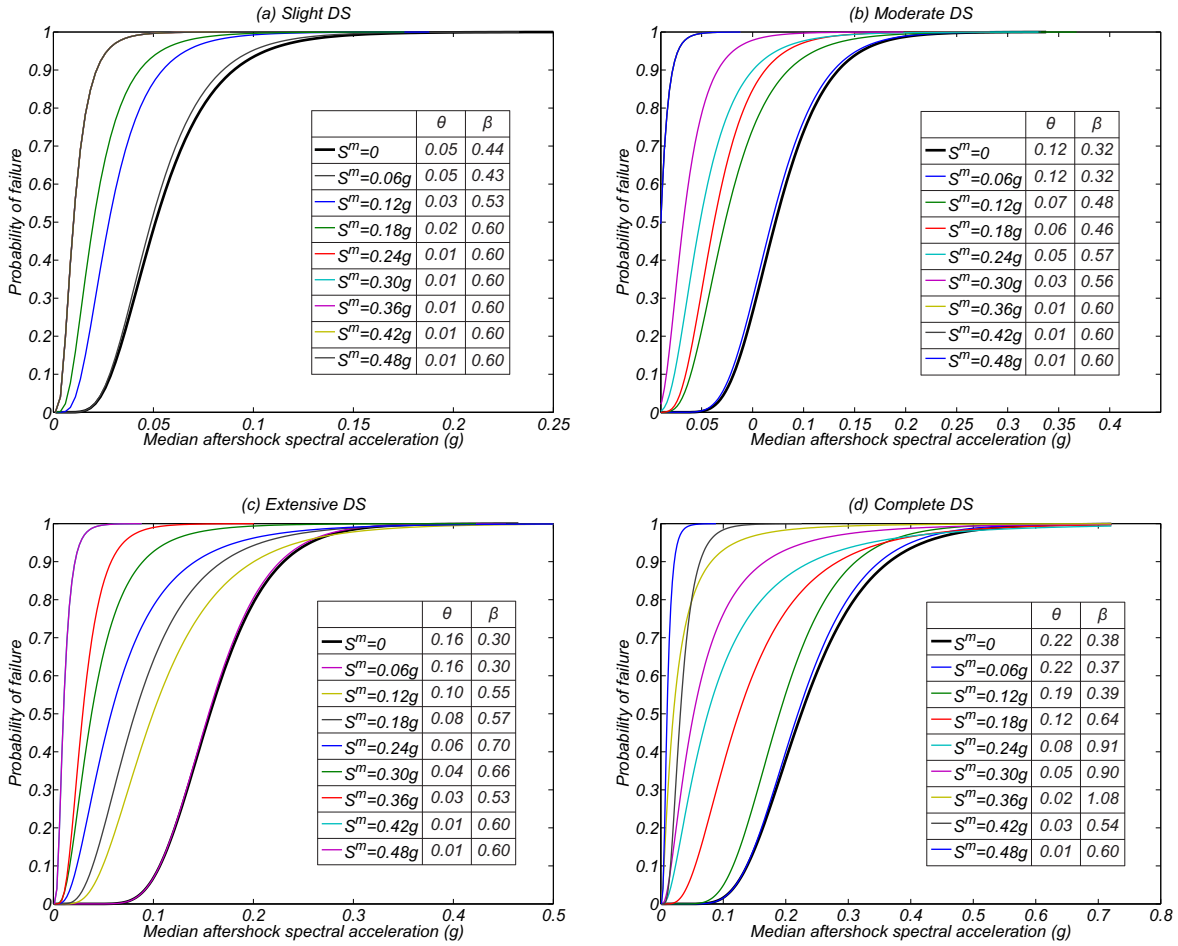

Figure 6.29: LA20 building - Aftershock fragility curves: (a) Slight DS; (b) Moderate DS; (c) Extensive DS; and (d) Complete DS

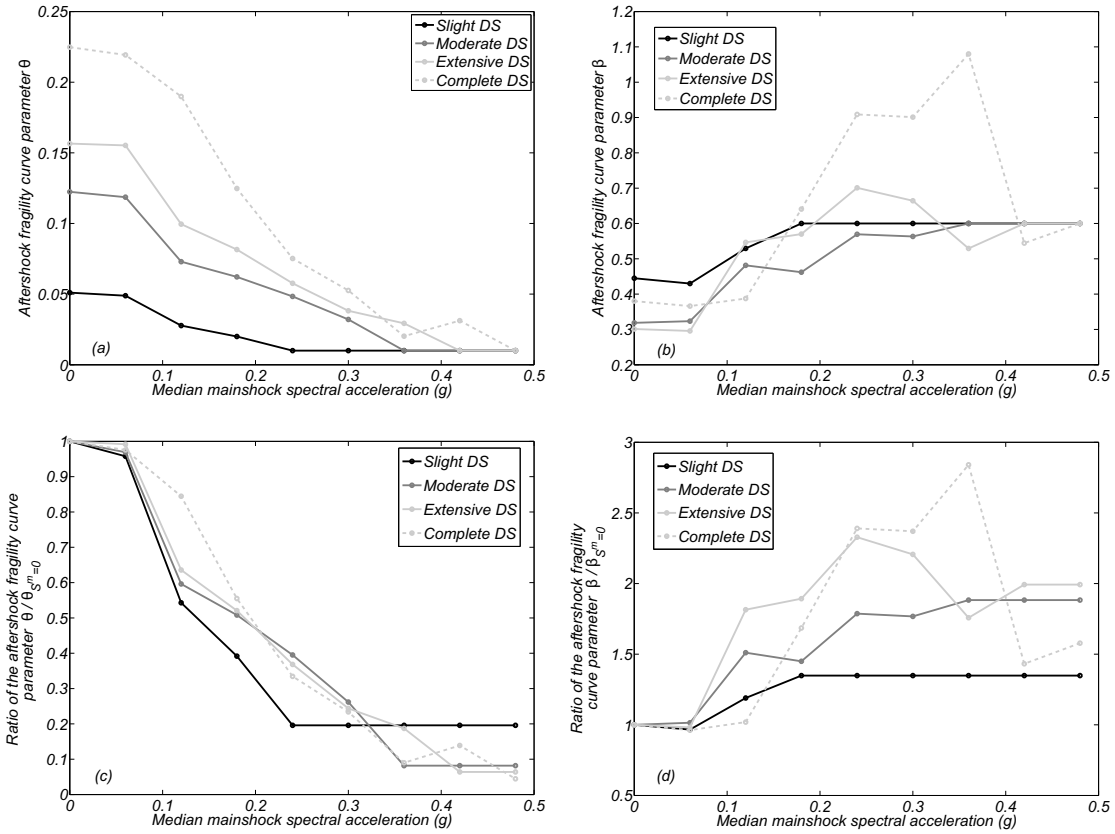

Figure 6.30: LA20 building - Variation of the aftershock fragility curve parameters as a function of the mainshock spectral acceleration: (a) variation of the θ parameter; (b) variation of the β parameter; (c) ratio $\theta/\theta_{S^m=0}$; and (d) ratio $\beta/\beta_{S^m=0}$

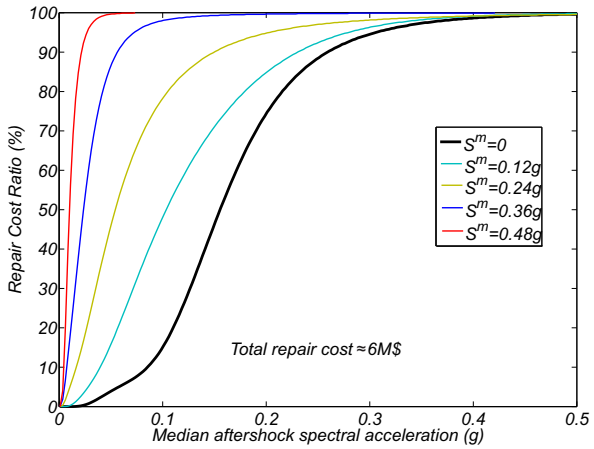

Figure 6.31: LA20 building - Estimated structural repair cost ratio as a function of the aftershock spectral acceleration

of beam in the span from that of beam-column connections.

Two-dimensional models of a 3-, 9-, and 20-story steel buildings, designed for the SAC project for Los Angeles, California, were implemented in the OpenSees framework. For simulating the mainshock-aftershock sequence of events, ten different mainshock and aftershock ground motion records were combined. The spectral accelerations at fundamental periods of the buildings were used to simulate mainshock and aftershock intensities that follow lognormal distributions. "Back-to-back" mainshock-aftershock incremental dynamic analyses are performed for each combination of mainshock-aftershock, while failure is defined in terms of the exceedance of an interstory drift threshold. It is worth noting that the results presented here are sensitive to the frequency content of the ground motions (both aftershock and mainshock), period elongation due to cyclic deterioration in stiffness from the mainshock, and the definition of the fundamental period of the frame structures. These important factors are not considered herein, and as discussed in Faggella *et al.* [226] can only be adequately accounted for by using a vector-valued ground motion intensity measure. The use of vector-valued ground motion intensity measures falls outside the scope of this chapter.

Application of the reliability-based robustness assessment showed the importance of considering the aftershock in the evaluation of safety of structures under seismic events, as a significant increase in failure probability was observed when mainshock-aftershock sequences were considered. Moreover, this study showed that the LA9 building, although initially more susceptible to failure than the LA3 and LA20 buildings, presented significantly higher robustness for the aftershock events ($\beta_r = 41.52$ for LA9 versus $\beta_r = 19.32$ and $\beta_r = 11.31$ for LA3 and LA20, respectively). In fact, robustness is defined in terms of the increase in probability of failure considering damage, and LA9, although less safe than LA3 and LA20 under a mainshock alone, presents a lower reduction in reliability index when cascading events are considered. Thus, it can also be concluded that the probabilities of failure for multiple hazards requires explicit modeling of the hazards and simulation methods need to accurately model the damage induced by the cascading hazards. Finally, mainshock-aftershock fragility curves and repair cost ratios were derived based on the results obtained with the proposed framework. Some threshold values were derived that may be useful for the development of future probabilistic studies and risk assessment methodologies. Interesting trends were identified in what concerns the variation of fragility curve parameters as a function of mainshock intensity. However, these need more scrutiny in future works due to the low number of ground motions considered in this work.

6.11 Dissemination

This part of the research program resulted in the following outputs.

1. Scientific paper published in the Journal of Structural Engineering

   Scope: Presentation of the reliability-based framework for quantifying structural robustness considering the occurrence of a mainshock followed by aftershocks. The application of the proposed framework is exemplified through the study of the three SAC steel moment frame buildings.

Complete reference: Ribeiro, F., Barbosa, A., and Neves, L. (2014). "Application of Reliability-Based Robustness Assessment of Steel Moment Resisting Frame Structures under Post-Mainshock Cascading Events." Journal of Structural Engineering, 140, SPECIAL ISSUE: Computational Simulation in Structural Engineering, A4014008.

2. Poster presentation made at the XV World Congress on Earthquake Engineering (2012)

   Scope: Presentation of the general formulation for structural robustness assessment under post-earthquake cascading events. A case study is presented for a 3-story steel moment resisting frame located in Lisbon, Portugal. In this case study a triggering mainshock is followed by: (i) an aftershock, or (ii) direct column removal that induces localized damage on the structure (which can lead to partial collapse) and then followed by an aftershock. Through quantification of the structural safety under a mainshock alone and comparing it with the safety associated with these sequences of events, it is possible to assess the robustness in these scenarios.

   Complete reference: Ribeiro, F., Barbosa, A., and Neves, L. (2012). "Seismic Robustness Assessment of Code Compliant Steel Moment Resisting Frame Under Seismic Triggered Sequences of Events." In: XV World Congress on Earthquake Engineering. Lisbon, Portugal.

3. Oral presentation made by Professor André R. Barbosa at the International Conference on Structural Safety and Reliability, ICOSSAR (2013)

   Scope: Presentation of the framework for structural robustness considering mainshock-aftershock sequences. A new reliability-based robustness index was presented, which overcomes issues identified in the most used indices. The application of the framework and the new robustness index is exemplified through the study of the three SAC steel moment frame buildings.

   Complete reference: Ribeiro, F., Barbosa, A., and Neves, L. (2013). "Reliability-Based Robustness Assessment of Structures Subjected to Post-Mainshock Hazard Events." In: ICOSSAR 2013. New York, U.S.A.

Chapter 7

Robustness Assessment of Structures Considering Post-Earthquake Fire

7.1 Scope

In this Chapter a probabilistic framework for performance-based structural engineering (PBSE) for fire following earthquake is proposed. This framework allows for the estimation of decision variables similarly to what is done in the PEER PBEE. The theoretical aspects of the framework are detailed herein. However, before applying this framework, a sensitivity study is carried out in order to contribute to the identification of the most important variables in steel fire response and to the definition of trends in what concerns to the relationship between fire intensity and structural performance. In this context, the work is divided in two main parts, a sensitivity study and an incremental fire analysis. The development of these preliminary studies is deemed necessary prior to the study of the fire following earthquake case.

7.2 Introduction

The problem of fire following large earthquakes raises significant concerns in earthquake prone areas. The evaluation of the occurrence and consequences of fires following earthquakes are a highly nonlinear and uncertain problem. This Chapter presents a probabilistic framework for performance-based structural engineering (PBSE) that includes both earthquake and fire performance assessment, namely in the specific case of fire following earthquakes. This probabilistic framework can be seen as an extension of the performance-based earthquake engineering (PBEE) methodology developed by the Pacific Earthquake Engineering Research (PEER) center in the past decades. The proposed framework represents a first step towards a rational methodology for fire following earthquake performance assessment of structures.

However, the execution of structural fire analysis can be cumbersome due to large number of variables influencing structural response. As a consequence, a preliminary study, which aims at identifying the most important variables affecting the response of steel structures under and immediately after being subjected to thermal fire loading, is conducted in this Chapter. Two case study examples are presented, which use the thermal tools of the Open System for Earthquake Engineering Simulation (OpenSees) framework. Structural

fire analyses are conducted considering different fire scenarios and a set of seven random variables. Peak and residual deformations are tracked in order to assess structural response. In addition, pushover and pushdown analyses are carried out to evaluate the structural capacity to sustain further load after fire. Tornado Diagram Analysis (TDA) is used to evaluate the sensitivity of the structural response to each variable.

The results obtained are used to validate the OpenSees Thermal modeling tools, as well as identify the most important parameters and variables when performing fire analysis. The relationship between fire loading, deformations, and vertical load bearing capacity, is also analyzed through incremental fire analysis. These conclusions are important to improve the efficiency of probabilistic-based engineering methods considering fire demands, namely by reducing the computational cost associated with the consideration of a large number of variables. The results of this sensitivity analysis will be used in the future application of the proposed PBSE for fire following earthquake.

7.3 Literature Review

7.3.1 Structural Fire Simulation

The study of structural fire has received significant attention in the last decades. In fact, despite the widely known advantages of steel structures, namely in what concerns lightweight, high strengh, appealing architecture, ease of erection, and recyclable materials, issues related to fire resistance have been identified [227–229]. Extensive numerical and experimental analyses have been performed to assess the behavior of isolated members and/or connections as well as building structures under fire loading.

Johansson [230] presents a review of numerical experiments and put into the context of traditional compartment fire experiments. Takagi and Deierlein [231] evaluated the design equations of EC3 and AISC for prediction of member resistance capacity at elevated temperatures through an extensive experimental study and comparison with numerical results.

Among the numerical studies that have been developed, most of the structural fire analyses have been performed using the ABAQUS [232], or the SAFIR [233] finite element programs. Vassart et al. [234] perform a benchmark study between ABAQUS, ANSYS [235] and SAFIR. Memari and Mahmoud [229] analyzed the three SAC Steel Project LA buildings under single-bay fires using ABAQUS. Eurocode 3 prescriptions were used when modeling thermal behavior of steel members. Several fire scenarios were considered and conclusions on local and global response of the three buildings were taken.

Garlock and Quiel [236], using SAFIR program, examined the interaction between the perimeter column and the beam that frames into it through the study of a steel high-rise building subjected to a large fire. Sun et al. [228] implemented a static-dynamic analysis in the Vulcan software [237] for performing progressive collapse studies of frame structures under fire. Several case studies were analyzed and different collapse mechanisms were compared in the context of progressive collapse. Loading ratio, beam sizes, and bracing system influence on collapse resistance was deeply investigated.

For studying combined hazards, such as the case of earthquake-fire, a versatile and efficient software is required. In this context, the OpenSees framework has been successfully used in simulating multiple hazard risk scenarios, making it suitable to be used in this work. In fact, an extensive fire module was implemented in the OpenSees framework by Jiang et

al. [238]. Using this framework, Jiang et al. [239] investigated the effect of different bracing system in the progressive collapse resistance of steel frames under fire. Khorasani et al. [240] implemented in OpenSees a new steel model that proved to accurately capture cooling phase and efficiently simulate cumulative degradation of steel under multiple hazards.

These studies followed a deterministic approach in modeling fire conditions and structural response. However, the uncertainty related to this topic require probabilistic studies to be developed so that general conclusions may be taken and used in Performance-Based Engineering (PBE) methods. As a consequence, probabilistic studies have recently been applied to study fire demands [241–244] . For example, Ramroth and Asaro [244] carried out various types of sensitivity analyses and an uncertainty analysis of a model for the thermal decomposition and heat transfer through a composite panel. Coupling of three models were accomplished: a thermal model, a model of mechanical property degradation with temperature, and a thermo-mechanical structural model. A total of 11 random variables were considered and results highlight how the input parameters affected the results, as well as quantify the expected variability in the model output.

Conclusions of these probabilistic studies contribute to the development of PBE methods that include fire such as the application of the PEER performance based earthquake engineering framework to structures in fire proposed by Lange et al. [242].

7.3.2 Performance-Based Fire Engineering

In this context, in this work a preliminary proposal for performance-based structural engineering for fire following earthquake is presented. Quiel and Marjanishvili [245] developed a multi-hazard analysis by introducing an initial damage on the structure that is simulated by direct column removal. Subsequently, the bays adjacent to the removed column are subjected to fire loading. Braxtan and Pessiki [246], Memari *et al.* [247], and Faggiano and Mazzolani [248] have also developed studies on the behavior of steel frames under fire following earthquake.

Despite these relevant works, a single and universally accepted approach for performance-based structural engineering of building structures for fire following earthquakes has not been proposed to date. In this work, a performance-based structural engineering framework for fire following earthquake is developed.

Performance-based structural engineering for fire conditions has received little attention by the structural engineering community. However, it has been investigated by fire safety engineers in the past decades and several performance-based assessment and design frameworks for fire conditions have been proposed in the literature [249–252]. Hamilton [251] proposed a performance-based fire engineering (PBFE) approach that was developed based on an adaptation of the PEER PBEE framework, and was proposed to be a single, generally accepted framework for PBFE.

The work of Hamilton [251] is summarized in the following paragraphs to illustrate how the PBEE framework can be adapted for PBFE and later to serve as the basis of the framework being proposed herein for the performance-based structural engineering for fire following earthquake. Table 7.1 lists the required attributes for PBEE and the corresponding ones for PBFE. It is worth noting that for the first three analytical processes (hazard analysis, structural analysis, and damage analysis) there are two different rows for the different hazards: seismic hazard and fire hazards. However, for the loss analysis, the model parameters and measurable outcomes that can be used as decision variables are identical for both

seismic and fire hazard.

The first step in a performance-based assessment is the characterization and quantification of the hazard. Hamilton [251] developed a PBFE framework for steel structures and defined the fire intensity measure (IM_F - note that the subscript F is introduced to differentiate the fire intensity measure from the ground motion intensity measure IM) to be the "maximum steel temperature", which corresponds to the maximum temperature in the structural element. In PBFE, the definition of a realistic "fire hazard curve", $\nu(IM_F)$, is of crucial importance to the development of reasonable loss results. The fire hazard curve can be given by:

$$\nu(IM_F) = \int \int dP(IM_F|FO)dP(FO|F)\nu(F) \tag{7.1}$$

where $\nu(F)$ corresponds to the probability of ignition, $dP(FO|F)$ is the conditional probability of flashover conditional on the occurrence of given ignition, and $dP(IM_F|FO)$ is the probability of the structural element reaching a certain temperature, given flashover. The IM_F proposed by Hamilton [251] was considered to be appropriate since it can directly relate the induced temperatures in the steel member to structural EDPs through nonlinear structural analysis [252,253] and thus would tend to be a good candidate for a "sufficient" IM. A "sufficient" IM would also have to be a proxy of the model parameters described in Table 7.1 (compartment geometry, ventilation, etc.). The evolution of a fire in a structure is usually dependent upon the form of the structure as well as its features. It may therefore be necessary to develop a suitable catalogue of fires to each structure, to determine the intensity measure and the engineering demand parameters. However, as noted by Hamilton [251], this is not always the case, as the large deformations of local collapse (an example of an EDP) could change the compartment layout, further allowing the spread of fire (horizontally or vertically), and change ventilation conditions, for example. Nonetheless, in the absence of a more consistent indicator, it was considered by Hamilton that the maximum temperature in the structural element would be a sound IM.

The next step in PBFE is the estimation of the EDPs conditional on IM_F. This step corresponds to the time-history response analysis of a nonlinear finite-element model of the structure. In the estimation of $EDP|IM$ in a seismic structural analysis, ground motion records are selected to match characteristics of the IM (see Baker [218], for example) and the structure is then subjected to these ground motion records. Similarly, in PBFE a fire loading time-history and different fire scenarios need to be defined [252]. The characterization of realistic scenarios for fire loading needs to be developed by fire safety engineers.

Once the EDPs have been computed, the next step in the PBFE is the quantification of the DM. As stated by Hamilton [251], based on the work of Tide [254], fire-damaged structures can be subdivided into three categories of increasing damage, which can be simply described as: no damage, damaged but repairable, beyond repair (failure).

With respect to the fire following earthquake, a performance-based design approach has been presented by Faggiano *et al.* [255]. Nonetheless, a single and universally accepted approach for performance-based structural engineering of building structures for fire following earthquakes has not been proposed to date. In this work, a performance-based structural engineering framework for fire following earthquake is developed. Thus, a unified performance-based engineering approach needs to be selected. The main characteristic of the framework to be used is that it has to be flexible enough to be able to include additional analytical steps and generalized random variables in order to adequately account for se-

Table 7.1: Required attributes for PBEE and PBFE (adapted from Hamilton [251])

Analytical Process	Generalized Random Variable	Hazard	Model parameters	Outcomes
Hazard Analysis	IM	Seismic	Magnitude, distance, fault parameters, site soil conditions	Sa(T1), PGA, PGV, CAV, Arias Intensity, Duration
		Fire	Compartment geometry, ventilation, fire insulation, exposure of structural elements, fuel load	Maximum temperature in a structural component, duration and shape of sustained temperature loading
Demand Analysis	EDP	Seismic	Foundation and structural mechanical properties, hysteretic behavior and damping	Inter-story drift, floor acceleration, component forces and deformations
		Fire	Thermo-mechanical properties of materials, thermo-mechanical properties of connections, sustained (gravity) loading	Component forces and deformations
Damage Analysis	DM	Seismic	Experimentally calibrated structural component fragilities, acceleration sensitive component fragilities	Damage states associated with deformation and strength limits, damages states associated with limits to non-structural elements
		Fire	Experimentally calibrated structural component fragilities, experimentally calibrated smoke barriers and thermal barriers	Damage states associated with deformation and strength limits, damage states w.r.t. to thermal barriers and smoke barriers
Loss Analysis	DV	Seismic and Fire	Occupancy and first responders, lifeline recovery, community recovery	Direct losses (loss of life, reconstruction costs), indirect losses (cost associated with downtime, lack of business resilience)

quential hazards (e.g., fire following earthquake, mainshock-aftershock). Herein, the PBEE developed by PEER is selected as the main framework for unifying the performance assessment for fire following earthquake of building structures. The extensions made to the PBEE framework and its implications in what concerns future implementations are discussed next.

7.4 Framework

The probabilistic framework for PBSE for fire following earthquake proposed in this work is illustrated in Figure 7.1. Comparing this with Figure 1.12, it can be seen that the PBSE framework for fire following earthquake considers three additional steps (boxes with red background) that link the seismic damage analysis to the loss analysis. These three analytical steps are: (a) probabilistic conditional fire hazard analysis (conditional on the occurrence of a ground motion with a specific seismic IM), (b) probabilistic conditional fire demand analysis, and (c) probabilistic conditional fire damage analysis. In these analytical steps the generalized variables defined by Hamilton [251] are used to characterize the fire analyses steps.

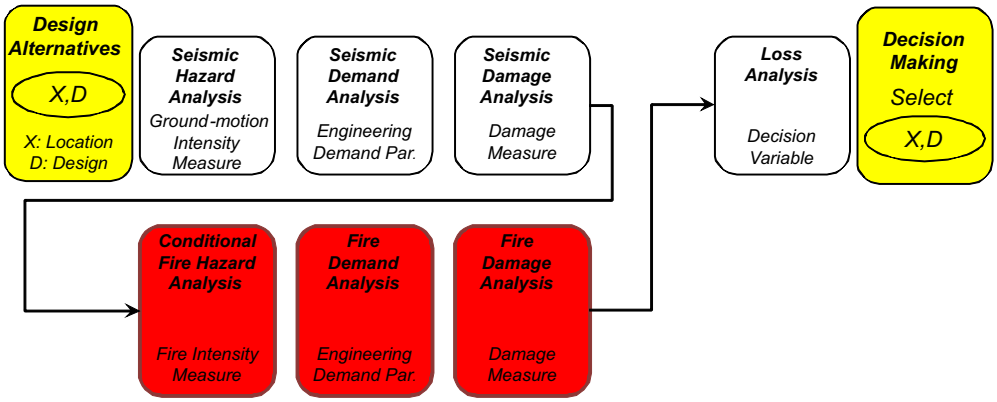

Figure 7.1: Probabilistic framework for performance-based structural engineering for fire following earthquake

It is worth noting that the sequential nature of the cascading hazards is visible in Figure 7.1. It is assumed that, if the fire occurs, it will take place immediately after the mainshock, or within a sufficiently short time window such that the previous seismic damage analysis results still hold. Thus, at the end of the seismic damage analysis step and given that the mainshock IM has occurred, the structure can be considered to be in a current damage state DS. The first step in the fire following earthquake analysis is the conditional fire hazard analysis and results in an intensity measure, IM_F. The fire hazard analysis result, IM_F, and the damage state DS_i are both conditional on the occurrence of the mainshock characterized by an IM. In this step several considerations must be made in the analysis, which relate to the model parameters listed in Table 7.1.

Once the fire intensity measure is computed, the conditional fire demand analysis step is performed. The term "conditional" is again employed because the nonlinear finite-element model analysed has to be able to realistically capture the damage state DS_i and therefore the structural analysis to fire loading is performed not on the initial intact structure, but on the mainshock-damaged structural model. The nonlinear finite-element model also needs to

adequately model the thermo-mechanical parameters of the structural elements and connections. Once the EDPs are estimated these have to be linked to the DMs. This analytical step is identical to the PBFE counter part proposed by Hamilton [251].

Under these assumptions, the annual rate of exceedance of a given level of loss is given a specific IM level is given by:

$$\begin{aligned}\nu_F(DV|DM) &= \int_{DM_F}\int_{EDP_F}\int_{IM_F}\int_{DS_i} P(DV_F|DM_F,DS_i) \\ & dP(DM_F|EDP_F,DS_i)dP(EDP_F|IM_F,DS_i)d\nu_F(IM_F,DS_i|IM)\end{aligned} \tag{7.2}$$

where:

- IM refers to the mainshock and is also needed to define the fire following earthquake ignition rate [256–258] - see Equation 7.3

- $\nu(IM_F, DS_i|IM)$ corresponds to the joint mean annual rate of occurrence of a fire that exceeds a given value of IM_F and damage state DS_i, for a structure that was subjected to a mainshock IM, and is given by the expression:

$$\nu(IM_F,DS_i|IM) = \int\int dP(IM_F,DS_i|FO,IM)dP(FO|F,IM)\nu(F|IM) \tag{7.3}$$

  where all terms shown in Equation 7.1 are first conditioned on IM and dependence on DS_i only shows up in the third term from the right; this is due to that fact that both ignition and flashover are considered to be independent of the current damage state DS_i, an assumption which does not hold for the case of the fire intensity measure IM_F since the maximum temperature in the structural members will depend on the current state of damage, namely in what may relate to exposure of rebar, cracked concrete, or damage to insulation and barriers of steel components, for example.

- the terms $P(DV_F|DM_F, DS_i)$, $dP(DM_F|EDP_F, DS_i)$, and $dP(EDP_F|IM_F, DS_i)$ are obtained in a similar fashion as in PBFE.

7.5 Sensitivity Study on Structural Fire Response

7.5.1 Description

The objective of this study is to identify the most important variables affecting the response of steel structures under and immediately after being subjected to thermal fire loading. Two case study examples are presented, which use the thermal tools of the Open System for Earthquake Engineering Simulation (OpenSees) framework. Structural fire analyses are conducted considering different fire scenarios and a set of seven random variables. Peak and residual deformations are tracked in order to assess structural response. In addition, pushover and pushdown analyses are carried out to evaluate the structural capacity to sustain further load after fire. TDA is used to evaluate the sensitivity of the response to each variable.

7.5.2 Methodology

Random Variables

Modeling fire behavior involves several phenomena, namely combustion, heat transfer, among others. The definition of parametric fire curves depends on the compartment opening factor O, the thermal inertia b of surrounding infrastructure, geometry of compartment, fire growth rate and fire load density. In this work, fire load density is considered as a random variable, while the remaining parameters are assumed to be deterministic. Khorasani *et al.* [259] propose that fire load density, q_{fd}, is given, for "light-weight" compartments, by:

$$q_{fd} = exp\left[6.951 - 0.0047(A_f \times 10.76) + 0.5712\,\varepsilon(q_{fd})\right] \tag{7.4}$$

where A_f is the room plan area in m^2, $\varepsilon(q_{fd})$ is a random variable with a standard normal distribution, and q_{fd} is in MJ/m^2. Equation 7.4 is used to define parametric time-temperature curves as proposed in Eurocode 1 (EC1) [260]. There are two points worth mentioning with respect to the form of Equation 7.4. First, when $\varepsilon(q_{fd}) = 0$, Equation 7.4 yields a fire load density that is similar to the characteristic fire load density in EC1 (q_{fk}). Second, due to the assumption that $\varepsilon(q_{fd})$ is standard normal, q_{fd} follows a lognormal distribution.

In this work, a simplified method, which is presented in Eurocode 3 (EC3) [261], is used to calculate time-temperature curves in steel sections. This method is based on the concept of section factor (or "section massivity factor"), S_{mf}. This parameter takes into account the member cross-section area, A, its perimeter exposed to fire, $P_h = S_{mf} \times A$, as well as the emissivity, conductivity, mass density, and steel specific heat. Herein, the parameters used to define the section factor are considered as deterministic, thus the temperature inside the steel elements depends only on the temperature at the surface of the element, which is a function of the fire load density that is conditional on an assumed fire scenario.

Table 7.2 lists the random variables considered in this study. Live loads are assumed to follow a Gamma distribution, based on models proposed in the Probabilistic Model Code (PMC) [262]. Uncertainties related to fire load, and also steel mechanical properties are also considered in this work. The uncertainty on the mechanical properties is considered at two levels: (i) ambient temperature ($20°C$), and (ii) elevated temperatures. At the ambient temperature, the yield strength, F_y, and the modulus of elasticity, E_0, are taken as random variables, defined based on values in PMC. In addition, the uncertainty in the yield strength, modulus of elasticity, and thermal elongation at elevated temperatures is accounted for by considering probabilistic models developed recently [263].

While at ambient temperature the reference steel yield strength is usually associated with a 0.2% offset, $F_{y,0.2\%}$, the EC3 provides two reference values for the yield strength at elevated temperatures: (i) proportional limit strength, F_P; and (ii) effective yield strength, which is associated with a strain equal to 2%, $F_{y,2\%}$. According to EC3, degradation of mechanical properties under increasing temperatures is controlled by three deterministic reduction coefficients $K_{y,\theta}$, $K_{P,\theta}$, and $K_{E,\theta}$, associated with the effective yield strength, proportional limit, and elastic modulus of elasticity, respectively. Following the approach in Khorasani *et al.* [263], $K_{y,\theta}$ and $K_{E,\theta}$ are considered as random variables, while $K_{p,\theta}$ is considered to be deterministic and equal to the EC3 proposal.

Khorasani *et al.* [263] compiled a big amount of data obtained over the last decades in experimental tests of steel members subjected to high temperature. Based on these results, empirical expressions were proposed to model the variation of steel thermomechanical properties due to thermal variation. The variation is given by reduction coefficients

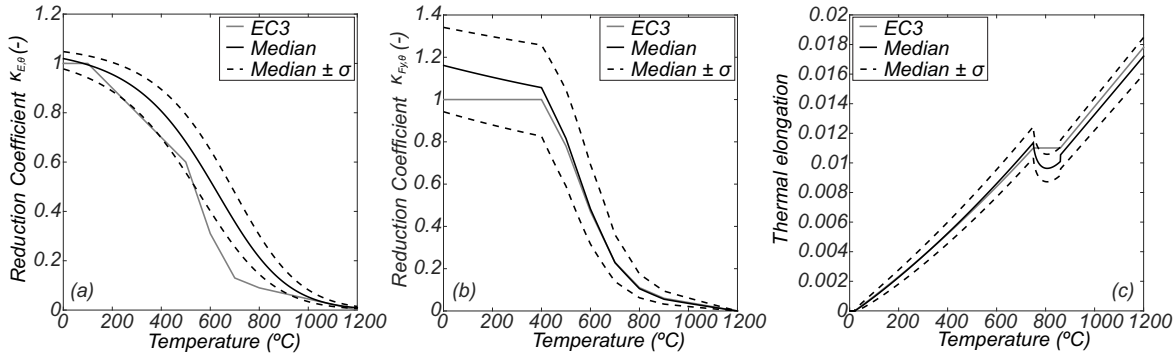

Figure 7.2: Thermomechanical model of Eurocode 3 and proposed models by Khorasani *et al.* [240] for deterioration of: (a) Young's modulus; (b) yield strength; and (c) thermal elongation.

that are normalized values, meaning that the parameter at each temperature is a function of the parameter at the ambient temperature. The effective yield strength reduction coefficient corresponds to $K_{y,\theta} = F_{y,2\%}/F_{y,0.2\%}$ and is given by:

$$k_{y,\theta} = 1.7 \times \frac{exp(logit(\hat{k^*}_{y,\theta}) + 0.412 - 0.81 \times 10^{-3}\theta + 0.58 \times 10^{-6}\theta^{1.9} + 0.43 \times \varepsilon(F_y))}{exp(logit(\hat{k^*}_{y,\theta}) + 0.412 - 0.81 \times 10^{-3}\theta + 0.58 \times 10^{-6}\theta^{1.9} + 0.43 \times \varepsilon(F_y)) + 1} \tag{7.5}$$

where $\varepsilon(F_y)$ is a random variable that follows a standard normal distribution; $\hat{k^*}_{y,\theta} = (\hat{k}_{y,\theta} + 10^{-6})/1.7$, where $\hat{k}_{y,\theta}$ is the normalized effective yield strength based on EC3, and $logit(\hat{k^*}_{y,\theta}) = ln(\hat{k^*}_{y,\theta}/(1 - \hat{k^*}_{y,\theta}))$. This expression may yield values larger than 1.0 for temperatures up to $550°C$, as shown in Figure 7.2(b). The normalized modulus of elasticity, represented in Figure 7.2(a), is given by:

$$k_{E,\theta} = 1.1 \times \frac{exp(2.54 - 2.69 \times 10^{-3} \times \theta - 2.83 \times 10^{-6}\theta^2 + 0.36 \times \varepsilon(E))}{exp(2.54 - 2.69 \times 10^{-3} \times \theta - 2.83 \times 10^{-6}\theta^2 + 0.36 \times \varepsilon(E)) + 1} \tag{7.6}$$

Finally, the thermal elongation, which is represented in Figure 7.2(c), is computed by:

$$\frac{\Delta l}{l} = \begin{cases} \left(\sqrt{\frac{\Delta l}{l}} - 1.28 \times 10^{-3} + 3.96 \times 10^{-6} \times \theta + 0.0039 \times \varepsilon(Th)\right)^2 & \theta < 750°C \\ \left(\sqrt{\frac{\Delta l}{l}} + [1.69 + 0.64(\theta - 750) - 1.7(\theta - 750)^{0.81} + 3.7 \times \varepsilon(Th)] \times 10^{-3}\right)^2 & 750°C \leq \theta < 860°C \\ \left(\sqrt{\frac{\Delta l}{l}} - 2.32 \times 10^{-3} + 0.173 \times 10^{-6} \times (\theta - 860) + 0.0037 \times \varepsilon(Th)\right)^2 & 860 \leq \theta < 1200°C \end{cases} \tag{7.7}$$

The uncertainty in the proposed models is introduced by variables $\varepsilon(F_y)$, $\varepsilon(E)$, and $\varepsilon(Th)$ [263]. If these are set to zero, the proposed model is equivalent to a deterministic approach based on EC3.

These models were implemented by Khorasani *et al.* [263] in OpenSees. However, the model are adapted in this work in order to include the variability of thermomechanical properties (controlled by the variables ϵ) as input variables.

The models were defined considering collected experimental data at various temperature levels, influencing the slopes in Figure 7.2. The uncertainty in the anchor temperature values used to define the straight lines have not been characterized experimentally. However, a pilot study performed by the authors (not shown herein in the interest of brevity) showed that the impact of uncertainty in these values is negligible on structural response.

Table 7.2: Random variables considered and supporting references

Variable	Description	Probabilistic distribution	Mean value, μ		Standard deviation, σ		Ref.
			Example 1	Example 2	Example 1	Example 2	
$LL\ [kN/m]$	Live Load	Gamma	1.0	2.5	0.52	0.64	Vrouwenvelder [264]
$\varepsilon(q_{fd})$	Fire load ε	Normal	0		1		Khorasani *et al.* [259]
$E\ [Gpa]$	Elastic mod.	Normal	210	200	6.3	6.0	Vrouwenvelder [262]
$F_y\ [Mpa]$	Yield strength	Log-Normal	355	300	24.9	21.0	Vrouwenvelder [262]
$\varepsilon(E)$	Elastic mod. ε	Normal	0		1		Khorasani *et al.* [263]
$\varepsilon(Fy)$	Yield strength reduction ε	Normal	0		1		Khorasani *et al.* [263]
$\varepsilon(Th)$	Thermal Elongation ε	Normal	0		1		Khorasani *et al.* [263]

ε refers to uncertainty in the models for material properties at elevated temperatures

Structural fire analysis

The structural fire analysis is divided into three main stages: (i) definition of the time-temperature relationship that corresponds to the idealized fire scenario; (ii) definition of the time-history of temperatures in structural elements; and (iii) structural fire response assessment. An efficient and accurate FE model, which accounts for the variation of the thermomechanical properties of the material, is required. Interaction between mechanical deformations imposed by external loads and imposed temperature should also be efficiently simulated. In this work, the OpenSees framework is used to perform structural fire analysis. Nonlinear static analysis with load control are performed to assess structural performance under fire. The Newton-Raphson method is used to solve the nonlinear system of equations and a maximum time-step of ten seconds is considered. An adaptive convergence scheme, which reduces the time-step or changes the numerical method, is employed when convergence issues are found.

During fire, local member behavior and global structure displacements are tracked in order to assess structural performance. Computed vertical and horizontal drifts are used to evaluate beam and column performance, respectively.

Pushover following fire and pushdown following fire analyses

In this work, the capacity of the structure to withstand additional vertical and horizontal loading following fire is analyzed. Pushover analyses are performed by a nonlinear static analysis with displacement control. Likewise structural fire analysis, to solve the nonlinear equations the Newton-Raphson method is used, with an adaptive convergence scheme. A mass proportional lateral load is applied, after the end of fire analysis, for performing pushover analysis. Structural capacity to resist horizontal load after fire is evaluated through the computation of the base shear associated with a threshold interstory drift. Pushover analyses are conducted by incrementally increasing the horizontal displacement of the left-end node of the structures at the upper floor. On the other hand, pushdown analysis is carried out by applying a uniform vertical load in all beams. Structural capacity to resist vertical loading after fire is assessed through the computation of the total vertical load associated with a member vertical deflection of $L/50$. Pushdown analyses are conducted by imposing an increase in the vertical displacement of the mid-node of the beam at the top of the heated compartment. The tolerance convergence criterion of the analyses is based on the norm of the displacements increment and is equal to 10^{-6}.

Sensitivity analysis

The sensitivity of structural response due to the uncertainty in the random variables considered is evaluated through TDA [265–267]. In TDA, each random variable is perturbed

from the median value, one at a time, to upper and lower bounds. That is, when one random variable is selected for perturbation, all other variables are set at their median values. The response for each perturbed input variable is then computed by subjecting the structural model to the fire loading. For a given random variable, the range of structural responses obtained for different perturbations are defined as "swing" of the response, which is considered as a measure of sensitivity of the response to the perturbation in the given random variable. The lower and upper bounds are often taken as the 10^{th} and 90^{th} percentiles of each variable, respectively. The "swing" in the response is estimated here using the dispersion index ID which is given by:

$$ID = \frac{max(R^{X,90\%}, R^{X,10\%}, R^{X,median}) - min(R^{X,90\%}, R^{X,10\%}, R^{X,median})}{R^{X,median}} \tag{7.8}$$

where $R^{X,median}$, $R^{X,10\%}$ and $R^{X,90\%}$ are the structural response recorded when random variable X is equal to its median, percentiles 10% and 90%, respectively.

7.5.3 OpenSees Thermal Framework - Verification and Validation

The OpenSees framework (v2.4.2, r5540) is used herein for the analysis of steel structures subject to fire. A displacement-based formulation is adopted when modeling frame members. The cross section discretization makes uses of uniaxial fibers [268]. The extended version of OpenSees, also known as OpenSees Thermal [269], includes improvements on the material steel model implemented [240], namely in what concerns the cooling phase [270–272].

Even though OpenSees thermal has been validated and verified, except for the cooling phase [240,253,269,273–275], an additional verification example is developed herein that includes the cooling phase. This is particularly important to make sure that subsequent pushdown or pushover loads can be reliably applied. The structure used for validation is based on the study developed by Santiago *et al.* [276] and consists in a single beam subjected to a parametric fire, represented in Figure 7.3(a). Geometrical and material properties are represented in this figure, which also shows the variation of temperature on the mid-web of cross section. The temperature variation along cross section is defined based on data presented in Santiago *et al.* [276]. Figure 7.3(b) compares results obtained using SAFIR and OpenSees. The results show great agreement between OpenSees and SAFIR results presented in Santiago *et al.* [276]. In results obtained with both software, the responses in the heating phase and the cooling phase are similar. The small differences in the results are believed to be caused by formulation differences between the two software, namely in what concerns displacement-based elements and second order effects, and on the assumptions made when using OpenSees with respect to the temperature profile along the height of the section.

7.5.4 Case study 1

General description

The selected structure for this case study is the "ZSH" structure [277], which is shown in Figure 7.4. Two different fire scenarios are considered. In scenario 1, only the left bay is

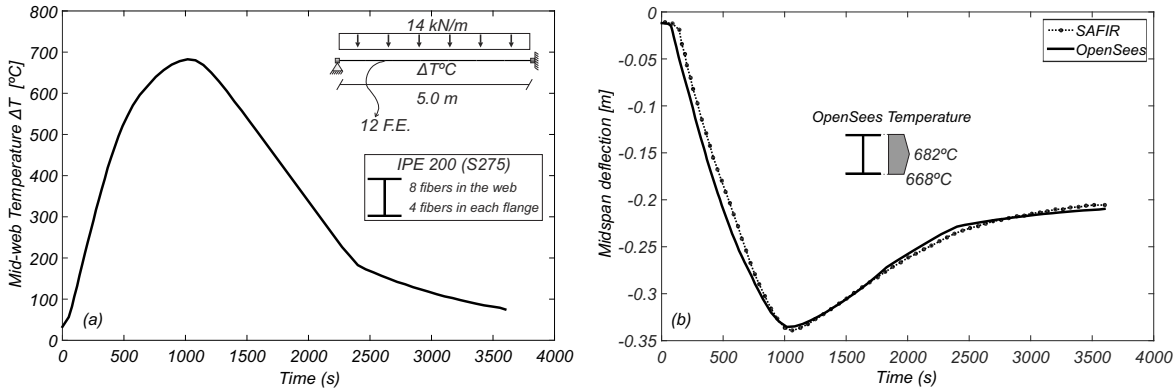

Figure 7.3: Verification example: (a) time-temperature curve; and (b) vertical displacement of mid-span beam as a function of time.

subject to fire loading, thus both columns and beam are heated. In scenario 2, the two bays are subject to fire and, consequently, all members of the structure are heated.

Modeling approach

The steel frame is composed of IPE80 I-shaped sections with St 37 steel grade, mean modulus of elasticity and yield strength at ambient temperature of 210GPa and 355MPa, respectively. All supports are pinned. Each member is composed by four finite elements. Cross sections are discretized in four fibers at each flange and eight along the web. The dead load and the live load in the model corresponds to a uniformly distributed load of 1.60 kN/m that is applied on the beams.

For defining the parametric curve of fire load scenario, some deterministic parameters are chosen. In this case study, the opening factor O was taken equal to $0.10m^{1/2}$, the section factor equal to $370m^{-1}$ and compartment area equal to $3.6m^2$. For TDA analysis, the resulting median value of fire load density is $870.39MJ/m^2$, which corresponds to a maximum member temperature of 996°C. The remaining variables are described in Section 7.5.2 and mean values summarized in Table 7.2. For both fire scenarios, TDA during and after fire are performed.

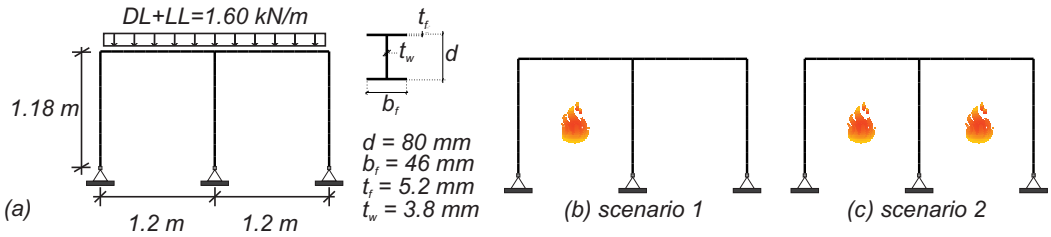

Figure 7.4: Case Study 1: (a) structural model; (b) fire scenario 1; and (c) fire scenario 2.

Sensitivity to uncertain parameters in peak and residual deformations

Figure 7.5 shows, for fire scenario 1, the tornado diagrams associated with peak and residual deformations. In what concerns the analysis of peak deformations, review of Figure 7.5 indicates a low influence of the yield strength, F_y, and modulus of elasticity, E_0, at the

ambient temperature. Fire load density has a large effect on the peak values of deflections, as well as on the residual deformations. In fact, $\varepsilon(q_{fd})$ has the largest ID in all response measures, except in the normalized peak vertical deflection. Nevertheless, it is worth noting that the dispersion of the response is low, specially for the peak deflections.

Figure 7.7 shows the dispersion index ID (Equation 7.8) of the seven random variables obtained by performing structural fire analysis considering fire scenarios 1 and 2. In these plots ID values increase concentrically, i.e. larger values of ID indicating higher importance of variables uncertainty are represented in the center of the plot. Figure 7.7(a) to 7.7(d) show that for peak deflections both scenarios yield similar results. Main differences are observed in residual deflections. Variables $\varepsilon(q_{fd})$, $\varepsilon(Th)$, and $\varepsilon(F_y)$ are the ones with largest swing and, consequently, largest ID.

Sensitivity to uncertain parameters in post-fire structural capacity

Structural capacity to withstand horizontal and vertical loading is assessed through computation of the base shear associated with lateral structural instability (estimated to be reached at an horizontal deflection of approximately 20cm) and the total vertical load associated with a vertical deflection of $L/50$, respectively.

In what concerns post-fire pushover, the uncertainty in the model for the effective yield strength reduction, $\varepsilon(F_y)$, is the random variable that induces larger dispersion in structural capacity (see Figure 7.6(a)), followed by F_y and LL. On the opposite spectrum, the uncertainty in the model of the fire load, $\varepsilon(q_{fd})$, has a low influence on structural capacity to resist horizontal actions after fire. In fact, after cooling, steel mechanical properties recover their initial values. Thus, unless large residual plastic strains are achieved during the fire loading, the influence of fire loading in post-fire structural capacity is negligible, as observed in this case.

For post-fire pushdown, $\varepsilon(q_{fd})$ and $\varepsilon(E)$ have the largest ID in fire scenario 1 (Figure 7.6(b)). As represented in this figure, two different instability modes are observed, which lead to the very large ID of these two variables. On the 90^{th} percentile analyses (and on the analyses of the remaining variables) a lateral instability mode is observed. Otherwise, on the 10^{th} percentile analyses, the instability occurs due to beam bending. Figure 7.7(f) shows that, for scenario 2, the dispersion of $\varepsilon(q_{fd})$ and $\varepsilon(E)$ decreases due to fire loading symmetry, which leads to the occurrence of a post-fire lateral instability mode in all analyses.

7.5.5 Case study 2

A three-bay three-story steel frame designed by Haukaas and Scott [278], shown in Figure 7.8, is the object of this case study. Ten fire scenarios are considered in this case study, as represented in Figure 7.8.

Modeling approach

The frame is composed of IPE250 I-shaped sections. Geometric parameters of the structural model are considered deterministic. Self-weight is constant in all beams and equal to $187.5N/m$. The mean elastic modulus and yield stress are 200GPa and 300MPa, respectively.

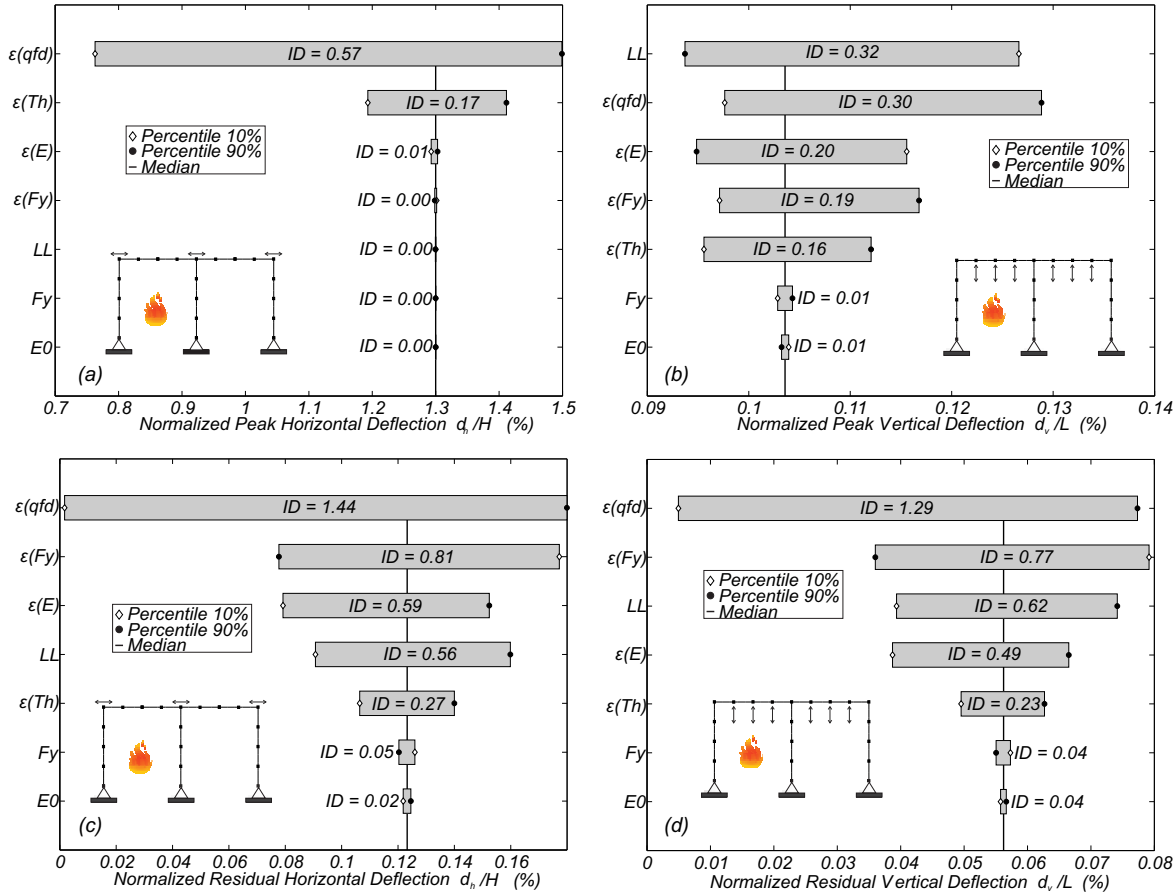

Figure 7.5: Tornado diagrams for fire scenario 1: (a) normalized peak horizontal deflection; (b) normalized peak vertical deflection; (c) normalized residual horizontal deflection; (d) normalized residual vertical deflection.

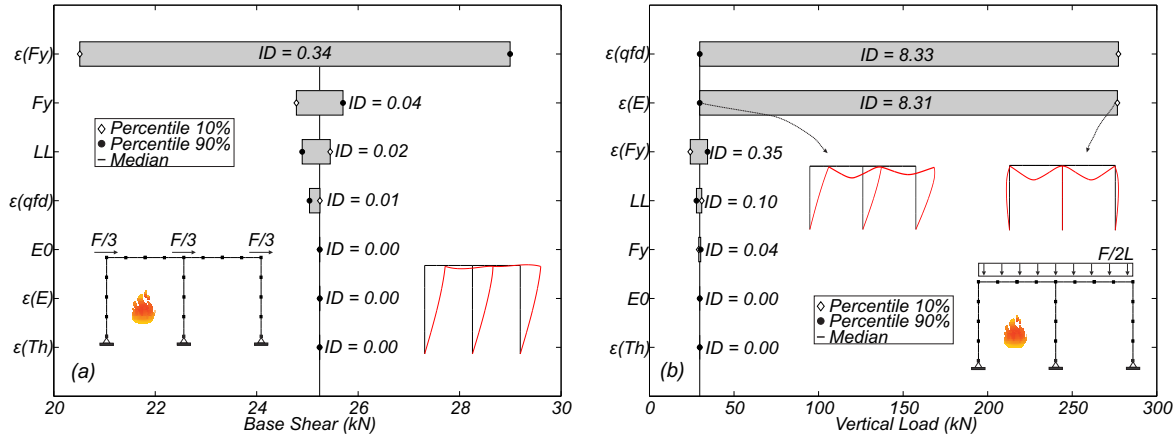

Figure 7.6: Tornado diagrams associated with post-fire analyses for fire scenario 1: (a) pushover analysis; and (b) pushdown analysis.

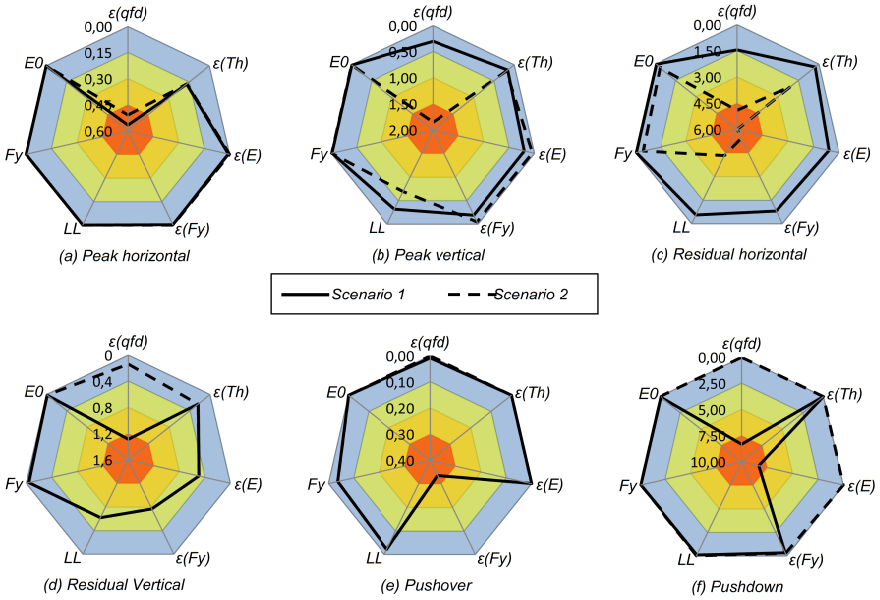

Figure 7.7: Dispersion index associated with: (a) peak horizontal deflection; (b) peak vertical deflection; (c) residual horizontal deflection; (d) residual vertical deflections; (e) post-fire pushover load; and (f) post-fire pushdown load.

Live load, whose mean value is equal to 2.5kN/m, is considered following Vrouwenvelder [262]. Parametric fire curves follow prescriptions of EC3, and are generated considering an opening factor O equal to $0.10m^{1/2}$ and $25m^2$ of compartment area. The resulting median value of fire load density is $489.03MJ/m^2$. Section factors were calculated for the following cases: beams heated on 3 sides, columns heated on 1 side, and columns heated on 2 sides, yielding the values $85.2m^{-1}$, $17.6m^{-1}$, and $35.2m^{-1}$, respectively. For these three cases, the peak member temperature associated with the median value of fire load is 553°C, 253°C, and 385°C, respectively.

In the case of fires located in the middle or in the upper floors, only the surrounding columns and the beams above fire location are heated following Memari and Mahmoud [229]. This is supported by experimental tests that concluded that since the heat flow rises, the temperature at the base of the compartment is approximately equal to the ambient temperature [261].

Sensitivity to uncertain parameters in peak and residual deformations

In Figure 7.9 the ID associated with each of the seven random variables are represented for all fire scenarios in radar plots. Plots (a), (b), and (c) correspond to the ID of the peak horizontal deflections, while plots (d), (e), and (f) correspond to the ID of the residual horizontal deflections. Plots (a) and (d) are associated with fire scenarios 2, 3, and 8, which correspond to fires located in the first floor. Plots (b) and (e) are associated with fire scenarios 4, 5, and 9, which correspond to fires located in the second floor. Finally, plots (c) and (f) are associated with fire scenarios 6, 7, and 10, which correspond to fires located in the upper story. Fire scenario 1 is present in all plots as a reference scenario. These plots indicate that the fire load is the most relevant variable for all fire scenarios. The uncertainty in thermal elongation is the other variable that has shown non negligible indices, namely for peak

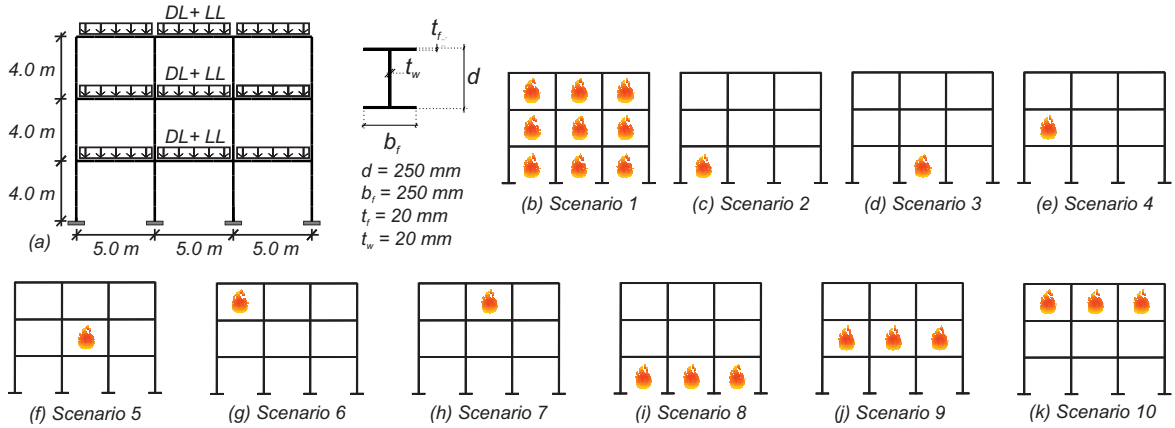

Figure 7.8: Case Study 2: (a) structural model; (b) to (k) show fire scenarios 1 to 10.

deflections. Although the same trend is observable for both peak and residual deflections, one can conclude that the ID associated with residual deflections vary greatly among fire scenarios. For example in plot (f) it is possible to see that ID associated with $\varepsilon(q_{fd})$ in scenario 1 is significantly larger than that associated with other scenarios, which are close to zero. Figure 7.10 shows the ID associated with peak and residual vertical deflections. This figure indicates that the same conclusions taken for horizontal deflections hold for vertical deflections.

Sensitivity to uncertain parameters in post-fire structural capacity

In this case study, structural capacity to resist horizontal load after fire is evaluated through the computation of the base shear associated with an interstory drift of 8%, which corresponds to an horizontal deflection of approximately 30cm. As referred before, a member vertical deflection of $L/50$, which corresponds to a drift of 2%, is considered to assess the structural capacity to resist vertical loads after fire.

After conducting pushover analyses for all fire scenarios, similar responses were obtained as represented in Figures 7.11(a) to 7.11(c). These figures indicate that $\varepsilon(F_y)$ and F_y are the main variables influencing structural capacity to withstand horizontal loads. At the same time, uncertainty in live load should not be neglected. On the other hand, uncertainty in fire load does not influence post-fire structural response. The reversible condition of the steel properties justify this behavior, as already stated in case study 1.

Figure 7.11 also shows the radar plots of the pushdown analyses (plots (d) to (f)). Mixed results are obtained in these analyses as the ID vary greatly among the variables and between scenarios. Each variable causes significant variation in at least one fire scenario. The variable that proved to be significant in terms of sensitivities of the response for most of the scenarios, and simultaneously induces largest ID, is the thermal elongation $\varepsilon(Th)$. The influence of the remaining variables is not constant and a general trend cannot be identified.

Sensitivity to vertical load distribution in post-fire structural capacity

Figure 7.12 shows the tornado diagram obtained by imposing pushdown vertical loads on a single bay following fire scenarios 1 and 2. The locations where the loads where applied are shown in the figure. As one can observe $\varepsilon(F_y)$ and F_y are the variables that most influence

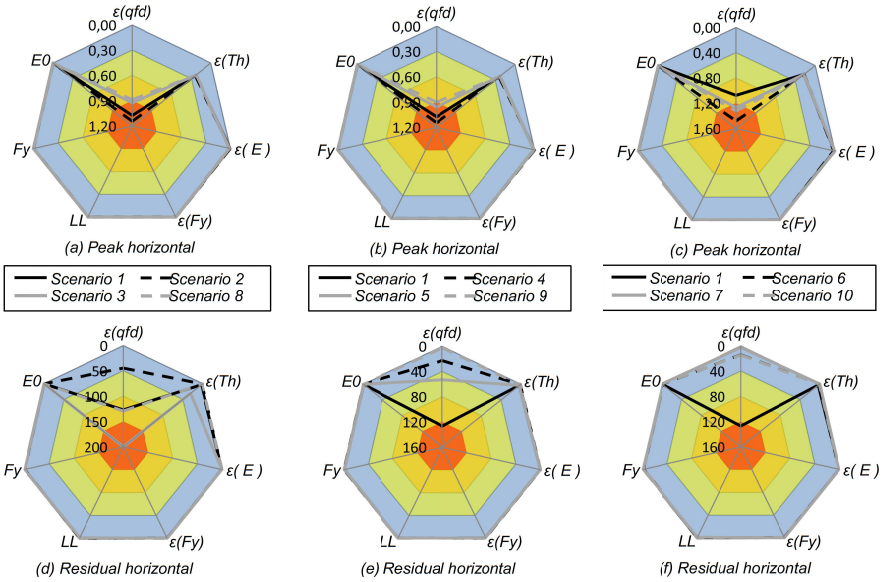

Figure 7.9: Dispersion index associated with the peak and residual horizontal deflections: (a) and (d) scenarios 1, 2, 3, and 8; (b) and (e) scenarios 1, 4, 5, and 9; and (c) and (f) scenarios 1, 6, 7, and 10.

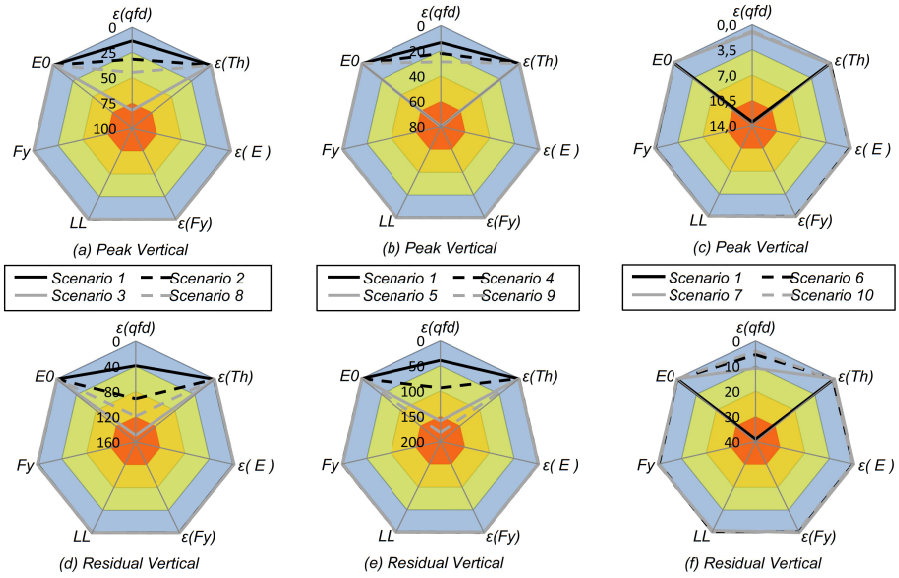

Figure 7.10: Dispersion index associated with the peak and residual vertical deflections: (a) and (d) scenarios 1, 2, 3, and 8; (b) and (e) scenarios 1, 4, 5, and 9; and (c) and (f) scenarios 1, 6, 7, and 10.

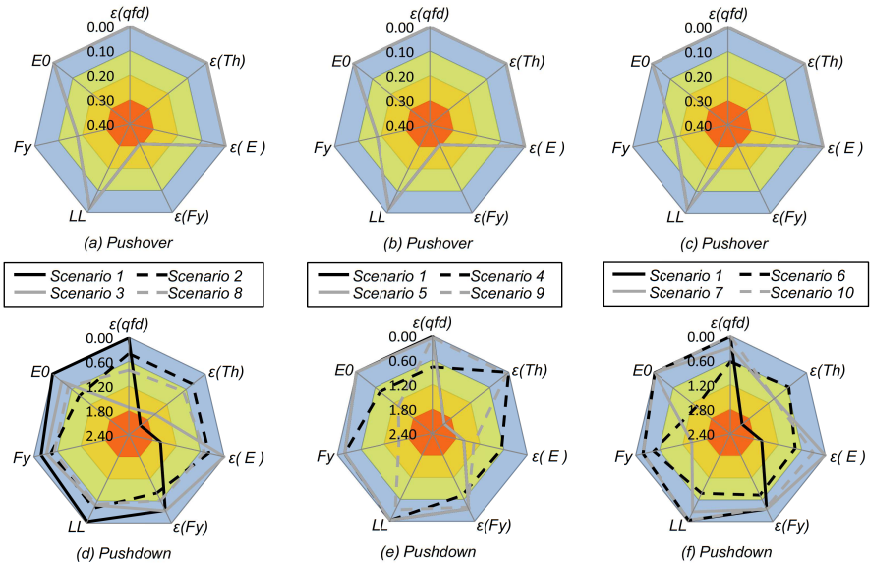

Figure 7.11: Dispersion index associated with the pushover and pushdown forces: (a) and (d) scenarios 1, 2, 3, and 8; (b) and (e) scenarios 1, 4, 5, and 9; and (c) and (f) scenarios 1, 6, 7, and 10.

the vertical load carrying capacity. This is in contrast with the results in Figure 7.11 for scenario 1, where the most significant variable was $\varepsilon(Th)$. In order to illustrate the differences induced by the different load pattern, Figure 7.13 shows the radar plots of pushdown analyses carried out with the original load pattern (load in all beams) and the modified version (single bay loads). The differences are also visible when analyzing the collapse mechanisms for these two fire scenarios, represented in Figure 7.13(b) to 7.13(e). These figures show that when applying a single bay load the failure occurs in beams while when the load is applied in two or more bays, the failure mode is a mixed mode which includes failure of beams and columns. Although for scenario 2 the computed ID are not significantly different, for scenario 1 significant changes are obtained. These observations indicate that for post-fire assessment of building structures the sensitivity to load patterns and collapse mechanisms need to be carefully accounted for.

7.6 Incremental Fire Analysis

7.6.1 Description

In order to investigate the effect of fire load variation on the structural response and stability, incremental fire analyses (IFA) are performed subsequently. This analysis is inspired in incremental dynamic analysis [54], but instead of nonlinear dynamic time-history analyses, incremental structural fire analyses are performed. In these analyses all variables are assumed constant and taken equal to their median value [279], except the fire load that is incrementally increased. For each value of fire load, a structure fire analysis is performed and the structural response recorded. Thirteen different intensities are considered here for the fire load. IFA allows to investigate the relationship between fire load and structural response,

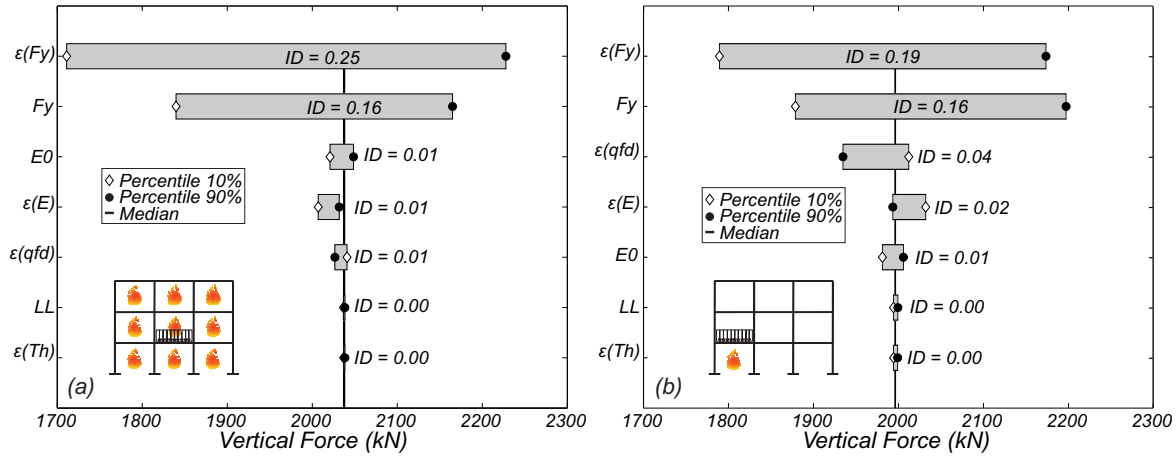

Figure 7.12: Tornado diagrams associated with post-fire pushdown with the modified load pattern (single bay loads) for: (a) fire scenario 1; and (b) fire scenario 2.

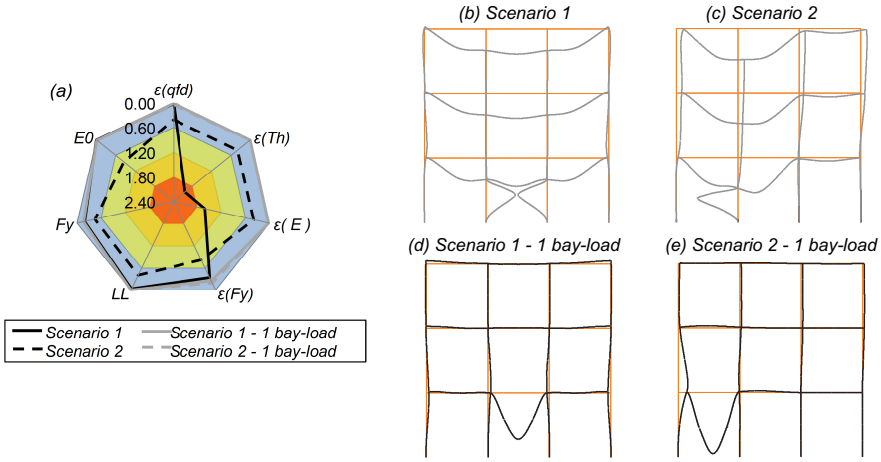

Figure 7.13: Radar plot and deformed shapes (amplification factor of 10) illustrating the influence of load distribution in pushdown analysis for fire scenarios 1 and 2: (a) radar plot; (b) and (c) deformed shapes for vertical pushdown load in all bays; and (d) and (e) deformed shapes for vertical pushdown load in a single bay.

namely in what concerns peak and residual deformations. Thirteen different intensities are considered for the fire load. These include the median value, the 10^{th} and 90^{th} percentiles, the median plus and minus standard deviation, as well as another eight intensities. The maximum intensity considered is 1500 MJ/m^2, which corresponds to a large value with only 1% of probability of exceedance, according to the probability function defined in Section 7.5.2.

Two different analyses are carried out. In the first one, the fire analysis is stopped at the instant of maximum temperature. At this instant a pushdown analysis is performed in order to assess the vertical load carrying capacity of the damaged structure. This capacity is deemed fundamental for fire fighters and rescue teams to act during fire loading. In the second analysis, the complete fire analysis is performed. After the end of structural fire analysis, a pushdown analysis is also carried out. This analysis intends to evaluate the residual resistant capacity of the structure, which is important for reoccupation decisions, inspections, and post-fire risk analysis. In both analyses, the pushdown is executed by imposing and incrementally increasing vertical load. Vertical load configurations are represented in Figure 7.14. In total, 260 incremental fire analyses are performed, which correspond to thirteen fire intensities, ten fire scenarios, and two types of pushdown analyses.

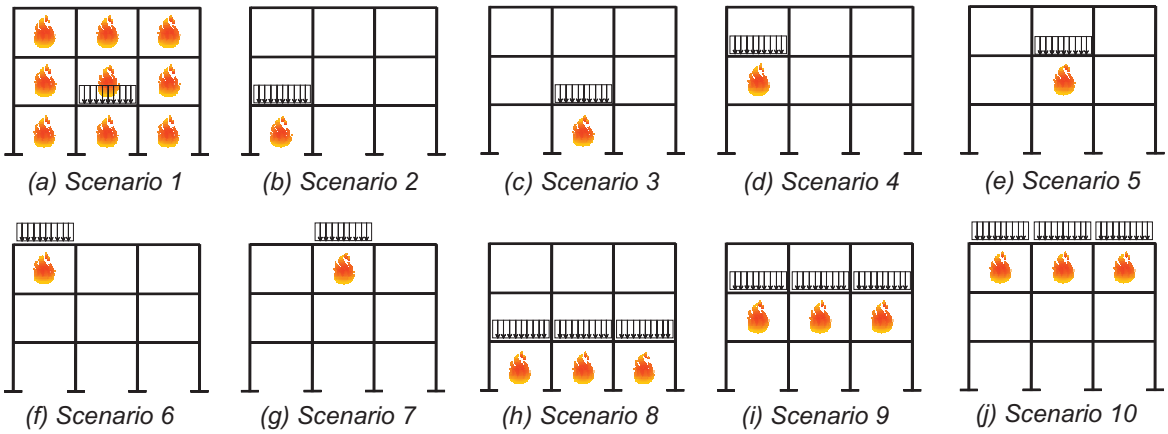

Figure 7.14: 3-Story steel frame structure pushdown load distribution for Incremental Fire Analysis

7.6.2 Peak and Residual Deformations

Figure 7.15 shows peak and residual deflections of the structure. Figures 7.15(a) and 7.15(b) show peak and residual horizontal deflections, respectively. Figures 7.15(c) and 7.15(d) show the peak and residual vertical deflections, respectively. Peak horizontal deflections increase with fire load until $\varepsilon(q_{fd})(90\%)$. After this, the peak horizontal deflections either remains unchanged, which holds for most of the scenarios, or a slight increase with constant rate is observed for scenarios 1, 6, and 10. This indicates that the horizontal deflections are not influenced by fire loads larger than $\varepsilon(q_{fd})(90\%)$. However, larger fire loads do influence vertical deflections. In fact, Figure 7.15(b) shows that for a fire load slight above the $\varepsilon(q_{fd})(median)$ an abrupt increase in the vertical deflections exists for most of the scenarios. This increase leads to violation of the threshold vertical deflection of $L/250$. Only scenarios 6, 7, and 10 do not record this increase. This is due to the fact that in these scenarios fire occurs at the upper floor. As a consequence, the decrease in members stiffness occur only

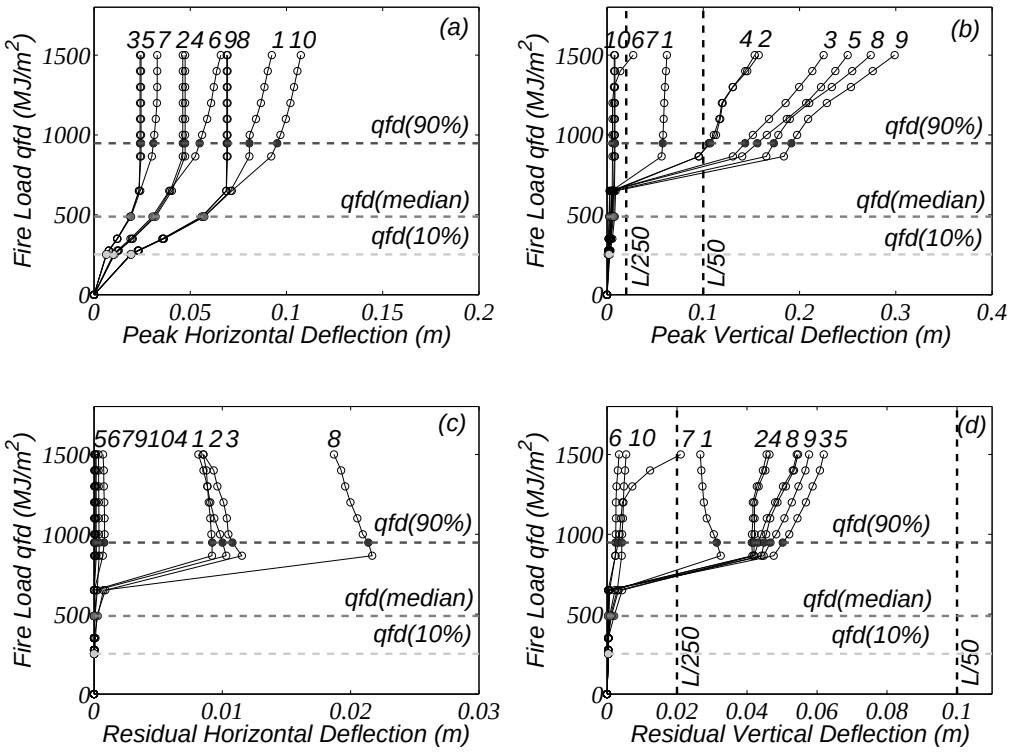

Figure 7.15: Deflections as a function of fire load obtained through incremental fire analysis: (a) peak horizontal deflections; (b) peak vertical deflections; (c) residual horizontal deflections; and (d) residual vertical deflections

is less stressed beams and columns leading to lower vertical deflections. The same observations can be made for residual horizontal and vertical deflections based on Figures 7.15(c) and 7.15(d), respectively. Moreover, Figures 7.15(b) and 7.15(d) also indicate that for fire loads larger than $\varepsilon(q_{fd})(median)$ most of the scenarios lead to violation of the threshold deflection value of $L/250$, for both peak and residual response. In fact, for peak response most of the scenarios also violate the threshold value of $L/50$, which indicates failure.

7.6.3 Vertical Load Carrying Capacity

Figure 7.16 shows the relationship between total pushdown load and fire load. Figure 7.16(a) is associated with the pushdown analysis performed at the instant of maximum fire temperature, while Figure 7.16(b) is associated with pushdown executed after fire analysis. Different trends are identified in both analyses. First, at the instant of maximum temperature, pushdown load that leads the structure to exceed the threshold value of $L/50$ decreases linearly until the vertical axis is crossed, which is at approximately 900 MJ/m^2. At this point the peak deflection is already larger than $L/50$, thus indicating that structure is not stable and any additional load can pose safety threat. Second, the pushdown analysis performed after fire analysis, leads to a complete different trend. This analysis shows that the pushover load that leads to violation of the defined threshold is independent of the fire load. It is worth noting that after fire initial (intact) thermomechanical material properties are restored. Al-

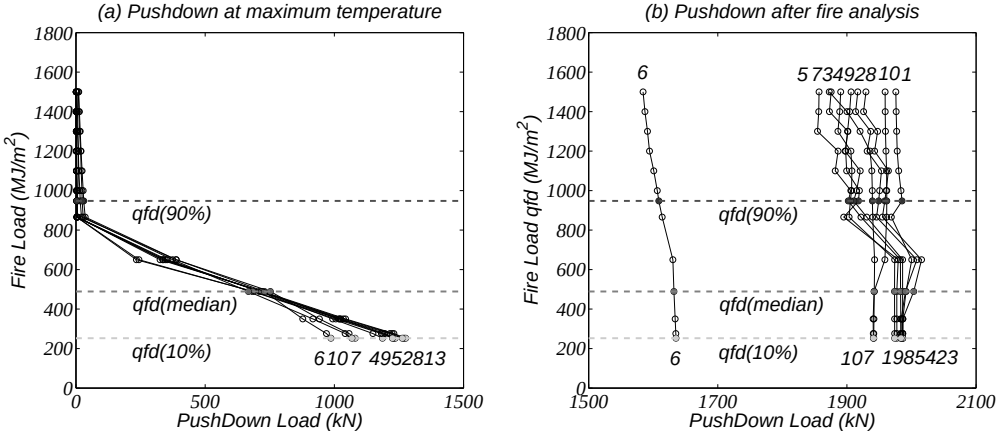

Figure 7.16: Pushdown (vertical) load inducing a vertical deflection of $L/50$ as a function of fire load: (a) at the instant of maximum temperature; and (b) after fire analysis

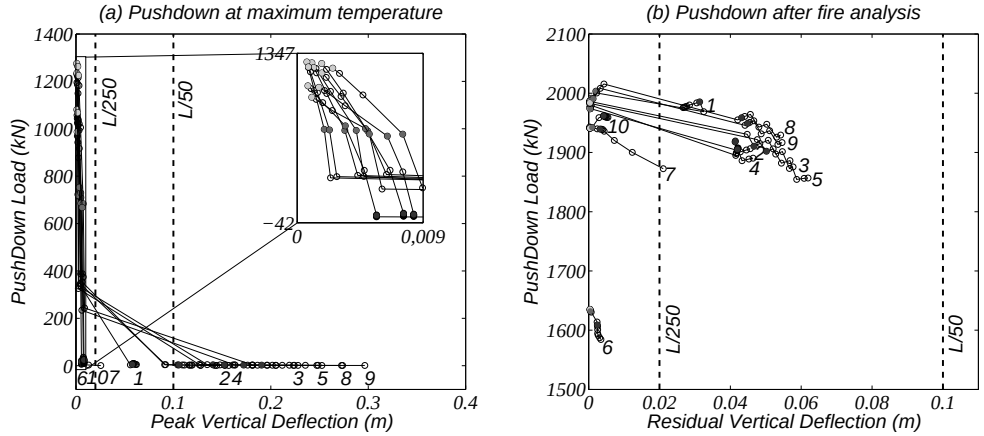

Figure 7.17: Pushdown (vertical) load inducing a vertical deflection of $L/50$ as a function of: (a) peak vertical deflection at the instant of maximum temperature; and (b) residual vertical deflection after fire analysis

though residual deformation exist, this fact leads to restoration of the resistant capacity of the structure in what concerns vertical loads.

Figure 7.17 helps to investigate the relationship between vertical deflections and pushdown load. In Figure 7.17(a), which shows the pushdown load as a function of the peak vertical deflection at the instant of maximum temperature. This figure indicates that the pushdown load decreases with a very high rate with the increase of the vertical deflection. After a vertical deflection of about 0.01m the pushdown load is null for all scenarios. As stated before, for the pushdown performed consecutively to the fire analysis different observations are made. Figure 7.17(b) shows that the pushdown load is somewhat independent of the residual vertical deflection. However, a slight decrease in pushdown load can be seen for larger values of deflection. This holds for the entire range of analyzed fire intensities.

7.7 Conclusion

A probabilistic methodology for performance-based structural engineering for fire following earthquakes was proposed in this Chapter. This methodology is based on the Total Probability Theorem and builds on methodologies developed recently, namely work done by Hamilton (2011). The proposed procedure can be used to compute decision variables (DV) that relate to expected loss of facilities located in seismic regions considering both mainshock and fire hazard events. The loss analysis framework is disaggregated into the following basic probabilistic components: (1) seismic hazard analysis, (2) seismic demand analysis, (3) seismic damage analysis, (4) conditional fire hazard analysis, (5) conditional fire demand analysis, (6) conditional fire damage analysis, and (7) loss analysis for both earthquake hazard and fire following earthquake hazard. The proposed methodology incorporates the state-of-the-art modelling of fire hazard analysis and fire structural analysis. A scalar fire intensity measure IM_F is defined and it is assumed to be a sufficient IM.

The proposed methodology is a first step in development of a performance-based structural engineering approach for fire following earthquake. However, structural fire analysis can be cumbersome partially due to the large number of variables influencing structural performance and the associated computational cost. Therefore, the objective of the second part of this Chapter is to identify the most important parameters affecting structural response during and after fire. In this work, two case studies are analyzed by using the OpenSees framework and the recently developed thermal tools. The first case study corresponds to an experimentally tested one-story two-bay steel structure, while the second case study is based on a 3-story steel moment resisting frame building. Some modifications were introduced in the model code in order to perform sensitivity analyses, which are executed using the TDA. In TDA, the range of structural responses obtained from perturbations of each variable is computed, providing an insight on the importance of each variable for structural fire response.

Structural response is assessed by means of a structural fire analysis, pushover following fire, as well as pushdown following fire. Parametric fire curves and steel thermomechanical properties are probabilistically defined based on recent studies. Structural fire analyses are conducted with a set of seven random variables and considering different fire scenarios. In order to assess the structural response during fire, peak and residual deformations are tracked. In addition, for post-fire structural capacity assessment, pushover and pushdown analyses are carried out.

The results show that uncertainty in five of the seven random variables considered produce significant perturbations in the response. These are the live load, fire load, and three model errors considered in elevated temperature models. The uncertainty in yield strength and modulus of elasticity at ambient temperature has impact mainly in post-fire structural response due to reversible characteristics of steel thermomechanical properties. Although uncertainty in fire load density tends to be the most relevant parameter influencing peak deformations during fire, the obtained results indicate that it has a negligible influence on the structural capacity to withstand horizontal loading. This is due to the fact that after cooling, steel mechanical properties have recovered their initial values. As a consequence, unless significant residual plastic strain are recorded, post-fire structural capacity is similar to the intact capacity.

The results of this work are important to improve the efficiency of probabilistic-based engineering methods considering fire demands. Future work is needed in order to assess

the influence of these variables considering multiple hazards, for example fire following earthquake.

Research is still needed to (1) improve the probabilistic description of the conditional fire hazard analysis, namely in the models that define ignition rates as a function of the IM used in the seismic structural analysis, which can be obtained through regression analysis of existing ignitions data for fires following an earthquake; (2) define sufficient and efficient IMF (scalar or vector-valued) for different structures consisting with different materials; (3) define appropriate performance objectives for fire following earthquake engineering problems; (4) relate the target performance objectives and the DVs obtained using the proposed PBSE methodology with feasible design procedures; and (5) validate the applicability of the proposed framework through application to a case study making use of the thermal modeling tools that have been tested and analyzed in a significant part of this Chapter.

7.8 Dissemination

This part of the research program resulted in the following outputs.

1. Scientific paper to be submitted to the Fire Safety Journal (in collaboration with Mr. Rúben Rosário, FCT-UNL)

   Scope: Perform a comprehensive sensitivity study that helps identifying the most important variables in steel fire response. To this effect, two case studies are presented and a Tornado Diagram Analysis is performed.

   Tentative title: Sensitivity Analysis of Steel Frames Under Fire.

2. Oral presentation made by Professor André R. Barbosa at the First International Conference on Performance-Based and Life-Cycle Structural Engineering (2012)

   Scope: Presentation of a probabilistic framework for performance-based structural engineering (PBSE), which includes earthquake performance assessment and fire performance assessment, namely in the special case of fire following earthquakes. This framework can be seen as an extension of the performance-based earthquake engineering (PBEE) methodology developed by the Pacific Earthquake Engineering Research (PEER).

   Complete reference: Barbosa, A., Neves, L., and Ribeiro, F. (2012). "Preliminary Proposal For Performance-Based Structural Engineering For Fire Following Earthquake." In: First International Conference on Performance-Based and Life-Cycle Structural Engineering. Hong Kong, China.

3. Oral presentation to be made at the National Conference on Seismology and Earthquake Engineering (Sísmica 2016) to be held at Azores in May 2016 (abstract accepted; paper submitted in January 2016)

   Scope: This study aims at identifying the most important variables affecting the response of steel structures under and immediately after being subjected to structural fire loading. Two case study examples are presented, which use the thermal tools of the Open System for Earthquake Engineering Simulation (OpenSees) framework.

Complete reference: Ribeiro, F., Rosário, R., Barbosa, A., and Neves, L. (2016). "Sensitivity Analysis of Steel Moment Frames Subjected to Structural Fire Using the OpenSees Framework". In: National Conference on Seismology and Earthquake Engineering (Sísmica 2016). São Miguel, Azores.

Chapter 8

Conclusions

8.1 Work Overview

This thesis is intended to contribute to the study of post-earthquake structural safety and performance considering multiple secondary hazard events. In spite of the changes in the design and assessment methods in the last decades, current codes limit seismic analysis to the study of an isolated seismic event. However, the occurrence of secondary hazard events, such as aftershocks, fires, blasts, and tsunamis are frequent after major seismic events. In fact, major historical earthquakes have shown that this consideration may not be sufficient to guarantee the desired structural performance in accidental scenarios. After a large intensity earthquake, buildings that have not collapsed are potentially damaged and, consequently, more vulnerable to secondary events that follow an earthquake. Due to this, an increase in the probability of failure and in the estimated losses are expected.

Studies on the post-earthquake structural response have only been developed by the scientific community in the last decade. In spite of that, a unified methodology to investigate the capacity of structures to face post-earthquake multiple hazards has not been proposed. Such a methodology is fundamental in order to gather data that would allow to integrate post-earthquake hazards in design and assessment of structures through semi-probabilistic rules. This thesis adds on the current efforts on two main points: (1) the development of numerical tools that are able to simulate the behavior of steel moment resisting frames (SMRF's) under multiple cascading hazard events, namely sequential seismic events and fire following earthquake; and (2) the development of methodologies to assess the capacity of structures to resist post-earthquake multiple hazards, namely aftershocks and fire.

As extremely rare events are being studied, the most effective way to assess the influence of these events on structural safety is to compute robustness metrics associated with mainshock-damaged structure and the intact structure, considering the secondary multiple hazard events. Reliability-based measures that allow for estimation of the structural capacity to face these extreme events are used.

Although the proposed methodologies are general and can be applied to any structural typology and material type, this thesis is focused on pre-Northridge SMRF structures. Thus, the developed numerical tools focus on this type of structures.

The developed numerical models are based on finite-length plastic hinge elements as these present several advantages over the traditional concentrated plastic hinge approach, namely in what concerns user modeling effort and computational cost. Additionally, this approach allows for monitoring the local response that may be important at least until buck-

ling of the plastic hinge. The finite-length plastic hinge section behavior can be defined through fiber sections or by directly assigning moment-curvature flexural response. In the case moment-curvature laws are applied to define hinge section flexural behavior, a formulation to ensure that the correct stiffness is obtained throughout the analysis is needed.

8.2 Main Outcomes

8.2.1 Development of Enhanced Finite Element Models for Seismic Analysis

In what concerns the development of numerical tools, a new formulation and implementation of a finite-length plastic hinge integration scheme that allows for the use of empirically calibrated moment-rotation laws to define hinge section behavior in finite-length plastic hinge force-based element integration was developed. This formulation is based on section flexural stiffness modification parameters that are computed at the beginning of the analysis as a function of the user defined plastic hinge lengths. It is demonstrated that the use of scaled but not calibrated moment-rotation laws leads to significant errors in both local and global responses and is therefore not adequate for structural analysis. Nonlinear static analyses of steel beams and a pushover analysis of a SMRF were performed considering different plastic hinge lengths in order to validate the proposed formulation. Even though this formulation has only been tested with multi-linear moment-rotation laws, it is, in principle, possible to use it with other constitutive laws, where moment-rotation can be related to moment-curvature by a user-defined plastic hinge length.

Based on this formulation, a calibration of recently developed Modified Ibarra-Medina-Krawinkler models (ModIMK) models was performed in order to use these models in both finite-length plastic hinge elements and in the traditional concentrated plastic hinge approach. The simple case studies analyzed in this study indicated that models using finite-length plastic hinge elements are more stable, accurate, and versatile than the concentrated plastic hinge models. The new implementation of the ModIMK was carried out in the Open System for Earthquake Engineering Simulation (OpenSees) framework.

Brittle connections were modeled by adding fracture elements at the end of the finite-length plastic hinge members. The fracture elements consisted in zero-length rotational springs. This approach is similar to the concentrated plastic hinge approach, except that the element interior is composed by a nonlinear element. This presents obvious advantages of clear separation between member and connection nonlinearities and, consequently, enable different modeling choices to be made on both sides in an independent manner. A case study of 3- and 9-story Los Angeles SAC Steel Project buildings, which allows for assessing the influence of considering brittle connections both on the fragility curves computation and in the estimated repair cost. Obtained results indicate that for low levels of deformation, the influence of brittle connections is negligible because very few nonlinearities exist. For mid and high levels of deformation are expected when brittle connections are accounted for in the model. As deformations increase the difference between the results obtained with rigid connection models and brittle connections models increases. The 9-story building recorded lower differences between the estimated repair cost obtained with a rigid connection model and a brittle connection model. This is due to the more efficient distribution of damage among the elements and long the building height.

8.2.2 Influence of Ground Motion Duration on Structural Damage

A comprehensive study on the influence of earthquake ground motion duration on structural damage is performed. The development of this study is important as present codes, as well as performance-based design methodologies, are typically based on response and damage measures calibrated for short duration shallow crustal earthquakes. A case study of the 3-, 9-, and 20-story Seattle SAC Steel Project buildings is presented. The obtained results indicate that for low values of spectral acceleration, there is no visible influence of ground motion duration on deformations and damage; for large spectral accelerations, longer duration motions tend to induce larger peak IDRs and damage indices. The median response between the two sets of ground motions is similar until approximately 4% peak IDR. Above this level, the long duration ground motions tend to induce larger deformations under the same values of spectral acceleration. Moreover, the relationship between the peak interstory drift ratio and damage indices was found to be increasingly nonlinear with increasing ground motion duration. The largest damage indices were obtained for the 20-story building as a consequence of the concentration of damage; on the other hand, the design of the 9-story building efficiently distributed deformations over the height.

8.2.3 Robustness Assessment of Structures Considering Post-Earthquake Aftershocks

A general framework methodology is proposed in order to compute robustness measures considering aftershocks. Then, a reliability based robustness assessment methodology for SMRF structures subjected to post-mainshock seismic events is proposed, based on the proposed general methodology. Robustness is computed through comparison of the structural reliability index under a mainshock, considering the undamaged structure, and under an aftershock applied to the mainshock-damaged structure. A case study of the 3-, 9-, and 20-story Los Angeles SAC Steel Project buildings is presented.

For structures expected to form strong-column weak-beam failure mechanisms, a finite element modeling approach was presented in which columns were modeled using force-based fiber-section distributed plasticity elements and beams were modeled using a recently proposed phenomenological bilinear model with deterioration. The models used for the columns directly account for axial load bending moment interaction. For the beams, the deterioration behavior defined for the plastic hinges is fundamental for accurate performance assessments under mainshock-aftershock sequences. A finite-length plastic hinge model is used due to its ability to model plastic hinge lengths explicitly and to separate the behavior of beam in the span from that of beam-column connections.

The obtained results show the importance of considering the aftershock in the evaluation of safety of structures under seismic events, because a significant increase in failure probability is observed when mainshock- aftershock sequences are considered. Moreover, this study shows that the LA9 building, although initially more susceptible to failure than LA3 and LA20, presents significantly higher robustness for the aftershock events. This confirms the observations made previously. Thus, it can also be concluded that the probabilities of failure for multiple hazards requires explicit modeling of the hazards and simulation methods need to accurately model the damage induced by the cascading hazards. Finally, mainshock-aftershock fragility curves and repair cost ratios were derived based on the results obtained with the proposed framework. Some threshold values were derived that may

be useful for the development of future probabilistic studies and risk assessment methodologies.

8.2.4 Robustness Assessment of Structures Considering Post-Earthquake Fire

An extension of the Pacific Earthquake Engineering Research (PEER) Performance-Based Earthquake Engineering (PBEE) is proposed in order to account for fire. However, the application of this methodology was hindered by the verification of the OpenSees thermals models. A sensitivity analysis was also carried out in order to identify the most important parameters affecting structural response during and after fire. The obtained results show that the uncertainty in yield strength and modulus of elasticity at ambient temperature has impact mainly in post-fire structural response due to reversible characteristics of steel thermomechanical properties. Although uncertainty in fire load density tends to be the most relevant parameter influencing peak deformations during fire, the obtained results indicate that it has a negligible influence on the structural capacity to withstand horizontal loading. This is due to the fact that after cooling, steel mechanical properties have recovered their initial values. As a consequence, unless significant residual plastic strains are recorded, post-fire structural capacity is similar to the intact capacity. These results are important to improve the efficiency of probabilistic-based engineering methods considering fire demands. The assessment of post-earthquake fire is envisioned to be finished in the near future.

8.3 Limitations and Future Developments

In what concerns the development of numerical models, the formulation presented for the finite-length plastic hinge elements was validated at the section level for bending moments and rotations only. However, similar approaches may be used in the future for cases in which the interaction between bending and axial deformations is considered. In addition, this formulation is based on a user-defined plastic hinge length. The definition of such variable may pose an additional responsibility on the analyst as accurate information on the structure that allows the estimation of this value may not be available. The fact that the plastic hinge length is kept constant throughout the analysis is also an important simplification, as it recognized that the plastic hinge length varies from the moment the first yield occurs in the hinge section to the full plasticity of the section is obtained.

The developed models that account for the brittle connection fracture need to be supported by additional studies that better estimate the fracture rotation, especially of the top beam-flange connections, for example through laboratory tests of MRF connections with slabs. It is worth noting that this model defines the fracture as a function of the moment at which the fracture rotation is attained by the member. This is a significant limitation as it hinders fatigue-based fractures to occur. Fatigue is responsible for most of the fractures in SMRF's. However, its characterization is extremely complex and the definition of a simple model such as the one proposed in this work can improve the quality of the results, if compared to the assumption of rigid connections.

The seismic hazard modeling follows a simplified approach in this work, namely in what concerns the characterization of mainshock and aftershocks. In future works, the relationship between mainshock and aftershocks should be accounted for. Moreover, the use of the

spectral acceleration at the fundamental period of vibration of the intact structure as intensity measure presents significant disadvantages as the variation of the dynamic properties of the structure due to the mainshock damage is not considered. One possible way to overcome this issue is the use of vector-value intensity measures. In this case, intensity measures may be accurately computed in both pre- and post-mainshock states.

The modeling of fire loading also follows a simplified approach in this work, mainly due to the lack of publicly available data on fire testing on buildings. A more complex and precise model for fire load modeling should be considered in the future.

Future work is envisioned to investigate the influence of panel zones and shear connections of the gravity frames on the results obtained with the proposed methodologies. Further work, considering different types of buildings and different modeling assumptions, namely in what concerns modeling different failure mechanisms (e.g., low-cycle fatigue, shear failure, or connection failure) and materials (RC, timber, etc.) is also necessary. Further work is also required in order to develop accurate relationships between ground motion intensity measures and structural damage indices to be used within performance-based earthquake engineering frameworks.

Bibliography

[1] D. Wald, K. Lin, K. Jaiswal, and B. Bradley, *The 09/03/2010 Darfield earthquake and its aftershocks, including the 02/21/2011 Christchurch event*, U.S. Geological Survey, National Earthquake Information Center, 2011.

[2] O. Norio, T. Ye, Y. Kajitani, P. Shi, and H. Tatano, "The 2011 eastern japan great earthquake disaster: Overview and comments," *International Journal of Disaster Risk Science*, vol. 2, no. 1, pp. 34–42, 2011.

[3] H. Krawinkler, F. Zareian, D. Lignos, and L. Ibarra, "Significance of modeling deterioration in structural components for predicting the collapse potential of structures under earthquake excitations. Part 2," in *Advances in Performace-Based Earthquake Engineering*, vol. 13, Geotechnical, Geological and Earthquake Engineering, 2010, pp. 173–181.

[4] D. G. Lignos and H. Krawinkler, "Deterioration modeling of steel components in support of collapse prediction of steel moment frames under earthquake loading," *ASCE Journal of Structural Engineering*, vol. 137, no. 11, pp. 1291–1302, 2011.

[5] SAC, "Experimental investigations of beam-column subassemblages," Earthquake Engineering Research Center, University of California at Berkeley, Tech. Rep., 1996, Report No. SAC 96-01.

[6] M. Bruneau, S. E. Chang, R. T. Eguchi, G. C. Lee, T. D. O'Rourke, A. M. Reinhorn, M. Shinozuka, K. Tierney, W. A. Wallace, and D. Von Winterfeldt, "A framework to quantitatively assess and enhance the seismic resilience of communities," *Earthquake Spectra*, vol. 19, no. 4, pp. 733–752, 2003.

[7] C. S. Holling, "Resilience and stability of ecological systems," *Annual Review of Ecology and Systematics*, vol. 4, no. 1, pp. 1–23, 1973.

[8] A. Wildavsky, *Searching for Safety*. New Brunswick, NJ: Transaction Publishers, 1991.

[9] J. F. Home and J. E. Orr, "Assessing behaviors that create resilient organizations," *Employment Relations Today*, vol. 24, no. 4, pp. 29–39, 1997.

[10] S. Ainuddin and J. K. Routray, "Institutional framework, key stakeholders and community preparedness for earthquake induced disaster management in balochistan," *Disaster Prevention and Management: An International Journal*, vol. 21, no. 1, pp. 22–36, 2012.

[11] P. H. Longstaff, N. J. Armstrong, K. Perrin, W. Parker, and M. Hidek, *Building Resilient Communities: A Preliminary Framework for Assessment*. Monterey, CA.: Naval Postgraduate School; Center for Homeland Defense and Security, 2010.

[12] C. S. Renschler, S. Roussie, and M. Minkowski, *Linking a Collaborative Platform and Multi-hazard Models to Support the Integrated Management of Extreme Events*. University at Buffalo (SUNY), NY.: MCEER, Multidisciplinary Center for Earthquake Engineering Research, 2007.

[13] P. Franchin and F. Cavalieri, "Probabilistic assessment of civil infrastructure resilience to earthquakes," *Computer-Aided Civil and Infrastructure Engineering*, vol. 30, no. 7, pp. 583–600, 2015.

[14] R. Faturechi and E. Miller-Hooks, "A mathematical framework for quantifying and optimizing protective actions for civil infrastructure systems," *Computer Aided Civil and Infrastructure Engineering*, vol. 29, no. 8, pp. 572–589, 2014.

[15] J Baker, M Schubert, and M Faber, "On the assessment of robustness," *Structural Safety*, vol. 30, no. 3, pp. 253–267, 2008.

[16] V. Silva, M. Marques, J. M. Castro, and H. Varum, "Development and application of a real-time loss estimation framework for portugal," *Bulletin of Earthquake Engineering*, vol. 13, no. 9, pp. 2493–2516, 2015.

[17] C. W. Zobel, "Representing perceived tradeoffs in defining disaster resilience," *Decision Support Systems*, vol. 50, no. 2, pp. 394 –403, 2011.

[18] D. J. Alesch, G. F. Dargush, M. Grigoriu, W. J. Petak, and D. Von Winterfeldt, "Decision models: Approaches for achieving seismic resilience," MCEER Research Progress and Accomplishments 2001-2003, Tech. Rep. MCEER-03-SP01, 2003, pp. 97–114.

[19] M. Faber, *Risk and safety in civil, surveying and environmental engineering - lecture notes*, Swiss Federal Institute of Technology, 2006.

[20] U. Starossek, "Progressive collapse of structures: Nomenclature and procedures," *Structural Engineering International*, vol. 16, no. 2, 2006.

[21] D. Asprone, R. De Risi, and G. Manfredi, "Defining structural robustness under seismic and simultaneous actions: An application to precast RC buildings," *Bulletin of Earthquake Engineering*, vol. 14, no. 2, pp. 485–499, 2016.

[22] Y. Alashker, H. Li, and S. El-Tawil, "Approximations in progressive collapse modeling," *Journal of Structural Engineering*, vol. 137, no. 9, pp. 914–924, 2011.

[23] M. Sasani, A. Werner, and A. Kazemi, "Bar fracture modeling in progressive collapse analysis of reinforced concrete structures," *Engineering Structures*, vol. 33, no. 2, pp. 401–409, 2011.

[24] E. Cavaco, J. Casas, L. Neves, and A. Huespe, "Robustness of corroded reinforced concrete structures: A structural performance approach," *Structure and Infrastructure Engineering*, vol. 9, no. 1, pp. 42–58, 2013.

[25] L. Neves and P. Cruz, "Introducao a analise probabilistica simplificada da seguranca estrutural," *Revista Engenharia Civil*, vol. 1, no. 12, pp. 65–80, 2001.

[26] U. Starossek and M. Haberland, "Approaches to measures of structural robustness," *Structure and Infrastructure Engineering*, vol. 7, no. 7-8, pp. 625–631, 2011.

[27] D. Frangopol and J. Curley, "Effects of damage and redundancy on structural reliability," *ASCE Journal of Structural Engineering*, vol. 113, no. 7, pp. 1533–1549, 1987.

[28] N. C. Lind, "A measure of vulnerability and damage tolerance," *Reliability Engineering and System Safety*, vol. 48, no. 1, pp. 1–6, 1995.

[29] U. Starossek and M. Wolff, "Design of collapse-resistant structures," in *JCSS and IABSE Workshop on Robustness of Structures*, 2005.

[30] B. Izzuddin, A. Vlassis, A. Elghazouli, and D. Nethercot, "Progressive collapse of multi-storey buildings due to sudden column loss - Part I: Simplified assessment framework," *Engineering Structures*, vol. 30, no. 5, pp. 1308 –1318, 2008.

[31] BS5950, *British standard - structural use of steelwork in building. code of practice for design*, 2000.

[32] M.-H. Tsai and B.-H. Lin, "Investigation of progressive collapse resistance and inelastic response for an earthquake-resistant RC building subjected to column failure," *Engineering Structures*, vol. 30, no. 12, pp. 3619 –3628, 2008.

[33] V. D. Biagi and B. Chiaia, "Complexity and robustness of frame structures," *International Journal of Solids and Structures*, vol. 50, no. 22-23, pp. 3723 –3741, 2013.

[34] F. Jalayer, L. Elefante, I. Iervolino, and G. Manfredi, "Knowledge-based performance assessment of existing RC buildings," *Journal of Earthquake Engineering*, vol. 15, no. 3, pp. 362–389, 2011.

[35] M. Akiyama and D. Frangopol, "Life-cycle design of bridges under multiple hazards: Earthquake, tsunami, and continuous deterioration," in *Safety, Reliability, Risk and Life-Cycle Performance of Structures and Infrastructures*, G. Deodatis, B. R. Ellingwood, and D. M. Frangopol, Eds., London: CRC Press - Taylor and Francis Group, 2013.

[36] N. Komendantova, R. Mrzyglocki, A. Mignan, B. Khazai, F. Wenzel, A. Patt, and K. Fleming, "Multi-hazard and multi-risk decision-support tools as a part of participatory risk governance: Feedback from civil protection stakeholders," *International Journal of Disaster Risk Reduction*, vol. 8, pp. 50 –67, 2014.

[37] A. Belejo and A. Barbosa, "Mainshock - aftershock interaction diagram for a 3D plan-asymmetric structure," in *11th World Congress on Computational Mechanics (WCCM XI)*, 2014.

[38] SEAOC, "Vision 2000 - A framework for performance based design, volumes i, ii, iii," Structural Engineers Association of California, Vision 2000 Committee, Sacramento, California, Tech. Rep., 1995.

[39] ATC, "Guidelines and commentary for seismic rehabilitation of buildings," Applied Technology Council, Redwood City, California, Tech. Rep. ATC-33.03, 1995.

[40] S. Gunay and K. M. Mosalam, "PEER Performance-Based Earthquake Engineering Methodology, revisited," *Journal of Earthquake Engineering*, vol. 17, no. 6, pp. 829–858, 2013.

[41] J. W. Baker and A. C. Cornell, "A vector-valued ground motion intensity measure consisting of spectral acceleration and epsilon," *Earthquake Engineering and Structural Dynamics*, vol. 34, no. 10, pp. 1193–1217, 2005.

[42] G. L. Yeo and C. Cornell, "Stochastic characterization and decision bases under time-dependent aftershock risk in performance-based earthquake engineering," Pacific Earthquake Engineering Research Center - College of Engineering, Tech. Rep., 2005, PEER Report 2005/13.

[43] O.-S. Kwon and A. Elnashai, "The effect of material and ground motion uncertainty on the seismic vulnerability curves of RC structure," *Engineering Structures*, vol. 28, no. 2, pp. 289 –303, 2006.

[44] A. K. Kazantzi, T. D. Righiniotis, and M. K. Chryssanthopoulos, "Fragility and hazard analysis of a welded steel moment resisting frame," *Journal of Earthquake Engineering*, vol. 12, no. 4, pp. 596–615, 2008.

[45] IPQ, *NP EN 1998-1 (2010): Eurocode 8 - Design of structures for earthquake resistance. Part 1: General rules, seismic actions and rules for buildings*, Instituto Português da Qualidade, 2010.

[46] S. Freeman, "Development and use of capacity spectrum method," in *6th US National Conference on Earthquake Engineering*, Seattle, 2000.

[47] P. Fajfar, P. Gaspersic, and D. Drobnic, "A simplified nonlinear method for seismic damage analysis of structures," in, ser. Seismic Design Methodologies for the Next Generation of Codes. Proceedings of International Conference at Bled, Slovenia. A.A. Balkema, Rotterdam/Brookfield: Fajfar, P. and Krawinkler, H. (Eds.), 1997.

[48] M. Priestley and G. Calvi, "Concepts and procedures for direct displacement-based design and assessment," in, ser. Seismic Design Methodologies for the Next Generation of Codes. Proceedings of International Conference at Bled, Slovenia. A.A. Balkema, Rotterdam/Brookfield: Fajfar, P. and Krawinkler, H. (Eds.), 1997.

[49] P. Tothong and C. A. Cornell, "Structural performance assessment under near-source pulse-like ground motions using advanced ground motion intensity measures," *Earthquake Engineering and Structural Dynamics*, vol. 37, no. 7, pp. 1013–1037, 2008.

[50] N. Shome, C. A. Cornell, P. Bazzurro, and J. E. Carballo, "Earthquakes, records, and nonlinear responses," *Earthquake Spectra*, vol. 14, no. 3, pp. 469–500, 1998.

[51] Y. Huang, A. Whittaker, N. Luco, and R. Hamburger, "Scaling earthquake ground motions for performance-based assessment of buildings," *Journal of Structural Engineering*, vol. 137, no. 3, pp. 311–321, 2011.

[52] N. Luco, P. Bazzurro, and C. Cornell, "Dynamic versus static computation of the residual capacity of a mainshock-damaged building to withstand an aftershock," in *13th World Conference on Earthquake Engineering*, Vancouver, Canada, 2004.

[53] G. Deierlein, H. Krawinkler, and A. Cornell, "A framework for performance-based earthquake engineering," in *Pacific conference on earthquake engineering, New Zealand Society for Earthquake Engineering*, 2003, pp. 1–8.

[54] D. Vamvatsikos and C. Cornell, "Incremental dynamic analysis," *Earthquake Engineering and Structural Dynamics*, vol. 31, no. 3, pp. 491–514, 2002.

[55] J. W. Baker, "Efficient analytical fragility function fitting using dynamic structural analysis," *Earthquake Spectra*, vol. 31, no. 1, pp. 579–599, 2015.

[56] F. Jalayer, "Direct probabilistic seismic analysis: Implementing non-linear dynamic assessments," PhD thesis, Dept. of Civil and Environmental Engineering, Stanford University, Stanford, CA., 2003.

[57] B. A. Bradley, "A generalized conditional intensity measure approach and holistic ground-motion selection," *Earthquake Engineering & Structural Dynamics*, vol. 39, no. 12, pp. 1321–1342, 2010.

[58] I. Iervolino, M. Giorgio, C. Galasso, and G. Manfredi, "Conditional hazard maps for secondary intensity measures," vol. 100, no. 6, pp. 3312–3319, 2010.

[59] T. Lin, C. B. Haselton, and J. W. Baker, "Conditional spectrum-based ground motion selection. Part I: Hazard consistency for risk-based assessments," *Earthquake Engineering & Structural Dynamics*, vol. 42, no. 12, pp. 1847–1865, 2013.

[60] J. Bommer and A. Acevedo, "The use of real earthquake accelerograms as input to dynamic analysis," *Journal of Earthquake Engineering*, vol. 8, no. Sup1, pp. 43–91, 2004.

[61] I. Iervolino, G. Maddaloni, and E. Cosenza, "Eurocode 8 compliant real record sets for seismic analysis of structures," *Journal of Earthquake Engineering*, vol. 12, no. 1, pp. 54–90, 2008.

[62] I. Iervolino and G. Manfredi, "A review of ground motion record selection strategies for dynamic structural analysis," in *Modern Testing Techniques for Structural Systems*, ser. CISM International Centre for Mechanical Sciences, O. Bursi and D. Wagg, Eds., vol. 502, Springer Vienna, 2008, pp. 131–163.

[63] M. Araújo, L. Macedo, M. Marques, and J. M. Castro, "Code-based record selection methods for seismic performance assessment of buildings," *Earthquake Engineering and Structural Dynamics*, vol. 45, no. 1, pp. 129–148, 2016.

[64] ASCE 41-13, *Seismic Evaluation and Retrofit of Existing Buildings*. Reston, VA: American Society of Civil Engineers, 2014.

[65] NZS 1170-5, *Structural design actions - Part 5: Earthquake actions*. Authority of New Zealand Structure Verification Method B1/VM1, 2004.

[66] A. Veletsos and N. Newmark, "Effect of inelastic behaviour on the response of simple systems to earthquake motions," in *2th World Conference on Earthquake Engineering*, Tokyo, Japan, 1960.

[67] J. Lybas and M. Sozen, "Effect of beam strength ratio on dynamic behaviour of reinforced concrete coupled walls," University of Illinois, Urbana Champaign, USA, Tech. Rep., 1977, Report SRS No. 444.

[68] M. Roufaiel and C. Meyer, "Analytical modeling of hysteretic behavior of r/c frames," *Journal of Structural Engineering*, vol. 113, no. 3, pp. 429–444, 1987.

[69] S. McCabe and W. Hall, "Assessment of seismic structural damage," *Journal of Structural Engineering*, vol. 115, no. 9, pp. 2166–2183, 1989.

[70] P. Fajfar, "Equivalent ductility factors, taking into account low-cycle fatigue," *Earthquake Engineering and Structural Dynamics*, vol. 21, no. 10, pp. 837–848, 1992.

[71] G. H. Powell and R. Allahabadi, "Seismic damage prediction by deterministic methods: Concepts and procedures," *Earthquake Engineering and Structural Dynamics*, vol. 16, no. 5, pp. 719–734, 1988.

[72] C. Malaga-Chuquitaype and A. Elghazouli, "Evaluation of Fatigue and Park and Ang damage indexes in steel structures," in *Proceedings of the 15th World Conference on Earthquake Engineering*, Lisbon, Portugal, 2012.

[73] S. Mehanny and G. Deierlein, "Assessing seismic performance of composite (RCS) and steel moment framed buildings," in *12th World Conference on Earthquake Engineering*, 2000.

[74] A. Teran-Gilmore and J. O. Jirsa, "A damage model for practical seismic design that accounts for low cycle fatigue," *Earthquake Spectra*, vol. 21, no. 3, pp. 803–832, 2005.

[75] Y. Park and A. Ang, "Mechanistic seismic damage model for reinforced concrete," *Journal of Structural Engineering*, vol. 111, no. 4, pp. 722–739, 1985.

[76] R. E. Valles, A. M. Reinhorn, S. K. Kunnath, C. Li, and A. Madan, *IDARC 2D version 4.0: A program for the inelastic damage analysis of buildings*, National Center for Earthquake Engineering Research - State University of New York at Buffalo, 1996.

[77] FEMA355C, *State of the art report on systems performance of steel moment frames subjected to earthquake ground shaking*, SAC Joint Venture for the Federal Emergency Management Agency, Washington, DC, 2000.

[78] C.-H. Loh, C.-H. Mao, J.-R. Huang, and T.-C. Pan, "System identification and damage evaluation of degrading hysteresis of reinforced concrete frames," *Earthquake Engineering and Structural Dynamics*, vol. 40, no. 6, pp. 623–640, 2011.

[79] S. Kunnath, A. Reinhorn, and Y. Park, "Analytical modeling of inelastic seismic response of r/c structures," *Journal of Structural Engineering*, vol. 116, no. 4, pp. 996–1017, 1990.

[80] S. Kunnath, R. Valles-Matox, and A. Reinhorn, "Evaluation of seismic damageability of a typical r/c building in midwest united states," in *11 th World Conference on Earthquake Engineering*, 1996.

[81] Y. J. Park, A. H. Ang, and Y. K. Wen, "Damage-limiting aseismic design of buildings," *Earthquake Spectra*, vol. 3, no. 1, pp. 1–26, 1987.

[82] ATC, "ATC-58: Seismic performance assessment of buildings," Applied Technology Council, 266p, Redwood City, California, Tech. Rep. Draft Report, 2012.

[83] FEMA-P-695, *Quantification of building seismic performance factors*, ATC - Applied Technology Council, 2009.

[84] L. F. Ibarra and H. Krawinkler, "Global collapse of frame structures under seismic excitations," The John A. Blume Earthquake Engineering Research Center, Department of Civil Engineering, Stanford University, Tech. Rep. 152, 2005.

[85] K. Porter, R. Kennedy, and R. Bachman, "Creating fragility functions for performance-based earthquake engineering," *Earthquake Spectra*, vol. 23, no. 2, pp. 471–489, 2007.

[86] L. Eads, E. Miranda, H. Krawinkler, and D. G. Lignos, "An efficient method for estimating the collapse risk of structures in seismic regions," *Earthquake Engineering & Structural Dynamics*, vol. 42, no. 1, pp. 25–41, 2013.

[87] N. Shome, "Probabilistic seismic demand analysis of nonlinear structures," Department of Civil and Environmental Engineering, Stanford University, Tech. Rep., 1999.

[88] C. Haselton and G. Deierlein, "Assessing seismic collapse safety of modern reinforced concrete frame buildings," The John A. Blume Earthquake Engineering Center, Stanford University, Tech. Rep. 156, 2007.

[89] A. B. Liel and G. G. Deierlein, "Assessing the collapse risk of california's existing reinforced concrete frame structures: Metrics for seismic safety decisions," John A Blume Earthquake Engineering Center Report, Stanford University, Tech. Rep., 2008, Report No. 166.

[90] D. Vamvatsikos and C. A. Cornell, "Applied incremental dynamic analysis," *Earthquake Spectra*, vol. 20, no. 2, pp. 523–553, 2004.

[91] M. Shinozuka, M. Feng, J. Lee, and T. Naganuma, "Statistical analysis of fragility curves," *Journal of Engineering Mechanics*, vol. 126, no. 12, pp. 1224–1231, 2000.

[92] J. W. Baker and C. A. Cornell, "Vector-valued ground motion intensity measures for probabilistic seismic demand analysis," John A. Blume Earthquake Engineering Center, Stanford, CA, Tech. Rep. 150, 2005.

[93] D. Straub and A. D. Kiureghian, "Improved seismic fragility modeling from empirical data," *Structural Safety*, vol. 30, no. 4, pp. 320 –336, 2008.

[94] N. Basoz and J. Mander, "Enhancement of the highway transportation module in hazus," National Institute of Building Sciences, Tech. Rep. Final Report, 1999.

[95] ASCE, *Seismic rehabilitation of existing buildings*, ASCE/SEI 41-06, American Society of Civil Engineers, Structural Engineering Institute - Reston VA., 2007.

[96] FEMA, "FEMA-p795: Quantification of building system performance and response factors - component equivalency methodology," Applied Technology Council, prepared for the Federal Emergency Management Agency, Tech. Rep., 2011.

[97] D. Vamvatsikos, A. Kazantzi, and M. Aschheim, "Performance-based seismic design: Avant-garde and code-compatible approaches," *ASCE-ASME Journal of Risk and Uncertainty in Engineering Systems, Part A: Civil Engineering*, vol. 2, no. 2, pp. –, 2016.

[98] C. Cornell, F. Jalayer, R. Hamburger, and D. Foutch, "Probabilistic basis for 2000 SAC Federal Emergency Management Agency steel moment frame guidelines," *Journal of Structural Engineering*, vol. 128, no. 4, pp. 526–533, 2002.

[99] D. Vamvatsikos, "Accurate application and second-order improvement of SAC/FEMA probabilistic formats for seismic performance assessment," *Journal of Structural Engineering*, vol. 140, no. 2, pp. –, 2014.

[100] N. Lazar and M. Dolsek, "Incorporating intensity bounds for assessing the seismic safety of structures: Does it matter?" *Earthquake Engineering & Structural Dynamics*, vol. 43, no. 5, pp. 717–738, 2014.

[101] A. Gupta and H. Krawinkler, "Seismic demands for performance evaluation of steel moment resisting frame structures," The John A. Blume Earthquake Engineering Center, Tech. Rep. 132, 1999.

[102] M. H. Scott and G. L. Fenves, "Plastic hinge integration methods for force-based beam-column elements," *ASCE Journal of Structural Engineering*, vol. 132, no. 2, pp. 244–252, 2006.

[103] R. Clough, K. Benuska, and E. Wilson, "Inelastic earthquake response of tall buildings," in *Third World Conference on Earthquake Engineering*, Wellington, New Zealand, 1965.

[104] M. Giberson, "Two nonlinear beams with definitions of ductility," *Journal of the Structural Division*, vol. 95, no. 2, pp. 137–157, 1969.

[105] T. Takeda, M. Sozen, and N. Nielson, "Reinforced concrete response to simulated earthquakes," *ASCE Journal of the Structural Division*, vol. 96, no. 12, pp. 2557–2573, 1970.

[106] J. Pincheira, F. Dotiwala, and J. D'Souza, "Seismic analysis of older reinforced concrete columns," *Earthquake Spectra*, vol. 15, no. 2, pp. 245–272, 1999.

[107] M. Sivaselvan and A. Reinhorn, "Hysteretic models for deteriorating inelastic structures," *ASCE Journal of Engineering Mechanics*, vol. 126, no. 6, pp. 633–640, 2000.

[108] R. Medina and H. Krawinkler, "Evaluation of drift demands for the seismic performance assessment of frames," *ASCE Journal of Structural Engineering*, vol. 131, no. 7, pp. 1003–1013, 2005.

[109] PEER/ATC, "Modeling and acceptance criteria for seismic design and analysis of tall buildings," Pacific Earthquake Engineering Research Center/Applied Techonology Council, Berkeley, CA, 72-1, 2010.

[110] E. Spacone and F. Filippou, *A Beam Model for Damage Analysis of Reinforced Concrete Structures Under Seismic Loads*. Department of Civil Engineering, University of California, 1992.

[111] A. Neuenhofer and F. Filippou, "Evaluation of nonlinear frame finite-element models," *ASCE Journal of Structural Engineering*, vol. 123, no. 7, pp. 958–966, 1997.

[112] R. Taylor, "The nonlinear seismic response of tall shear wall structures," PhD thesis, Department of Civil Engineering, University of Canterbury, 207pp, 1977.

[113] Y. Kang, *Nonlinear geometric, material and time dependent analysis of reinforced and prestressed concrete frames*. UC-SESM Report No. 77-1, University of California, Berkeley, 1977.

[114] B. Alemdar and D. White, "Displacement, flexibility, and mixed beam–column finite element formulations for distributed plasticity analysis," *Journal of structural engineering*, vol. 131, no. 12, pp. 1811–1819, 2005.

[115] A. Calabrese, J. Almeida, and R. Pinho, "Numerical issues in distributed inelasticity modeling of RC frame elements for seismic analysis," *Journal of Earthquake Engineering*, vol. 14, no. S1, pp. 38–68, 2010.

[116] S. El-Tawil and G. G. Deierlein, "Stress-resultant plasticity for frame structures," *Journal of Engineering Mechanics*, vol. 124, no. 12, pp. 1360–1370, 1998.

[117] J. Coleman and E. Spacone, "Localization issues in force-based frame elements," *ASCE Journal of Structural Engineering*, vol. 127, no. 11, pp. 1257–1265, 2001.

[118] D. Addessi and V. Ciampi, "A regularized force-based beam element with a damage plastic section constitutive law," *International Journal for Numerical Methods in Engineering*, vol. 70, no. 5, pp. 610–629, 2007.

[119] M. Berry, D. Lehman, and L. Lowes, "Lumped-plasticity models for performance simulation of bridge columns," *ACI Structural Journal*, vol. 105, no. 3, 2008.

[120] R. D. Cook, D. S. Malkus, M. E. Plesha, and R. J. Witt, *Concepts and Applications of Finite Element Analysis*. Wiley; 4 edition, 2001.

[121] F. Zareian and R. A. Medina, "A practical method for proper modeling of structural damping in inelastic plane structural systems," *Computers & Structures*, vol. 88, no. 1-2, pp. 45–53, 2010.

[122] E. Spacone, F. Filippou, and F. Taucer, "Fibre beam-column model for non-linear analysis of R/C frames: Part I. formulation," *Earthquake Engineering and Structural Dynamics*, vol. 25, no. 7, pp. 711–726, 1996.

[123] M. H. Scott and K. L. Ryan, "Moment-rotation behavior of force-based plastic hinge elements," *Earthquake Spectra*, vol. 29, no. 2, pp. 597–607, 2013.

[124] P. N. Souza, R. Fateman, J. Moses, and C. Yapp, *The Maxima book*. http://maxima.sourceforge.net, 2003.

[125] R. De Borst, M. Crisfield, J. Remmers, and C. Verhoosel, *Nonlinear finite element analysis of solids and structures*. John Wiley & Sons, 2012.

[126] M. Scott and G. Fenves, "Krylov subspace accelerated Newton algorithm: Application to dynamic progressive collapse simulation of frames," *ASCE Journal of Structural Engineering*, vol. 136, no. 5, pp. 473–480, 2010.

[127] D. G. Lignos, "Sidesway collapse of deteriorating structural systems under earthquake excitations," PhD thesis, Department of Civil and Environmental Engineering, Stanford University, Stanford California, 2008.

[128] D. Lignos and H. Krawinkler, "Development and utilization of structural component databases for performance-based earthquake engineering," *ASCE Journal of Structural Engineering*, vol. 139, no. 8, pp. –, 2013.

[129] F. McKenna, G. Fenves, and M. Scott, *Open System for Earthquake Engineering Simulation (OpenSees)*. University of California, Berkeley, CA, 2000.

[130] F. Bruneau, C.-M. Uang, and A. Whittaker, *Ductile design of steel structures*. 1998.

[131] L. F. Ibarra, R. A. Medina, and H. Krawinkler, "Hysteretic models that incorporate strength and stiffness deterioration," *Earthquake Engineering and Structural Dynamics*, vol. 34, no. 12, 2005.

[132] S. Mazzoni, F. McKenna, M. H. Scott, and G. L. Fenves, *The OpenSees command language manual, Version 2.0*, Pacific Earthquake Eng. Research Center, Univ. California at Berkeley, 2009.

[133] M. Rahnama and H. Krawinkler, "Effects of soft soil and hysteresis model on seismic demands," *John A. Blume Earthquake Engineering Center Report*, no. 108, 1993.

[134] J.-Y. Wu, "New enriched finite elements with softening plastic hinges for the modeling of localized failure in beams," *Computers and Structures*, vol. 128, no. -, pp. 203–218, 2013.

[135] A. Saritas and F. Filippou, "Frame element for metallic shear-yielding members under cyclic loading," *Journal of Structural Engineering*, vol. 135, no. 9, pp. 1115–1123, 2009.

[136] A. Saritas and F. C. Filippou, "Inelastic axial-flexure-shear coupling in a mixed formulation beam finite element," *International Journal of Non-Linear Mechanics*, vol. 44, no. 8, pp. 913–922, 2009.

[137] K. Elwood and J. Moehle, "Dynamic collapse analysis for a reinforced concrete frame sustaining shear and axial failures," *Earthquake Engineering & Structural Dynamics*, vol. 37, no. 7, pp. 991–1012, 2008.

[138] UBC, *"Structural Engineering Design Provisions", Uniform Building Code, vol. 2*, International Conference of Building Officials, 1994.

[139] N. Luco, "Probabilistic seismic demand analysis, SMRF connection fractures, and near-source effects," PhD thesis, Department of Civil and Environmental Engineering, Stanford University, Stanford, California, 2002.

[140] G. Xu and B. Ellingwood, "Probabilistic robustness assessment of pre-Northridge steel moment resisting frames," *Journal of Structural Engineering*, vol. 137, no. 9, pp. 925–934, 2011.

[141] D. Bonowitz and N. Youssef, "SAC survey of steel moment-resisting frame building affected by the 1994 Northridge eathquake," SAC, Tech. Rep., 1995, in Surveys and Assessment of Damage to Building Affected by the Northridge Earthquake of January 17, 1994 (SAC 95-06).

[142] N. Luco and C. A. Cornell, "Effects of connection fractures on SMRF seismic drift demands," *ASCE Journal of Structural Engineering*, vol. 126, no. 1, pp. 127–136, 2000.

[143] E. P. Popov, T.-S. Yang, and S.-P. Chang, "Design of steel MRF connections before and after 1994 Northridge earthquake," *Engineering Structures*, vol. 20, no. 12, pp. 1030 –1038, 1998.

[144] B. Maison and D. Bonowitz, "How safe are pre-northridge WSMFs? A case study of the SAC Los Angeles nine-story building.," *Earthquake spectra*, vol. 15, no. 4, pp. 766–789, 1999.

[145] H. Idota, L. Guan, and K. Yamazaki, "Statistical correlation of steel members for system reliability analysis," in *9th international conference on structural safety and reliability (ICOSSAR)*, Osaka, Japan, 2009.

[146] M. D. McKay, R. J. Beckman, and W. J. Conover, "A comparison of three methods for selecting values of input variables in the analysis of output from a computer code," *Technometrics*, vol. 21, no. 2, pp. 239–245, 1979.

[147] A. Olsson, G. Sandberg, and O. Dahlblom, "On latin hypercube sampling for structural reliability analysis," *Structural Safety*, vol. 25, no. 1, pp. 47 –68, 2003.

[148] Dames & Moore Inc., "Survey of damaged steel moment frame buildings," SAC, Tech. Rep., 1998, draft report on SAC Phase 2 Task 3.1.2, version 1.00.

[149] V. Prakash, G. Powell, and S. Campbell, "DRAIN-2DX base program description and user guide, version 1.0," Department of Civil Engineering, University of California, Berkeley CA, Tech. Rep., 1993, Report No. UCB/SEMM-93/17 and 18.

[150] C. Uang, Q. Yu, A. Sadre, D. Bonowitz, and N. Youssef, "Performance of a 13-story steel moment-resisting frame damaged in the 1994 Northridge earthquake," Structural Systems Research Project, University of California, San Diego, Tech. Rep. SSRP -95/04, 1995.

[151] S. K. Kunnath, "Enhancements to program IDARC: Modeling inelastic behavior of welded connections in steel moment-resisting frames," NIST, Gaithersburg, Md, Tech. Rep., 1995, NIST GCR 95-673.

[152] J. F. Hall, "Seismic response of steel frame buildings to near-source ground motions," *Earthquake Engineering & Structural Dynamics*, vol. 27, no. 12, pp. 1445–1464, 1998.

[153] J. Song, "Seismic reliability evaluation of steel frames with damaged welded connections," PhD thesis, John Hopkins University, Baltimore, 1998.

[154] K. Lee and D. Foutch, "Seismic performance evaluation of pre-Northridge steel frame buildings with brittle connections," *Journal of Structural Engineering*, vol. 128, no. 4, pp. 546–555, 2002.

[155] C. Wang and Y. Wen, "Evaluation of pre-Northridge low-rise steel buildings. i: Modeling," *Journal of Structural Engineering*, vol. 126, no. 10, pp. 1160–1168, 2000.

[156] H. Li and S. El-Tawil, "Three-dimensional effects and collapse resistance mechanisms in steel frame buildings," *Journal of Structural Engineering*, vol. 140, no. 8, A4014017, 2014.

[157] S. Islam, "Analysis of two steel moment resisting frame buildings damaged during the Northridge earthquake," National Institute of Standards and Technology, Tech. Rep., 1995.

[158] SAC, "Analytical and field investigations of buildings affected by the Northridge earthquake of january 17, 1994," SAC Joint Venture, Tech. Rep., 1995, Rep. No. SAC 95-04, parts 1 and 2.

[159] SAC, "Protocol for fabrication, inspection, testing, and documentation of beam- column connection tests and other experimental specimens," Structural Laboratory, The University of Michigan, Tech. Rep., 1998, Report No. SAC/BD-97/02.

[160] SAC, "Connection test summaries," SAC, Tech. Rep. 96-02, 1997.

[161] K. Lee, B. Stojadinovic, S. C. Goel, A. G. Margarian, J. Choi, A. Wongkaew, B. P. Reyher, and L. D.-Y, "Parametric tests on unreinforced connections, volume i - final report," SAC, Tech. Rep. SAC/BD-00/01, 2000.

[162] J. C. Anderson, R. G. Johnston, and J. E. Partridge, "Testing of damaged steel moment resisting connections," in *11th World Conf. on Earthquake Engrg.*, Acapulco, Mexico, 1996.

[163] A. Kazantzi, D. Vamvatsikos, and D. Lignos, "Seismic performance of a steel moment-resisting frame subject to strength and ductility uncertainty," *Engineering Structures*, vol. 78, no. 1, pp. 69 –77, 2014.

[164] M. Dolsek, "Incremental dynamic analysis with consideration of modeling uncertainties," *Earthquake Engineering & Structural Dynamics*, vol. 38, no. 6, pp. 805–825, 2009.

[165] L. R. Barroso and S. Winterstein, "Probabilistic seismic demand analysis of controlled steel moment-resisting frame structures," *Earthquake Engineering & Structural Dynamics*, vol. 31, no. 12, pp. 2049–2066, 2002.

[166] D. Thain, T. Tannenbaum, and M. Livny, "Distributed computing in practice: The Condor experience.," *Concurrency - Practice and Experience*, vol. 17, no. 2-4, pp. 323–356, 2005.

[167] P. Somerville, N. Smith, S. Punyamurthula, and J. Sun, "Development of ground motion time histories for phase II of the FEMA/SAC steel project," SAC Background Document, Tech. Rep., 1997, Rep. No. SAC/BD-97/04.

[168] E. Erduran, "Evaluation of Rayleigh damping and its influence on engineering demand parameter estimates," *Earthquake Engineering & Structural Dynamics*, vol. 41, no. 14, pp. 1905–1919, 2012.

[169] S. Shi and D. Foutch, "Evaluation of connection fracture and hysteresis type on the seismic response of steel buildings," Department of Civil and Environmental Engineering, University of Illinois at Urbana-Champaign, Tech. Rep. UILU-ENG-97-2005, 1997.

[170] FEMA351, *Recommended seismic evaluation and upgrade criteria for existing welded steel moment-frame buildings*, SAC Joint Venture for the Federal Emergency Management Agency, Washington DC, 2000.

[171] R. Chandramohan, J. W. Baker, and G. G. Deierlein, "Quantifying the influence of ground motion duration on structural collapse capacity using spectrally equivalent records," *Earthquake Spectra*, vol. 32, no. 2, pp. 927–950, 2016.

[172] R. S. Yeats, *Living with earthquakes in the Pacific Northwest: A Survivor's Guide, second edition*, Oregon State Univ Press, 2004.

[173] J. Hancock and J. J. Bommer, "A state-of-knowledge review of the influence of strong-motion duration on structural damage," *Earthquake Spectra*, vol. 22, no. 3, pp. 827–845, 2006.

[174] R. Green and G. Terri, "Number of equivalent cycles concept for liquefaction evaluations - revisited," *Journal of Geotechnical and Geoenvironmental Engineering*, vol. 131, no. 4, pp. 477–488, 2005.

[175] J. Bray, "Simplified seismic slope displacement procedures," English, in *Earthquake Geotechnical Engineering*, ser. Geotechnical, Geological and Earthquake Engineering, K. Pitilakis, Ed., vol. 6, Springer Netherlands, 2007, pp. 327–353.

[176] A. Nassar and H. Krawinkler, "Seismic demands for SDOF and MDOF systems," English, John A. Blume Earthquake Engineering Center, California, Tech. Rep., Jun. 1991. (visited on 03/08/2013).

[177] Y. H. Chai, "Incorporating low-cycle fatigue model into duration-dependent inelastic design spectra," *Earthquake Engineering and Structural Dynamics*, vol. 34, no. 1, pp. 83–96, 2005.

[178] E. Miranda, "Evaluation of site-dependent inelastic seismic design spectra," *Journal of Structural Engineering*, vol. 119, no. 5, pp. 1319–1338, 1993.

[179] I. Iervolino, G. Manfredi, and E. Cosenza, "Ground motion duration effects on nonlinear seismic response," *Earthquake Engineering and Structural Dynamics*, vol. 35, no. 1, pp. 21–38, 2006.

[180] A. Dutta and J. Mander, "Energy based methodology for ductile design of concrete columns," *ASCE Journal of Structural Engineering*, vol. 127, no. 12, pp. 1374–1381, 2001.

[181] G. Manfredi, M. Polese, and E. Cosenza, "Cumulative demand of the earthquake ground motions in the near source," *Earthquake Engineering and Structural Dynamics*, vol. 32, no. 12, pp. 1853–1865, 2003.

[182] M. Raghunandan and A. B. Liel, "Effect of ground motion duration on earthquake-induced structural collapse," *Structural Safety*, vol. 41, pp. 119–133, 2013.

[183] J. Ruiz-Garcia, "On the influence of strong-ground motion duration on residual displacement demands," *Earthquakes and Structures*, vol. 4, no. 1, pp. 327–44, 2010.

[184] R. Song, Y. Li, and J. W. Van de Lindt, "Impact of earthquake ground motion characteristics on collapse risk of post-mainshock buildings considering aftershocks," *Engineering Structures*, vol. 81, pp. 349 –361, 2014.

[185] J. J. Bommer and A. Martinez-Pereira, "The effective duration of earthquake strong motion," *Journal of Earthquake Engineering*, vol. 3, no. 02, pp. 127–172, 1999.

[186] J. Bommer, J. Cepeda, J. Hasbun, W. Salazar, A. Suarez, A. Udias, N. Ambraseys, E. Buforn, J. Cortina, R. Madariaga, P. Mendez, J. Mezcua, and D. Papastamatiou, "A new digital accelerograph network for El Salvador," *Seismological Research Letters*, vol. 68, no. 3, pp. 426–437, 1997.

[187] R. Tremblay, "Development of design spectra for long-duration ground-motions from cascadia subduction earthquakes," *Canadian Journal of Civil Engineering*, vol. 25, no. 6, pp. 1078–1090, 1998.

[188] F. Luca, E Chioccarelli, and I Iervolino, "Preliminary study of the 2011. Japan earthquake ground motion record," Dipartimento di Ing. Strut., Univ. di Napoli Federico II., Italy, Tech. Rep., 2011, p.12.

[189] J. Foschaar, J. Baker, and G. Deierlein, "Preliminary assessment of ground motion duration effects on structural collapse," in *15th World Conference on Earthquake Engineering*, 2012.

[190] W. Suzuki, S. Aoi, H. Sekiguchi, and T Kunugi, "Source rupture process of the 2011 Tohoku-Oki earthquake derived from the strong-motion records," in *15th World Conference on Earthquake Engineering*, 2012.

[191] K-net, *Strong-motion seismograph networks (k-net,kik-net)*, 2012. (visited on 03/03/2013).

[192] R. L. Boroschek, V. Contreras, D. Y. Kwak, and J. P. Stewart, "Strong ground motion attributes of the 2010 mw 8.8 maule, chile, earthquake," *Earthquake Spectra*, vol. 28, no. S1, S19–S38, 2012.

[193] H. Ghofrani, G. M. Atkinson, and K. Goda, "Implications of the 2011 M9.0 Tohoku Japan earthquake for the treatment of site effects in large earthquakes," *Bulletin of Earthquake Engineering*, vol. 11, no. 1, pp. 171–203, 2013.

[194] Y. Long, "Effect of subduction zone earthquakes on sdof bridge models," Master's thesis, Oregon State University, Corvallis, Oregon, 2012.

[195] PEER, *Pacific Earthquake Engineering Research (PEER) NGA Database*, http://www.peer.berkeley.e 2002.

[196] S. L. Kramer, *Geotechnical Earthquake Engineering*. Prentice Hall, 1996.

[197] A. Teran-Gilmore, "Performance-based earthquake-resistant design of framed buildings using energy concepts," PhD thesis, University of California at Berkeley, 1996.

[198] L. Tirca, L. Chen, and R. Tremblay, "Assessing collapse safety of cbf buildings subjected to crustal and subduction earthquakes," *Journal of Constructional Steel Research*, vol. 115, no. 1, pp. 47–61, 2015.

[199] D. Vamvatsikos and C. Cornell, "Tracing and post-processing of ida curves: Theory and software implementation," RMS Program, Stanford University, Tech. Rep., 2001, Report No. RMS-44.

[200] R. Song, Y. Li, and J. W. Van de Lindt, "Loss estimation of steel buildings to earthquake mainshock-aftershock sequences," *Structural Safety*, vol. 61, pp. 1–11, 2016.

[201] N. Newmark and E. Rosenbleuth, *Fundamental of Earthquake Engineering*. Prentice-Hall, 1971.

[202] U. Starossek and M. Haberland, "Measures of structural robustness–requirements and applications," in *ASCE SEI Structures Congress - Crossing Borders*, Vancouver, Canada, 2008.

[203] J. Ruiz-García, "Mainshock-aftershock ground motion features and their influence in building's seismic response," *Journal of Earthquake Engineering*, vol. 16, no. 5, pp. 719–737, 2012.

[204] M Fragiacomo, C Amadio, and L Macorini, "Seismic response of steel frames under repeated earthquake," English, *Engineering Structures*, vol. 26, no. 13, 2021–2035, 2004.

[205] K Lee and D. Foutch, "Performance evaluation of damaged steel frame buildings subjected to seismic loads," English, *ASCE Journal of Structural Engineering*, vol. 130, no. 4, 588–599, 2004.

[206] Q. Li and B. R. Ellingwood, "Performance evaluation and damage assessment of steel frame buildings under mainshock-aftershock earthquake sequences," *Earthquake Engineering and Structural Dynamics*, vol. 36, no. 3, pp. 405–427, 2007.

[207] N. Luco, M. C. Gerstenberger, S. Uma, H. Ryu, A. B. Liel, and M. Raghunandan, "A methodology for post-mainshock probabilistic assessment of building collapse risk," in *Pacific Conference on Earthquake Engineering*, Auckland, New Zealand, 2011.

[208] H. Ryu, N. Luco, S. Uma, and A. Liel, "Developing fragilities for mainshock-damaged structures through incremental dynamic analysis," in *Pacific Conference on Earthquake Engineering*, Auckland, New Zealand, 2011.

[209] P. Bazzurro, C. Cornell, C. Menun, M. Motahari, and N. Luco, "Advanced seismic assessment guidelines," Pacific Earthquake Engineering Research Center - College of Engineering, Tech. Rep., 2006, PEER Report 2006/5.

[210] G. L. Yeo and C. A. Cornell, "Building life-cycle cost analysis due to mainshock and aftershock occurrences," *Structural Safety*, vol. 31, no. 5, pp. 396–408, 2009.

[211] F. Jalayer, D. Asprone, A. Prota, and G. Manfredi, "A decision support system for post-earthquake reliability assessment of structures subjected to aftershocks: An application to L'Aquila earthquake, 2009," *Bulletin of Earthquake Engineering*, vol. 9, no. 4, pp. 997–1014, 2011.

[212] P. Reasenberg and L. Jones, *Earthquake hazard after a mainshock in California*. Science, 1989, pp. 1173–1175.

[213] Y. Li, R. Song, and J. Van De Lindt, "Collapse fragility of steel structures subjected to earthquake mainshock-aftershock sequences," *Journal of Structural Engineering*, vol. 140, no. 12, p. 04 014 095, 2014.

[214] Y. Yin and Y. Li, "Loss estimation of light-frame wood construction subjected to mainshock-aftershock sequences," *Journal of Performance of Constructed Facilities*, vol. 25, no. 6, pp. 504–513, 2011.

[215] N. Nazari, J. Van de Lindt, and Y. Li, "Quantifying changes in structural design needed to account for aftershock hazard," *Journal of Structural Engineering*, vol. 141, no. 11, pp. –, 2015.

[216] M. Faizian, H. Schalcher, and M. Faber, "Consequence assessment in earthquake risk management using damage indicators," in *First International Forum on Engineering Decision Making (IFED)*, 2004.

[217] M. Petersen, A. Frankel, S. Harmsen, C. Mueller, K. Haller, R. Wheeler, R. Wesson, Y. Zeng, O. Boyd, D. Perkins, N. Luco, C. Field E.H. Wills, and K. Rukstales, "Documentation for the 2008 update of the united states national seismic hazard maps," U.S. Geological Survey Open-File Report 2008-1128, Tech. Rep., 2008, 61 p.

[218] J. Baker, "Probabilistic structural response assessment using vector-valued intensity measures," *Earthquake Engineering and Structural Dynamics*, vol. 36, no. 13, pp. 1861 –1883, 2007.

[219] N. Jayaram and J. Baker, "Statistical tests of the joint distribution of spectral acceleration values," *Bulletin of the Seismological Society of America 2008*, vol. 98, no. 5, pp. 2231–2243, 2008.

[220] FEMA356, *Prestandard and commentary for the seismic rehabilitation of buildings: FEMA-356*, 2000.

[221] Y. Li, R. Song, J. Van de Lindt, N. Nazari, and N. Luco, "Assessment of wood and steel structures subjected to earthquake mainshock-aftershock," in *XV World Conference on Earthquake Engineering*, Lisbon, Portugak, 2012.

[222] J. D. Newell and C.-M. Uang, "Cyclic behavior of steel wide-flange columns subjected to large drift," *Journal of structural engineering*, vol. 134, no. 8, pp. 1334–1342, 2008.

[223] D. G. Lignos, Y. Chung, T. Nagae, and M. Nakashima, "Numerical and experimental evaluation of seismic capacity of high-rise steel buildings subjected to long duration earthquakes," *Comput. Struct.*, vol. 89, no. 11-12, pp. 959–967, 2011.

[224] N. Luco and C. A. Cornell, "Effects of connection fractures on smrf seismic drift demands," *ASCE Journal of Structural Engineering*, vol. 126, no. 1, pp. 127–136, 2000.

[225] A. D. Kiureghian, "Structural reliability methods for seismic safety assessment: A review," *Engineering Structures*, vol. 18, no. 6, pp. 412 –424, 1996.

[226] M. Faggella, A. R. Barbosa, J. P. Conte, E. Spacone, and J. I. Restrepo, "Probabilistic seismic response analysis of a 3-D reinforced concrete building," *Structural Safety*, vol. 44, no. 0, pp. 11 –27, 2013.

[227] G.-L. F. Porcari, E. Zalok, and W. Mekky, "Fire induced progressive collapse of steel building structures: A review of the mechanisms," *Engineering Structures*, vol. 82, pp. 261–267, 2015.

[228] R. Sun, Z. Huang, and I. W. Burgess, "Progressive collapse analysis of steel structures under fire conditions," *Engineering structures*, vol. 34, pp. 400–413, 2012.

[229] M. Memari and H. Mahmoud, "Performance of steel moment resisting frames with RBS connections under fire loading," *Engineering Structures*, vol. 75, pp. 126–138, 2014.

[230] N. Johansson, "Numerical experiments and compartment fires," *Fire Science Reviews*, vol. 3, no. 1, pp. 1–12, 2014.

[231] J. Takagi and G. G. Deierlein, "Strength design criteria for steel members at elevated temperatures," *Journal of Constructional Steel Research*, vol. 63, no. 8, pp. 1036–1050, 2007.

[232] ABAUS, "Abaqus 6.14: Analysis user's manual. volume 2. theory manual," Dassault Systemes, Tech. Rep., 2011.

[233] J. Franssen, V. Kodur, and J Mason, "Safir: A computer program for analysis of structures submitted to the fire," *University of Liege, Belgium*, vol. 2001, no. 5.2, 1998.

[234] O. Vassart, L.-G. Cajot, M. O'Connor, Y Shenkai, C Fraud, B. Zhao, J. De la Quintana, J Martinez de Aragon, J.-M. Franssen, and F. Gens, "3D simulation of industrial hall in case of fire. Benchmark between ABAQUS, ANSYS and SAFIR," in *10th International Fire Science & Engineering Conference*, Interscience, 2004.

[235] P. Kohnke, *ANSYS theory reference*. Ansys, 1999.

[236] M. M. Garlock and S. E. Quiel, "The behavior of steel perimeter columns in a high-rise building under fire," *Engineering Journal - American Institute of Steel Construction*, vol. 44, no. 4, p. 359, 2007.

[237] VULCAN, "Vulcan: A computer program for analysis of structures subject to the fire," VULCAN, Tech. Rep., 2010.

[238] J. Jiang, L. Jiang, P. Kotsovinos, J. Zhang, A. Usmani, F. McKenna, and G.-Q. Li, "OpenSees software architecture for the analysis of structures in fire," *Journal of Computing in Civil Engineering*, vol. 29, no. 1, pp. –, 2013.

[239] J. Jiang, G.-Q. Li, and A. Usmani, "Effect of bracing systems on fire-induced progressive collapse of steel structures using OpenSees," *Fire Technology*, vol. 51, no. 5, pp. 1249–1273, 2015.

[240] N. E. Khorasani, M. E. Garlock, and S. E. Quiel, "Modeling steel structures in OpenSees: Enhancements for fire and multi-hazard probabilistic analyses," *Computers and Structures*, vol. 157, pp. 218 –231, 2015.

[241] Q. Guo and A. E. Jeffers, "Finite-element reliability analysis of structures subjected to fire," *Journal of Structural Engineering*, vol. 141, no. 4, pp. –, 2015.

[242] D. Lange, S. Devaney, and A. Usmani, "An application of the PEER performance based earthquake engineering framework to structures in fire," *Engineering Structures*, vol. 66, pp. 100–115, 2014.

[243] E. Nigro, A. Bilotta, D. Asprone, F. Jalayer, A. Prota, and G. Manfredi, "Probabilistic approach for failure assessment of steel structures in fire by means of plastic limit analysis," *Fire Safety Journal*, vol. 68, pp. 16 –29, 2014.

[244] W. Ramroth, P Krysl, and R. Asaro, "Sensitivity and uncertainty analyses for fe thermal model of frp panel exposed to fire," *Composites Part A: Applied Science and Manufacturing*, vol. 37, no. 7, pp. 1082–1091, 2006.

[245] S. E. Quiel and S. M. Marjanishvili, "Fire resistance of a damaged steel building frame designed to resist progressive collapse," *Journal of Performance of Constructed Facilities*, vol. 26, no. 4, pp. –, 2012.

[246] N. L. Braxtan and S. P. Pessiki, "Post-earthquake fire performance of sprayed fire-resistive material on steel moment frames," *Journal of Structural Engineering*, vol. 137, no. 9, pp. 946–953, 2011.

[247] M. Memari, H. Mahmoud, and B. Ellingwood, "Post-earthquake fire performance of moment resisting frames with reduced beam section connections," *Journal of Constructional Steel Research*, vol. 103, pp. 215–229, 2014.

[248] B. Faggiano and F. M. Mazzolani, "Fire after earthquake robustness evaluation and design: Application to steel structures," *Steel Construction*, vol. 4, no. 3, pp. 183–187, 2011.

[249] M. Johann, L. Albano, R. Fitzgerald, and B. Meacham, "Performance-based structural fire safety," *Journal of Performance of Constructed Facilities*, vol. 20, no. 1, pp. 45–53, 2006.

[250] D. Rini and S. Lamont, "Performance based structural fire engineering for modern building design," in *Structures Congress 2008*, ch. 247, pp. 1–12.

[251] S. Hamilton, "Performance-based fire engineering for steel framed structures: A probabilistic methodology," PhD thesis, Stanford University, 2011.

[252] Y. Wang, I. Burgess, F. Wald, and M. Gillie, *Performance-Based Fire Engineering of Structures*. Ebook Library. Web: Hoboken: CRC Press, 2012.

[253] A. Usmani, J. Zhang, J. Jiang, Y. Jiang, and I. May, "Using OpenSees for structures in fire," *Journal of Structural Fire Engineering*, vol. 3, no. 1, pp. 57–70, 2012.

[254] R. Tide, "Integrity of structural steel after exposure to fire," *AISC Engineering Journal (FirstQuarter)*, pp. 26–38, 1998.

[255] B. Faggiano, M. Esposto, F. Mazzolani, and R. Landolfo, "Fire analysis on steel portal frames damaged after earthquake according to performance based design," in *Proceedings of the Workshop COST C26 action*, 2007, pp. 35–40.

[256] C. Scawthorn, J. Eidinger, and A. Schiff, *Fire following earthquake*. ASCE Publications, 2005.

[257] S. Lee, R. Davidson, N. Ohnishi, and C. Scawthorn, "Fire following earthquake-reviewing the state-of-the-art of modeling," *Earthquake Spectra*, vol. 24, no. 4, pp. 933–967, 2008.

[258] E. Kelly and R. Tell, "Modeling the number of ignitions following an earthquake: Developing prediction limits for overdispersed count data," Energy Department Natural Phenomena Hazards (NPH) Workshop, Maryland, Tech. Rep. LA-UR-11-01857, 2011.

[259] N. E. Khorasani, M. Garlock, and P. Gardoni, "Fire load: Survey data, recent standards, and probabilistic models for office buildings," *Engineering Structures*, vol. 58, pp. 152–165, 2014.

[260] CEN, *Eurocode 1: Actions on structures, part 1-2: General actions - actions on structures exposed to fire*, 2002.

[261] IPQ, *NPEN1993-1: 2010, Eurocode 3 - Design of steel structures.* Instituto Português da Qualidade, 2010.

[262] T. Vrouwenvelder, "The JCSS probabilistic model code, Part 3: Resistance models," *Structural Safety*, vol. 19, no. 3, pp. 245–251, 1997.

[263] N. E. Khorasani, P. Gardoni, and M. Garlock, "Probabilistic fire analysis: Material models and evaluation of steel structural members," *Journal of Structural Engineering*, vol. 141, no. 12, pp. –, 2015.

[264] T. Vrouwenvelder, "The JCSS probabilistic model code, Part 2: Load models," *Structural Safety*, vol. 19, no. 3, pp. 245–251, 1997.

[265] O. C. Celik and B. R. Ellingwood, "Seismic fragilities for non-ductile reinforced concrete frames–role of aleatoric and epistemic uncertainties," *Structural Safety*, vol. 32, no. 1, pp. 1–12, 2010.

[266] K. A. Porter, J. L. Beck, and R. V. Shaikhutdinov, "Sensitivity of building loss estimates to major uncertain variables," *Earthquake Spectra*, vol. 18, no. 4, pp. 719–743, 2002.

[267] M Faggella, A Barbosa, J. Conte, E Spacone, J. Restrepo, A. Santini, and N. Moraci, "Seismic assessment of r/c building structure through nonlinear probabilistic analysis with high-performance computing," in *AIP Conference Proceedings*, vol. 1020, 2008, p. 930.

[268] F. McKenna, M. H. Scott, and G. L. Fenves, "Nonlinear finite-element analysis software architecture using object composition," *Journal of Computing in Civil Engineering*, vol. 24, no. 1, pp. 95–107, 2009.

[269] J. Jiang and A. Usmani, "Modeling of steel frame structures in fire using OpenSees," *Computers & Structures*, vol. 118, pp. 90–99, 2013.

[270] S. E. Quiel and M. E. Garlock, "Closed-form prediction of the thermal and structural response of a perimeter column in a fire," *Open Construction and Building Technology Journal*, vol. 4, no. 1, pp. 64–78, 2010.

[271] J. El-Rimawi, I. Burgess, and R. Plank, "The treatment of strain reversal in structural members during the cooling phase of a fire," *Journal of constructional steel research*, vol. 37, no. 2, pp. 115–135, 1996.

[272] J.-M. Franssen, "The unloading of building materials submitted to fire," *Fire safety journal*, vol. 16, no. 3, pp. 213–227, 1990.

[273] S. Selamet, "Fire performance of an unprotected composite beam behavior with finite beam end restraints, rebar size and locations," in *Application of Structural Fire Engineering*, Prague, Czech Republic, 2013.

[274] P. Kotsovinos and A. Usmani, "The world trade center 9/11 disaster and progressive collapse of tall buildings," *Fire technology*, vol. 49, no. 3, pp. 741–765, 2013.

[275] Y.-Q. Jiang, "Development and application of a thermal analysis framework in OpenSees for structures in fire," PhD thesis, The University of Edinburgh, 2013.

[276] A Santiago, L Simoes da Silva, P Vila Real, and J. Franssen, "Effect of cooling on the behaviour of a steel beam under fire loading including the end joint response," in *Proceedings of the 9th International Conference on Civil and Structural Engineering Computing, ed. Topping, BHV, Civil-Comp Press, Stirling, United Kingdom, paper*, vol. 65, 2003.

[277] A. Rubert and P. Schaumann, "Structural steel and plane frame assemblies under fire action," *Fire Safety Journal*, vol. 10, no. 3, pp. 173–184, 1986.

[278] T. Haukaas and M. H. Scott, "Shape sensitivities in the reliability analysis of nonlinear frame structures," *Computers & structures*, vol. 84, no. 15, pp. 964–977, 2006.

[279] B. R. Ellingwood, "Load combination requirements for fire-resistant structural design," *Journal of Fire Protection Engineering*, vol. 15, no. 1, pp. 43–61, 2005.

Appendix A

Chapter 2 - Computation of the Section Flexural Stiffness Modification Parameters

The following code was implemented in the *wxMaxima* software [124].

- Unknowns

$$\beta_1, \beta_2, \beta_3 \tag{A.1}$$

- Input data

$$\begin{aligned} y &: [0, 8/3 \times L_{pI}, L - 8/3 \times L_{pJ}, L]; \\ w &: [L_{pI}, 3 \times L_{pI}, 3 \times L_{pJ}, L_{pJ}]; \\ mp &: [\alpha_1 \times 6 \times L_{pI}/L, \beta_1, \beta_3, \alpha_2 \times 6 \times L_{pJ}/L]; \end{aligned} \tag{A.2}$$

- Computation of the element flexibility matrix (flexural terms only)

$$f_1 : \mathbf{matrix}([0,0],[0,0]); \tag{A.3}$$

  - Plastic hinges integration points

$$\begin{aligned} \mathbf{for} \quad i \quad &: \quad 1 \quad \mathbf{to} \quad 4 \quad \mathbf{do} \\ (f_1 \quad &: \quad f_1 + \mathbf{transpose}(\mathbf{matrix}([0,0],[y[i]/L-1, y[i]/L])). \\ &\quad \mathbf{matrix}([0,0],[y[i]/L-1, y[i]/L]) \times w[i]) \times \\ &\quad (1/(mp[i] * EI)); \end{aligned} \tag{A.4}$$

  - Interior region

$$\begin{aligned} f_1 \quad &: \quad f_1 + \mathbf{integrate}(\mathbf{transpose}(\mathbf{matrix}([0,0],[x/L-1, x/L])). \\ &\quad \mathbf{matrix}([0,0],[x/L-1, x/L]) \times (1/(\beta_2 \times EI)), \\ &\quad x, 4 \times L_{pI}, L - 4 \times L_{pJ}); \end{aligned} \tag{A.5}$$

- Computation of the target flexibility matrix using a *CPH* model (flexural terms only)

  - *CPH* model parameters

$$\begin{aligned} EI_{mod} \quad &: \quad EI \times (n_{Factor} + 1)/n_{Factor}; \\ K_{spring} \quad &: \quad n_{Factor} \times 6 \times EI_{mod}/L; \\ mp_2 \quad &: \quad [(\alpha_1)/(1 + n_{Factor} \times (1 - \alpha_1)), (\alpha_2)/(1 + n_{Factor} \times (1 - \alpha_2))]; \end{aligned} \tag{A.6}$$

  - Model flexibility matrix

$$\begin{aligned} f_2 \quad &: \quad \mathbf{matrix}([1/(mp_2[1] \times k_{spring}), 0], [0, 1/(mp_2[2] \times k_{spring})]); \\ f_2 \quad &: \quad f_2 + \mathbf{integrate}(\mathbf{transpose}(\mathbf{matrix}([0,0],[x/L-1, x/L])). \\ &\quad \mathbf{matrix}([0,0],[x/L-1, x/L]) \times (1/(EI_{mod})), \\ &\quad x, 0, L); \end{aligned} \tag{A.7}$$

- Solve the system of equations for obtaining unknowns

$$\begin{aligned} eq_1 \quad &: \quad f_1[1,1] = f_2[1,1]; \\ eq_2 \quad &: \quad f_1[1,2] = f_2[1,2]; \\ eq_3 \quad &: \quad f_1[2,2] = f_2[2,2]; \\ sol \quad &: \quad solve([eq_1, eq_2, eq_3], [\beta_1, \beta_2, \beta_3]); \end{aligned} \tag{A.8}$$

- Although the previous step already gives a solution for the problem, it is useful to obtain the solution without dependency on n_{Factor}. Thus, the solution, sol, is evaluated when n tends to infinity

$$\mathbf{limit}(sol, n_{Factor}, inf); \tag{A.9}$$

APPENDIX A. CHAPTER 2 - COMPUTATION OF THE SECTION FLEXURAL STIFFNESS MODIFICATION PARAMETERS

Appendix B

Chapter 6 - Model Validation

Table B.1: LA3 building - Comparison between results obtained with the developed models and the ones developed by Luco and Cornell (2000)

Ground Motion	Sa(T1) (g)	IDRmax (Luco and Cornell 2000)	Story of IDRmax (Luco and Cornell 2000)	ForceBased+Zero-length_Hardening				ForceBased+Zero-length_Bilin				ForceBased+Modified-Radau_Hardening				ForceBased+Modified-Radau_Bilin			
				Converged	IDRmax	Story (IDRmax)	Error	Converged	IDRmax	Story (IDRmax)	Error	Converged	IDRmax	Story (IDRmax)	Error	Converged	IDRmax	Story (IDRmax)	Error
LA01	0.678	0.021	2	Y	0.022	2	7.5	Y	0.022	2	7.3	Y	0.022	2.000	7.1	Y	0.022	2	7.6
LA02	1.269	0.025	2	Y	0.025	2	0.2	Y	0.025	2	1.7	Y	0.024	2.000	0.1	Y	0.025	2	2.8
LA03	0.882	0.022	2	Y	0.023	2	5.3	Y	0.023	2	5.6	Y	0.023	2.000	4.7	Y	0.023	2	7.5
LA04	0.531	0.014	3	Y	0.015	3	4.8	Y	0.015	3	4.8	Y	0.015	3.000	5.2	Y	0.015	3	5.2
LA05	0.490	0.017	2	Y	0.017	2	1.0	Y	0.017	2	1.0	Y	0.017	2.000	1.2	Y	0.017	2	1.2
LA06	0.415	0.013	2	Y	0.013	2	2.1	Y	0.013	2	2.1	Y	0.013	2.000	2.4	Y	0.013	2	2.4
LA07	0.647	0.018	2	Y	0.019	2	8.9	Y	0.019	2	9.0	Y	0.019	2.000	8.9	Y	0.019	2	9.0
LA08	0.892	0.024	3	Y	0.025	3	5.3	Y	0.026	3	5.9	Y	0.026	3.000	4.5	Y	0.026	3	5.3
LA09	1.084	0.029	2	Y	0.027	2	4.8	Y	0.027	2	6.6	Y	0.027	2.000	4.6	Y	0.027	2	5.7
LA10	0.934	0.027	3	Y	0.028	3	2.0	Y	0.028	3	2.3	Y	0.028	3.000	2.2	Y	0.028	3	2.5
LA11	0.810	0.034	3	Y	0.034	2	1.0	Y	0.034	2	1.2	Y	0.034	2.000	2.3	Y	0.034	2	2.8
LA12	0.628	0.023	3	Y	0.022	3	2.4	Y	0.022	3	3.1	Y	0.023	3.000	1.2	Y	0.022	3	1.6
LA13	1.072	0.029	3	Y	0.030	3	0.4	Y	0.030	3	0.8	Y	0.029	3.000	0.9	Y	0.030	3	0.4
LA14	1.263	0.029	3	Y	0.032	3	12.2	Y	0.033	3	14.1	Y	0.031	3.000	10.1	Y	0.032	3	12.4
LA15	1.208	0.037	2	Y	0.038	2	3.8	Y	0.039	2	4.1	Y	0.038	2.000	3.4	Y	0.039	2	3.9
LA16	1.410	0.041	3	Y	0.044	3	8.0	Y	0.045	3	9.6	Y	0.043	3.000	6.4	Y	0.044	3	8.3
LA17	0.612	0.020	3	Y	0.021	3	1.3	Y	0.021	3	1.4	Y	0.020	3.000	0.0	Y	0.020	3	0.2
LA18	0.873	0.027	3	Y	0.030	3	11.8	Y	0.030	3	10.7	Y	0.030	3.000	9.6	Y	0.030	3	11.7
LA19	0.792	0.020	3	Y	0.021	3	3.0	Y	0.021	3	3.0	Y	0.021	3.000	3.2	Y	0.021	3	3.3
LA20	1.208	0.028	2	Y	0.029	2	1.3	Y	0.028	2	2.5	Y	0.028	2.000	0.5	Y	0.028	2	2.1
LA21	2.698	0.046	3	Y	0.048	3	4.4	Y	0.050	3	8.7	Y	0.047	3.000	2.7	Y	0.050	3	9.6
LA22	2.643	0.059	3	Y	0.060	3	1.2	Y	0.062	3	5.9	Y	0.059	3.000	0.7	Y	0.062	3	4.6
LA23	0.716	0.024	3	Y	0.024	3	0.7	Y	0.024	3	1.1	Y	0.024	3.000	0.8	Y	0.024	3	0.3
LA24	1.453	0.046	3	Y	0.045	3	2.7	Y	0.048	3	4.4	Y	0.044	3.000	4.7	Y	0.047	3	1.4
LA25	1.966	0.054	3	Y	0.053	3	3.5	Y	0.061	3	12.1	Y	0.055	3.000	1.6	Y	0.060	3	9.8
LA26	2.295	0.055	3	Y	0.060	3	8.4	Y	0.063	3	14.9	Y	0.059	3.000	7.2	Y	0.062	3	13.5
LA27	0.996	0.058	2	Y	0.061	2	4.8	Y	0.063	2	9.0	Y	0.060	2.000	3.3	Y	0.063	2	8.1
LA28	1.421	0.049	3	Y	0.054	3	9.7	Y	0.054	3	9.2	Y	0.053	3.000	7.4	Y	0.053	3	7.1
LA29	0.946	0.022	3	Y	0.022	3	0.6	Y	0.022	3	0.3	Y	0.022	3.000	0.5	Y	0.022	3	0.3
LA30	0.874	0.033	2	Y	0.031	3	3.8	Y	0.031	2	3.7	Y	0.031	2.000	3.9	Y	0.031	2	4.6
LA31	2.002	0.036	3	Y	0.038	3	7.2	Y	0.040	3	10.9	Y	0.039	3.000	7.3	Y	0.037	3	3.8
LA32	2.107	0.042	3	Y	0.043	3	2.7	Y	0.044	3	4.3	Y	0.043	3.000	1.2	Y	0.043	3	2.9
LA33	1.787	0.033	3	Y	0.035	3	4.7	Y	0.035	3	4.6	Y	0.035	3.000	4.9	Y	0.035	3	4.8
LA34	1.218	0.029	1	Y	0.028	2	2.3	Y	0.029	2	0.2	Y	0.028	1.000	2.6	Y	0.029	2	0.3
LA35	1.106	0.078	3	Y	0.085	3	9.4	Y	0.092	2	17.6	Y	0.085	3.000	8.3	Y	0.090	2	15.2
LA36	1.511	0.066	2	Y	0.071	2	7.1	Y	0.065	3	1.4	Y	0.070	2.000	6.6	Y	0.066	3	0.7
LA37	1.522	0.077	2	Y	0.073	2	0.6	Y	0.081	2	4.9	Y	0.076	2.000	1.7	Y	0.081	2	5.3
LA38	1.821	0.121	2	Y	0.125	3	3.7	Y	0.246	3	104.0	N	0.122	3.000	0.9	N	0.213	3	
LA39	1.002	0.033	2	Y	0.037	3	10.6	Y	0.037	3	11.4	Y	0.036	3.000	7.8	Y	0.036	3	8.8
LA40	0.914	0.076	3	Y	0.084	3	10.5	Y	0.094	3	24.1	Y	0.082	3.000	7.9	Y	0.092	3	21.0
						Average Error :	4.6			Average Error :	8.7			Average Error :	4.0			Average Error :	5.6

Table B.2: LA9 building - Comparison between results obtained with the developed models and the ones developed by Luco and Cornell (2000)

Ground Motion	Sa(T1) (g)	IDRmax (Luco and Cornell 2000)	Story of IDRmax (Luco and Cornell 2000)	ForceBased+Zero-length_Hardening				ForceBased+Zero-length_Bilin				ForceBased+Modified-Radau_Hardening				ForceBased+Modified-Radau_Bilin			
				Converged	IDRmax	Story (IDRmax)	Error	Converged	IDRmax	Story (IDRmax)	Error	Converged	IDRmax	Story (IDRmax)	Error	Converged	IDRmax	Story (IDRmax)	Error
LA01	0.481	0.023	3	Y	0.026	8	13.7	Y	0.026	8	13.3	Y	0.027	8.000	16.3	Y	0.026	8	13.4
LA02	0.380	0.022	8	Y	0.018	1	14.4	Y	0.020	1	7.4	Y	0.020	1.000	8.7	Y	0.020	1	8.3
LA03	0.520	0.029	4	Y	0.030	4	3.3	Y	0.030	4	4.0	Y	0.029	4.000	1.0	Y	0.029	4	1.5
LA04	0.308	0.024	3	Y	0.026	2	7.6	Y	0.026	2	8.8	Y	0.025	2.000	5.1	Y	0.026	2	6.0
LA05	0.483	0.041	1	Y	0.044	1	7.1	Y	0.046	1	10.8	Y	0.043	1.000	5.1	Y	0.045	1	8.5
LA06	0.287	0.019	2	Y	0.021	2	8.8	Y	0.022	2	11.0	Y	0.021	2.000	9.4	Y	0.02	2	10.1
LA07	0.345	0.019	8	Y	0.018	8	2.5	Y	0.017	8	5.9	Y	0.018	8.000	4.5	Y	0.018	8	4.5
LA08	0.278	0.019	8	Y	0.018	8	5.4	Y	0.017	8	12.1	Y	0.017	8.000	10.8	Y	0.017	8	10.7
LA09	0.425	0.032	8	Y	0.033	7	4.3	Y	0.035	7	11.6	Y	0.035	7.000	9.9	Y	0.035	7	9.9
LA10	0.180	0.023	8	Y	0.024	8	4.8	Y	0.023	8	3.1	Y	0.023	8.000	3.3	Y	0.023	8	3.3
LA11	0.480	0.023	8	Y	0.024	8	2.6	Y	0.024	8	3.5	Y	0.024	8.000	2.8	Y	0.024	8	3.0
LA12	0.171	0.020	9	Y	0.019	9	7.0	Y	0.017	9	14.9	Y	0.017	9.000	16.2	Y	0.017	9	16.2
LA13	0.295	0.023	9	Y	0.023	8	0.4	Y	0.023	8	1.1	Y	0.023	8.000	1.3	Y	0.023	8	1.4
LA14	0.311	0.022	9	Y	0.023	9	2.9	Y	0.024	9	8.6	Y	0.023	9.000	6.3	Y	0.023	9	6.5
LA15	0.255	0.030	8	Y	0.030	8	1.4	Y	0.031	8	2.4	Y	0.031	8.000	2.1	Y	0.03	8	2.3
LA16	0.526	0.041	8	Y	0.041	8	0.1	Y	0.043	8	3.4	Y	0.042	8.000	0.8	Y	0.042	8	1.6
LA17	0.643	0.030	8	Y	0.029	8	4.7	Y	0.028	8	5.6	Y	0.029	8.000	3.9	Y	0.028	8	5.8
LA18	0.488	0.020	8	Y	0.020	8	0.3	Y	0.021	8	3.6	Y	0.021	8.000	3.4	Y	0.02	8	3.9
LA19	0.126	0.022	9	Y	0.021	8	2.7	Y	0.022	8	0.1	Y	0.022	8.000	0.2	Y	0.022	8	0.4
LA20	0.388	0.024	8	Y	0.025	8	1.2	Y	0.025	8	2.7	Y	0.025	8.000	3.2	Y	0.025	8	3.6
LA21	0.553	0.038	9	Y	0.038	8	0.3	Y	0.045	8	18.8	Y	0.038	8.000	1.4	Y	0.038	8	1.8
LA22	0.475	0.045	8	Y	0.042	8	7.6	Y	0.042	8	5.8	Y	0.042	8.000	6.6	Y	0.042	8	6.6
LA23	0.390	0.024	8	Y	0.024	8	1.4	Y	0.024	8	0.8	Y	0.024	8.000	0.6	Y	0.024	8	0.5
LA24	0.925	0.151	1	Y	0.139	2	8.1	N				Y	0.108	1.000	28.7	N	395.760	3	
LA25	0.415	0.033	8	Y	0.033	3	0.7	Y	0.034	2	3.0	Y	0.034	8.000	3.0	Y	0.034	8	2.1
LA26	0.856	0.042	7	Y	0.041	7	1.9	Y	0.040	7	4.6	Y	0.041	7.000	2.6	Y	0.040	7	3.2
LA27	1.046	0.040	8	Y	0.036	8	8.8	Y	0.035	8	12.4	Y	0.036	8.000	10.0	Y	0.035	8	12.5
LA28	0.794	0.035	2	Y	0.037	2	4.3	Y	0.037	2	5.7	Y	0.037	2.000	3.3	Y	0.037	2	3.5
LA29	0.349	0.027	8	Y	0.024	8	9.7	Y	0.025	8	5.3	Y	0.025	8.000	6.9	Y	0.025	8	5.7
LA30	0.678	0.065	1	Y	0.068	2	4.6	N				Y	0.059	2.000	9.9	Y	0.07	2	8.9
LA31	0.285	0.029	8	Y	0.030	8	4.8	Y	0.031	8	9.1	Y	0.031	8.000	6.6	Y	0.033	8	15.8
LA32	0.381	0.032	8	Y	0.034	8	4.6	Y	0.032	8	0.4	Y	0.032	8.000	0.1	Y	0.032	8	1.3
LA33	0.925	0.038	4	Y	0.037	4	3.9	Y	0.037	4	4.1	Y	0.039	4.000	1.6	Y	0.040	4	4.6
LA34	0.872	0.039	4	Y	0.038	4	2.4	Y	0.039	4	1.8	Y	0.039	4.000	0.0	Y	0.04	4	3.7
LA35	1.401	0.097	1	Y	0.102	2	5.1	N				Y	0.099	2.000	2.0	N	0.425	3	
LA36	1.559	0.104	1	Y	0.107	2	2.7	Y	0.140	1	34.5	Y	0.103	2.000	1.1	N	0.13	2	
LA37	0.834	0.060	3	Y	0.064	3	5.9	Y	0.084	3	40.0	Y	0.061	4.000	1.5	Y	0.066	3	10.0
LA38	1.091	0.070	4	Y	0.071	4	1.5	N				Y	0.072	4.000	2.4	Y	0.088	3	25.1
LA39	0.354	0.028	8	Y	0.029	8	1.3	Y	0.029	8	3.5	Y	0.029	8.000	2.5	Y	0.029	8	2.6
LA40	0.995	0.048	3	Y	0.050	3	5.4	Y	0.056	3	16.6	Y	0.048	3.000	0.1	Y	0.05	3	7.1
						Average Error :	4.5			Average Error :	8.4			Average Error :	5.1			Average Error :	6.4

Table B.3: LA20 building - Comparison between results obtained with the developed models and the ones developed by Luco and Cornell (2000)

Ground Motion	Sa(T1) (g)	IDRmax (Luco and Cornell 2000)	Story of IDRmax (Luco and Cornell 2000)	ForceBased+Zero-length_Hardening				ForceBased+Zero-length_Bilin				ForceBased+Modified-Radau_Hardening				ForceBased+Modified-Radau_Bilin			
				Converged	IDRmax	Story (IDRmax)	Error	Converged	IDRmax	Story (IDRmax)	Error	Converged	IDRmax	Story (IDRmax)	Error	Corverged	IDRmax	Story (IDRmax)	Error
LA01	0.147	0.018	19	Y	0.016	19	13.7	Y	0.015	19	14.4	Y	0.016	19.000	10.9	Y	0.015	19	14.4
LA02	0.078	0.013	19	Y	0.014	19	7.4	Y	0.014	19	7.6	Y	0.014	19.000	7.9	Y	0.014	19	7.7
LA03	0.269	0.027	4	Y	0.027	3	1.7	Y	0.030	3	9.1	Y	0.026	3.000	3.9	Y	0.030	3	9.4
LA04	0.267	0.043	4	Y	0.043	4	1.4	Y	0.037	4	13.2	Y	0.042	4.000	1.7	Y	0.046	4	6.1
LA05	0.344	0.037	4	Y	0.032	4	13.2	Y	0.027	3	25.8	Y	0.034	4.000	7.3	Y	0.035	4	5.4
LA06	0.197	0.023	4	Y	0.021	4	6.0	Y	0.022	4	3.2	Y	0.021	4.000	6.5	Y	0.022	4	3.2
LA07	0.344	0.022	3	Y	0.019	2	15.0	Y	0.020	3	11.6	Y	0.019	3.000	16.5	Y	0.020	3	12.2
LA08	0.131	0.014	2	Y	0.016	2	16.8	Y	0.016	2	17.9	Y	0.016	2.000	14.4	Y	0.016	2	16.9
LA09	0.196	0.030	2	Y	0.036	2	19.2	Y	0.037	2	23.3	Y	0.035	2.000	14.9	Y	0.037	2	22.3
LA10	0.188	0.019	3	Y	0.021	2	8.6	Y	0.021	2	9.8	Y	0.020	2.000	6.4	Y	0.021	2	8.9
LA11	0.109	0.020	14	Y	0.020	14	1.0	Y	0.020	14	0.7	Y	0.019	14.000	1.6	Y	0.019	14	1.7
LA12	0.097	0.012	19	Y	0.012	19	0.8	Y	0.012	1	0.9	Y	0.012	19.000	0.0	Y	0.012	1	0.5
LA13	0.142	0.018	12	Y	0.017	2	3.3	Y	0.017	2	2.9	Y	0.017	19.000	2.1	Y	0.017	2	1.9
LA14	0.166	0.021	3	Y	0.021	3	2.7	Y	0.022	3	4.1	Y	0.021	3.000	1.5	Y	0.021	3	2.6
LA15	0.132	0.015	19	Y	0.016	19	10.3	Y	0.016	19	10.1	Y	0.016	19.000	10.1	Y	0.016	19	9.0
LA16	0.085	0.023	18	Y	0.023	19	2.1	Y	0.023	19	2.0	Y	0.023	19.000	2.6	Y	0.023	19	3.1
LA17	0.123	0.012	2	Y	0.013	2	11.5	Y	0.013	2	12.7	Y	0.013	2.000	9.8	Y	0.013	2	10.8
LA18	0.116	0.023	2	Y	0.025	2	10.4	Y	0.026	2	12.5	Y	0.025	2.000	8.4	Y	0.025	2	11.5
LA19	0.057	0.016	20	Y	0.016	20	1.5	Y	0.016	20	1.4	Y	0.016	20.000	1.6	Y	0.016	20	2.6
LA20	0.111	0.016	4	Y	0.016	2	1.3	Y	0.016	2	1.9	Y	0.016	2.000	0.1	Y	0.016	2	1.1
LA21	0.237	0.025	19	Y	0.026	19	3.2	Y	0.026	19	3.6	Y	0.026	19.000	3.0	Y	0.026	19	2.6
LA22	0.235	0.027	18	Y	0.027	19	2.0	Y	0.027	19	2.4	Y	0.027	19.000	0.6	Y	0.027	19	0.5
LA23	0.175	0.017	4	Y	0.018	4	3.7	Y	0.018	4	4.7	Y	0.017	4.000	2.3	Y	0.017	4	2.8
LA24	0.456	0.042	5	Y	0.040	3	6.8	Y	0.044	5	3.4	Y	0.041	3.000	4.1	Y	0.043	3	1.8
LA25	0.215	0.028	3	Y	0.029	3	5.5	Y	0.032	3	14.0	Y	0.028	3.000	0.6	Y	0.031	3	9.8
LA26	0.138	0.025	3	Y	0.025	3	1.8	Y	0.026	3	2.5	Y	0.025	3.000	1.0	Y	0.025	3	1.4
LA27	0.200	0.034	4	Y	0.035	3	3.4	Y	0.036	3	5.1	Y	0.037	3.000	9.0	Y	0.038	3	12.2
LA28	0.190	0.043	2	Y	0.047	2	8.4	Y	0.050	3	17.0	Y	0.046	3.000	6.3	Y	0.050	3	16.2
LA29	0.186	0.016	18	Y	0.017	2	2.9	Y	0.017	2	6.0	Y	0.016	2.000	0.9	Y	0.018	2	10.3
LA30	0.497	collapse		N	20.111	2		N	0.708	4		N	98.888	3.000		N	10.853	5	
LA31	0.264	0.042	3	Y	0.049	3	18.6	Y	0.025	2	39.0	Y	0.049	3.000	16.7	Y	0.072	3	72.8
LA32	0.277	0.030	3	Y	0.033	3	9.5	Y	0.038	3	26.5	Y	0.033	3.000	8.2	Y	0.034	3	12.7
LA33	0.304	0.062	3	Y	0.066	3	6.5	N	1.798	5		Y	0.064	3.000	2.9	N	8.958	5	
LA34	0.274	0.061	3	Y	0.070	3	13.8	N	1.161	4		Y	0.067	3.000	9.5	N	0.112	4	
LA35	0.513	0.116	3	Y	0.114	3	1.8	N	0.777	4		Y	0.100	4.000	13.5	N	8.764	5	
LA36	0.501	0.132	2	Y	0.106	3	19.2	N	0.276	4		Y	0.101	4.000	23.4	N	8.736	5	
LA37	0.432	0.058	2	Y	0.063	3	9.5	N	1.540	5		Y	0.062	3.000	8.1	N	10.781	5	
LA38	0.483	0.091	3	Y	0.107	3	17.0	N	0.615	5		Y	0.095	3.000	4.3	N	11.183	5	
LA39	0.135	0.017	3	Y	0.018	3	2.9	Y	0.018	3	4.3	Y	0.018	3.000	1.7	Y	0.018	3	3.2
LA40	0.332	0.052	4	Y	0.054	4	3.5	N	0.066	3		Y	0.053	4.000	1.6	N	8.508	5	
						Average Error :	7.4			Average Error :	9.8			Average Error :	6.3			Average Error :	9.3